MAX PLANCK INSTITUTE
OF COLLOIDS
AND INTERFACES

Multiresponsive Complex Emulsions: Concepts for the Design of Active and Adaptive Liquid Colloidal Systems

Dissertation

zur Erlangung des akademischen Grades

"doctor rerum naturalium"

(Dr. rer. nat.)

in der Wissenschaftsdisziplin "Colloid and Interface Science"

eingereicht an der Mathematisch-Naturwissenschaftlichen Fakultät der Universität Potsdam

vorgelegt von

Saveh Arman Djalali

September 2022

aus Meerbusch

Hauptbetreuer: Prof. Dr. Dr. h.c. Markus Antonietti

Erstgutachter: Prof. Dr. Dr. h.c. Markus Antonietti

Direktor für „Kolloidchemie" am Max-Planck-Institut für Kolloid- und

Grenzflächenforschung und ordentlicher Professor an der Universität

Potsdam

Zweitgutachter: Prof. Dr. Andreas Taubert

Institut für Chemie – Lehrstuhl für Physikalische und Theoretische Chemie

Universität Potsdam

Drittgutachter: Prof. Dr. Matthias Karg

Lehrstuhl für Kolloide und Nanopartikel an der Heinrich-Heine Universität

Düsseldorf

Heinrich-Heine Universität Düsseldorf

Mentor: Dr. Lukas Zeininger

Emmy Noether Group Leader

Max-Planck-Institut für Kolloid- und Grenzflächenforschung

Declaration

Die vorliegende Dissertation, mit dem Titel „Multiresponsive Complex Emulsions: Concepts for the Design of Active and Adaptive Liquid Colloidal Systems", entstand im Zeitraum zwischen Januar 2020 und September 2022 am Max-Planck Institut für Kolloid- und Grenzflächenforschung, unter der Betreuung von Dr. Lukas Zeininger und Prof. Dr. Dr. h.c. Markus Antonietti. Hiermit erkläre ich gemäß der „Promotionsordnung der Mathematisch-Naturwissenschaftlichen Fakultät der Universität Potsdam" vom 18.09.2013, dass die vorliegende Arbeit eigenständig von mir verfasst wurde, Zitate kenntlich gemacht und ausschließlich die angegebenen Hilfsmittel und Quellen verwendet wurden.

This dissertation, with the title 'Multiresponsive Complex Emulsions: Concepts for the Design of Active and Adaptive Liquid Colloidal Systems', was written between January 2020 and September 2022 at the Max Planck Institute of Colloids and Interfaces, under the supervision of Dr. Lukas Zeininger and Prof. Dr. Dr. h.c. Markus Antonietti. In accordance with the "Doctoral Regulations of the Faculty of Mathematics and Natural Sciences of the University of Potsdam" of 18 September 2013, I hereby declare that this thesis was written by myself, that citations are clearly marked and that I used only the tools and sources indicated.

Potsdam, den   13.01.23

(Saveh Arman Djalali)

Abstract

Complex emulsions are dispersions of kinetically stabilized multiphasic emulsion droplets comprised of two or more immiscible liquids that provide a novel material platform for the generation of active and dynamic soft materials. In recent years, the intrinsic reconfigurable morphological behavior of complex emulsions, which can be attributed to the unique force equilibrium between the interfacial tensions acting at the various interfaces, has become of fundamental and applied interest. As such, particularly biphasic Janus droplets have been investigated as structural templates for the generation of anisotropic precision objects, dynamic optical elements or as transducers and signal amplifiers in chemo- and bio-sensing applications. In the present thesis, switchable internal morphological responses of complex droplets triggered by stimuli-induced alterations of the balance of interfacial tensions have been explored as a universal building block for the design of multiresponsive, active, and adaptive liquid colloidal systems. A series of underlying principles and mechanisms that influence the equilibrium of interfacial tensions have been uncovered, which allowed the targeted design of emulsion bodies that can alter their shape, bind and roll on surfaces, or change their geometrical shape in response to chemical stimuli. Consequently, combinations of the unique triggerable behavior of Janus droplets with designer surfactants, such as a stimuli-responsive photosurfactant (AzoTAB) resulted for instance in shape-changing soft colloids that exhibited a jellyfish inspired buoyant motion behavior, holding great promise for the design of biological inspired active material architectures and transformable soft robotics.

In situ observations of spherical Janus emulsion droplets using a customized side-view microscopic imaging setup with accompanying pendant dropt measurements disclosed the sensitivity regime of the unique chemical-morphological coupling inside complex emulsions and enabled the recording of calibration curves for the extraction of critical parameters of surfactant effectiveness. The deduced new "responsive drop" method permitted a convenient and cost-efficient quantification and comparison of the critical micelle concentrations (CMCs) and effectiveness of various cationic, anionic, and nonionic surfactants. Moreover, the method allowed insightful characterization of stimuli-responsive surfactants and monitoring of the impact of inorganic salts on the CMC and surfactant effectiveness of ionic and nonionic surfactants. Droplet functionalization with synthetic crown ether surfactants yielded a synthetically minimal material platform capable of autonomous and reversible adaptation to its chemical environment through different supramolecular host-guest recognition events. Addition of metal or ammonium salts resulted in the uptake of the resulting hydrophobic complexes to the hydrocarbon hemisphere, whereas addition of hydrophilic ammonium compounds such as amino acids or polypeptides resulted in supramolecular assemblies at the hydrocarbon-water interface of the droplets. The multiresponsive material platform enabled interfacial complexation and

thus triggered responses of the droplets to a variety of chemical triggers including metal ions, ammonium compounds, amino acids, antibodies, carbohydrates as well as amino-functionalized solid surfaces.

In the final chapter, the first documented optical logic gates and combinatorial logic circuits based on complex emulsions are presented. More specifically, the unique reconfigurable and multiresponsive properties of complex emulsions were exploited to realize droplet-based logic gates of varying complexity using different stimuli-responsive surfactants in combination with diverse readout methods. In summary, different designs for multiresponsive, active, and adaptive liquid colloidal systems were presented and investigated, enabling the design of novel transformative chemo-intelligent soft material platforms.

Zusammenfassung

Komplexe Emulsionen sind Dispersionen kinetisch stabilisierter mehrphasiger Emulsionströpfchen, die aus zwei oder mehreren nicht mischbaren Flüssigkeiten bestehen und eine neuartige Materialplattform für die Herstellung aktiver und dynamischer weicher Materialien darstellen. In den letzten Jahren haben komplexe Emulsionen aufgrund ihres intrinsisch rekonfigurierbaren morphologischen Verhaltens, dass auf ein einzigartiges Kräftegleichgewicht zwischen den an den verschiedenen Grenzflächen wirkenden Grenzflächenspannungen zurückzuführen ist, zunehmendes wissenschaftliches Interesse erfahren. So wurden insbesondere zweiphasige Janus-Tropfen als strukturelle Vorlagen für die Erzeugung anisotroper Präzisionsobjekte, dynamischer optischer Elemente oder als Wandler und Signalverstärker in Chemo- und Bio-Sensorik-Anwendungen untersucht. In der vorliegenden Arbeit wurden schaltbare interne morphologische Veränderungen komplexer Tröpfchen erforscht, die durch Stimulus-induzierte Verschiebungen des Grenzflächenspannungsgleichgewichts ausgelöst werden. Diese können als universelle Bausteine für das Design multiresponsiver, aktiver und adaptiver flüssiger kolloidaler Systeme dienen. Es wurde eine Reihe von grundlegenden Prinzipien und Mechanismen zur Beeinflussung des Grenzflächenspannungsgleichgewichtes erforscht, die die gezielte Entwicklung von formverändernden, sich an Oberflächen bindenden und in Reaktion auf chemische Stimuli verändernden Emulsionskörpern ermöglicht. Die Kombination des einzigartigen responsiven Verhaltens von Janus-Tropfen mit maßgeschneiderten Tensiden erlaubt die Erschließung von biologisch inspirierten aktiven Materialarchitekturen. So führte beispielsweise die Funktionalisierung von Janus-Tropfen mit einem photo-responsiven Tensid (AzoTAB) zu formverändernden weichen Kolloiden, die ein von Quallen inspiriertes Schwimmverhalten zeigten und damit vielversprechend für die Anwendung im Forschungsfeld der transformierbaren „soft-robotics" sind.

Die *in-situ*-Beobachtung von sphärischen Janus-Emulsionströpfchen mit einem Seitenansichts-Mikroskop und begleitenden Pendant-Drop-Messungen ermöglichten es das Empfindlichkeitsregime der einzigartigen chemisch-morphologischen Kopplung innerhalb komplexer Emulsionen offenzulegen. Die resultierende Kalibrierungskurve erlaubt die Extraktion von kritischen Parametern der Tensidwirksamkeit. Die daraus abgeleitete neue "responsive drop"-Methode ermöglicht eine einfache, kosteneffiziente Quantifizierung der kritischen Mizellenkonzentrationen (CMCs) und einen Vergleich der Wirksamkeit verschiedener kationischer, anionischer und nichtionischer Tenside. Darüber hinaus ermöglichte die Methode eine aufschlussreiche Charakterisierung Stimuli-responsiver Tenside und die Überwachung des Einflusses anorganischer Salze auf die CMC und die Tensidwirksamkeit ionischer und nichtionischer Tenside. Die Funktionalisierung von Tröpfchen mit synthetischen Kronenether-Tensiden führte zu einer synthetisch minimalen Materialplattform, die in

der Lage ist, sich durch verschiedene supramolekulare Wirts-Gast-Erkennungsereignisse selbständig und reversibel an ihre chemische Umgebung anzupassen. Die Zugabe von Metall- oder Ammoniumsalzen hatte eine Aufnahme der resultierenden hydrophoben Komplexe in die Kohlenwasserstoff-Hemisphäre zur Folge, während die Zugabe von hydrophilen Ammoniumverbindungen wie Aminosäuren oder Polypeptiden zu supramolekularen Assemblierungen an der Kohlenwasserstoff-Wasser-Grenzfläche der Tröpfchen führte. Die multiresponsive Materialplattform ermöglicht die Grenzflächenkomplexierung und damit die morphologische Reaktion der Tröpfchen auf eine Vielzahl von chemischen Triggern, darunter Metallionen, Ammoniumverbindungen, Aminosäuren, Antikörper, Kohlenhydrate sowie aminofunktionalisierte feste Oberflächen.

Im letzten Kapitel werden die ersten dokumentierten optischen Logikgatter und kombinatorischen Logikschaltungen auf der Grundlage von komplexen Emulsionen vorgestellt. Zur Realisierung von Tropfen-basierten Logikgattern unterschiedlicher Komplexität wurden die einzigartigen rekonfigurierbaren und multiresponsiven Eigenschaften komplexer Emulsionen ausgenutzt. Dabei wurden Stimuli-responsive Tenside in Kombination mit unterschiedlichen Auslesemethoden verwendet. Zusammenfassend wurden verschiedene Designs für multiresponsive, aktive und adaptive flüssige kolloidale Systeme vorgestellt und untersucht, die die Entwicklung neuartiger chemo-intelligenter weicher Materialplattformen ermöglichen.

„Suche nicht nach Glück. Sei glücklich."

— Dr. med. Mehdi Djalali (1942-2021)

Table of Contents

1   Introduction

»Nobody ever figures out what life is all about, and it doesn't matter. Explore the world. Nearly everything is really interesting if you go into it deeply enough.«

- Richard Feynman

According to the quote above by Richard Feynman, a famous US physicist and Nobel laureate of 1965 who contributed to the theory of quantum electrodynamics (QED), even seemingly simple structures and objects offer a tremendous depth if only they are studied carefully enough.[1] At the latest after the invention of the microscope in the 16th-17th century, it became clear that a whole cosmos of complex structures is hidden in a world that is not accessible by the mere eye, which is equally impressive and versatile as the macroscopic world that surrounds us.[2]

If you look at a weevil, for example, it may appear at first glance to be a primitive creature with a conspicuous iridescent body shell. However, if you start to examine the brilliant, metallic shine of the shell more closely, it turns out that nanostructures are arranged in three-dimensional patterns in the scales of chitin, similar to the atoms or molecules in a crystal grid.[3] These structures influence the path of incoming light waves resulting in the appearance of a special type of coloration, which are structural colors. The chitin shells of most insects shine with the help of structural colors.[4] Some insects have extremely thin grooves on their shells, which then act as diffraction grids.[5] Most commonly, insects use stacks of gossamer platelets that reflect light. By the superposition of the light waves, certain wavelengths are cancelled out, resulting in a specific color.[6] The color impression created relies on the angle of the incident light. Depending on the viewing angle, this results in different color tones.[6] The three-dimensional nanostructures of the weevils, which are also referred to as photonic crystals, are so specifically arranged in each scale that their color appears the same from every viewing angle, which proves very useful as a warning color or camouflage color.[7]

If we look at even smaller structures such as macromolecules like deoxyribonucleic acid (DNA), we see that they are composed of a few individual molecules. To be precise, they are made of six different chemical building blocks: one sugar, a phosphate group, and four different nucleic bases.[8] But the many proteins derived from the sequence of nucleic bases are largely responsible for the highly complex processes within an organism.[9] And so one can go on and on and consider atomic components. Leaving out dark matter, all matter in the universe consists of three distinct atomic building blocks, namely protons, neutrons and electrons.[10] Nevertheless, everything we see, including ourselves is a product of the emergence of these three building blocks.[11]

1 Introduction

Once this seemingly universal principle has been internalized, even such simple-looking systems as, for example, two-phase emulsion droplets, which are the subject of this thesis, offer an unbelievable wealth of exciting and versatile aspects that are worth discovering and illuminating. In fact, often the little things in life are quickly overlooked, but are of no less importance.

2   Motivation

Living organisms require constant information processing for survival.[12] A cell as an independent living being or as a building block of a complex organism can be viewed as a dynamic information-processing system that responds to and interacts with a constantly changing environment.[13] In cells, information is being processed and transmitted at multiple levels, from the gene regulatory network that coordinates operations between the genetic information encoded in the cell's DNA and its intracellular information-processing infrastructure (RNA and proteins) to chemical pathways, to the interaction with the environment.[14] How this multilevel information processing, including enzymatic amplification, regulatory feedback, and parallel metabolic pathways, is achieved is still poorly understood.[15] For example, what a cell interprets as information and what as noise in a highly dynamic environment remains an open question.[16] Furthermore, in biological information processing, sustainable, energy- and resource-saving processes are carried out in the ongoing operation of the cell.[13]

To make decisions, cells process information according to logical rules and are therefore comparable to man-made computers.[13, 14, 17] However, natural systems that can be considered biomolecular computers differ in structure and function from silicon-based information processing devices.[18, 19] Classic computers process information based on binary encoding, whereas biological systems process information on several levels, from individual proteins to cellular networks, which allows higher information throughput.[20] This characteristic, combined with their adaptability, gives them a special status as a source of inspiration for the future development of novel information processing systems, including bio- and chemosensors that can emulate reactions and interactions of natural systems, providing a direct understanding of their environment.[21]

To better examine these complex behaviors, it may be beneficial to design and investigate analogous systems that mimic the processes in biological systems but have a much simpler architecture.[22] In an era of growing resource scarcity, there is a need for cheap and efficient solutions that are inspired by nature and keep pace with the increasing demands of a modern, environmentally conscious society.[23] Within this context, the aim of the thesis is to create concepts for the design of soft colloidal systems as a cost-efficient and stimuli-responsive material platform to decipher the active and adaptive molecular dynamics of biological information processing and to pave the way for the next generation of automated, adaptive and parallel processing sensing devices.

3 Theoretical Background

3.1 Emulsions

Emulsions are a class of disperse systems consisting of one or more immiscible fluid phases dispersed within another immiscible liquid phase.[24, 25] Emulsions can be single emulsions (one phase dispersed in another) or multiple emulsions (emulsions of emulsions).[26] A dispersed phase or internal phase is referred to as a constituent that forms droplets in an emulsion system; whereas a continuous phase is the surrounding liquid in which droplets are suspended. Depending on the spatial distribution of the oil or water phases, emulsions can be divided into two different types. If an oil is dispersed in a water phase, it is called an oil-in-water (O/W) emulsion.[27] Common examples of this type of emulsion are milk, cream or vinaigrette.[28] Conversely, if water is dispersed in an oil phase, one speaks of a water-in-oil (W/O) emulsion, as in the case of butter and margarine (Figure 1).[26, 28] Due to their special properties, emulsions are ubiquitous in daily life and in various industries, e.g. cosmetics (shampoos), food (milk, ice cream), agriculture (pesticides) and pharmaceuticals (vaccine adjuvants).[29-32] A material comprising both an oil and water allows for incorporation of selectively soluble reagents to either phase, increasing system complexity and specialized delivery capabilities for desired applications. For example, oil-soluble active pharmaceutical ingredients can be applied dermally in the form of oil-in-water emulsions, which allows the medication to retain a high water content, providing the skin with sufficient moisture.[33] The high water content also leads to a cooling effect, which can relieve itching. In addition, O/W emulsions are easy to apply, are absorbed quickly and do not leave a greasy film.[29]
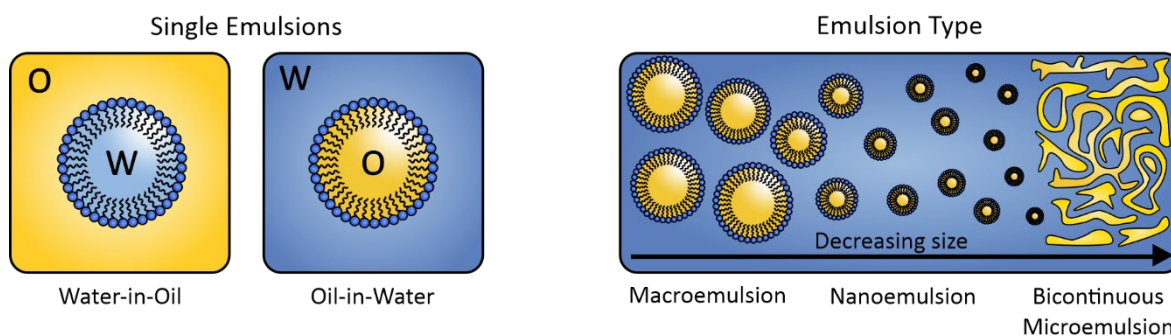
Figure 1. Schematic representations of emulsion systems (left) and different types, classified by size (right).

An emulsion can further be classified by their droplet diameter: Macroemulsions have a droplet diameter of 1 µm – 1 mm, nanoemulsions have a diameter of 20 – 500 nm, whereas microemulsions consist of either globular or interconnected bicontinuous domains with varying diameters of 1 – 100 nm (Figure 1).[25, 34, 35] In addition, different size classifications of emulsion types can be found. The most important differentiating factor between micro- and macroemulsions is their thermodynamic

stability.[25, 36] While microemulsions can spontaneously form from separate phases into dispersions because they are thermodynamically stable, macro- and nanoemulsions - the focus of this thesis - are thermodynamically unstable systems and can only be kinetically stabilized.[36] This means an energy input and emulsifying agents are needed to compensate the unfavorable thermodynamics.

3.1.1   Emulsion Formation and Stability

The process of emulsion formation is called "emulsification". There are several methods of emulsification, including shaking, mixing with rotor-stator systems, high-pressure homogenizers and ultrasound generators, or liquid injection through porous membranes.[25] The emulsification process usually requires a significant amount of mechanical energy, to disperse one of the liquids in the form of small droplets in the continuous phase.[37] Upon droplet formation, the interface between the phases is significantly increased. The liquids tend to reduce their interface to a minimum; therefore, an increase in interface is possible only if sufficient energy is supplied.[26] The work that must be expended on drop division is:

$$\Delta W = \gamma \Delta A \tag{1}$$

where ΔW is the work to be expended, ΔA is the increase in interface and the interfacial tension γ is the proportionality factor between the phases to be emulsified. The interfacial tension results from unequal cohesive forces acting on molecules located inside the phase and on molecules sitting at the interface.[38] The molecules of a liquid, which are located inside the phase, experience equal cohesive forces in all directions, resulting in a net force of zero. However, molecules localized at the interface are not surrounded by the same molecules on all sides and thus do not experience attractive interactions from all directions (Figure 2). In consequence, the molecules at the interface are pulled towards the inside of the phase, resulting in a directed force – the interfacial tension γ.[38] Depending on the phases involved, this force is either called surface tension σ when considering air/liquid or air/solid interfaces or interfacial tension γ, if the interface is between any two phases.[24]
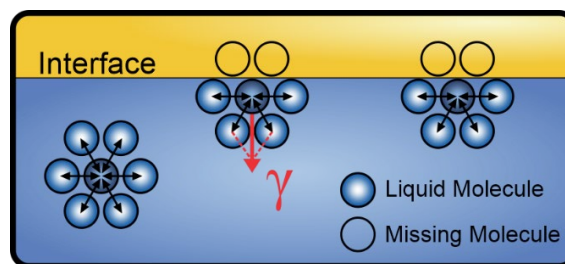

Figure 2. Illustration of the cohesive forces acting on molecules of a liquid and the resulting interfacial tension γ, which is directed to the interior of the phase.

3 Theoretical Background

As long as the interfacial tension is not γ = 0, an emulsion is very susceptible to coalescence processes, which leads to a decrease in ΔA and subsequently in ΔW.[24] The thermodynamic stability of an emulsion system can be considered using the Gibbs-Helmholtz equation:

$$\Delta G_{form} = \gamma \Delta A - T \Delta S_{conf} \tag{2}$$

where ΔG_{form} is the change in free energy in forming dispersions from separate phases, ΔA is the change in interfacial surface area, γ is the interfacial tension between the phases, T is temperature, and ΔS_{conf} is the configuration entropy. As in the previous equation, the first term γΔA describes the change in interfacial free energy for more surface area between two immiscible phases and is thus positive. The entropy (ΔS_{conf}) is a measure of the extent of disorder in the system and hence measures the extent of size reduction of the organic phase (or increase in droplet number). The increasing disorder during the formation of an emulsion means a positive ΔS contributing to the stability. Since in macroemulsions generally γΔA >> TΔS_{conf}, ΔG_{form} becomes positive, which leads to emulsification being non-spontaneous and thermodynamically unfavorable.[39] Without stabilizing components called emulsifiers, which are reducing the interfacial tension γ between the liquid phases, and therefore the γΔA term, the dispersed droplets would rapidly phase separate to reduce the interfacial area between the immiscible phases. The reduction of the interfacial free energy results in a lower ΔG_{form}, meaning the system is relatively more thermodynamically stable, albeit with a positive ΔG_{form}. However, emulsifiers also provide a barrier at the interface and prevent coalescence through a steric barrier or through electrostatic interactions, which provides kinetic stability to the emulsion system. As a result, macroemulsions stabilized with emulsifiers are thermodynamically metastable.[40]

Due to the metastability of emulsions, they change their properties with time. There are several paths that can lead to emulsion rupture, also known as demulsification. Evolution and eventually demulsification proceeds through a series of steps, which can be flocculation, creaming/sedimentation and Ostwald ripening (Figure 3).[27] In flocculation, smaller droplets are attracted to each other, forming larger aggregates without losing their droplet identity. It is the result of the van der Waals attraction between the emulsion droplets and occurs when there is no sufficient repulsion to keep the droplets apart to distances where the van der Waals attraction is weak.[41] Flocculation can be reversible by supplying energy to the system through shaking or stirring. Another emulsion instability phenomenon is gravitational separation, which occurs as creaming or sedimentation. They appear in almost all emulsion systems where there is a difference in density between the two phases. If the dispersed phase is the denser of the two phases, the separation process is called sedimentation, while

the reverse case is called creaming.[42] The gravitational separation rate v of the emulsion droplets can be described by the Stokes' law:[43]

$$v = \frac{2}{9} \cdot \frac{r^2 \cdot g(\rho_1 - \rho_2)}{\eta}$$

(3)

where r^2 is the spherical radius of the droplet, g is the acceleration due to gravity, ρ_1 is the density of the dispersed phase, ρ_2 is the density of the continuous phase and η is the viscosity of the continuous phase. Simple strategies to suppress sedimentation or creaming are minimizing the density difference between the phases, adding weighting agents to the phase with the lower density, reducing the droplet radius or increasing the viscosity of the continuous phase.[26]

Ostwald ripening results from the mutual solubility of the liquid phases, which is not negligible. In emulsions, which are usually polydisperse, the smaller droplets have greater solubility compared to the larger ones because solubility increases as the radius of the droplet decreases.[44] The smaller droplets shrink and their molecules diffuse into the bulk and deposit on the larger droplets (Figure 3). Over time, the size distribution of the droplets shifts to larger volumes. By using emulsifiers that are strongly adsorbed at the emulsion interface, such as polymeric surfactants, Ostwald ripening can be significantly reduced.[28]
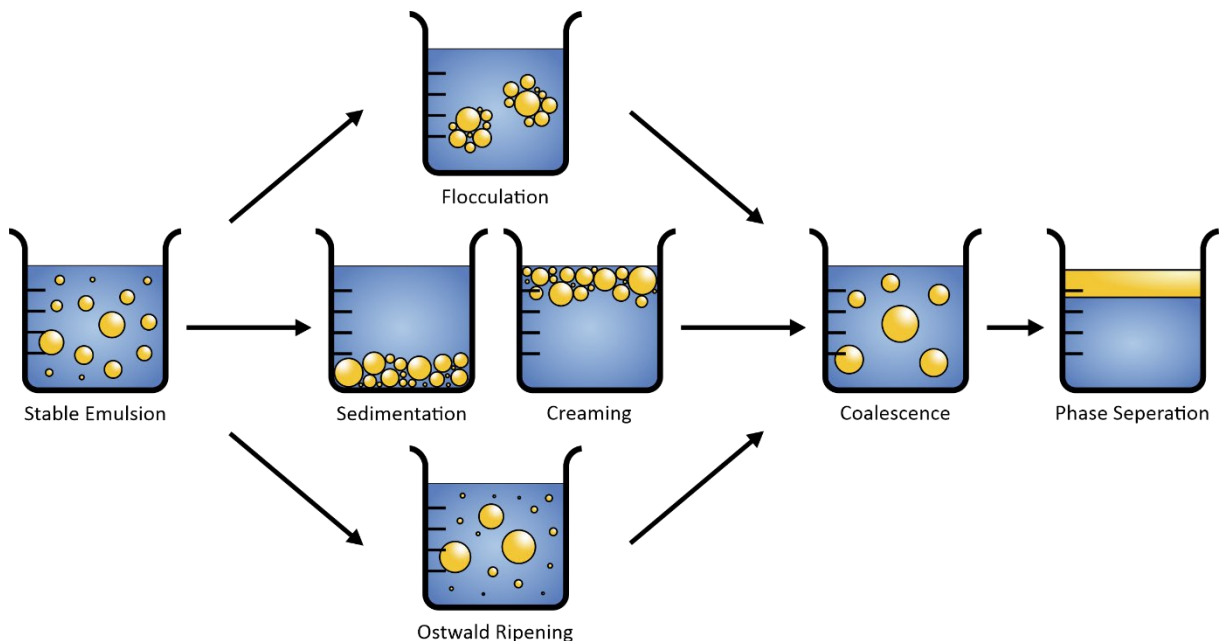

Figure 3. Schematic representation of instability mechanisms of emulsions.

When two or more droplets come into contact and merge to form a single droplet of greater volume, this event is called coalescence. Droplets merge when the emulsifying agent layer does not provide a

sufficient steric or electrostatic barrier.[41] Such a process is energetically favorable as long as the interfacial tension value is positive. In addition, the merging of the droplets significantly reduces the interfacial area between the immiscible liquids, thus reducing the γΔA term of equation 2. If this process continues until two separate continuous phases have formed, it is called demulsification (Figure 3).[27] The process is macroscopically apparent consequence of the microscopic process of droplet coalescence. In such an event, the identity of individual droplets is lost, along with the physical and chemical properties of the emulsion.

3.1.2   Classification of Emulsifiers and Stabilizers

A distinction can be made between substances that reduce the interfacial tension between the immiscible phases, which are called emulsifiers and those that create a physical barrier between the emulsion droplets without affecting the interfacial tension, known as stabilizers.[27] Of the possible additives, most are called surfactants because they are effective in lowering the interfacial tension between the two liquid phases. Other additives such as polymers and solid particles function primarily as stabilizers, rather than emulsifiers.[24]

Surfactants, which are amphiphilic molecules, usually consist of a polar or hydrophilic head group and a nonpolar or hydrophobic tail.[45] They are classified according to their head group type as ionic (anionic and cationic), nonionic, and amphoteric (zwitterionics) surfactants. Nonionic surfactants have polar headgroups and they include, among other representatives, glycol and glycerol esters, polyoxyethylene esters, alkyl crown ethers, sorbitan esters (Spans), polysorbates (Tweens) and alkyl polyglycosides.[45, 46] The hydrophobic part of the nonionic surfactant may be alkyl, fluoroalkyl or steroidal in nature. Examples of commercial nonionic hydrocarbon (HC) and fluorocarbon surfactants (FC), which have been used in this work, are Trition (Triton X-100) that consists of a hydrophilic polyethylene oxide chain and a hydrophobic aromatic hydrocarbon group and Zonyl FS-300, which consists of a hydrophilic polyethylene oxide chain and a fluorinated alkyl chain (Figure 4). Anionic surfactants contain anionic functional groups at their head, such as sulfonate, sulfate (e.g. sodium dodecyl sulfate, SDS), phosphate, and carboxylates.[34] Whereas cationic surfactants contain cationic functional groups at their head, such as pH-dependent primary, secondary, or tertiary amines and permanently charged quaternary ammonium cations as in the case of the surfactant cetyl trimethylammonium bromide (CTAB) (Figure 4).[47] Emulsion stabilization by electrostatic repulsion is generated by the adsorption of ionic surfactants that form a charged layer at the interface. A double layer is then created by the counterions, which creates charged droplets. Each of the charged droplets

is repelled due to strong repulsive forces, thus preventing coalescence.[26] Figure 4 shows the chemical structures of some of the previously mentioned surfactants.
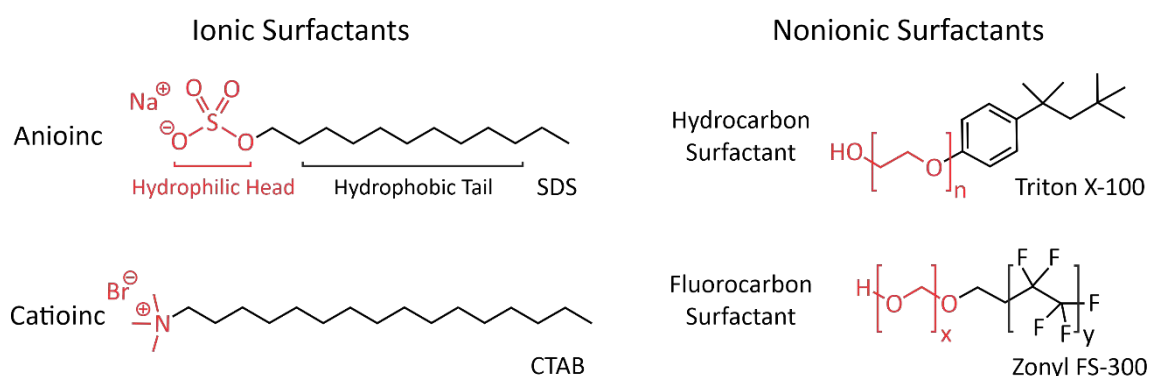
Figure 4. Examples of ionic surfactants (left): sodium dodecyl sulfate (SDS), cetyl trimethylammonium bromide (CTAB) and nonionic surfactants (right): Triton X-100 and Zonyl FS-300.

The molecular structure and geometry of surfactants determines the type of emulsions they can stabilize. Since the selection of a suitable emulsifier is of crucial importance for many applications, chemists have developed various rules and systems over the years to facilitate this selection as a user. For example the Bancroft rule, named after Wilder Dwight Bancroft, an American physical chemist who proposed it in the 1910s, states that the type of emulsion is dictated by the emulsifier and that the phase in which an emulsifier is more soluble constitutes the continuous phase.[48, 49] Even though many deviations from this general rule are documented, it still finds its application today as a practical rule of thumb.[50, 51]

In 1954, William C. Griffin formally introduced the hydrophilic-lipophilic balance (HLB) scale to characterize the tendency of a surfactant to form W/O or O/W emulsions.[52] Griffin proposed formulas for the HLB value calculation for molecular structures, producing numbers between 0 and 20 on an arbitrary dimensionless scale. The HLB values are a direct measure of the hydrophilic character of a surfactant: The larger the value, the more hydrophilic the compound. Surfactants with high HLB values (>10) tend to form O/W emulsions whereas surfactants with low HLB values (<6) act as good emulsifier for W/O emulsions.[34] Although the HLB system does not always provide a sufficient prediction for a given system, the system was subsequently expanded by others and has found extensive practical use.[53]

One characteristic property of surfactants is that they spontaneous aggregate in solution and form well-defined structures such as spherical micelles, bilayers, cylinders, etc..[45] At low concentrations, the surfactants are dissolved as single molecules. In aqueous solutions, the surfactants tend to adsorb

at the air-water interface, with their hydrocarbon tails oriented towards the vapor phase.[34] The surface tension decreases strongly with increasing concentration. At a certain concentration, the critical micelle concentration (CMC), this decrease stops.[54] Above the CMC, the surface tension remains almost constant and the surfactant molecules assembly into ordered micelle structures (Figure 5). Both phenomena, the adsorption at the air-liquid interface as well as the assembly into ordered micelle structures are entropically driven by the so called hydrophobic effect. The effect can be explained as follows: The overall entropy gain by disrupting the hydrogen-bond networks of the water molecules around the hydrophobic tails during assembly is higher than the entropy loss resulting from ordered assembly. To measure the CMC value, which is a major characteristic of surfactants, many methods have been developed. Most of them are measuring changes in physical parameters such as surface or interfacial tension, electric conductivity, absorbance, or fluorescence.[55] The most common techniques for determining interfacial tensions and CMC values at liquid-liquid interfaces are based on force or optical tensiometers, such as the Du-Noüy ring, the Wilhelmy plate, the pendant drop or the spinning drop method.[38]
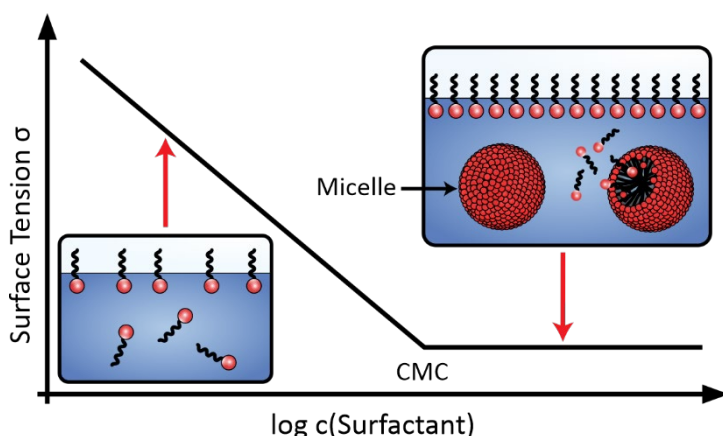
Figure 5. Schematic illustration of the surface tension as a function of surfactant concentration.

As mentioned at the beginning of the chapter, besides the classical surfactants, also polymers and even biopolymers such as polysaccharides and proteins can act as emulsifiers (Figure 6).[56] For example, caseins, in monomeric or micellar form, or whey proteins are the primary emulsifiers in diary emulsions.[57] Because of their amphiphilic structure, milk proteins function as surface-active ingredients in emulsions and they contribute to the stability of the emulsion droplets by a combination of electrostatic and steric stabilization mechanisms.[58] Apart from the tendency of a less sufficient effectiveness at lowering interfacial tensions, the adsorption process for polymers is generally very slow relative to the timescale of the emulsification process due to their molecular size.[59] The same applies for stabilizing colloids.[60]

Emulsions stabilized solely by particles are referred to as Pickering emulsions (Figure 6).[61] In addition, due to their "surfactant-free" character, Pickering emulsions are often used for cosmetic and pharmaceutical applications to eliminate adverse effects of molecular surfactants such as irritation.[62, 63] Many types of solid and gel particles have been demonstrated to be efficient stabilizers for Pickering emulsions, such as calcium carbonate and barium sulfate nanoparticles, silica, laponite, and magnetic particles.[60, 64] Particles can be non-amphiphilic particles (e.g. clay or silica) or amphiphilic Janus particles (named after the two-faced Roman god)[65], which consist of two hemispheres with different surface polarities.[66] The adsorption of particles at the interface is driven by the resulting reduction in interfacial area between the liquids. A mechanical barrier is formed in Pickering emulsions through the formation of a thick layer of solid particles, preserving the Pickering emulsions from coalescence and Ostwald ripening. The adsorption of particles is dependent on their wettability.[67] In the case of O/W Pickering emulsions, the particles are wetted more by the water phase (hydrophilic particle). Conversely, W/O are formed when particles are wetted more by the oil phase (hydrophobic particle). Optimal stabilization is achieved when the particles are equally wetted by both phases (particle is not too hydrophilic or too hydrophobic). Figure 6 schematically shows the stabilization of emulsions by the various emulsifiers and stabilizers discussed above.
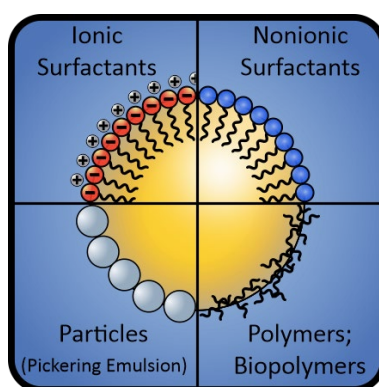
Figure 6. Schematic representation of an oil-in-water emulsion stabilized with surfactants, polymers/biopolymers and particles.

3.1.3   Emulsification Techniques

The principle of the emulsion production is based on the creation of new interfaces by shaking, stirring, beating, turbulent mixing, by the effect of shear forces or by ultrasound treatment.[68] Thus, the lower the interfacial tension of the liquids to be emulsified, the easier it is to form emulsions. The production of emulsions is always associated with a division of the inner phase, which requires the supply of mechanical or chemical energy.[69] Each emulsification technique comes with different advantages and

disadvantages. Often one property is compromised in favour of another, e.g. monodispersity with low throughput or small droplet sizes with high energy input. Depending on the application and the requirements of the emulsion to be produced, it is necessary to weigh up which properties are relevant. Among the most common emulsification techniques, a rough distinction can be made between four different categories: rotor-stator systems, fluid mechanics, ultrasonic generators and microstructured systems.[27, 68, 69]

Rotor-stator systems are the most widely used systems in the industry for producing surfactant-stabilized emulsions and Pickering emulsions.[70] They are easy to handle, cost-effective and very flexible to use. The simplest form of a rotor-stator system is a rotating unit (stirrer) in a static component, the stirring tank (stator) (Figure 7). The size of the emulsion droplets is mainly determined by the shear forces generated in the turbulent zone in the gap between the stirrer and the stator. With increasing stirring intensity and duration, the droplet size decreases. A disadvantage of this method is the high polydisersity that is observed in a given sample, caused by a highly inhomogeneous and unspecific energy input.[71] In fluid mechanic systems such as vortex mixers, a uniform energy input provides better mixing of the liquids and thus tends to result in a smaller size distribution of the emulsion droplets.[70]

The ultrasonic process has been known for a long time in research as a method for the production of emulsions with particularly small droplet sizes (< 200 nm).[72] The emulsifying effect is produced by a sonotrode, which performs mechanical oscillations in the ultrasonic range (> 20 kHz) (Figure 7). Another possibility of generating sound waves is a liquid pipe.[70] Here, a metal plate is made to vibrate by the flow of a liquid. As the ultrasonic waves pass through the liquid mixture, alternating high pressure (compression) / low pressure (expansion) cycles create tiny cavities the vessel (vacuum bubbles).[73] During the compression/expansion cycles, the vacuum bubbles grow until they reach a size at which they cannot absorb any more energy. When the vacuum bubbles implode, ultrasonic elongational stress forces and turbulences are created, that break up the droplets of the dispersed phase and mix the liquids evenly together. High-performance ultrasonic emulsification reliably produces nanoemulsions with a very uniform size distribution.[74] This makes ultrasonic emulsification the preferred method for producing oil-in-water micro- and nanoemulsions with high emulsion stability. However, ultrasonic emulsification is not applicable for the preparation of macroemulsions.[75]
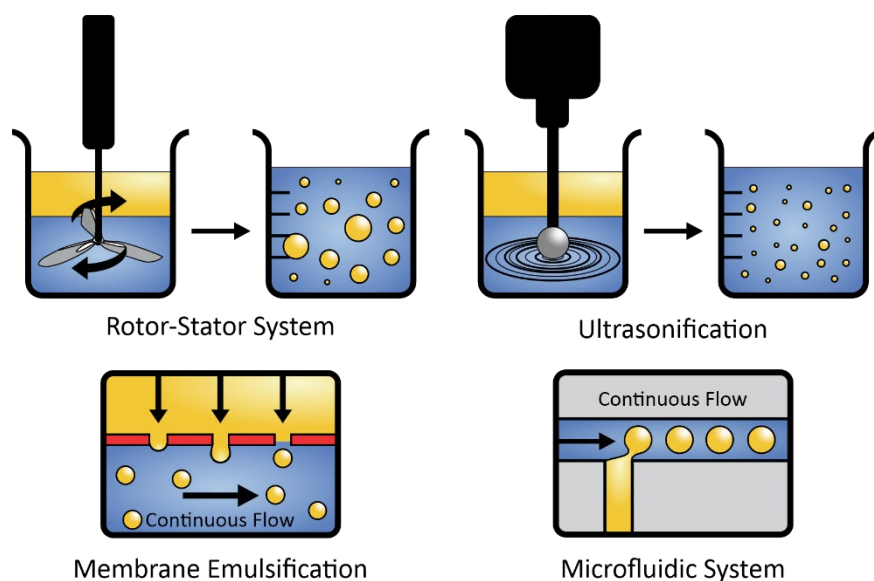
Figure 7. Illustration of different emulsification techniques for the production of single emulsions.

For the formation of emulsions with very defined droplet sizes, microstructured systems use miniaturized components such as membranes and microchannels.[70, 76] In membrane emulsification, the disperse phase or a pre-mixture is forced through a membrane, forming small droplets at the pore exits of the membrane (Figure 7). The continuous phase is guided past the membrane with a flow. This entrains the droplets and thus disperses them. This can be done either continuously or in a batch process. In the batch process, the flow is usually generated by an agitator in the vessel.[77] By using the membrane emulsification method, much narrower droplet distributions can be produced compared to other methods. In addition, a large variation of the average droplet diameter is possible due to the large selection of membranes. However, the main limitation of emulsification with membranes is the low flow rate associated with monodisperse emulsions, which is a major problem for industrial applications.[78]

A similar good control over the dispersity of the droplets is also achievable with microfluidic technology.[79] In microfluidics, processes similar to membrane emulsification are used. Here the dispersed and continuous phase are not passed through a membrane, but through microchannels, which are milled into a chip made of glass or plastic.[80] If the two liquids are in individual channels, droplets can form at the intersection of these channels. The dispersed phase flows into the continuous phase and forms a droplet at the pore opening (Figure 7). In shear-driven emulsification systems, the formed droplet is detached and dispersed into the continuous phase through shear exerted by the flow of continuous phase. The continuous phase can flow in cross flow (T-, Y-branches) or in co-flow.[81] By varying the channel size and the flow rate, almost perfectly monodisperse droplets can be produced. Nevertheless, the microfluidic chips are very susceptible to impurities that can disrupt the

entire process.[82] Apart from single emulsions some of these methods are also suitable for producing double or multiple emulsions.[83] This is discussed in more detail in chapter 3.2.2.

3.2   Reconfigurable Complex Emulsions

Multiple emulsions, as part of complex emulsions, are polydispersed systems where two or more immiscible phases are dispersed in another phase or even more complex systems with three or more immiscible phases and a high structural complexity.[84] Typically, the internal droplet phase will be miscible with or identical to the final continuous phase. Such double emulsions may be water-in-oil-in-water (W/O/W) emulsions, where the internal and external phases are aqueous; or oil-in-water-in-oil (O/W/O), which have the reverse composition.[85] Other internal configurations can also be Janus (droplets with equal hemispheres of two immiscible liquids dispersed in a third one), multilayered emulsions or dispersed internal micro-droplets.[83, 86] Complex emulsions with different internal configurations are shown in figure 8.
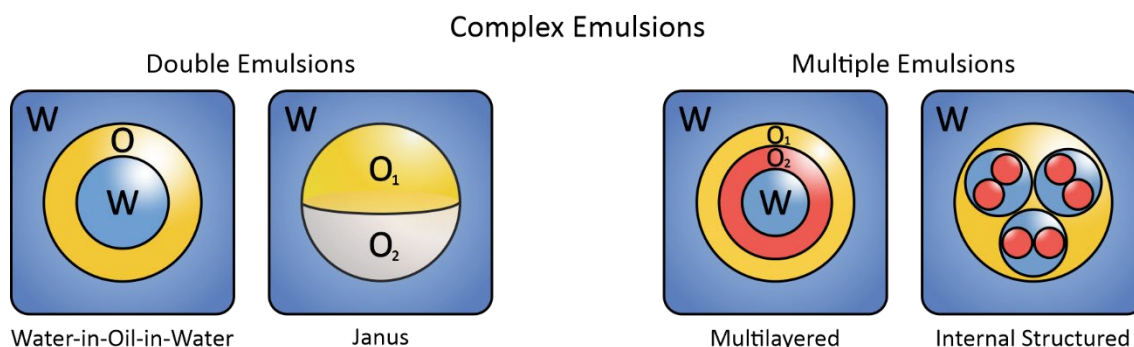
Figure 8. Schematic representations of complex emulsion systems with different internal configurations.

William Seifriz firstly presented the concept of double emulsions, as a representative of complex emulsions, in 1925.[87] However, the W/O/W double emulsions studied by Seifriz quickly destabilized and turned into single emulsions. He suspected that they were an unstable transitional state between water-in-oil (W/O) and oil-in-water (O/W) emulsions and justified the instability with physical arguments. Thus, he hypothesized that the Laplace pressure (which depends on the droplet size and surface tension) leads to increased pressure in the inner droplets compared to the pressure on the oil sphere, resulting in pressure equilibration and eventual collapse of the double emulsion structure.[88] Although such systems have been known for almost a century, only in the last two decades the underlying physics of their formation have been reported.[89] In particular, double or Janus emulsions were both theoretically described and generated by Koetz et al. and Guzowski et al..[90-93] Due to the profound understanding of the thermodynamics of such systems, the research interest has increased

significantly.[94] Especially double emulsions compromising two immiscible oils (e.g. hydrocarbon (HC) and fluorocarbon (FC) oils) dispersed in water, that dynamically reconfigurable in response to interfacial tension changes of their environment, have recently received considerable attention.[94, 95]

The mutual immiscibility of hydrocarbons and fluorocarbons results from their different polarizability. While hydrocarbons are considered hydrophobic due to their nonpolar nature, fluorocarbons are both hydrophobic and lipophobic, meaning that they form a separate phase when dispersed with hydrocarbons in water.[95] The special properties of fluorocarbons can be explained by the high electronegativity of fluorine compared to hydrogen. Since the high electronegativity of fluorine reduces the polarizability of the C-F bond, fluorocarbons form only weak induced dipoles, which are the basis of the London dispersion force (Van der Waals interactions).[96] As a result, fluorocarbons have low intermolecular attractive forces and are not only hydrophobic and lipophobic, but also exhibit ftlower surface tensions, lower evaporation enthalpies, and lower viscosities compared to liquids with comparable boiling points.[96] In addition, the low attractive forces between the fluorocarbon molecules makes the liquids compressible and good solvents for gases.[97] Due to the significant density difference between the droplet internal phases ($\rho_{fluorocarbon} > \rho_{hydrocarbon}$), the droplet phases in the biphasic droplet systems align in a specific orientation along the gravitational direction. While the lighter hydrocarbon phase is at the top, the heavier fluorocarbon phase is arranged below.Typical hydrocarbons for the preparation of double emulsions can be alkanes (hexane, heptane,...), aromatics (diethylbenzene, toluene, …) or substituted phthalates (diethyl phthalate, dibutyl phthalate, …), whereas as fluorocarbons the corresponding perfluorinated analogues (perfluorohexane, perfluorotoluene, …), hydrofluoroethers, such as 2-(trifluoromethyl)-3-ethoxydodecafluorohexane (HFE-7500) and methoxyperfluorobutane or perfluorinated amines like perfluorotributylamine (FC-43) can be used (Figure 9).[94]
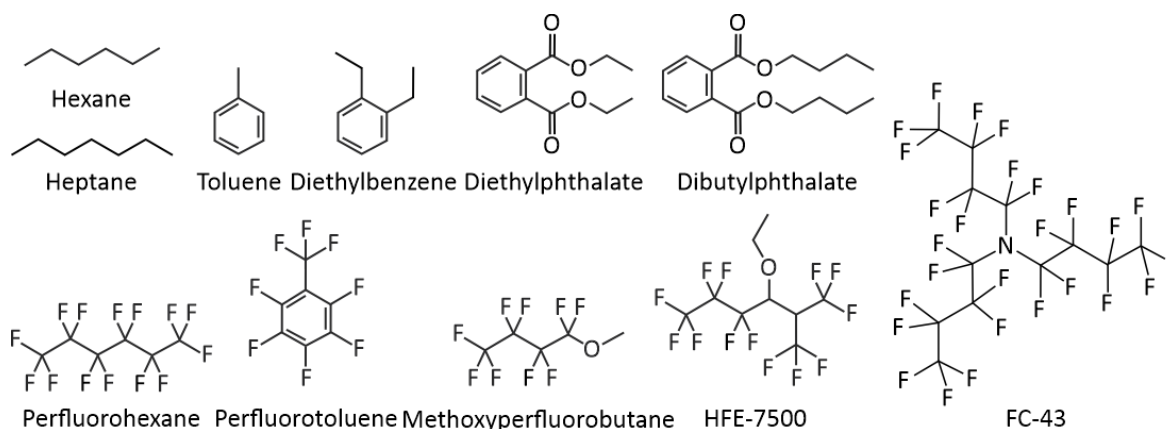

Figure 9. Chemical structures of several hydrocarbons (top) and fluorocarbons (bottom) that can be used for the preparation of biphasic complex emulsions.

There are also a variety of options for other oil droplet components, raging from vegetable oil[98], silicone oil[99, 100], ionic liquids[101] until liquid crystals.[102, 103] Nevertheless, hydrocarbon and fluorocarbon oil droplets remain the most reported due to the possibility of using an efficient thermal-induced phase separation technique for preparation, which will be discussed in detail in chapter 3.2.2. These types of complex emulsions, which are also referred to as dynamic complex emulsions because of their reconfigurability, have the intrinsic advantage that interfacial tension variations transduce into a change in the internal shape of the droplets whereas the overall emulsion stability remains intact. Droplet geometries can be controllably alternated after emulsification between encapsulated double emulsion (HC/FC/W or FC/HC/W) and Janus configurations by triggering changes in the surfactant concentration or effectiveness.[90, 92] Owing to this unique morphological response to targeted chemical stimuli, dynamic complex emulsions have been exploited in a number of applications, including as tunable microlenses[104], optical waveguides[105, 106], scaffolds for the fabrication of anisotropic solid objects[107-109], motile particle systems[110-112], and as transducers and signal amplifiers in improved chemo- and biosensing platforms.[113-116]

In addition to bi- and multiphasic oil droplets dispersed in water, also aqueous two-phase systems (ATPS) dispersed in organic media have been reported.[117] Even though water based complex droplets show the same interfacial tension-dependent morphology changing behavior as biphasic oil-in-water systems, the latter are more promising for the preparation of stimuli responsive droplets, as they have two interfaces with different chemistries. Selective modification of only one of the two interfaces, on which many stimuli responsive sensing schemes rely, appears to be difficult in aqueous systems since both hemispheres are comprised of water.[94] To understand the unique behavior of dynamic reconfigurability, which is crucial for most of the applications, the geometry of biphasic complex emulsions is discussed in more detail in the following chapter.

3.2.1   Morphologies of Biphasic Complex Emulsion Droplets

The geometry of complex Janus emulsions that consists of two immiscible hydrocarbon and fluorocarbon oils surrounded by a third immiscible aqueous phase is controlled by three competing interfacial tensions that act at the respective interfaces of the droplet.[90] The three acting interfacial tensions are the interfacial tension of the hydrocarbon-water interface γ_{HC}, of the fluorocarbon-water interface γ_{FC} and between the droplet phases – the hydrocarbon-fluorocarbon interface $\gamma_{HC/FC}$. The internal morphologies of as-produced Janus emulsion droplets are highly uniform across a sample, as they solely reflect this force-balance of interfacial tensions. For the case of working temperatures close to the critical temperature of the internal fluids, the overall droplet shape is nearly spherical because

the interfacial tension between the droplet phases $\gamma_{HC/FC}$ is much smaller than the interfacial tensions between the droplet constituents and the aqueous medium γ_{HC} and γ_{FC}.[95] In addition, for droplets with diameters on the order of 100 µm, the internal interface can be considered to be spherical, because the ratio of gravitational to surface tension forces is negligible.[91] Within these limits, any changes in the values of external interfacial tensions do not affect the overall spherical droplet shape but cause variations in the curvature of the interface between the gravity aligned internal droplet phases. The reconfigurability and the transducer behavior of the droplets are based on these characteristics.

These physical relationships reveal that for the special case of a droplet in the 'perfect' Janus state, i.e. a droplet comprised of two perfect hemispheres, the two external interfacial tensions are equal ($\gamma_{HC} = \gamma_{FC}$). When $\gamma_{HC} \gg \gamma_{FC}$, the higher interfacial tension at the HC/W interface results in a minimization of HC/W interfacial area, and a hydrocarbon-in-fluorocarbon-in-water (HC/FC/W) encapsulated morphology is preferred. The inverse ($\gamma_{FC} \gg \gamma_{HC}$) is necessary for fluorocarbon-in-hydrocarbon-in-water (FC/HC/W) double emulsions (Figure 10).
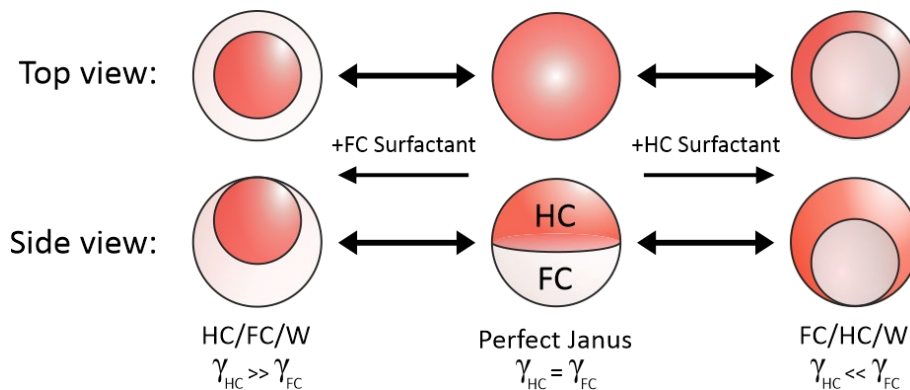
Figure 10. Top and side view images of the morphological changes of double emulsion droplets with adjustments in interfacial tension balances.

Marginal variations from the equilibrium Janus state induced by variations in the surfactant type, concentration or effectiveness cause immediate variations in the droplet morphology along the continuum between HC/FC/W and FC/HC/W encapsulated structures. By choosing surfactant combinations that address both interfaces (HC/W and FC/W) as independently as possible, the balance of the interfacial tensions and thus the droplet morphology can be individually tuned. The use of hydrocarbon surfactants (e.g. SDS or Triton) would favor the reduction of the HC/W interfacial tension γ_{HC} over that of the FC/W interface γ_{FC}. In consequence, this would lead to a reconfiguration of the emulsion droplets into those with a larger HC/W interface. If the concentration of a fluorinated surfactant (e.g. Zonyl) is increased, this would reduce γ_{FC} and the emulsion droplets would adopt a

morphology with an increased FC/W interface.[95] While the use of a single surfactant at different concentrations may have little impact on the droplet shape, mixing hydrocarbon and fluorocarbon surfactants in different ratios can tune droplet morphology to various Janus configurations. The change in morphology results in either a concave or convex shaped internal interface that can be readily observed and monitored by a horizontal imaging setup (Figure 11). The equilibrium angles between the different phases, which are the two contact angles θ_{HC} between the HC/W and HC/FC interfaces and θ_{FC} between the FC/W and HC/FC interfaces, can be obtained by the so called Neumann construction (Figure 11).[91]
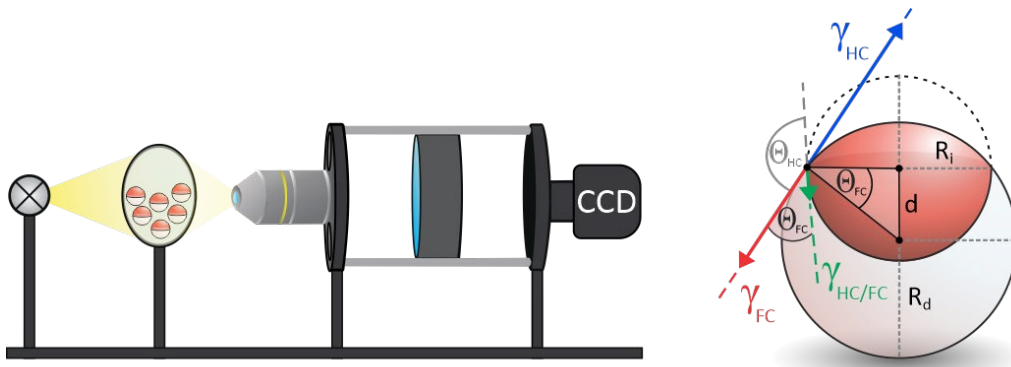
Figure 11. Schematic illustration of a horizontal imaging setup (left) and sketch of a double emulsion droplet viewed from the side with indicated contact angles θ_{HC} and θ_{FC}, the radius of the inner droplet R_i, the radius of the Janus droplet R_d and the distance between the centers of the two circles d (right).

To quantitatively describe the droplet morphology as a function of the surfactant type (HC- or FC-surfactants), ratio, and concentration, the contact angle θ_{FC} at the triple phase contact line can be used, which can be determined by side-view micrographs of the respective droplet configurations.[113] With the internal curvature being set by the balance of interfacial tensions at the external droplet interfaces (i.e. $\theta_{HC} + \theta_{FC} \rightarrow \pi$) the contact angle θ_{FC}, which ranges from 0° to 180°, can be used as the sole parameter for describing the morphology of the droplet (Figure 11) (In the following, the contact angle θ_{FC} will be referred to only as θ). In terms of the interfacial tensions, $\gamma_{HC} > \gamma_{FC}$ leads to a contact angle of $\theta < 90°$, the Janus state ($\gamma_{HC} = \gamma_{FC}$) corresponds to a contact angle of $\theta = 90°$ and $\gamma_{HC} < \gamma_{FC}$ would result in contact angle of $\theta > 90°$. Fully encapsulated droplet morphologies correspond to a contact angle of $\theta = 0°$ for a HC/FC/W double emulsion and of $\theta = 180°$ for a FC/HC/W double emulsion. The relation between the contact angles (θ_{HC} and θ_{FC}) and the interfacial tensions (γ_{HC}, γ_{FC} and $\gamma_{HC/FC}$), that define the balance of forces acting on the three-phase contact line, are also known as the Newmann triangle (Figure 12) and can be described with the following equations:

$$\gamma_{HC/FC}\cos(\theta_{HC}) + \gamma_{HC} + \gamma_{FC}\cos(\theta_{HC} + \theta_{FC}) = 0 \qquad (4)$$

$$\gamma_{HC/FC}\cos(\theta_{FC}) + \gamma_{FC} + \gamma_{HC}\cos(\theta_{HC} + \theta_{FC}) = 0 \tag{5}$$
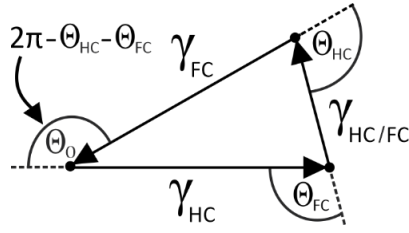
Figure 12. Schematic representation of the Neumann triangle, derived from the balance of interfacial tensions.

Applying the law of cosines, the contact angles can be determined from two circles that define the inner and outer interfaces of the droplets (Figure 11), according to equation 6 (with R_i: radius of inner droplet; R_d: radius of Janus droplet; and d: distance between the centers of the two circles):

$$\cos(\theta_{FC}) \rightarrow -\cos(\theta_{HC}) \rightarrow \frac{\gamma_{HC} - \gamma_{FC}}{\gamma_{HC/FC}} \rightarrow \frac{R_i^2 + R_d^2 - d^2}{2\,R_i R_d} \tag{6}$$

As previously mentioned, the morphology of two-phase complex emulsion droplets is set by the interfacial tensions between each of the constituents as well as with the surrounding medium. When the interfacial tension $\gamma_{HC/FC}$ between the two oils is too high compared to the interfacial tensions of the individual droplet phases towards the continuous phase, then the droplets will separate into droplets of each of the oils individually.[91] If the interfacial tension between the two oils and each of the oils with the surrounding medium are of similar magnitude, a variety of dumbbell type shapes can form. In this case $\theta_{HC} + \theta_{FC} > \pi$ applies, which means that the external contact angle θ_0 is reduced, resulting in the non-spherical droplet shape (Figure 13). Only if γ_{HC}, $\gamma_{FC} > \gamma_{HC/FC}$, biphasic droplets can be reconfigured between fully engulfed and Janus shapes. Figure 13 shows the different morphologies biphasic complex emulsions can assume depending on the balance of interfacial tensions.
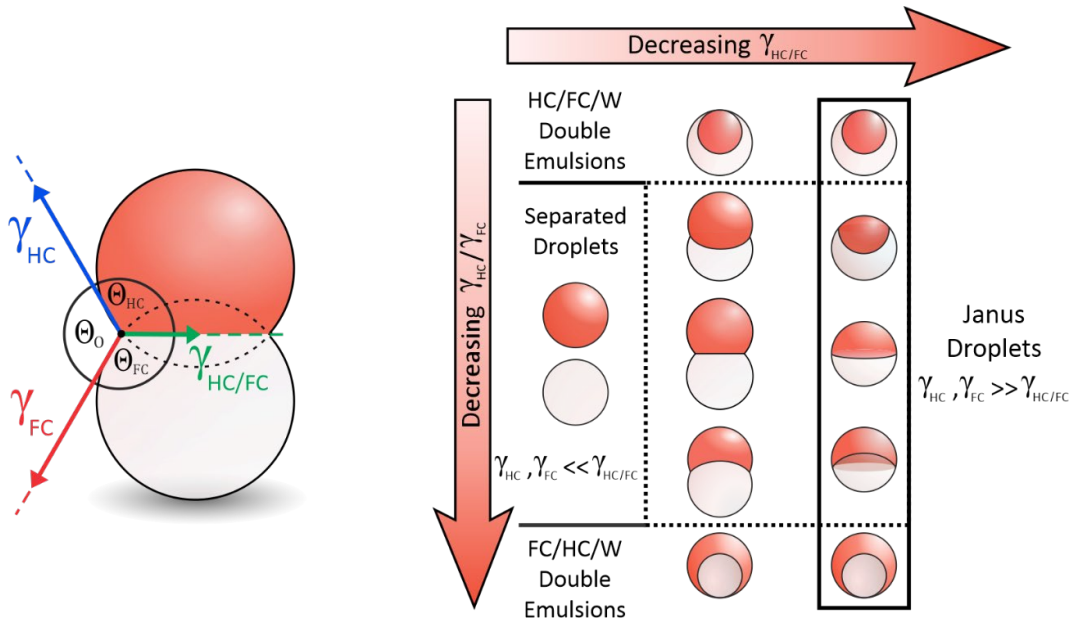
Figure 13. Possible morphologies of biphasic complex emulsions. The balance of interfacial tensions determines the droplet morphology, including separated droplets, dumbbell-like shapes, fully engulfed double emulsion configurations and Janus shapes.

The targeted generation and control of such dumbbell-like or snowman-like droplets is still largely unexplored and was investigated in this work (see chapter 5.1).

3.2.2   Generation of Complex Emulsions

In principle, most of the emulsification techniques discussed in Chapter 3.1.3 can also be used for the generation of complex emulsions. Similar to the preparation of single emulsions, each technique comes with its own advantages and disadvantages. The simplest but crudest emulsification technique for the fabrication of complex emulsions is the bulk homogenization method, which can be conducted in a single step and on a large scale. To generate double emulsions with this method, two immiscible oils are added to a surfactant-containing aqueous solution. High-shear forces are then applied through high-pressure homogenizers, vortex mixers, or ultrasound baths to mechanically breakup the droplet phases and mix them with the continuous phase. The droplet phases collide with each other under high turbulences. Since this happens very imprecisely, multiple emulsions generated by this method suffer from inhomogeneous droplet phase volumes and polydispersity (Figure 14a).[94]

The most prevalent and much more reliable method for the preparation of double emulsions is the two-step emulsification procedure, first reported by Matsumoto et al. in 1976.[118] In the first step a single emulsion is generated using a high-shear procedure. In the second emulsification step, double emulsions are obtained by dispersing the entire single emulsion in the final continuous phase using

surfactants. For a W/O/W system for example, in which the final continuous phase is aqueous, the single emulsion will be a W/O emulsion, which is then emulsified into the aqueous phase (Figure 14b). This procedure can also be performed on a large scale. The disadvantages associated with this conventional method are the wide size distribution and the inhomogeneous inner phase of the generated double emulsions. Emulsion droplets, which are generated by this process, have either one phase as the inner phase or are comprised of multiple micro-droplets.[88] Since the polydispersity issue inherent in single emulsion fabrication is further worsened in a two-step process, a reasonable size reproducibility is precluded.

Parallel progression in molecular analysis, biodefence, molecular biology and microelectronics led to the emergence of microfluidic technology more than 30 years ago.[119] As already described in chapter 3.1.3, in microfluidics the dispersed and the continuous phase are guided through capillary microchannels in a chip, which is usually made of poly(dimethylsiloxane) (PDMS).[120, 121] By controlling the shear with restricted geometry, the drawback of sequential emulsification with high shear can be overcome, allowing the production of nearly monodisperse emulsions. In 2004, Okushima et al. published the controlled production of monodisperse double emulsions in two steps by the series connection of two T-junctions in a microfluidic device.[122] One year later, Utada, a scientist in Weitz's research group, achieved the same in a single step using flow focusing of coaxial jets (Figure 14c).[123] This research allowed major advances in the generation of emulsions by microfluidics and enabled the precise production of internally structured multiple emulsions with high control over the size, shape and compartments of the emulsions.[86, 124, 125] Although the microfluidic process does not allow rapid mass production, it remains the dominant process for the production of monodisperse droplets.
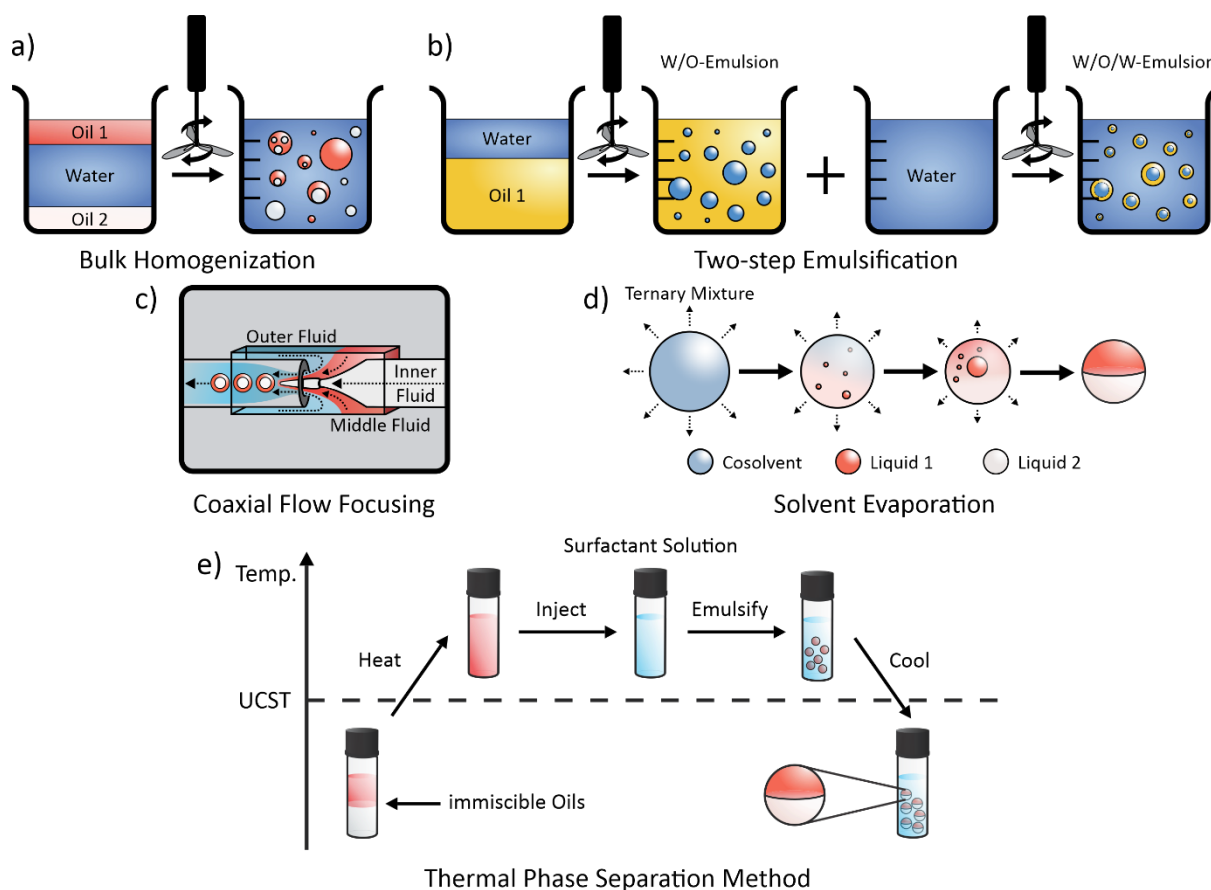
Figure 14. Approaches to the preparation of complex emulsions: a) bulk homogenization, b) two-step emulsification, c) coaxial flow focusing microfluidic setup, d) temperature-induced phase separation and e) solvent evaporation process.

In 2015, Zarzar, Swager and coworkers reported on the fabrication of complex emulsions with dynamically reconfigurable morphologies based on a thermal phase separation approach.[95] The complex emulsion droplets were fabricated in one step by emulsifying a single-phase mixture of hydrocarbon and fluorocarbon oils of equal volume in a surfactant-containing aqueous solution. The procedure works with fluids that are immiscible at room temperature but exhibit a lower (LCST) or upper critical solution temperature T_c (UCST). The immiscible HC and FC oils were heated above their UCST to generate a homogenous phase, which was subsequently emulsified by conventional or microfluidic techniques under elevated temperatures. Upon cooling, the induced phase-separation yielded structured emulsion droplets of HC and FC in water (Figure 14e). The fabrication method and the dynamic mechanism are general and represent a paradigm shift for the fabrication of complex emulsions with controllable morphologies via both microfluidic and scalable batch production.

However, phase separation can also be initiated by other methods. As Alex et al. have shown, double emulsions can be generated by the targeted evaporation of a co-solvent.[126] This solvent evaporation

process was developed as early as 1979 by Beck et al. for the generation of microcapsules from the biodegradable polymer polylactide (PLA).[127] In this method, the immiscible droplet phases are mixed by adding a compatible co-solvent to form a single-phase system. Various solvents can be used, such as acetonitrile, ethyl acetate, chloroform, benzene, or methylene chloride.[128] Subsequent evaporation of the solvent results in phase separation within the droplets (Figure 14d). Based on this method, many other studies have followed using the solvent evaporation process to create multiple emulsions in microfluidic systems.[129-132] The solvent evaporation method, the microfluidic approach and the temperature-induced phase separation all allow precise control over the volume distribution of the droplet phases. The solvent evaporation process has been used in this thesis to design snowman-like droplet systems (see chapter 5.1).

3.2.3   Optical Properties of Biphasic Complex Emulsions

Biphasic dynamic complex emulsions exhibit some unique optical properties. These special properties can be attributed to the biphasic anisotropic structure of the droplets, which contain liquids with two different refractive indices, and to their switchable internal curvature. Size control during fabrication using the previously described fabrication techniques allows precise control of the distinct phase volume ratios and radii of curvature. In addition, the droplet phases can be mixed with dyes or pigments to change their absorption or fluorescence properties. The density difference between droplet phases in optical complex emulsion systems ensures that gravity aligns the droplets of a monolayer all in the same direction. In most cases, this natural alignment is a useful property for a uniform optical response. In the following, the different optical properties, which can be used in several optical applications such as dynamic tunable lenses or as readout mechanisms for sensing schemes, will be discussed in detail. In this work, they were specifically exploited to implement them as readout mechanisms for droplet-based logic gates and circuits (see chapter 4.4).

3.2.3.1 Lensing Effect

Liquid soft materials offer certain advantages over solid ones in their application as lens materials. For example, the refractive indices of liquids are variable and adjustable while their surface roughness remains minimal.[133, 134] In particular, biphasic complex emulsions consisting of a hydrocarbon and a fluorocarbon phase appear as suitable material platform for dynamic microlenses in aqueous media. The low refractive index of the fluorocarbon phase ($n_{FC} < 1.33$) and the high refractive index of the hydrocarbon phase ($n_{HC} > 1.33$) compared to the surrounding water ($n_{water} = 1.33$) creates a refractive index difference at the droplets' internal interface that can refract incident light.[135, 136] Combined with

the dynamic tunability of Janus droplets, this results in a sensitive lens system that can be reconfigured by simply modifying the droplet morphology with changes in the interfacial tension equilibrium. Nagelberg et al. demonstrated both theoretically and experimentally that double emulsion droplets show different interactions with light depending on their configuration.[104] When the optically denser phase (HC) was located in the droplet core in the form of a HC/FC/W double emulsion, the incident light was focused, while the inverted droplet configuration (FC/HC/W) resulted in strong light scattering. Depending on the morphology, the internal interface assumes either a convex (HC/FC/W), planar (Janus) or concave (FC/HC/W) shape. In other words, dynamic complex emulsions can alter between a converging lens and a diverging lens with adjustable focal length in response to external stimuli. (Figure 15).
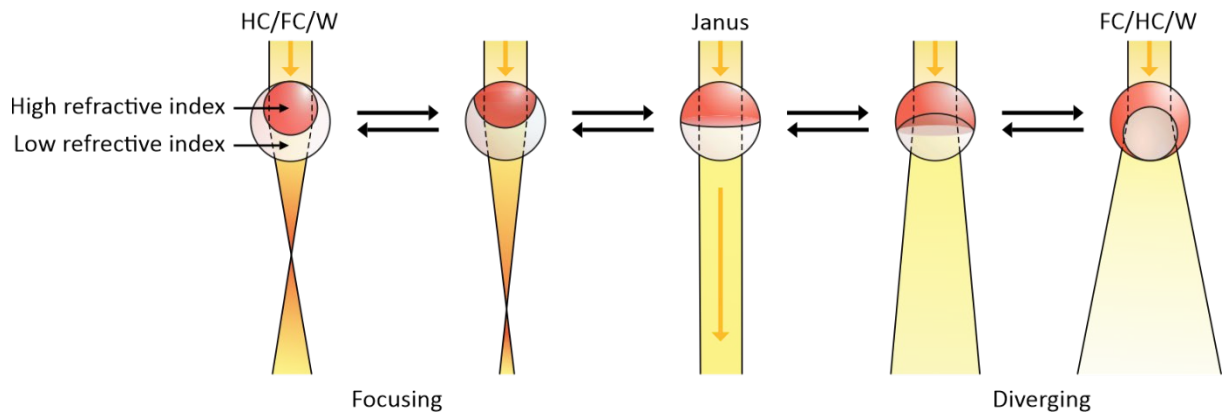
Figure 15. Dynamic double emulsions as microlenses. Side-view illustrations of double emulsions with different morphologies and corresponding propagation of light through the droplets. Depending on morphology, incident light can be focused or diverged.

When the incident light hits the bended internal interface with its refractive index contrast, it is refracted according to Snell's law:[137]

$$n_1 \sin \theta_1 = n_2 \sin \theta_2 \qquad (7)$$

n_1 and n_2 are the refractive indices of the two media and θ_1 and θ_2 represent the incident angle and refractive angle respectively. If light with the angle θ_1 hits the interface of the two media, it is reflected under an angle θ_2 depending on the refractive index contrast n_2/n_1. If the angle of incidence is too small, reflection occurs at the interface. This angle is called the critical angle of total internal reflection or critical angle θ_c.

Lauren et al. developed an optical readout mechanism based on the lensing effect of double emulsions to monitor enzyme activity.[138] Therefore, they used changes in the morphology of the complex emulsions, driven by enzyme-responsive surfactants, to manipulate the transmission of light through

a sample. The resulting changes in transmission in a monolayer of vertically oriented droplets caused by variations in the morphology have been visible to the naked eye. They quantitatively described the activity of α-amylase, lipase, and sulfatase in solution by using host-guest interactions and enzyme-degradable surfactants and showed that the simplicity of the optical sensing method has significant potential as a broadly deployable biosensing platform.

3.2.3.2 Directional Light Emission from Complex Emulsions

Besides incident light, which is influenced by variations in the droplet morphology, the droplet shape also affects the distribution of light emitted from the inside of fluorescent dye containing complex droplets. When an emissive dye is partitioned into the higher-index hydrocarbon phase of a HC/FC biphasic droplet, the light emitted after the excitation of the dye can take different trajectories trough the droplet phase.[139] If the light is emitted near the center, most of the light will be refracted through the interfaces and exits the droplet in a coincident direction. If the light is emitted near the internal interface of the complex droplet, total internal reflection (TIR) can occur depending on the curvature of the internal interface and the angle at which the light hits the interface. Figure 16 shows different possible trajectories of light being emitted from the HC phase of a two-phase droplet with a contact angle θ of less than 90° ($\gamma_{HC} > \gamma_{FC}$).

Figure 16. Illustration of 2D-ray diagrams of fluorescent light emitted in the high index HC phase of side-viewed droplets. Most of the emitted light will be refracted through the droplet interfaces (left), however some of the light emitted near the internal interface can undergo TIR (right). This light will most likely leave the droplet through the HC/W interface.

As indicated in figure 16, the reflected light rays can leave the droplet at the three-phase junction, resulting in emitting droplets exhibiting enhanced emission in vertical direction, in the opposite to the gravitational direction, when their internal interface is bent downwards (θ < 90°). The angular emission distribution of this effect and how the droplets' emission changes with morphology was studied by Nagelberg using raytracing simulations.[139] By performing a full angular emission distribution simulation in 3D, she discovered that the vertical emission intensity (0° above the droplets) for gravity

aligned emissive droplets with a contact angle of θ ≈ 27° is about 1.5-2 times higher than for perfect Janus droplets with a contact angle of θ = 90°. Droplets with a contact angle of 0° (HC/FC/W double emulsions) still showed a 1.4 times enhanced emission in vertical direction compared to Janus droplets. In addition, she found that the fluorescence properties of the multicomponent droplets depend on the droplet orientation, refractive index contrast, and exposure to chemicals with fluorescence quenching properties.[139] Figure 17 illustrates the phenomenon of enhanced light emission in vertical direction as a function of the droplet shape.
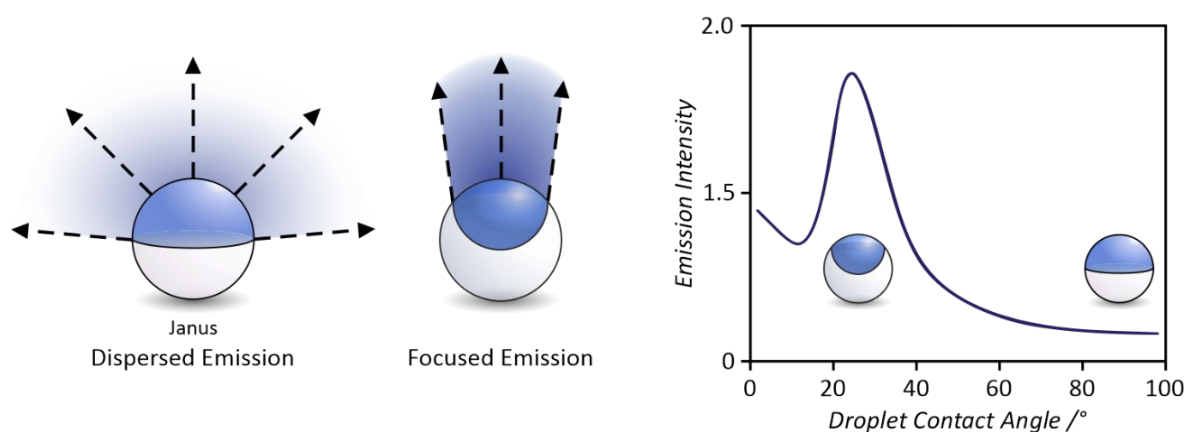
Figure 17. Illustration of emissive complex droplets, adapted from Trinh et al. (left).[116] Janus droplets exhibit dispersed fluorescent emission and low directed emission intensity. The curvature of the internal interface of droplets with a contact angle of θ < 90° facilitates total internal reflection and focuses the fluorescent emission. Idealized emission intensity as a function of the droplet shape (right).

Several works have used the morphology-dependent changes in the emission intensity of emissive complex droplets as a sensor readout mechanism to detect specific molecules or pathogens that cause slight changes in the surfactant effectiveness of the involved surfactants and thus changes of the droplet morphology.[113, 116, 140] In one study, researchers incorporated the fluorescent dye perylene to HC-FC complex emulsion droplets and functionalized the droplets HC-interface with boronic acid surfactants. They were able to detect the binding of poly- and monosaccharaides to boronic acid surfactant by generating a curve of normalized emission intensity vs contact angle, analyte concentration, and surfactant concentration and used these dynamic interface triggered morphology changes to create a rapid and sensitive method for the detection of the sugar-binding food-borne pathogen Salmonella enterica erovar Typhimurium.[113]

3.2.3.3 Structural Colors at Microscale Concave Interfaces

This chapter discusses the effect of structural colors observed near the three-phase contact line of biphasic complex emulsion droplets that can occur under certain circumstances. Principally, many different physical processes can generate color. Besides color pigments that produce color by absorbing a certain part of the electromagnetic spectrum and reflecting the remaining wavelengths, color can also be generated by light refraction.[141, 142] For example, color is created when white light is refracted in a prism or by finely dispersed water droplets in the air, leading to the formation of rainbows.[143] Another phenomenon for color emergence that is often found in nature is light interference caused by periodically arranged nanostructured surfaces.[5, 6] Thus, structural colors are considered to be among the most intense colors of all and are responsible for the iridescent colors of butterflies and certain bird species.[4]

It was first observed by Goodling et al. that a sample of monodisperse biphasic complex droplets show a colored ring when the droplets are illuminated from above with collimated white light.[144] This color varied with the viewing angle and the curvature of the droplet internal interface. However, this phenomenon is not limited to biphasic complex emulsion droplets, but applies generally to microscale concave interfaces.[145] These colors occur due to interference of collimated light taking different trajectories of total internal reflection along microscale concave interfaces. As the collimated light travels along these different trajectories through the concave structure, it undergoes a phase shift that depends on the number of bounces at the interface and the total distance traveled (Figure 18). The phase shift caused by the propagation of light depends on the wavelength of the light, so that the constructive interference differs for distinct wavelengths, resulting in color variations observed from certain directions.[144] The color seen for a given viewing direction depends on a variety of parameters, including the refractive contrast of the interface, the size of the concave interface and the opening angle.[139]

Compared to other microscale concave interfaces, a benefit of biphasic complex droplets is that they provide the unique ability to change the structural color through specific adjustments in droplet morphology. While Janus droplets show bright iridescent colors, depending on the curvature of their internal interface, fully encapsulated double emulsions do not reflect any color (Figure 18). This coloration can be further controlled by the droplets' size and thus the size of the internal interface, the volume ratio of the droplet phases and the refractive index contrast between the phases.
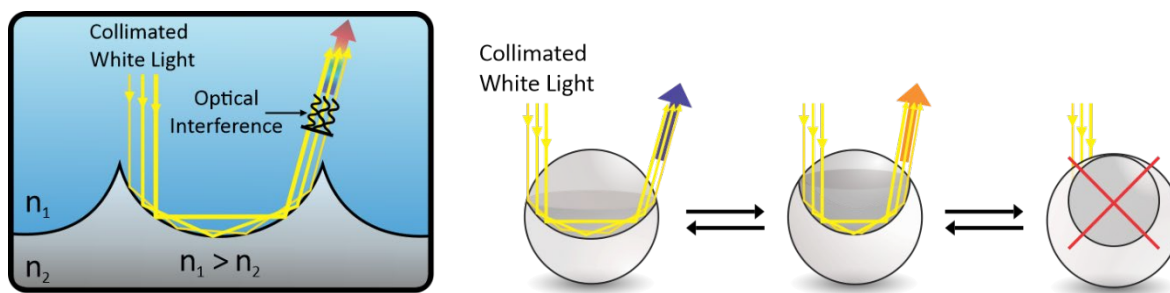
Figure 18. Schematic illustration of a concave geometry generating interference from TIR of incident light (left) and morphology-dependent occurrence of structural colors in biphasic complex emulsions (right). When collimated light hits a concave interface with a refractive index contrast it can undergo TIR. Different paths of TIR have different optical path lengths leading to a phase shift that causes interference and structural color.

The mechanism of generating color through optical interference in liquid complex emulsion systems has great promise for further exploration in color-based liquid displays or droplet sensors. However, it should be noted that the coloration is highly dependent on the volume ratio of the individual oil phases, the droplet size and on the curvature of the interface so that each morphology would need to be calibrated before use in sensing applications.

3.3   Stimuli-responsive Complex Emulsions

Complex emulsion droplets have proven of interest for the development of a cost efficient and easy to use sensing platform.[94] This chapter discusses how the droplets can be modified to respond to a wide range of different stimuli, making them optimal transducers for physical or chemical changes in their environment.

In the previous chapters, both the unique property of dynamic reconfigurability of biphasic complex emulsions (chapter 3.2.1) and their special optical properties have been discussed (chapter 3.2.3). To exploit these properties in a droplet-based sensing scheme, a common strategy is to use two different surfactants in one emulsion system. An inert surfactant, which is necessary to maintain the overall stability of the emulsion system and a stimuli-responsive surfactant that is designed to change its surfactant effectiveness in response to a specific trigger. The alterations in the balance of interfacial tensions caused in response to that trigger lead to a morphological reconfiguration of the droplets accompanied by changes in the optical properties. The optical signals can then be evaluated using one of the previous described readout methods. The dynamic and anisotropic character of the interfaces of biphasic complex emulsions allows manipulation of the interfacial tensions by various stimuli, such as light, pH, enzymes, chemical analytes, temperature and magnetic fields. Responsive surfactants are

designed to respond irreversibly or reversibly to stimuli *in situ*, causing structural transformations that lead to a change in their stabilizing ability.[146] For example, light-responsive surfactants such as spiropyran or azobenzene-based surfactants can undergo a reversible *cis-trans* isomerization depending on the wavelength of the incident light. One of the most common azobenzene-based surfactants, which was first mentioned by Shinkal et al. in 1982, is the cationic surfactant 4-butyl-4'-(3-trimethylammoniumpropoxy)phenylazobenzene (AzoTAB).[147] The thermodynamically more stable *trans*-isomer can be transformed into the bent *cis*-form by UV-light irradiation ($\lambda = 365$ nm), which is less effective in stabilizing O/W interfaces (Figure 19). In consequence, Janus droplets stabilized with this surfactant in combination with an FC surfactant undergo a morphological reconfiguration. The isomerization and thus the morphological transformation is reversible by irradiation with blue light ($\lambda = 470$ nm). In a recent study, Jia et al. used light-responsive surfactants with azobenzene moieties to visualize the altered stabilization properties due to the changed droplet morphology in a two-phase hydrocarbon-fluorocarbon emulsion system. They used the complex structure of the emulsions to form an on-off switch, changing the droplet morphology between an FC/HC/W double emulsion over a Janus configuration to an entirely inverted HC/FC/W double emulsion to turn the evaporation of a volatile phase on and off.[148]
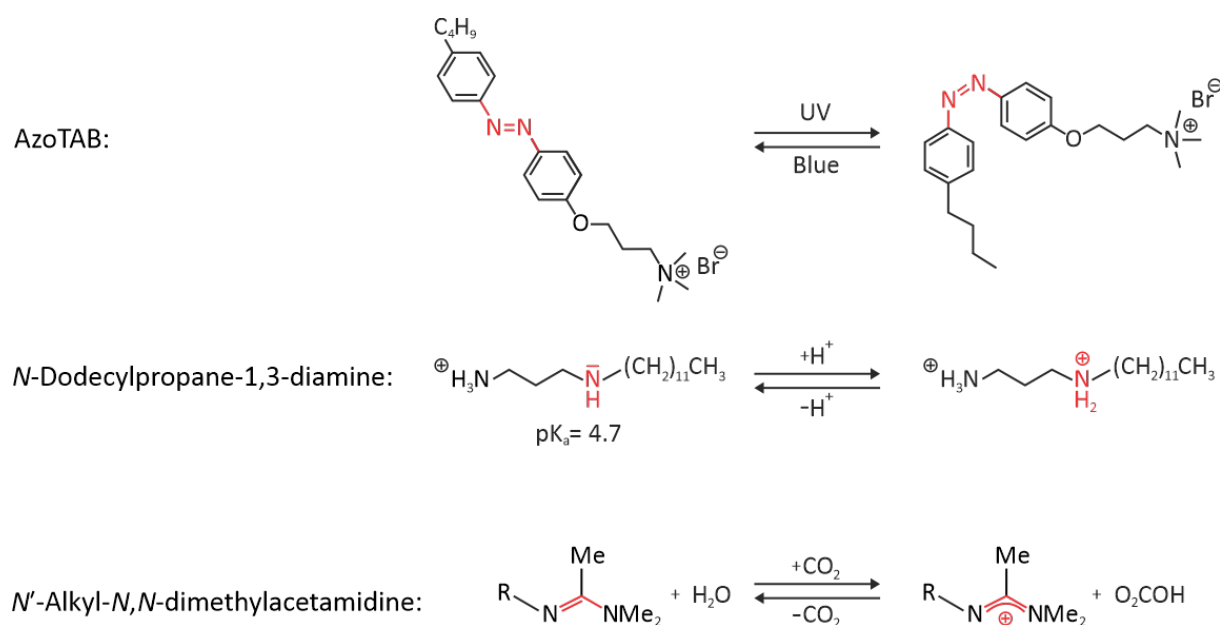

Figure 19. Chemical structures of different stimuli-responsive surfactants. From top to bottom: Light-responsive surfactant AzoTAB, pH-responsive surfactant *N*-dodecylpropane-1,3-diamine and CO_2-responsive *N'*-Alkyl-*N,N*-dimethylacetamidine that can be converted into *N'*-hexadecyl-*N,N*-dimethylacetamidinium bicarbonate in an atmosphere of carbon dioxide.[94, 146, 149]

Similarly, reversible manipulation of the Janus morphology can be obtained with pH-responsive surfactants. The presence of protic molecular scaffolds allows the protonation and deprotonation of the surfactant species, adjusting the charge and the hydrophilic-lipophilic balance. For example, the pH-responsive surfactant *N*-dodecylpropane-1,3-diamine can be switched between its deprotonated and less effective protonated form by increasing or decreasing the pH value of the continuous aqueous phase above or below the surfactant's pK_a value of 4.7 (Figure 19).[150] Surfactants, which react to the pH value, can also be irreversibly changed when for example acid or base- catalyzed chemical reactions cleave certain parts of the surfactant.[151]

A different variation of pH control is offered by CO_2-responsive surfactants. When long-chain alkyl amidine compounds such as *N'*-alkyl-*N*,*N*-dimethylacetamidine are exposed to an atmosphere of CO_2, they can be transformed into charged amidinium bicarbonates (Figure 19).[152] The reaction is reversible by bubbling gas such as nitrogen, argon or air through the surfactant solution at elevated temperatures, releasing carbon dioxide. These surfactants can also be used to stabilize O/W emulsions as well as Styrene-in-water emulsions and to function as switchable demulsifiers.[149]

3.4   Molecular Logic Gates and Combinational Logic Circuits

In our modern world, computers are part of almost everything we use in our daily life. Cars, smartphones, electric toothbrushes or even refrigerators all contain small computers in the form of embedded microchips. The reason for the rise of computer technology can be explained by the development of the transistor, which is the smallest component in computing devices. These numerous transistors (nowadays several billion transistors per chip), also known as logic gates, are densely wired together to perform logical operations. In 1965, around 11 years after the introduction of the transistor, Gordon Moore predicted that the transistor density would double every 18-24 months.[153] This prediction, which is known as Moore's Law, has been valid to this day for more than 50 years.[154]

Logic gates perform logical operations in a specific input-output signal pattern, according to the rules of Boolean algebra. Boolean algebra is a logic-based mathematical system with its own rules or laws used to define and reduce Boolean expressions.[155] The variables used in Boolean algebra have only one of two possible values, a logical "0" and a logical "1". However, an expression can have an infinite number of variables, all individually labeled to represent inputs to the expression, e.g. variables A, B, C, etc., giving us a logical expression A + B = C, but each variable can only be a 0 or 1.[156] This mathematical convention is necessary because in electronics, a voltage is either above a threshold

voltage and passed through a circuit or not. The binary state, where a signal either can be on (1) or off (0), is the basic property of every single computer.[157]

The specific signal pattern, which all logic gates possess, are listed in a so-called truth table containing all possible combinations of input-output states. There are three basic types of logic gates: the "NOT"-gate, the "AND"-gate and the "OR"-gate.[19] The "NOT" gate converts the input signal 1 to the output signal 0 and vice versa. Due to the inverse relationship between the input and output values, the "NOT" gate is often referred to as an inverter. Another very simple logic gate with only one output is the "YES" gate. The output of a logic "YES" gate reproduces the state of the input without any change. An input signal of 0 leads to an output signal of 0 and an input signal of 1 results analogously in an output signal of 1. Every more advanced logic gates, which obey different truth tables, can be seen as combinational circuits of the three basic logic gates and can be obtained by combining "NOT", "AND" and "OR" gates.[19] Combinational circuits are networks of logic gates that implement a Boolean logic function and whose output signals are determined solely by their current input values. Figure 20 shows the symbols for these three logical gates and their corresponding truth tables:

"NOT"-Gate			"AND"-Gate			"OR"-Gate		
In	Out		In_1	In_2	Out	In_1	In_2	Out
0	1		0	0	0	0	0	0
1	0		0	1	0	0	1	1
			1	0	0	1	0	1
			1	1	1	1	1	1
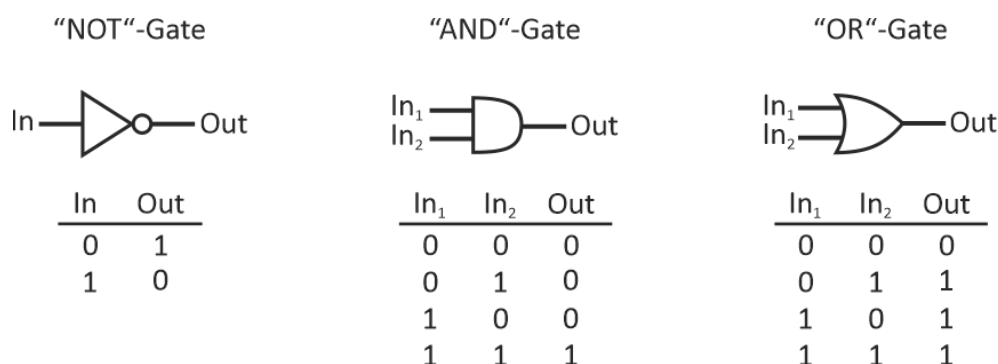
Figure 20. Symbols and truth tables of the NOT, AND and OR logic gates.

Even though Moore's Law has been proven to be valid for a very long time, it is only a matter of time before the ever-smaller lithographically generated silicon-based microchips encounter physical limitations. An alternative concept to today's top-down approach is the idea of using molecular logic gates to perform logic operations and mimic the transistors and circuits in computers. De Silva et al. first presented a molecular logic gate, based on fluorescent signaling in 1993, which laid the groundwork for the emergence of molecule-based logic gates.[158] For this purpose, she functionalized a 9,10-disubstituted anthracene derivative with two fluorescence quenching groups, an alkylamino functionality and a benzocrown ether moiety (Figure 21). Substituted anthracene derivatives are known for their fluorescent properties and the two quenching groups are both independently capable of quenching the emission by an excited state electron transfer.[159, 160] While the photoinduced

electron transfer (PET) in the alkylamino group can be inhibited by the addition of protons (H^+), the crown ether moiety requires the addition of sodium ions (Na^+). This was interpreted as a molecular AND logic gate meaning that in order to see the full fluorescence emission (output) of the molecule both input 1 (Na^+ ions) and input 2 (H^+ ions) must be added.[158] If only one of the chemicals is added, no fluorescence is observed. Figure 21 shows the chemical structure of the molecular AND gate designed by De Silva et al. and the corresponding truth table:

"AND"-Gate

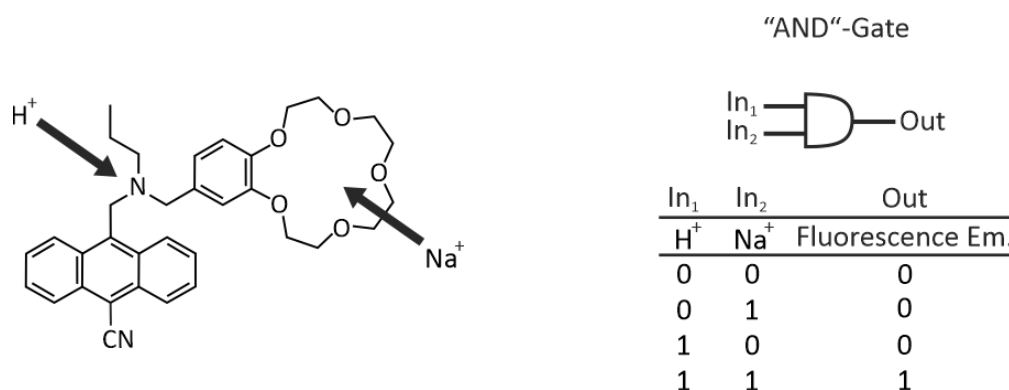| In$_1$	In$_2$	Out
H^+	Na^+	Fluorescence Em.
0	0	0
0	1	0
1	0	0
1	1	1

Figure 21. The first example of a molecular AND logic gate designed by De Silva et al. (left) and its corresponding truth table (right). Only if both inputs, H^* and Na^+ ions, are added, the fluorescence emission of the dye is overserved.

While silicon-based logic gates are limited to a single type of input, which is voltage, molecular logic gates have the advantage that they can respond to different changes of their environment such as light, pH, temperature or the presence of chemical analytes. This multiple way of information processing is the same as that used in biological systems. Within cells as well as between cells, information is exchanged from place to place by the use of messenger molecules. This process relies heavily on Brownian motion, which is remarkably fast at the scale of a cell.[161] Enzymatic regulations are working with selective supramolecular recognition and information in the transmission of nerve impulses in neurons is transmitted by the movement of ions through membranes.[13] Essentially, nature uses a variety of interconnected logic gates that control biological processes. These biological processes are connected by various chemical, electrochemical and supramolecular reactions/interactions with information processing and complex feedback loops taking place.[162]

Nevertheless, there are some fundamental differences between silicon-based and biological information processing. In the case of electronic computers, a clear distinction can be made between the physical hardware and the intangible software. While the hardware in computers is useless without the control of the software, the software is equally useless without a physical entity that can execute the commands. In biological systems, chemical structures and macromolecules such as

deoxyribonucleic acid (DNA) or proteins embody both software and hardware. While DNA serves as an information carrier in the cell and can be considered as software, in contrast, proteins, which act as machines in the cell, perform the functions of the organism without the constant interaction with DNA.

To approach the goal of "molecular computers" that use information processing at the molecular level, stimuli-responsive surfactants were attached to complex droplets in this work to create droplet-based logic gates and combinational logic circuits. Droplet-based logic gates allow the combination of different responsive surfactants in the same emulsion, creating systems that can process multiple physical and chemical stimuli simultaneously, as do biological systems (see chapter 4.4).

4 Results and Discussion

4.1 Chemical Design and Shape-control of Complex Emulsions

4.1.1 Introduction

Nature's ability to precisely control the shape and functionality of material structures in a range of biological systems is inspiring to pursuit for similar control in synthetic materials. For example, pine cones can autonomously alter their shape without cellular control in response to changes in water content of their environment.[163] This shape change, in which bending and twisting valves release the seeds, occurs through the combination of microstructural building blocks with different intrinsic properties and length scales. While many artificial shape-changing materials are based on inorganic or polymeric materials, multiphase microscale emulsion droplets offer potential as inexpensive and widely applicable alternative biomimetic active material that can controllably alter their shape in response to external stimulation.[164] As already mentioned in chapter 3.2.1, a multitude of different droplet shapes can be observed in two-phase complex emulsions, depending on the underlying balance of interfacial tensions. In particular, dumbbell- or snowman-shaped droplets have been reported previously, but their controlled generation and reversible manipulation has not been investigated in detail.[112, 132, 165, 166] In this section the chemical design, hence the controlled generation of non-spherical anisotropic complex emulsions, the influence of additives to tune the UCST of the participating oils during droplet fabrication and the stimuli-responsive shape-changing behavior of those soft materials were scrutinized.

4.1.2 Equilibrium of Interfacial Tensions

Complex droplets generated from immiscible liquid combinations with a UCST close to room temperature assume a nearly spherical shape. For example, the oils n-hexane and perfluorohexane (PFH) have a T_c of 23 °C and form almost perfect spherical emulsion droplets. Since the droplet shape of the complex emulsions is an expression of the force equilibrium between the three interfacial tensions, their ratio to each other is of central importance. When $\gamma_{HC/FC}$ increases in relation to γ_{HC} and γ_{FC}, the droplets try to minimize the HC/FC interface and adopt a snowman-like shape (Figure 23).[91]

The deviation from the spherical shape can also be visualized by considering the Neumann's constructions between two biphasic droplets with different internal interfacial tension values:
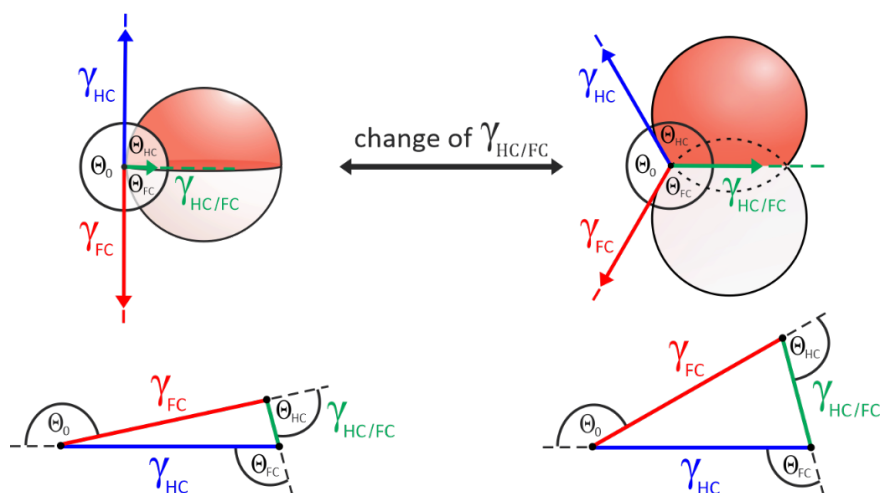
Figure 23. Neumann constructions of two biphasic droplets with different internal interfacial tensions. An increase of $\gamma_{HC/FC}$ leads to a reduction of the external contact angle θ_0, resulting in a non-spherical snowman-like droplet shape.

Consequently, an increase of $\gamma_{HC/FC}$ via variation of the solvent mixture lead to a deviation of the spherical droplet shape. The increase in $\gamma_{HC/FC}$ is accompanied by an increase of the critical solution temperature T_c. This can be exemplified by considering binary mixtures of n-alkanes and perflurorohexane. Table 1 shows UCST measurements of the homologous series of n-alkanes with perfluorohexane and their corresponding interfacial tension values taken from the literature.

Table 1. UCST measurements and Interfacial tension values of binary n-alkane/perfluorohexane (PFH) mixtures.

Solvent mixture	T_c [°C] (measured)	Interfacial tension γ [mNm^{-1}] (Literature values at 25°C)
Hexane / PFH	23.0	0.4*[167]
Heptane / PFH	43.5	0.6**[168]
Octane / PFH	64.2	–
Nonane / PFH	83.5	–
Decane / PFH	– (Evaporation of PFH)	3.1 ± 0.6[168]

*predicted from a model for capillary fluctuations at an interface fitted to X-ray reflectivity measurements.

**calculated

As can be seen in Table 1, the interfacial tension between PFH and the hydrocarbon oils increases as a function of the hydrocarbon chain length. Even though no interfacial tension values between PFH and

octane or nonane can be found in the literature, it can be assumed that the interfacial tension increases continuously along the homologous series of the n-alkanes. In addition, the data in Table 1 shows that the UCST correlates with the interfacial tension, which can also be confirmed by comparing the droplet shape of two emulsion samples with different hydrocarbon oils prepared in the same surfactant solution. While Janus droplets of hexane and PFH prepared in a aqueous solution of 0.5 wt.% SDS and 1.5 wt.% Zonyl assume a spherical shape, the droplets of octane and PFH in the same surfactant solution are slightly elongated in the vertical direction (Figure 22).

Figure 22. Side-view micrographs of hexane- (left) and octane-perfluorohexane Janus droplets (right) prepared in a surfactant solution containing 0.5 wt.% SDS and 1.5 wt.% Zonyl. The higher interfacial tension between octane and PFH leads to a slight elongation of the droplets in vertical direction.

With an increase of the internal interfacial tension $\gamma_{HC/FC}$ the outer contact angle θ_0 will be reduced, which leads to a partial separation of the droplet phases in the direction of a snowman-like shape. The smaller the contact angle θ_0, the greater the deviation from the ideal spherical droplet shape. Therefore, the external contact angle θ_0 can be used as a measure for the pronunciation of this deviation and serves as an expression of the ratio between the external interfacial tensions γ_{HC} and γ_{FC} against the internal interfacial tension $\gamma_{HC/FC}$. In the following chapter, several targeted modifications to the emulsion system are discussed to tune the droplet shape.

4.1.3   Tunability of the Droplet Shape

4.1.3.1 Variation of the Droplet Phase Composition

To investigate the influence of the liquid composition on droplet shape, emulsion droplets were generated containing diethylbenzene (DEB) and HFE-7500 in a 1:1 ratio and used as a reference. Droplets were fabricated via a temperature-induced phase separation approach. The UCST for this liquid combination was measured at T_c = 46 °C. By heating the liquid mixture in a 1:1 ratio above the UCST followed by an emulsification in an aqueous surfactant solution containing 0.5 wt.% SDS and 1.5 wt.% Zonyl, spherical complex emulsion droplets were obtained. By proportionally replacing the fluorocarbon HFE-7500 with another fluorocarbon, FC-43, which has a higher UCST towards DEB (T_c = 168 °C), a linear increase in UCST of the solvent mixture was observed with increasing

percentage of FC-43 in the fluorocarbon phase. The strictly linear increase in UCST with proportional replacement of the fluorocarbon phase by FC-43 was confirmed by additional T_c measurements in other liquid mixtures (Figure 24).
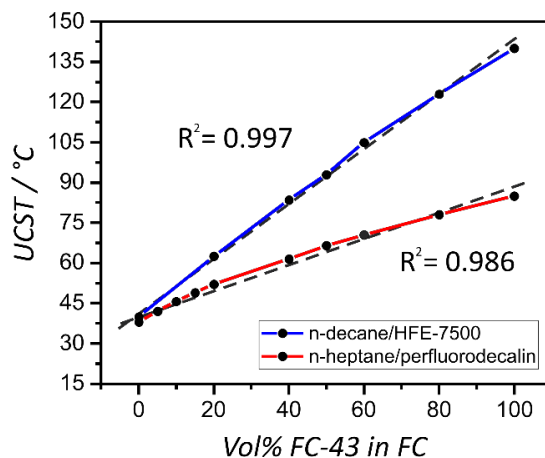

Figure 24. Critical solution temperature of n-decane/HFE-7500 and n-heptane/perfluorodecalin mixtures with increasing fraction of FC-43 in the fluorocarbon phase. The mixing temperature is following a strictly linear trend.

Emulsification of the modified liquid combinations in a surfactant solution containing 0.5 wt.% SDS and 1.5 wt.% Zonyl resulted in complex emulsion droplets that were elongated in vertical direction (Figure 25).

Figure 25. Influence of FC-43 content in the fluorocarbon phase of DEB/HFE-7500 Janus emulsions on the droplet shape. The higher the percentage of FC-43 in the fluorocarbon phase, the more pronounced the snowman shape.

The snowman-like droplet shape was more pronounced the greater the percentage of FC-43 in the fluorocarbon phase or the higher the mixing temperature T_c was. Contact angle measurements from the outer contact angle θ_0 revealed a linear decrease of the angle with increasing mixture temperature

(Figure 26 left). Accompanying interfacial tension measurements via pendant drop tensiometry also showed a linear correlation between the interfacial tension and the volume percentage of FC-43 in the liquid mixture (Figure 26 right).
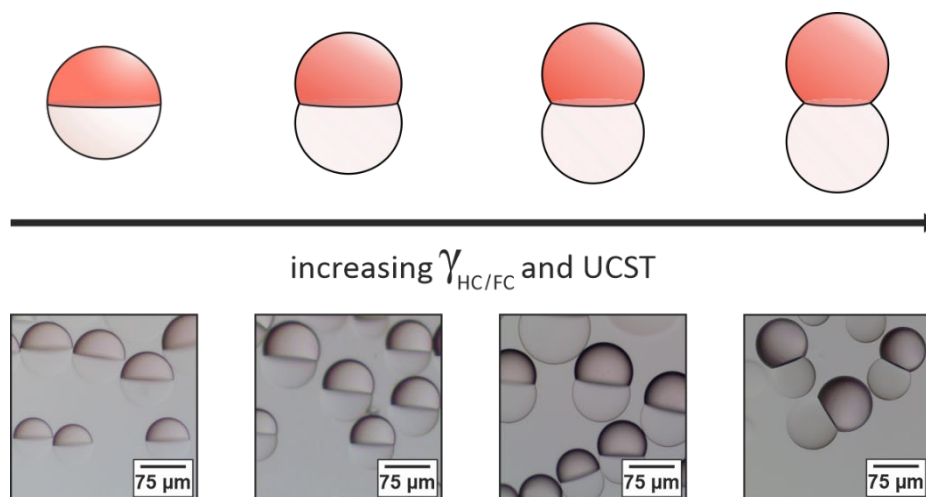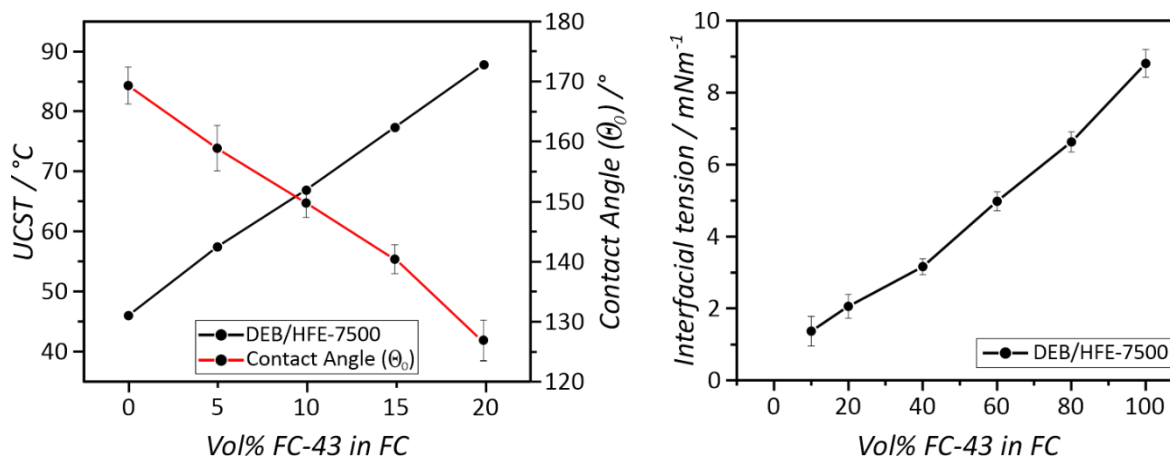

Figure 26. Influence of FC-43 content in the fluorocarbon phase of DEB/HFE-7500 Janus emulsions on the droplet shape. The higher the percentage of FC-43 in the fluorocarbon phase the higher the mixing temperature T_c (left) and the higher the interfacial tension between the droplet phases (right).

The adjustability and control of the droplet shape by specific variations in droplet phase composition was not limited to the DEB/HFE-7500 system and could also be applied to other liquid combinations such as n-decane/MPFB or n-heptane/PFH (Figure 27 left).
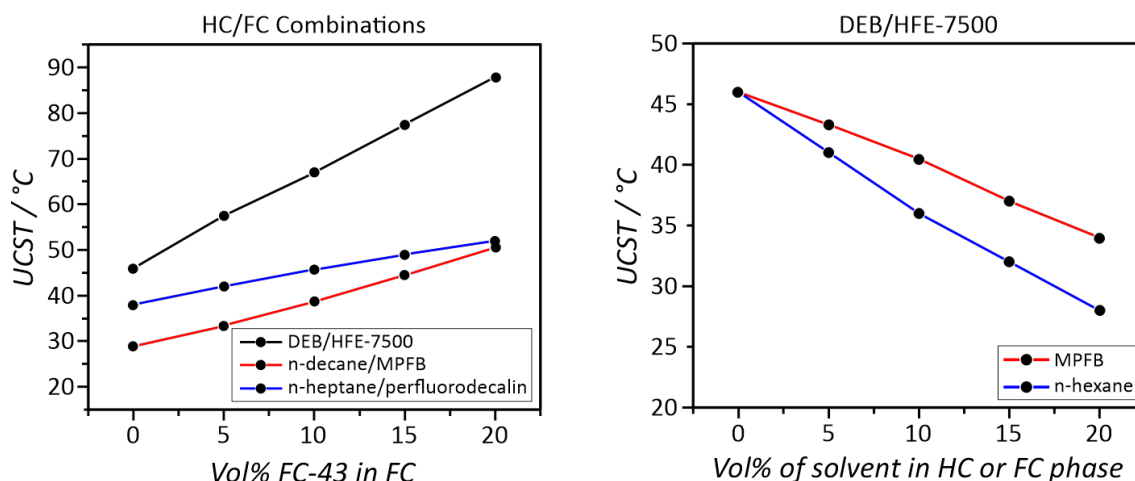
Figure 27. Influence of FC-43 content in the fluorocarbon phase of different oil combinations (left) and effect of MPFB and n-hexane content in the HC or FC phase on the UCST (right). The proportional replacement of DEB by n-hexane or of HFE-7500 by MPFB, reduces the UCST of the oil mixture.

These liquid combinations also showed a linear increase in UCST, yet with a different slope, the greater the proportion of FC-43 in the fluorocarbon phase was. Proportional replacement of HFE-7500 by the

fluorocarbon methoxyperfluorobutane (MPFB), which has a lower UCST towards DEB (T_c = -23 °C) than HFE-7500, lead to the contrary effect. The UCST of the oil mixture was lowered with increasing fraction of MPFB in the fluorocarbon phase (Figure 27 right). However, the change in UCST is not limited to the modification of the fluorocarbon phase, but can also be realized by varying the composition of the hydrocarbon phase. Analogous to the replacement of HFE-7500 with MPFB, the UCST liquid mixture can be gradually lowered by the proportional replacement of DEB by several hydrocarbons that have a lower UCST towards HFE-7500, such as n-hexane (Figure 27 right). As a result, emulsion droplets assume an increasingly spherical shape with decreasing UCST.

The UCST, and thus the drop shape, can be selectively modified and adjusted by changing the droplet phase composition. However, if one is dependent on unifluid and pure droplet phases, this method of tuning is not suitable. In addition, the relatively high mixing temperatures, which are necessary to generate snowman-like droplets are impractical for emulsion generation, as evaporation of the constituent oils is favored and can lead to uneven droplet phases. Further, heating the surfactant solution during the thermal phase separation approach to temperatures near the boiling point of water can also lead to evaporation of the continuous phase, which changes the surfactant concentration.

4.1.3.2 Additives to Solvent Combinations

To overcome the aforementioned droplet generation issues with the thermal phase separation approach, the preparation technique was combined with the solvent evaporation method described in chapter 3.2.2. In this approach, a basic distinction between two types of additives can be made: additives that remain in the system after addition or proportional replacement (e.g. FC-43, MPFB, n-hexane,...) and additives that only temporarily influence the properties of the mixture and leave the system again due to their volatility (e.g. methanol, dichloromethane (DCM) or diethyl ether). These co-solvents can form a homogenous single-phase system with the droplet phases at reduced temperature. Using a volatile compound as a co-solvent, the homogeneous solution gradually separates into two phases with progressive evaporation of the additive. This evaporation-driven process takes time, because the co-solvent molecules must first dissolve in the aqueous continuous phase before diffusing into the atmosphere.

With the addition of volatile co-solvents in a ratio of 1:1:1 (HC/FC/Co-solvent), droplets consisting of DEB and HFE-7500 could be generated in 0.5 wt.% SDS and 1.5 wt.% Zonyl with the same overall morphology but at significant lower temperatures. For example, droplets prepared with a 10 vol% fraction of FC-43 in the fluorocarbon phase (T_c = 67 °C) exhibited a contact angle of θ_0 = 152.8 ± 2.4°

4 Results and Discussion

(Figure 26 left). Droplets with the same shape could be generated at lower temperatures by adding volatile co-solvents such as methanol (T_c = 65.5 °C), DCM (T_c = 55.5 °C) or diethyl ether (T_c = 35 °C) (Figure 28).
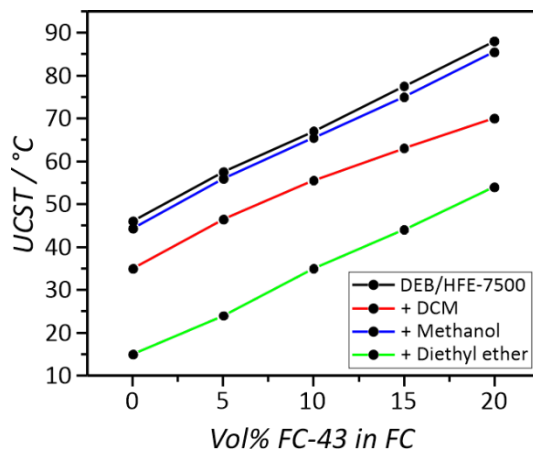

Figure 28. Effect of volatile co-solvent addition on the UCST of DEB/HFE-7500 oil mixtures. Volatile co-solvents can significantly decrease the T_c during emulsification, while maintaining the original droplet shape after full evaporation.

Methanol, which is not miscible with either the hydrocarbon or fluorocarbon phase due to its high polarity, showed the least effect on lowering the UCST. Diethyl ether, on the other hand, decreased the UCST of the two immiscible liquids so drastically that a homogeneous single-phase system was already present at room temperature. This can be attributed to the fact that diethyl ether exhibits good miscibility with both DEB and HFE-7500. However, the complex emulsion droplets produced by the addition of diethyl ether deviated toward a less pronounced snowman shape compared to the reference sample without volatile additives. Even after allowing the samples to rest overnight, the difference remained, indicating that diethyl ether does not completely evaporate from the system due to its good miscibility with both liquids. By adding dichloromethane (DCM), droplets containing 10 vol% of FC-43 could be generated already at a mixing temperature of Tc = 55.5 °C and exhibited the same droplet shape as the droplets generated without the addition of DCM after complete evaporation of the co-solvent. DCM thus showed the best overall properties to temporarily lower the UCST of the system. As with the variation of the droplet phase composition, the tunability of the mixing temperature with the addition of volatile co-solvents is not limited to the DEB/HFE-7500 system but can also be applied to other liquid combinations, although the compatibility and UCST-reducing ability of the co-solvents differs depending on the HC/FC oil combination (Figure 29).
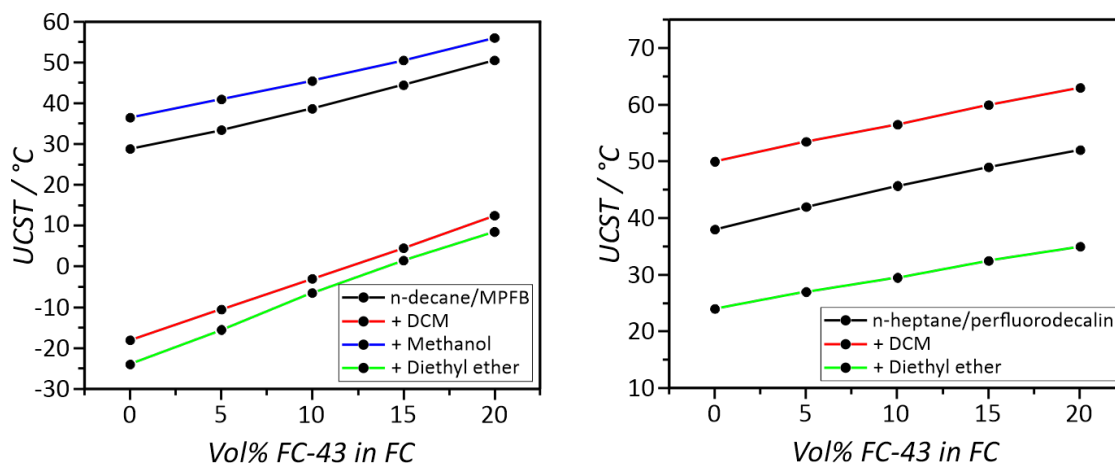
Figure 29. Effect of volatile co-solvent addition on the UCST of n-decane/MPFB (left) and n-heptane/perfluorodecalin (right) oil mixtures. Volatile co-solvents can significantly decrease the T_c during emulsification, while maintaining the original droplet shape after full evaporation. The addition of methanol to the n-decane/MPFB resulted in a slightly higher UCST, whereas the addition of methanol to the n-heptane/perfluorodecalin increased the UCST above the boiling point of methanol (65 °C). The increase in UCST after the addition of DCM shows that the compatibility and effect of co-solvents is individual and depends on the oil combination.

To investigate if the UCST alone is crucial for the shape of complex emulsion droplets, the droplet shapes of three emulsions with different oil combinations were compared. For this purpose, the emulsions were produced in the same aqueous surfactant solution (1.0 wt% SDS + 4.0 wt% Zonyl) and adjusted to the same mixing temperature (T_c = 63 °C) by proportional addition of FC-43 to the FC phase. Two of the emulsions were prepared using the DEB/HFE-7500 liquid combination. The first emulsion was adjusted to a UCST of 63 °C with 7.98 vol% of FC-43 in the fluorocarbon phase, whereas the other emulsion contained 15.0 vol% of FC-43 and was brought to a mixing temperature of T_c = 63 °C by the addition of DCM in a ratio of 1:1:1 (HC/FC/DCM). After complete evaporation of DCM, the latter exhibited a much more pronounced snowman shape with an external contact angle of θ_0 = 140.4 ± 2.5° compared to θ_0 = 153.7 ± 3.2° (Figure 30). This can be explained by the significantly higher fraction of FC-43 in the droplets' fluorocarbon phase. Thus, UCST was only temporarily lowered by the addition of DCM. Droplets generated from a mixture of n-decane/MPFB with 30.85 vol% FC-43 in the fluorocarbon phase exhibited a contact angle of θ_0 = 144.8 ± 2.8° despite the same UCST of 63 °C, demonstrating that the UCST of the particular liquid combination is not the only important factor determining the resulting shape of the emulsion droplets (Figure 30). Exemplary droplet side-view micrographs of the three different emulsions are shown in figure 30.
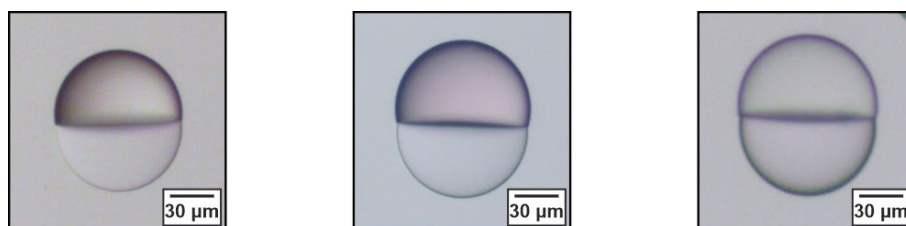
Figure 30. Side-view micrographs of Janus droplets prepared in 1.0 wt.% SDS and 4.0 wt.% Zonyl. DEB/HFE-7500 droplets with 7.98 vol% (left) and 15.0 vol% (middle) of FC-43 in the fluorocarbon phase and n-decane/MPFB with 30.85 vol% FC-43 (right). The droplets have a different shape, although they have the same UCST of 63 °C.

The UCST correlates with the interfacial tension $\gamma_{HC/FC}$ between the two immiscible liquids (Table 1 and Figure 26). However, the droplet shape remains an expression of all three underlying interfacial tensions, as mentioned above. Therefore, the chemical nature of the oils used is equally crucial, as it determines the interaction with the surfactants at the water-interface and thus the value for γ_{HC} and γ_{FC}.

4.1.3.3 Tuning the Droplet Shape via Variation of the Interfacial Tension Balance

To further investigate the influence of the external interfacial tensions γ_{HC} and γ_{FC} on the overall complex droplets' external shape, the liquid combination 1-bromohexane/perfluorodecalin was studied. The difference of this liquid combination compared to the previously studied systems is that the interfacial tension between the oils, which was measured to be at $\gamma_{HC/FC} = 5.28 \pm 0.18$ mNm^{-1} is not negligibly small. Complex emulsions were prepared in aqueous surfactant solutions with six different concentrations of SDS and Zonyl. Additionally, interfacial tension measurements were conducted via pendant drop tensiometry to determine the interfacial tensions of the oils with respect to the different surfactant solutions. The corresponding surfactant concentrations were adjusted so that the two external interfacial tensions, γ_{HC} and γ_{FC}, were as equal as possible to obtain perfect Janus droplets that only differ in their ratio between γ_{HC} and γ_{FC} versus $\gamma_{HC/FC}$. To express the external interfacial tensions (γ_{HC} and γ_{FC}) in one value ($\gamma_{external}$), the average of the two interfacial tensions between 1-bromohexane and the surfactant solution (γ_{HC}) and between perfluorodecalin and the surfactant solution (γ_{FC}) was taken. The different surfactant concentrations and the respective external interfacial values $\gamma_{external}$ of the six samples are listed in Table 2:

4 Results and Discussion

Table 2. Surfactant concentration and external interfacial tension values of six 1-bromohexane/perfluorodecalin emulsion samples.

Sample No.	SDS concentration [wt.%]	Zonyl concentration [wt.%]	External interfacial tension $\gamma_{external}$
1	0.01	0.005	20.62 ±0.42
2	0.02	0.01	17.68 ±0.29
3	0.03	0.025	14.73 ±0.39
4	0.05	0.05	10.42 ±0.35
5	0.1	0.1	8.87 ± 0.42
6	1.0	4.0	4.75 ± 0.47

The obtained Janus droplets differed greatly in their contact angle θ_0, although the droplet composition remained constant for all samples (Figure 31).
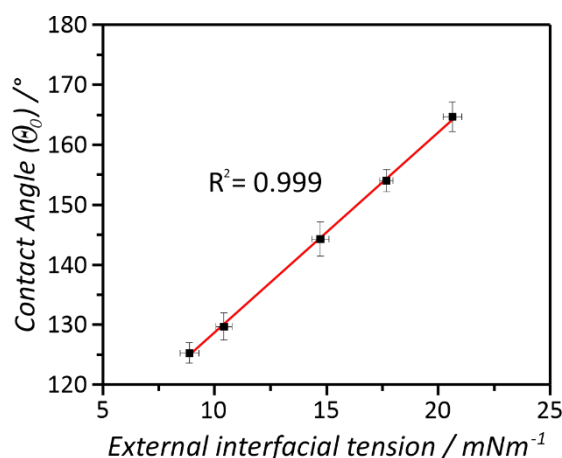

Figure 31. Outer contact angle θ_0 against the average external interfacial tension $\gamma_{external}$ of 1-bromohexane/perfluorodecalin emulsion droplets with different surfactant concentrations. The graphs shows a perfectly linear correlation between the droplet shape (θ_0) and the external interfacial tension $\gamma_{external}$.

The lower the applied surfactant concentration of the aqueous continuous phase was and consequently the higher external interfacial tension $\gamma_{external}$ was, the larger was the contact angle θ_0. Vice versa, the lower $\gamma_{external}$, the lower was the contact angle θ_0 and thus the deviation from the spherical drop shape (Figure 31). At high surfactant concentrations in sample 6 (1.0 wt.% SDS + 4.0 wt.% Zonyl), the measured external interfacial tension was lower than the internal interfacial tension between the two oils (4.75 ± 0.17 mNm^{-1} vs. 5.28 ± 0.18 mNm^{-1}). In consequence, the two oils formed two separate droplet phases, since there is no thermodynamic energetic incentive to form a

conjunct droplet. Consequently, the overall shape of the Janus emulsions can be influenced purely by altering the external interfacial tensions, since ultimately the ratio between γ_{HC} and γ_{FC} versus $\gamma_{HC/FC}$ is crucial.

4.1.4   Reversible Shape-changing Behavior of Stimuli-responsive Snowman Droplets

Based on the results of the targeted droplet shape modification, it was investigated whether the outer shape of the droplets can also be changed *in situ*. To change the droplet shape without actively changing the emulsion composition or the surfactant concentration of the continuous phase, a stimuli-responsive surfactant is required. Some stimuli-responsive surfactants that respond to external triggers are able to change the balance of interfacial tensions without persistently affecting the emulsion media. For this purpose, the photo-responsive surfactant 4-butyl-4'-(3-trimethyl-ammoniumpropoxy)phenyl-azobenzene (AzoTAB) was synthesized, which was already discussed in chapter 3.3 (for synthesis see chapter 10.3.1). AzoTAB, which preferably assembles at the HC/W interface of biphasic HC/FC complex emulsion droplets, can reversibly alter its surfactant effectiveness depending on the wavelength of the incident light. To realize a shape-changing droplet system, complex emulsion droplets were generated from n-decane and MPFB with 30 Vol% FC-43 in the FC phase ($T_c = 62.5 °C$) in a HC/FC ratio of 1:1. The droplets were emulsified in a surfactant solution containing 0.05 wt.% AzoTAB, 0.005 wt.% SDS and 0.1 wt.% Zonyl. SDS was added to improve the droplets' stabilization of the droplets. The obtained droplets exhibited a morphology with a dominant HC/W interface ($\gamma_{HC} < \gamma_{FC}$). Applying an external focused light beam, which was guided through a bifurcated fiber and focused on the vertical aligned sample, allowed to photo-switch the thermodynamically more stable trans-isomers locally into the cis-form via UV-light irradiation ($\lambda = 365$ nm). The light-triggered isomerization lead to a spherical to snowman-shaped transition of the emulsion droplets. With the application of blue light ($\lambda = 470$ nm) the isomerization and thus the change in droplet topology was reversible (Figure 32).
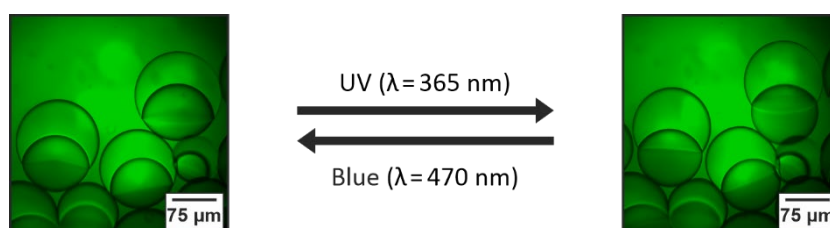

Figure 32. Light-triggered change in droplet topology of n-decane/MPFB complex droplets with 30 Vol% of FC-43 in the FC phase by alternating irradiation with UV- ($\lambda = 365$ nm) and blue light ($\lambda = 470$ nm).

To ensure permanent background illumination during the experiment without affecting the sample, it was constantly illuminated with green light (λ = 530 nm). The isomerization is accompanied by a local change in the hydrophobicity of the surfactant, resulting in a decrease in its surfactant effectiveness and consequently to an increase in γ_{HC}.

The shape changing behavior or the emulsion system can be explained as follows: With the triggered increase of γ_{HC}, the ratio of the external interfacial tensions γ_{HC} and γ_{FC} to the internal interfacial tension $\gamma_{HC/FC}$ increases, which is reflected in the spherical to snowman-like shape transition of the droplets. With a relatively high content of FC-43 (30 %) in the FC phase and a T_c of 62.5 °C, the selected droplet composition ensures a sufficiently high internal interfacial tension $\gamma_{HC/FC}$ for the occurrence of non-spherical droplets. Further, the initial surfactant concentration was intentionally chosen to be low in order to have a good ratio between external and internal interfacial tensions and to induce a large interfacial tension difference by applying the light trigger.

4.1.4.1 Jellyfish-inspired Motion of Stimuli-responsive Janus Emulsions

In the previously described shape-changing experiments, some degree of droplet motion was observed during the switch of the irradiated wavelength between UV- and blue light. To investigate whether the motion of the droplets due to the rapid change between spherical and elongated snowman shape exhibits a directionality, the volumes of the droplet phases were adjusted to match the density of the continuous phase. Therefore, the density of the FC phase modified with 30 Vol% of FC-43 was calculated first:

$$\rho(FC) = 0.3 \cdot \rho(FC\text{-}43) + 0.7 \cdot \rho(MPFB)$$

$$\Rightarrow \rho(FC) = 0.3 \cdot 1.86 \text{ g/mL} + 0.7 \cdot 1.52 \text{ g/mL}$$

$$\Leftrightarrow \rho(FC) = 1.622 \text{ g/mL}$$

Then the droplet phase volumes were calculated:

$$f(HC) \cdot \rho(HC) + f(FC) \cdot \rho(FC) = \rho(H_2O)$$

$$\Rightarrow x \cdot \rho(n\text{-decane}) + (1 - x) \cdot \rho(FC) = \rho(H_2O)$$

$$\Rightarrow x \cdot 0.730 \text{ g/mL} + (1 - x) \cdot 1.622 \text{ g/mL} = 0.997 \text{ g/mL}$$

$$\Leftrightarrow x = f(HC) = 0.701$$

$$<=> 1 - x = f(FC) = 0.299$$

Alternating irradiation of the density matched and vertical aligned complex emulsion droplets with UV- and blue light lead to a "jellyfish-like" movement of the droplets comprised of 71.1 Vol% HC phase and 29.9 Vol% FC phase. The switching shape variations between spherical and snowman droplet shapes lead to a buoyancy of the emulsion droplets through the continuous aqueous phase. The externally triggered vertical movement of the floating droplets is caused by their rapid expansion, which is accompanied by a directional displacement of the continuous phase (Figure 33).
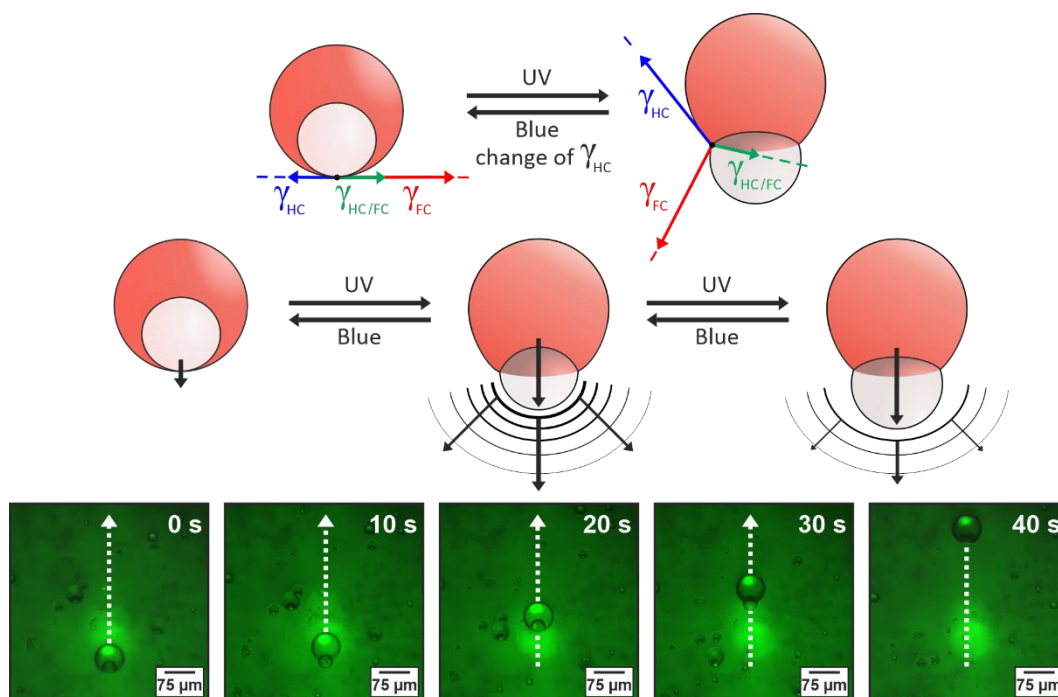

Figure 33. Jellyfish-inspired movement of complex emulsions through photo-induced isomerization of AzoTAB. The rapid elongation of the droplets caused by the bulging FC phase displaces the continuous phase, leading to buoyancy of the droplets in the vertical direction. The micrographs show the time-dependent movement of the droplets through the continuous medium with a buoyancy speed of ≈ 8.3 μm/s.

Due to the alternating inward and outward bulging FC phase, the droplets reached a buoyancy velocity of ≈ 8.3 μm/s. The stimuli-responsive shape-changing behavior and directional movement of the soft colloids demonstrates the close entanglement of internal structure and functionality and offers potential for the development of biomimetic active materials and reconfigurable soft robotics.[169]

4.1.5   Conclusion

Different variations of droplet composition and the targeted design of non-spherical anisotropic complex emulsions by combining the thermal phase separation approach and the solvent evaporation

method were discussed. In addition, the influence of additives and co-solvents on the UCST of the participating oils was studied in detail. It was found that the droplets' external shape can be adjusted by various modifications to the emulsion system. By changing the droplet phase composition, the UCST can be tuned which correlates with the degree of the snowman shape. However, if pure droplet phases are required, volatile co-solvents can be used that temporarily reduce the UCST of the oil mixture but leave the system over time through evaporation. Closer examination has revealed that it is not solely the UCST that determines the shape, but that the droplet shape is an expression of all three underlying interfacial tensions. Therefore, the chemical nature of the solvents is equally crucial as it determines the interaction with the surfactants at the droplet-water interface and thus the values for γ_{HC} and γ_{FC}. Additionally, it was shown that overall shape of the Janus emulsions can be influenced purely by altering the external interfacial tensions, since fundamentally the ratio between γ_{HC} and γ_{FC} versus $\gamma_{HC/FC}$ determines the droplet shape.

Experiments with the stimuli-responsive photo-surfactant AzoTAB revealed a shape-changing behavior of the soft colloids, which was dependent on the wavelength of the incident light. The photo-triggered contraction and expansion of the complex emulsion droplets was exploited in a jellyfish-inspired movement scheme. By fast changing the incident light between UV- (365 nm) and blue light (470 nm) the emulsion droplets experienced a buoyancy speed of $\approx 8.3\ \mu m/s$. These results offer high potential for a broad variety of biological inspired active material architectures and shape-changing soft robotics.

4.2   Quantitative in situ Determination of Surfactant Effectiveness using Reconfigurable Janus Emulsions

4.2.1   Introduction

Characterization of surfactants and extraction of their key parameters including their CMC as well as their effectiveness to lower the surface tension at interfaces, which evaluates their performance in a wide range of emulsion technologies, e.g. cleaning, manufacturing, oil recovery and other processes, requires accurate determination methods that work in a practical interfacial tension regime.[170-173] However, conventional methods for the determination of interfacial tensions such as force tensiometers are either most accurate for fluid interfaces with high interfacial tensions ($\gamma = 40\text{-}60\ mNm^{-1}$), or they are specifically designed for the quantification of ultralow interfacial tensions ($\gamma < 1\ mNm^{-1}$), like for instance the spinning drop method.[38] Additionally, most conventional techniques are typically associated with one or more of the following drawbacks: the need for

expensive and/or complicated equipment, requirement of additional computational add-ons and software, incapability to produce a real-time signal that prevents an *in situ* analysis of surfactant systems, involvement of tedious synthesis e.g. of chemical (fluorescent) probes, time- and/or sample-consuming procedure that requires a series of surfactant solutions with different concentrations, which must be prepared and measured individually.[174-177]

This chapter is focused on the unique chemical-morphological coupling inside biphasic O/W Janus emulsions. The droplet morphology is a function of the underlying interfacial tensions.[91, 95] Therefore, the correlation between the measured contact angle of the droplets and the interfacial tensions at the two droplet interfaces should be deciphered. The response of conventional O/W emulsions to changes in surfactant effectiveness and thus to changes in interfacial tensions results only in qualitative changes, e.g. changes in droplet size or stability.[149, 178, 179] In this context, a liquid-liquid transduction scheme based on reconfigurable complex emulsions is appealing as it allows the investigation of surfactants in their designated environment. *In situ* observations should be performed using a simple, customized side-view imaging setup to study the dynamic morphological changes of Janus emulsions in response to variations in surfactant type, concentration and ratio. With the aim of extracting actual interfacial tension values from droplet observations, a new method for the characterization of surfactants should be developed, that works in a convenient interfacial tension regime.

4.2.2   Janus Emulsions as Transducers

As already described in chapter 3.2.1, Janus emulsion droplets comprised of two dispersed fluids, have the intrinsic advantage that interfacial tension variations transduce into a change in the droplets' internal shape whereas the overall emulsion stability remains intact. For the case of working temperatures close to the critical temperature of the internal fluids, the overall droplet shape is nearly spherical. Cooling below T_c yields structured Janus emulsion droplets with highly uniform composition and morphology. After emulsification the droplet geometries can controllably altered by triggering changes in the surfactant effectiveness as the internal droplet morphology of Janus emulsions is exclusively controlled by a balance of interfacial tensions. These variations in droplet morphology, reflected in an either concave or convex shaped internal interface, can be readily observed and monitored by a horizontal imaging setup.[180]

To transform this unique chemical-morphological coupling inside biphasic Janus emulsions into a method that allows for an *in situ* determination of interfacial tensions, the morphological reconfiguration of heptane/perfluorodecalin Janus emulsions were measured for different fractions of

4   Results and Discussion

0.1 wt.% SDS (f_{SDS}), where the other fraction was 0.1 wt.% Zonyl. Parallel interfacial tension measurements at the interfaces of heptane-water (γ_{HC}) and perfluorodecalin-water (γ_{FC}) in the same variety of surfactant concentrations and ratios using the pendant-drop method (Figure 34) revealed the coincidence of the droplet morphology with the difference in interfacial tensions $\Delta IFT = \gamma_{FC} - \gamma_{HC}$ (Figure 35 left).[180]
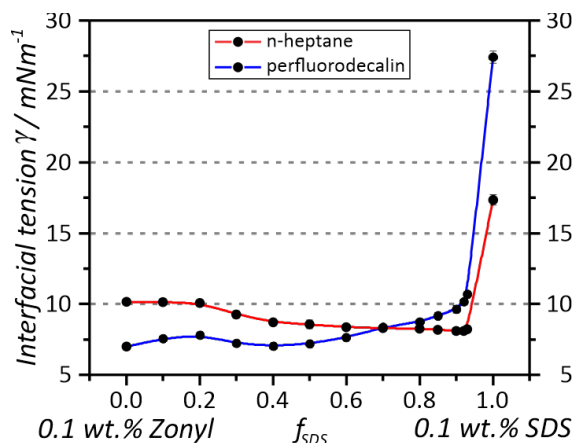

Figure 34. Interfacial tension of the perfluorodecalin-water- and the n-heptane-water interface as a function of the fraction of 0.1 wt.% SDS, f_{SDS}, where the other fraction is 0.1 wt.% Zonyl FS-300. At the crossing point of the two interfacial tensions ($\gamma_{HC} = \gamma_{FC}$) the droplets assume a perfect Janus shape. Interfacial tension error bars refer to N ≥ 5 measurements.
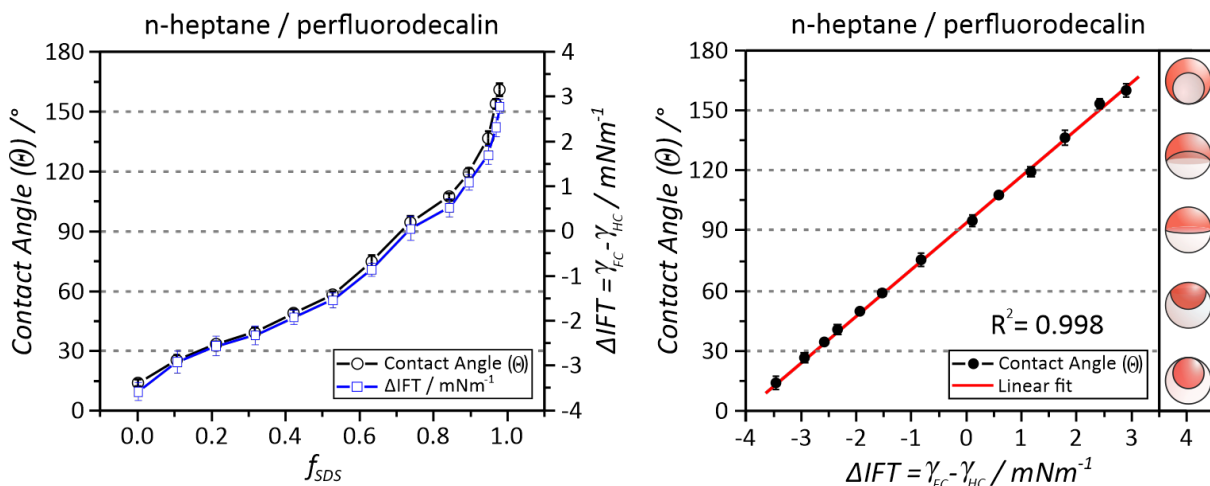
Figure 35. Droplet morphology of the heptane-perfluorodecalin system showing the contact angle (θ) and $\Delta IFT = \gamma_{FC} - \gamma_{HC}$ as a function of the fraction of 0.1 wt.% SDS, f_{SDS}, where the other fraction is 0.1 wt.% Zonyl (left). The reconfiguration of the droplet morphology coincides with ΔIFT at varying surfactant fractions. Linear calibration curve of droplet contact angle evolution versus differences in the balance of interfacial tensions (right). Contact angle error bars refer to N ≥ 10 and interfacial tension error bars to N ≥ 5 measurements.

Plotting the change in morphology against the difference in interfacial tensions ΔIFT resulted in a linear correlation curve, validating that the interfacial tension difference $\gamma_{FC} - \gamma_{HC}$ serves as the sole parameter determining the droplet configuration. Consequently, any given contact angle that lies within the dynamic range of droplet reconfiguration can be translated into an interfacial tension value. The calibration curve further reveals that a difference in the balance of interfacial tension of $\Delta\gamma \approx \pm 6.8$ mNm^{-1} suffices to completely invert the droplets morphology from one encapsulated double emulsion state to the other. This means that slight variations in interfacial tension in the order of $\Delta\gamma = \pm 0.5$ mNm^{-1} induce pregnant and readily detectable changes in the contact angle of $\Delta\theta \approx 13°$, which provides a reliable foundation for an accurate and sensitive droplet-based method to determine interfacial tensions. The implementation of an image processing program allowed a fast and convenient droplet morphology analysis to calculate the average contact angle of a sample. The program uses an adaptive threshold detection algorithm to distinguish areas with higher transparency from the opaque regions of the higher refractive index and dyed hydrocarbon phases and calculates θ_{FC} from the respective circles according to formula (6).

4.2.3   CMC and Surfactant Effectiveness Determination

The morphological response of reconfigurable Janus emulsions at dynamically increasing concentrations of well-established ionic and nonionic hydrocarbon surfactants was monitored using the side-view imaging setup. The measurements started with droplets in their encapsulated form (HC/FC/W) and the continuous concentration increase of HC surfactant led to a dynamic contact angle evolution along the Janus continuum, resulting in droplet morphology diagrams with a characteristic progression. The concentration of FC surfactant (Zonyl) was kept constant during the experiments to maintain the overall droplet stability and to serve as an internal standard. A typical graph showing the droplets' contact angle versus the concentration of the HC surfactant, in this case sodium bis(2-ethylhexyl) sulfosuccinate (AOT), is displayed in figure 36:
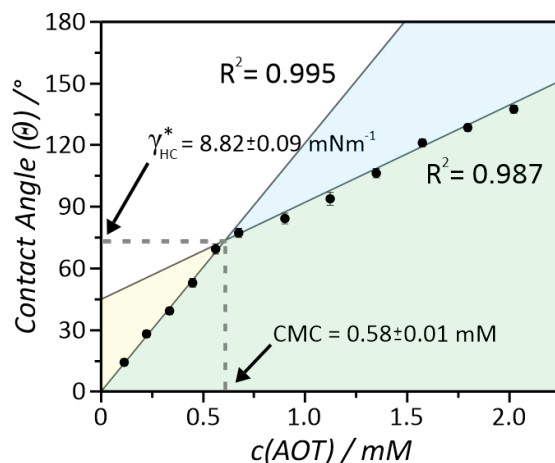
Figure 36. Morphology diagram of biphasic n-heptane/perfluorodecalin droplets in response to dynamic changes in the hydrocarbon surfactant (AOT) concentration. The fluorocarbon surfactant (Zonyl) was kept at a constant concentration of 0.1 wt.% throughout the experiment. Contact angle error bars refer to N ≥ 10 measurements.

The morphology diagram reveals a linear change in morphology up to a certain surfactant concentration of AOT followed by an abrupt decrease in slope with further increase in surfactant concentration. A closer look at the graphs confirmed that the point at which the slope changes corresponds to the CMC of AOT. The interfacial tension γ of a liquid is decreasing continuously with an increasing amount of surfactant in solution until the CMC is reached. Above the CMC, there is no major change noticeable and the interfacial tension stays at a constant value. This typical progression of interfacial tensions can be seen in measurements of the n-heptane-water interfacial tension at different SDS concentrations (Figure 37 left) and of the perfluorodecaline-water interfacial tension at different Zonyl concentrations measured via pendant drop (Figure 37 right).
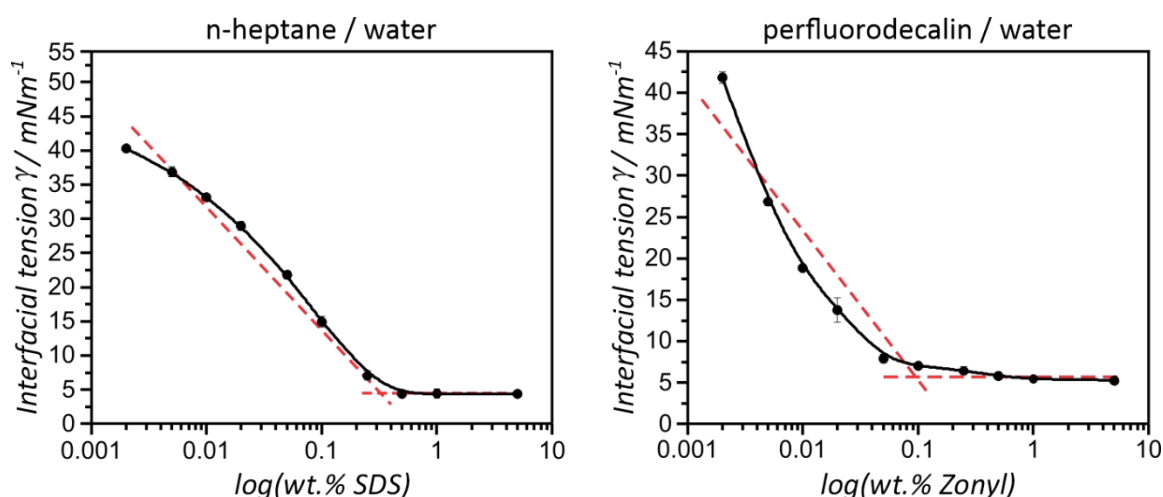

Figure 37. Interfacial tension of the n-heptane-water interface at different concentrations of SDS (left) and interfacial tension of the perfluorodecalin-water interface at different concentrations of Zonyl (right), measured

with the pendant drop method. The interfacial tension γ is decreasing until the CMC of SDS (≈ 0.237 wt.%) or Zonyl (≈ 0.115 wt.%) is reached. Interfacial tension error bars refer to N ≥ 5 measurements.

Since the droplets' contact angle θ correlates with ΔIFT, the morphology of the droplets changes rapidly at surfactant concentrations below the CMC due to the distinct shift in the corresponding interfacial tension. Below the CMC every newly added surfactant molecule will be adsorbed at the droplets' interface, which causes a fast decrease of γ. Once the CMC is reached, the interface is fully covered with surfactant molecules, hence the change in the droplets morphology is slowing down. Nevertheless, the contact angle (θ) does not remain constant and the morphology evolution continues to progress. A possible explanation for the progressive change in morphology could be a statistical displacement phenomenon: If the concentration of a hydrocarbon surfactant is increased above the CMC, fluorocarbon surfactant molecules are increasingly replaced in favor of hydrocarbon surfactant molecules since statistically there are significantly more hydrocarbon surfactant molecules in the vicinity of the droplet surface.

Similar curves as in figure 36 were obtained for all other surfactants tested (Figure S1-S3). Analysis of the resulting plots enabled a precise determination of the CMC values of the surfactants, and the experimentally measured values agreed well with reported literature values (Table 3).[181] Next, with the equation of the linear calibration curve (Figure 35) at hand, the contact angle at the CMC of the HC-surfactant could be directly translated into an interfacial tension value γ_{HC}*, which serves as a measure of the surfactant's effectiveness to stabilize the hydrocarbon-water interface (for further information see chapter 6.4). The extracted γ_{HC}* values were in good agreement to values obtained using the pendant drop method (Table 3).

Table 3. CMC and γ_{HC}* values for the commercial surfactants tested in this study. Standard deviations of the CMC and γ_{HC}* values refer to N ≥ 5 measurements.

Surfactant	CMC [mM] (Dynamic Drop Method)	CMC [mM] (Literature Values)[181]	γ_{HC}* [mN/m] (Dynamic Drop Method)	γ_{HC}* [mN/m] (Pendant Drop Method)
SDS	8.44 ± 0.17	8.10-8.60	5.07 ± 0.11	5.13 ± 0.24
Brij 58	0.076 ± 0.012	0.080	11.39 ± 1.82	10.79 ± 0.54
AOT	0.584 ± 0.011	0.680	8.82 ± 0.09	9.11 ± 0.27
Triton-X100	0.258 ± 0.003	0.18-0.25	7.60 ± 0.08	8.21 ± 0.53

CTAB	1.00 ± 0.05	0.95-1.32	7.28 ± 0.38	7.05 ± 0.35
Tween 20	0.063 ± 0.001	0.06-0.08	13.46 ± 0.09	13.06 ± 0.45

Especially at higher surfactant concentrations, extraction of accurate γ_{HC}^* values using the pendant droplet method proved to be much more difficult and time- and sample-consuming than *in situ* extraction via the responsive drop method due to the difficulty of maintaining a stable droplet volume over extended periods of time. This demonstrates the versatility of the complex hydrocarbon-fluorocarbon droplets' response for the investigation of a broad range of surfactants and interfaces.

Further, with the right choice of surfactant stock solutions, in this case in fractions of 0.4 wt.% AOT, f_{AOT}, where the other fraction was 0.4 wt.% Zonyl, it was possible to extract the surfactants's CMC values and the surfactants effectiveness γ_{HC}^* and γ_{FC}^* from the same graph (Figure 38).
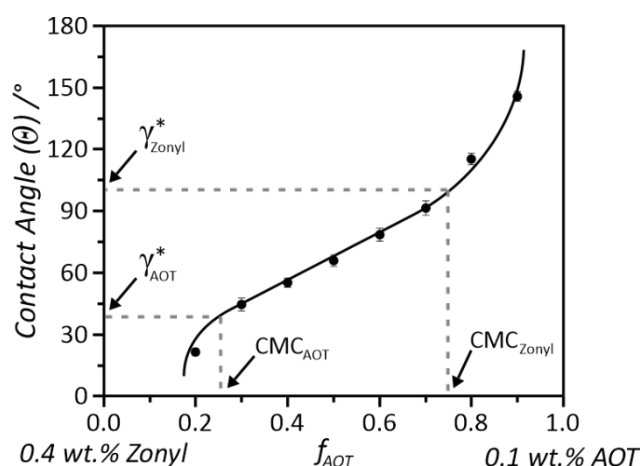

Figure 38. Typical morphological response of Janus droplets to dynamic variations in the ratio of hydrocarbon (here: AOT) and fluorocarbon (here: Zonyl) surfactants from which both the surfactants' CMC values and the interfacial tensions of surfactant stabilized fluid interfaces can be conveniently extracted. Contact angle error bars refer to N ≥ 10 measurements.

4.2.4   Influence of Salts on Biphasic Complex Emulsions

To investigate the dynamic morphological response of Janus emulsions to small varations in the salt concentration of their environment, biphasic Janus emulsion droplets comprised the hydrocarbon oil diethylbenzene and the fluorocarbon oil HFE-7500 (T_c = 47 °C) were generated using the established temperature-induced phase-separation approach. High salt concentrations can cause a destabilization of an emulsion system, i.e. flocculation or coalescence of droplets, which is followed by a macroscopic phase separation.[182] However, variations in the type and concentration of ionic species within the continuous phase are also known to affect the surfactant surface excess. By adding NaCl to the

emulsions, a significant effect on the droplet morphology was observed. The addition of 1 mM NaCl to emulsion droplets stabilized by 0.045 wt.% each of SDS and Zonyl resulted in an increase in contact angle from θ = 29.9° to 41.4°. The droplets' contact angle gradually evolved towards higher values with increasing ionic strength.[183]

The same effect, but more pronounced, was observed with the addition of divalent cations. 1 mM of Ca^{2+} caused a similar change in morphology as 50 times the amount of Na^+ ions. Interfacial tension measurements at different SDS concentrations and a fix Zonyl concentration of 0.5 wt.% via pendant drop tensiometry confirmed that the addition of 0.5 mM $CaCl_2$ significantly decreased the interfacial tension of the hydrocarbon-water interface, reducing the CMC of SDS from ≈ 8.4 mM to ≈ 3.3 mM (Figure 39 left). In close agreement to the pendant drop measurements, both the decrease in γ_{HC} and CMC induced by the addition of salt could be monitored by tracking the morphological transition using the responsive drop method (Figure 39 right).[183]
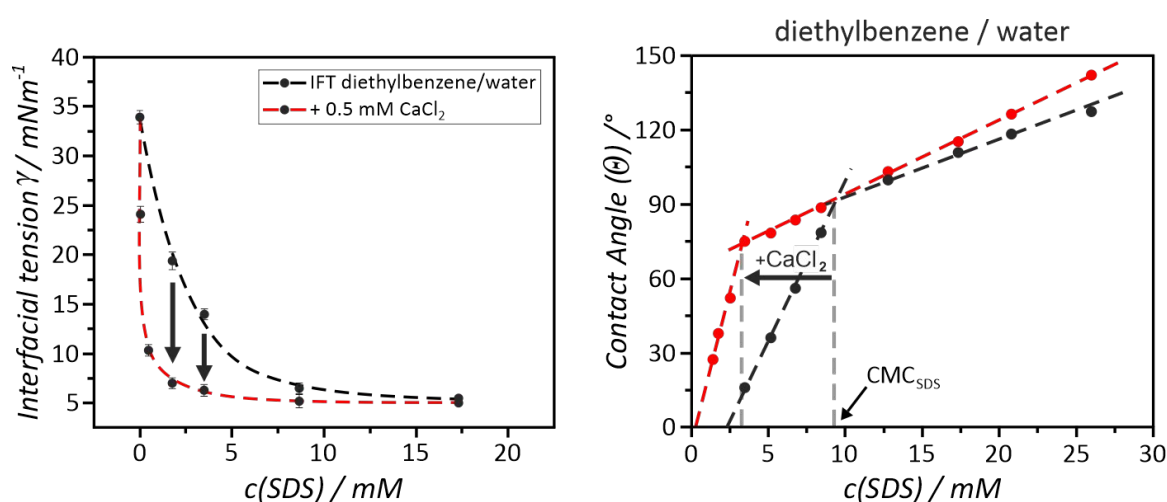

Figure 39. Influence of $CaCl_2$ addition on the surfactant effectiveness of SDS: interfacial tension measurements of the diethylbenzene-water interface with differing SDS concentrations (left) and contact angle evolution with increasing SDS concentrations in the presence and absence of 0.5 mM $CaCl_2$ (right). The Zonyl concentration was kept constant at 0.5 wt.%. Interfacial tension error bars refer to N ≥ 5 and contact angle error bars to N ≥ 10 measurements.

The results demonstrate an increase in the surfactant effectiveness of SDS through the addition of salt. The decrease in γ_{HC} and the CMC can be explained by the influence of the salt content on the surfactant properties.[184, 185] At elevated salt concentrations, the surfactant critical micelle concentration (CMC) decreases, while the micelle radius increases, which results in a decrease of the micellar zeta potential.[186] This influence depends on a series of parameters, including the surfactant concentration, valency and the size of the ions. Salt influences the surface excess (Γ) of the surfactant molecules,

causing a significant increase in Γ of ionic surfactants.[186] In the case of SDS and CaCl$_2$, the Ca^{2+} ions increase the solution activity and force ion pairing of the SDS molecules, which lowers the interfacial area per surfactant molecule. This leads to a reduction of the surfactant molecules' repulsive forces, increasing Γ$_{SDS}$ towards the maximum with the largest influence usually at concentrations below the CMC.[187, 188] As a result, the interfacial tension at the HC/W interface is lowered, inducing a quantifiable morphological change inside responsive Janus emulsions.

Reconfigurable Janus emulsions proved to be reliable transducers to track changes in salinity of water samples. Based on the sensitive chemical-morphological coupling inside Janus emulsions, Pavlovic et al. developed a convenient method for monitoring the hardness (Ca^{2+} and Mg^{2+} content) of water samples with Janus emulsions as optical probes, allowing a semi-quantitative analysis of drinking water.[183]

4.2.4.1 Counter-Ion and -Anion Effect on Charged Surfactants

To further investigate the influence of different monovalent cations on the surface excess of SDS, pendant drop measurements were performed in the presence and absence of 50 mM LiCl, NaCl, KCl and NH$_4$Cl. It was found that the decrease in HC/W interfacial tension varied depending on the cationic counter-ion (Figure 40 left).
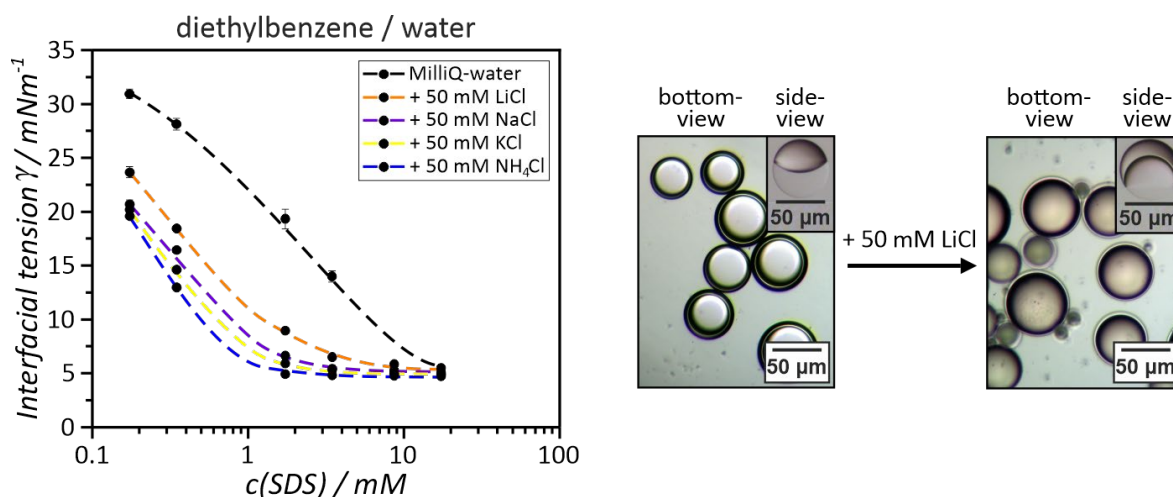

Figure 40. Interfacial tension measurements in the presence and absence of salts at different SDS concentrations (left). Bottom- and side-view micrographs of droplets captured with an inverted and side-view microscope demonstrating the morphological change caused by the addition of 50 mM LiCl (right). Interfacial tension error bars refer to N ≥ 5 measurements.

At a SDS concentration of 0.346 mM the addition of 50 mM LiCl caused a drop in interfacial tension from 28.15 mNm^{-1} to 18.46 mNm^{-1}. The addition of 50 mM NH$_4$Cl at the same SDS concentration evoked a more pronounced decrease to 12.98 mNm^{-1}. Microscopic observations of Janus droplets prepared in a surfactant mixture of f(SDS) = 0.85, with the total concentration SDS and Zonyl set to 0.09 wt.%, confirmed the morphological reconfiguration after the addition of 50 mM LiCl with a change from $\theta = 69°$ to $\theta = 118°$ (Figure 40 right). The effect of monovalent cations on γ_{HC} thereby closely followed the lyotropic (Hofmeister) series, so that larger and weakly hydrated cations such as NH$_4^+$ had a stronger effect on Γ_{SDS} than smaller and highly hydrated ions like Li$^+$. Larger cations can readily approach the water-oil interface due to their lower charge density and thinner hydration shell, causing SDS ion-pairing that results in a higher surface excess and consequently a lower interfacial area per surfactant molecule.[189] Smaller cations, on the other hand, have a weaker effect on the surface excess, as they are less able to cause ion-pairing due to their thicker hydration sphere.[190, 191] However, analogous measurements with varying counter-anions using KCl, KI and KNO$_3$ salts only had marginal effects on the interfacial tensions of SDS-stabilized interfaces and thus on the final droplet morphology (Figure 41).
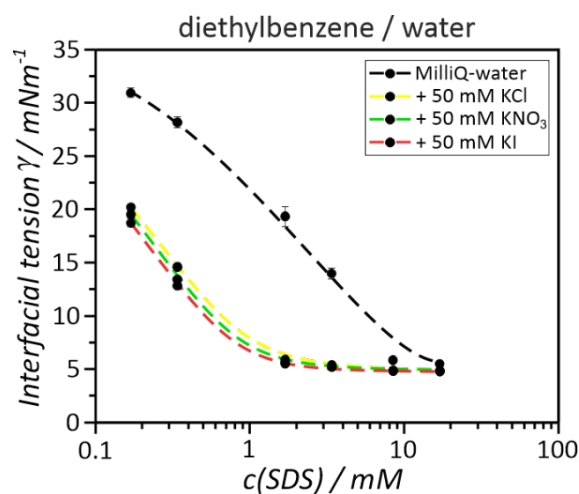
Figure 41. Interfacial tension measurements at different SDS concentrations in the presence and absence of KCl, KNO$_3$ and KI. The counter-anions only have marginal effects on the hydrocarbon-water interfacial tension. Interfacial tension error bars refer to N ≥ 5 measurements.

4.2.4.2 Counter-Ion Effect on Nonionic Surfactants

Since previous studies on the influence of salts on the effectiveness of nonionic surfactants have yielded partly contradictory results, interfacial tension measurements were also carried out with the widely used nonionic surfactant polyoxyethylen(20)-sorbitan-monooleat (Tween 80) under increased salt contents (Figure 42 left).[192-196] The pendant drop tensiometry measurements confirmed a

noticeable impact of the counter-ion on the effectiveness of Tween 80. The cation-dependent decrease in interfacial tension of Tween 80-stabilized diethylbenzene-water interfaces at varying surfactant concentrations was comparable to the previous results with the anionic surfactant SDS (Figure 42 right). This indicates that the Hofmeister series can potentially be extended to nonionic surfactants such as Tween 80. However, further measurements with other non-ionic surfactants are necessary for a clear confirmation of the hypothesis.
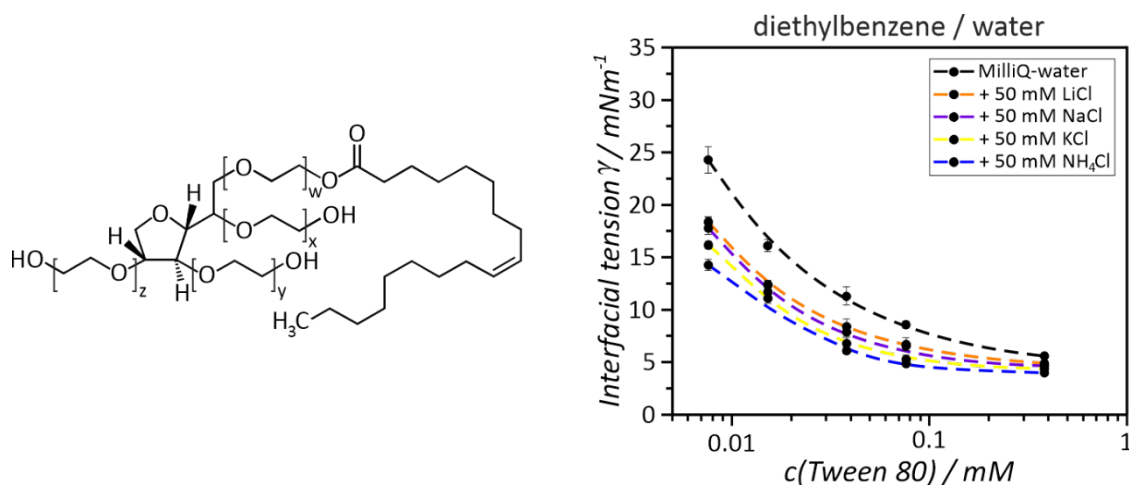

Figure 42. Chemical structure of the nonionic surfactant polyoxyethylen(20)-sorbitan-monooleat (Tween 80) (left) and interfacial tension measurements in the presence and absence of salts at different Tween 80 concentrations (right). Interfacial tension error bars refer to N ≥ 5 measurements.

4.2.5   Characterization of AzoTAB

The characterization of stimuli-responsive surfactants that can alter their surfactant effectiveness in response to physical or (bio-)chemical triggers is of interest because they can affect emulsion stability, colloidal aggregation, interfacial activity and the release of encapsulants.[146, 197] A thorough investigation of such systems is usually difficult using conventional characterization methods because examination is often limited to the thermodynamically stable configurations of the surfactants, as triggering events irreversibly change the structure of the system. To investigate whether the advantages of the responsive drop method can also be used for *in situ* monitoring of stimuli-responsive surfactants, biphasic n-heptane/perfluorodecalin Janus droplets were stabilized with the light-responsive surfactant AzoTAB.[148, 198]

By photo-switching the thermodynamically stable *trans*-isomer into the bent *cis*-form by UV-irradiation ($\lambda = 366$ nm) a change in hydrophobicity is induced that causes a morphological reconfiguration of complex emulsion droplets prepared in 0.25 wt% AzoTAB and 0.25 wt% Zonyl. The

complex emulsions have been irradiated until the droplets' topology reached a constant state. The resulting reduction in interfacial area of the HC/W interface was reversible by irradiation with a custom-designed blue LED (λ = 461 nm). The change in morphology could be readily observed with a side-view microscope (Figure 43 bottom). Contact angle measurements before and after the UV-light irradiation revealed a change in morphology from θ = 130.61 $\pm$ 1.97° (*trans*-AzoTAB) to θ = 75.18 $\pm$ 1.99° (*cis*-AzoTAB), which is a difference of $\Delta\theta$ = 55.43 $\pm$ 2.81°.
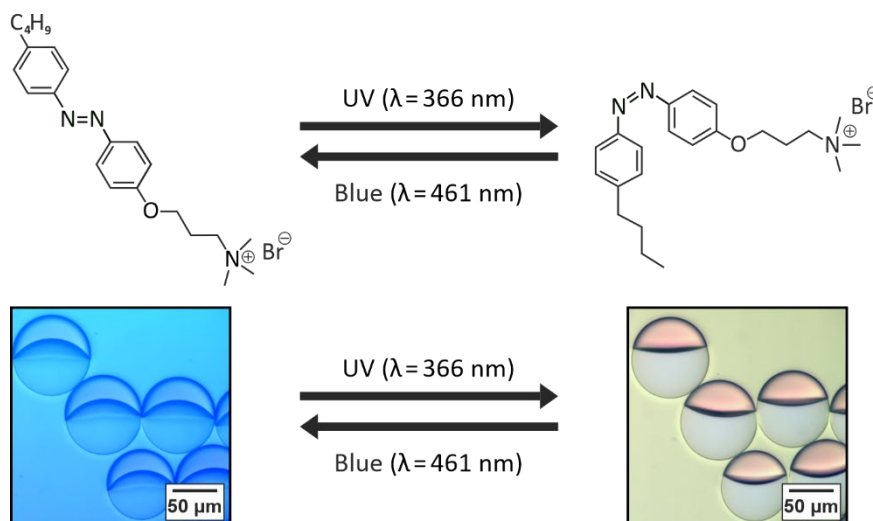
Figure 43. Light-triggered reconfiguration of Janus droplet morphology. Chemical structure of the light-responsive hydrocarbon surfactant (AzoTAB) (top). Optical micrographs of the Janus droplets' morphological transition in response to light-triggered variations in surfactant effectiveness (bottom).

Tracking the morphological transition between the two isomers *in situ* using the responsive droplet method at different concentrations of AzoTAB, while keeping the concentration of Zonyl constant at 0.06 wt%, yielded morphology diagrams that allowed CMC determination of both isomers (Figure 44).

4   Results and Discussion

Figure 44. Morphology diagram of biphasic n-heptane/perfluorodecalin droplets in response to light-triggered variations in droplet morphology as a function of the AzoTAB concentration. The fluorocarbon surfactant (Zonyl) was kept at a constant concentration of 0.0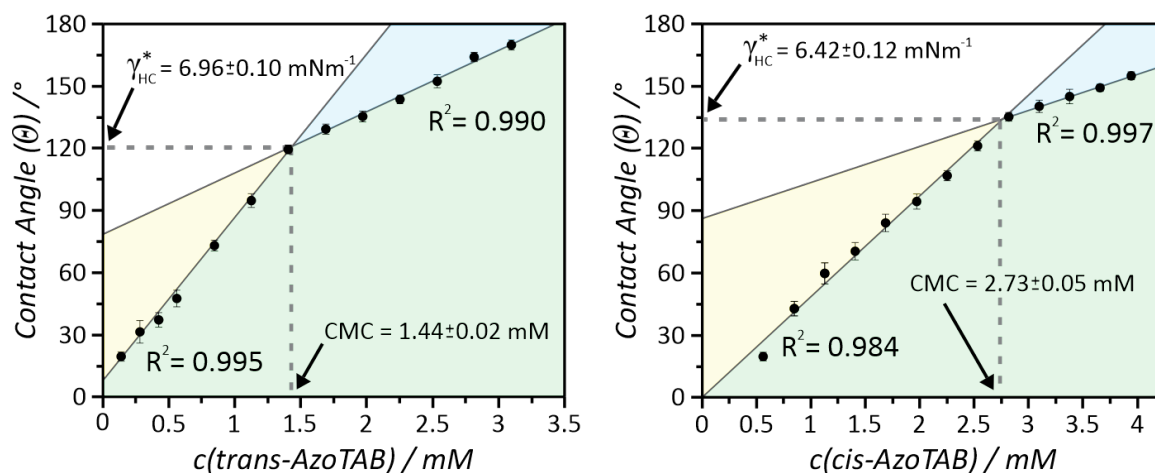6 wt.% throughout the experiment. The diagrams allowed determination of the CMC and γ_{HC}* values for the *trans*- (left) and *cis*-isomer (right). Contact angle error bars refer to N ≥ 10 measurements.

As a result, we observed a significant change in the CMC of the surfactant from 1.44 mM for the *trans*-isomer to 2.73 mM for the *cis*-isomer, but only small changes in the HC/W interfacial tension at the respective CMCs (γ_{trans}* = 6.96 mNm^{-1} vs. γ_{cis}* = 6.42 mNm^{-1}). Interfacial tension measurements via pendant drop tensiometry under UV-light irradiation were performed to quantify the actual change in interfacial tension at the HC/W interface at concentrations corresponding to the CMC of the AzoTAB-*trans*-isomer. The measurement revealed an interfacial tension decrease of $\Delta\gamma_{HC}$ = 2.66 ± 0.19 mNm^{-1}, which is in good contribution to the value of $\Delta\gamma_{HC}$ = 2.58 ± 0.15 mNm^{-1} that can be calculated using the equation of the calibration curve of figure 35 (see chapter 6.4).

Depending on the application, precise changes in interfacial tension may be desired using stimuli-responsive surfactants. It was found that the maximum change in droplet morphology of $\Delta\theta$ = 59.4° is evoked at concentrations close to the CMC of the *trans*-isomer and that the overall variation in HC/W interfacial tension and therefore droplet response can be fine-tuned and tailored towards a specific requirement by adding an additional non-responsive HC surfactant to the system. With the addition of 25 µM or 50 µM of the nonionic surfactant Triton X-100, the light-triggered change in morphology could be significantly reduced from $\Delta\theta$ = 59.4° to $\Delta\theta$ = 48.5° and $\Delta\theta$ = 39.9°, respectively (Figure 45).
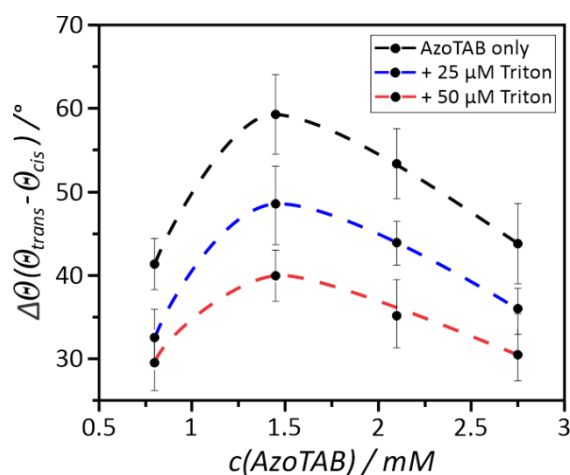

Figure 45. Light-triggered variations in droplet morphology as a function of the AzoTAB concentration with and without the addition of the nonionic surfactant Triton X-100. Contact angle error bars refer to N ≥ 10 measurements.

These results demonstrate that beside innovation in the characterization of classical surfactants the *in situ* read out capability offers particular practicability for the investigation of emulsion systems involving stimuli-responsive surfactants such as the light-responsive surfactant AzoTAB.

4.2.6   Conclusion

In this chapter, the unique chemical-morphological coupling inside biphasic O/W Janus emulsions was investigated. *In situ* observations of Janus emulsion droplets that undergo dynamic morphological transitions in response to variations in surfactant type, concentration and ratio with a simple customized side-view imaging setup allowed the investigation of surfactants within their designated environment. Complementary interfacial tension measurements via pendant-drop enabled the recording of a calibration curve that paved the way for a new approach to quantify marginal variations in interfacial tension and to determine surfactant CMC values of various cationic, anionic, and nonionic surfactants from morphological responses of Janus emulsions. In addition, the new "responsive drop" method allowed a convenient and cost-efficient quantitative comparison of the effectiveness of various cationic, anionic, and nonionic surfactants and proved particularly useful for the characterization of switchable surfactants.[180] The method was further optimized by automating the droplet contact angle measurement using an image processing algorithm, which helped to establish a fast and easy-to-use method tailored towards an intermediate interfacial tension regime between $\Delta\gamma = 0.5\text{-}6.8$ mNm^{-1}.

The established technique was then used to study the different influences of inorganic salts on surfactant-stabilized complex emulsions. *In situ* observation on droplet morphology upon addition of salts showed a stronger influence of divalent ions on surfactant effectiveness compared to monovalent ions, which was found to be a facile method for the on-site monitoring of water hardness.[183] Further, pendant drop measurements showed that different types and concentrations of cations within the aqueous continuous phase can significantly lower interfacial tensions of both SDS and Tween 80 stabilized hydrocarbon oil-water interfaces, while the effect of anions on the surfactant effectiveness was negligible.

4.3   Crown Ether-functionalized Complex Emulsions as a Multiresponsive Material Platform

4.3.1   Introduction

In natural systems, autonomous regulation of supramolecular recognition and binding-induced chemical events are essential processes by which they provide control over biological functions. Living organisms can dynamically adapt to multiple parallel or independent triggering events and changes in their chemical environment by exhibiting a specific programmed response.[199, 200] This specific response is based on multiple individual or combinations of independent chemical equilibrium-driven non-covalent interactions and covalent chemical transformations, which are processed by the organism with highest fidelity and substrate specificity.[201] The resulting self-regulation behavior and cross-check capability is fundamental for the high complexity achieved within biological systems, which are organized in hierarchical structural levels. Further, it enables complex emergent behavior observed in self-regulated multibody systems, allowing them to communicate, move, evolve, and self-organize into patterns or networks.[202-204]

One example of such a self-regulation of multiple independent chemical events is the constant fluid transport and mass exchange between cells that is autonomously controlled and driven through a continuous exchange of ions across the lipophilic cellular membranes. This process is essential for maintaining the hydrostatic and osmotic pressure balance as well as the membrane potential of the cell.[205] The recognition and transport of specific ions is also an important biomarker to many physiological and pathological processes, such as stimulus conduction in the muscles and brain or the perception of taste on the tongue.[206, 207] The permeation of ions across the lipophilic membrane barrier can be enabled by membrane proteins or ionophores.[208] Thereby, passive ion exchange is driven exclusively by chemical concentration gradients and chemical binding equilibria which, in contrast to active transport, does not require an external physical stimulus.[209] Synthetic crown ether-based compounds can successfully mimic natural ionophores by complexing metal ions in their hydrophilic binding pocket, enabling phase-transfer and transport of hydrophilic ions through a lipophilic barrier.[210, 211] Due to these properties crown ethers provide an exciting avenue to impart materials with responsive behavior, a concept that has been used in a variety of applications, including in phase-transfer catalysis, supramolecular polymers, protection groups, micelles or in molecular motors.[212-214]

The multifunctional, chemo-intelligent behavior of biological systems that are continuously exchanging chemical information, emerges from their complex and functional out-of-equilibrium assembled nature.[215, 216] A bio-inspired generation of such an active and adaptive operating self-regulated material platform, which is synthetically minimal, requires combining the concept of responsivity with a functional and stable out-of-equilibrium material platform. In this context, kinetically stabilized complex emulsions offer a versatile platform as they are highly dynamic and persist in a thermodynamically out-of-equilibrium state.[94] In surfactant-stabilized complex emulsions, molecules are continually exchanged between the emulsion droplets and the continuous phase and the metastable colloids can autonomously adapt their configuration to their chemical environment. This offers high potential for the creation of adaptive organized complex liquid colloids en route towards the generation of life-like cell-sized soft materials that exhibit autonomous chemo-intelligent capabilities.

In this chapter, the aim was to explore a synthetic minimal material platform based on crown ether-functionalized complex emulsions, which may help to better understand the underlying complex cascade mechanisms of ionophor-driven membrane transport. Therefore, two crown ether surfactants with different ring sizes should be synthesized. Complex emulsion droplets should be anisotropically functionalized with the crown ether surfactants and extensively studied for their supramolecular complexation properties to pave the way towards artificial dynamic and self-regulatory adaptive systems.[217, 218]

4.3.2   Characterization of Crown Ether Surfactants

Crown ether surfactants comprising a hydrophilic crown ether moiety functionalized with a lipophilic alkyl chain are another example of stimuli-responsive surfactants and were first synthesized and investigated by Cinquini et al. in 1975.[219] By attaching a lipophilic alkyl chain to a crown ether or cryptand the molecules can be converted into a surfactant, which is capable of forming micelles analogous to classical nonionic surfactants.[220] Crown ether surfactants can form stable complexes with different metal ions and polar organic species, resulting in a change in the hydrophilic-lipophilic balance of the molecule.[210, 220, 221] Crown ethers can be considered artificial ionophores that, similar to natural ionophores, can complexate metal ions within their hydrophilic binding pocket to allow phase-transfer and transport of hydrophilic ions through lipophilic barriers.[222, 223] After successful synthesis of the both crown ether compounds 4'-[*N*-dodecanoylamino]benzo-15-crown-5 (15-crown-5 surfactant) and 4'-[*N*-dodecanoylamino]benzo-18-crown-6 (18-crown-6 surfactant) (Figure 46) by attaching hydrophobic alkyl chains to hydrophilic benzocrown ether moieties, it was investigated if

they are able to stabilize the HC/W interface of complex emulsions comprising of two immiscible hydrocarbon and fluorocarbon oils (for synthesis details see chapter 10.3.2 and 10.3.3).
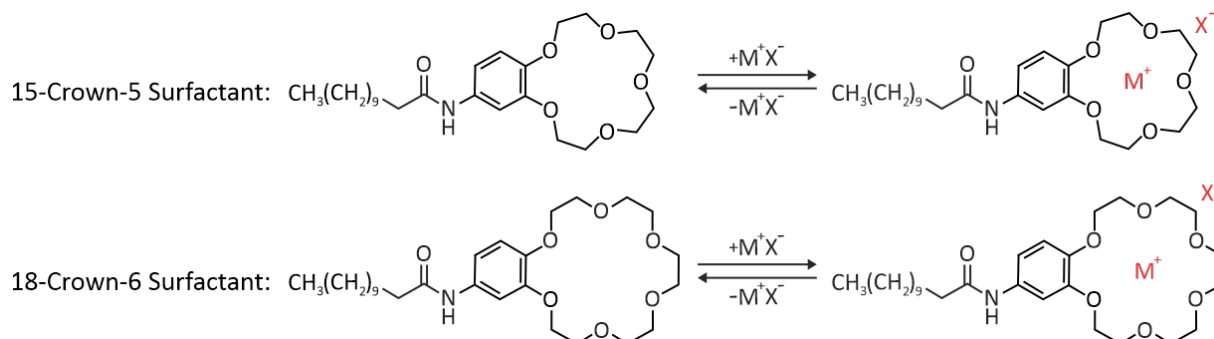

Figure 46. Chemical structure of the cation-responsive crown ether compounds 4'-[*N*-dodecanoylamino]benzo-15-crown-5 (15-crown-5 surfactant) (top) and 4'-[*N*-dodecanoylamino]benzo-18-crown-6 (18-crown-6 surfactant) (bottom).

A series of Janus emulsions were prepared consisting of toluene and a mixture of HFE-7500 and FC-43 (9:1) emulsified in a 1:1 ratio (T_c = 32 °C) in an aqueous solution of 0.05 wt.% Zonyl and at various concentrations of the corresponding crown ether compounds. The resulting droplet morphology diagram revealed that the contact angle (θ) of the droplets increases with increasing amount of the crown ether compounds (Figure 47). The fact that the droplets' contact angle is measurable and increases at higher concentrations, as well as the fact that a HC/W interface is observed without the addition of conventional hydrocarbon surfactants, indicates the surface-active properties of the crown ether compounds. Contact angle measurements from horizontal micrographs of the droplets at a surfactant concentration of 4 mgmL^{-1} gave a contact angle of θ = 21.2 ± 2.7° for the 15-crown-5 surfactant and a contact angle of θ = 40.7 ± 4.9° for the 18-crown-6 surfactant. The greater increase in contact angle caused by the 18-crown-6 surfactant can be attributed to the larger hydrophilic head group and thus higher surfactant effectiveness.
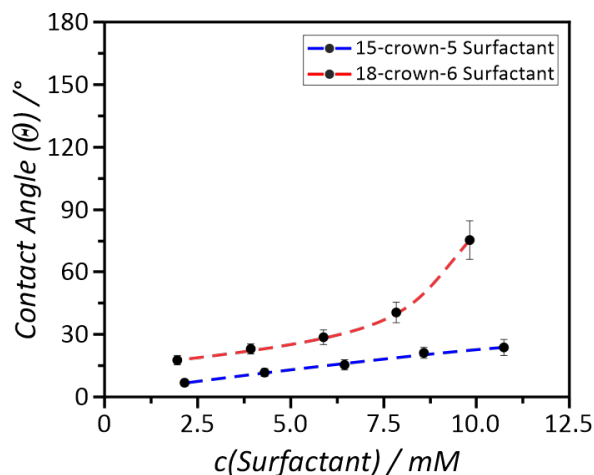
Figure 47. Droplet morphology diagram showing the correlation between the droplets' contact angle (θ) and the concentration of 15-crown-5- and 18-crown-6 surfactants measured in 0.05 wt.% pure Zonyl. Contact angle error bars refer to N ≥ 10 measurements.

However, at concentrations higher than 7.5 mM it was observed that the droplet stability slowly decreased, which was noticeable by the coalescence of the emulsion droplets after letting the emulsions rest for several hours. Moreover, at high surfactant concentrations above 10 mM, specifically at 12.89 mM of the 15-crown-5 surfactant and 11.77 mM of the 18-crown-6 surfactant, precipitation of the surfactants in the form of needle-shaped crystallites was found to occur, which also contributed to the destabilization of the emulsion (Figure 48).
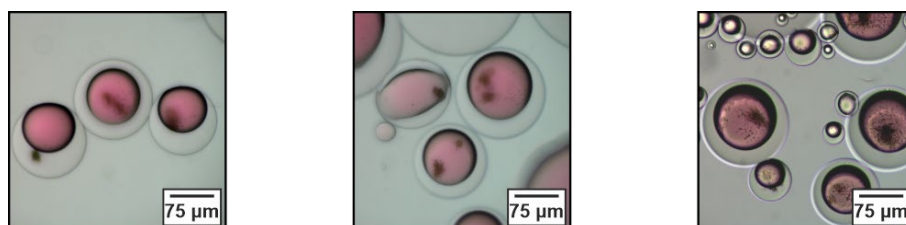
Figure 48. Side-view micrographs of Janus droplets prepared in 0.05 wt.% Zonyl and 12.89 mM 15-crown-5 surfactant (left and middle) or 11.77 mM 18-crown-6 surfactant (right). On the micrographs, the needle-shaped crystallites of the crown ether surfactants can be seen, which contribute to the destabilization of the droplets by precipitation.

To overcome the stability and precipitation issues in all of the following experiments, small amounts (0.015 wt.%) of the nonionic surfactant Triton X-100 were added to the emulsions to ensure their adequate stability. In addition, only low concentrations were used to prevent the precipitation of the surfactant.

The surfactant properties and their ability to reduce the interfacial tension between toluene and water was further quantified using the pendant-drop method. Pendant-drop tensiometry measurements at different concentration of the 15-crown-5 and 18-crown-6 surfactant were performed and showed a constant decrease of the water-toluene interfacial tension until the critical micelle concentration (CMC) of the surfactants was reached (Figure 49). The 15-crown-5 surfactant started to form micelles above a concentration of 3.73 mM, whereas the CMC of the 18-crown-6 surfactant was determined at a concentration of 5.23 mM. Both CMC´s have been determined at the crossing points of the respective linear fit functions.[224]
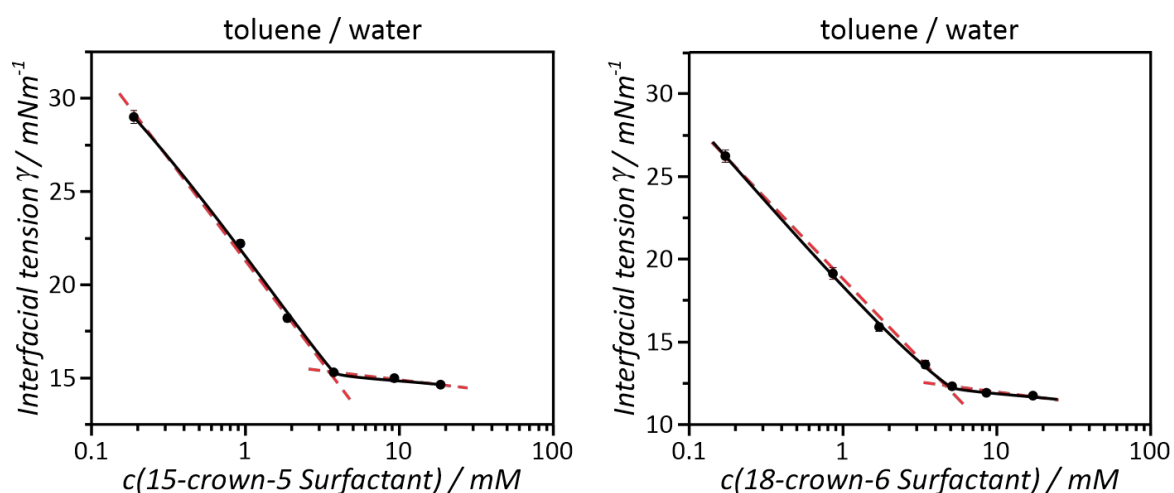

Figure 49. Interfacial tension of the toluene-water interface at different concentrations of the 15-crown-5 (left) and 18-crown-6 surfactant (right), measured with the pedant-drop method. The CMC´s were determined at the crossing points of the respective linear fit functions. Interfacial tension error bars refer to N ≥ 5 measurements.

To compare the maximal stabilization capabilities of crown ether surfactants with commercial nonionic surfactants the interfacial tensions γ between toluene and different aqueous surfactant solutions containing 0.1 wt.% of Brij 58, Triton-X100 and Tween 20 were measured via pendant drop. The concentrations of the surfactants were chosen higher in each case than the corresponding CMC values found in the literature.[181] Comparison of the obtained plateau values with the interfacial tension values that were measured at the highest concentration of each crown ether surfactant in the previous described pendant-drop experiment (Figure 49), showed that both crown ether surfactants effectively lowered the water-toluene interfacial tension comparable to the commercial surfactants (Figure 50). The interfacial tension between the pure solvents (water-toluene) was measured to be at $\gamma = 36.25 \pm 0.25$ mNm^{-1}.
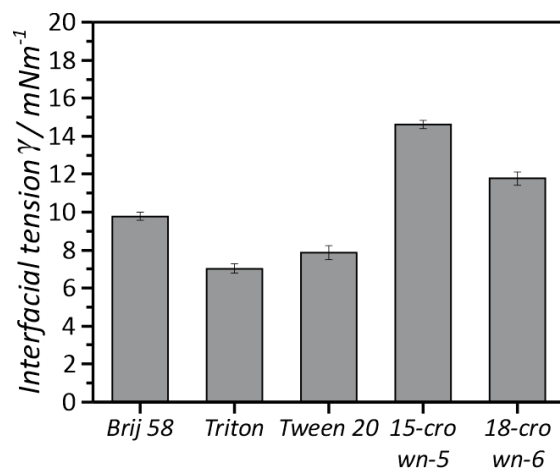
Figure 50. Interfacial tension plateau values of different commercial nonionic surfactants in comparison to the plateau values of the 15-crown-5 and 18-crown-6 surfactant. The diagram shows that the surfactants effectiveness of the crown ether surfactants are in a comparable range of commercial nonionic surfactants. Interfacial tension error bars refer to N ≥ 5 measurements.

4.3.3   Ion Sensing Experiments

Prior to the actual supramolecular complexation experiments, computational chemistry calculations were performed by Dr. Pablo Simón Marqués to get a theoretical impression of the complexation process of crown ether surfactants. The density functional theory (DFT) calculations of the 15-crown-5 surfactant before and after the complexation of a sodium cation indicated localized electron rich regions stemmed from the oxygen atoms out of the plane of symmetry in the absence of metals in the electrostatic surface potential of the synthetic crown ether surfactant (Figure 51). Together with the neutral character of the aliphatic chain, the amphipathic distribution of crown ether derivative provides the molecule a tensioactive character.

Upon complexation of a sodium cation, the macrocycle geometry suffers a reorganization, reducing the electron rich regions due to the oxygen coordination and the positive charge introduced by the sodium cation (Figure 51). The predominantly green-yellow colors of the electrostatic surface potential after complexation of Na^+ imply a hydrophobic character of the chelated compound, which might make it more stable in the organic phase of biphasic complex emulsions than at the HC/W interface after complexation.
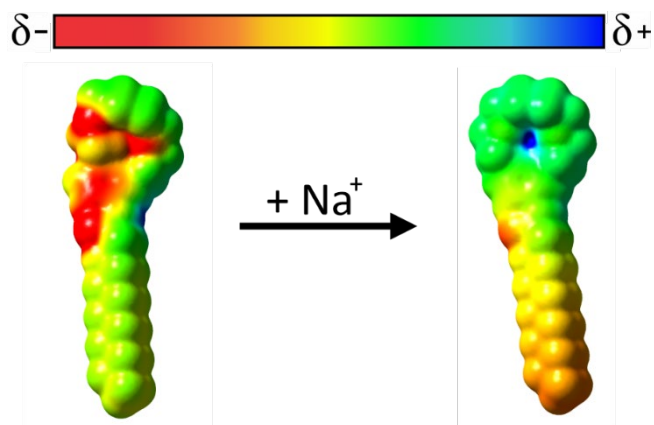
Figure 51. Molecular electrostatic surface potential for the 15-crown-5 ether surfactant, metal-free (left) and after complexation of a Na⁺ ion (right).

To study the complexation of inorganic metal salt on crown ether-functionalized complex emulsions, Janus emulsions were prepared as previously described. The addition of 0.015 wt.% Triton to the emulsions helped to bring the small changes of the droplets' contact angle (θ) during recognition events to the visible range. The starting morphology of the complex droplets functionalized with 1.96 mM of the 18-crown-6 surfactant was measured at θ = 74.0 ± 5.3°. Upon addition of 0.1 mM of potassium acetate, it was observed that the droplets transitioned from their Janus configuration towards a more encapsulated double emulsion morphology (θ = 50.4 ± 3.4°). Crown ether moieties are known to form hydrophobic complexes upon coordination to suitable metal ions, which can result in a phase transfer of the metal salts into the organic droplet phase. The reduced effectiveness of the crown ether surfactants subsequently leads to an increase of the hydrocarbon-water interfacial tension.[224]

The morphology transition was reversible, i.e., after decreasing the metal ion concentration in the continuous phase by dilution, the emulsion droplets reversibly adapted to their environment via expanding the HC/W interface ultimately returning to the starting droplet morphology. To confirm the phase transfer of the metal salts to the organic droplet phase, confocal micrographs of the droplets after complexation of a fluorescent marker were recorded. Complexation of the riboflavin derivative potassium 2-(7,8-dimethyl-2,4-dioxo-10-((2S,3S,4R)-2,3,4,5-tetraace-toxypentyl)-4,10-dihydropyrimi-do[4,5-b]quinolin-3(2H)yl)acetate (K-TARF) (Figure 52 left) yielded double emulsion droplets with the dye compartmentalized within the hydrocarbon phase (Figure 52 middle and right). The light emission of complex droplets was measured in presence and absence of the 18-crown-6 surfactant after the addition of K-TARF. The confocal microscope images revealed that the light emission clearly increased

when the crown ether surfactant was present, highlighting the fact that crown ether surfactants mediate the uptake of the fluorescence dye to the hydrocarbon phase.[224]
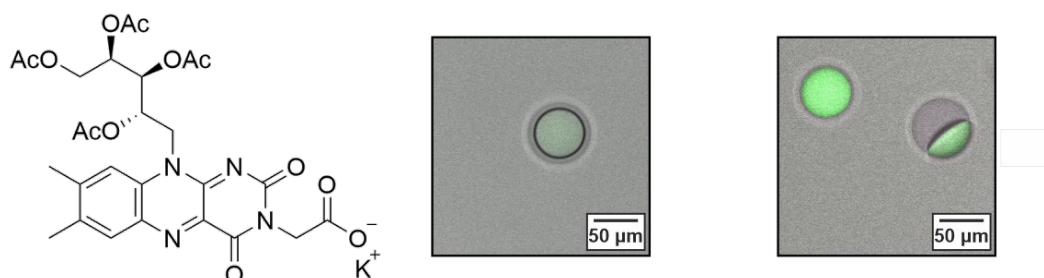

Figure 52. Chemical structure of the riboflavin derivative K-TARF (left) and inverted confocal optical micrographs of emissive complex droplets (middle and right). The micrographs show an emissive emulsion in absence (middle) and presence of the 18-crown-6 surfactant (right) after the addition of the K-TARF fluorescent dye, displaying weak emission in the upper hydrocarbon phase (middle) and strong emission in the upper hydrocarbon phase (right) due to better uptake mediated by the crown ether surfactant.

In a simple experiment, it was demonstrated that the K-TARF dye is insoluble in of the hydrocarbon droplet phase, which was toluene, but was up taken in the solvent when small amounts of the 18-crown-6 surfactant were added. After one week, the sample without the crown ether surfactant was still colorless whereas the other sample remained clearly yellow in color.
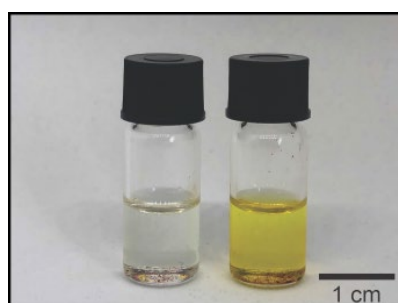
Figure 53. Solubility test of the K-TARF dye. In the left vial: toluene and the fluorescent dye K-TARF. In the right vial: toluene and the fluorescent dye K-TARF with small amounts of the 18-crown-6 surfactant. The image was captured after one week.

Next, the ability of crown ether-functionalized double emulsions to detect various metal and ammonium ions was quantified. Therefore, the droplet response upon addition of different types and concentrations of metal and ammonium acetates was monitored. During the experiments, the crown ether surfactant concentration was kept constant with $c = 2.15$ mM for the 15-crown-5 surfactant and $c = 1.96$ mM for the 18-crown-6 surfactant. Horizontal imaging of the droplets allowed to visually follow the molecular recognition events *in situ* and quantify the association constants via

determination of the associated changes in the droplet morphology (Δθ). It was observed that during the interfacial recognition events of different metal ions, the contact angles of the droplets gradually decreased with higher salt concentrations (Figure 54). Depending on the cavity size of the two different crown ether surfactants, droplets functionalized with the 15-crown-5 surfactant transitioned into a fully encapsulated morphology most rapidly upon addition of small concentrations (0.5 mM) of sodium acetate, whereas the highest affinity of the 18-crown-6 surfactant was determined towards barium acetate.[224] The observed trend was in accordance to the binding affinities of the two crown ethers reported in the literature.[225] In the following, the morphology transition graphs of the two crown ether surfactants are shown.
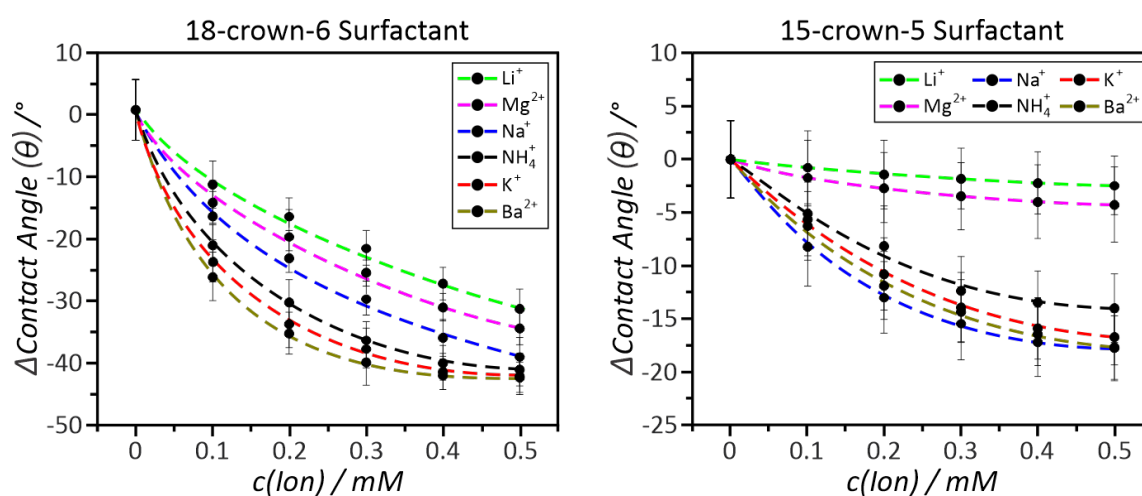

Figure 54. Droplet morphological transition upon addition of metal and ammonium ions. Encapsulation of several metal and ammonium salts performed with the 15-crown-5 (left) and 18-crown-6 surfactant (right). Contact angle error bars refer to N ≥ 10 measurements.

The respective association constants for the interfacial complexation of the different metal and ammonium ions by the two crown ether surfactants were obtained by non-linear regression of the previous shown morphology transition graphs (Figure 54) by using the following equation, which describes the general binding isotherm for a simple 1:1 binding system as a hyperbolic function[226]:

$$\Delta\theta = \frac{1}{2}\left([G] + [H]_0 + \frac{1}{K_A}\right) - \sqrt{\left([G] + [H]_0 + \frac{1}{K_A}\right)^2 + 4[H]_0 \cdot [G]} \tag{8}$$

With $K_A = \frac{[HG]}{[H][G]}$: association constant; [G]: metal ion concentration; $[H]_0$: crown ether concentration, $\Delta\theta$: change in droplet contact angle. Subsequently, the highest association constant of the 18-crown-6 surfactant was determined for barium acetate with $K_A = 2.43 \cdot 10^5$ M^{-1} (Figure 55 left). Among different alkali metal ions, the calculated constants document the intrinsic affinities of the

15-crown-5 surfactant towards the smaller sodium ions ($K_A = 1.49 \cdot 10^4$ M^{-1}) (Figure 55 right). In comparison, the 18-crown-6 surfactant displayed higher affinity towards larger potassium ions ($K_A = 1.20 \cdot 10^5$ M^{-1}).
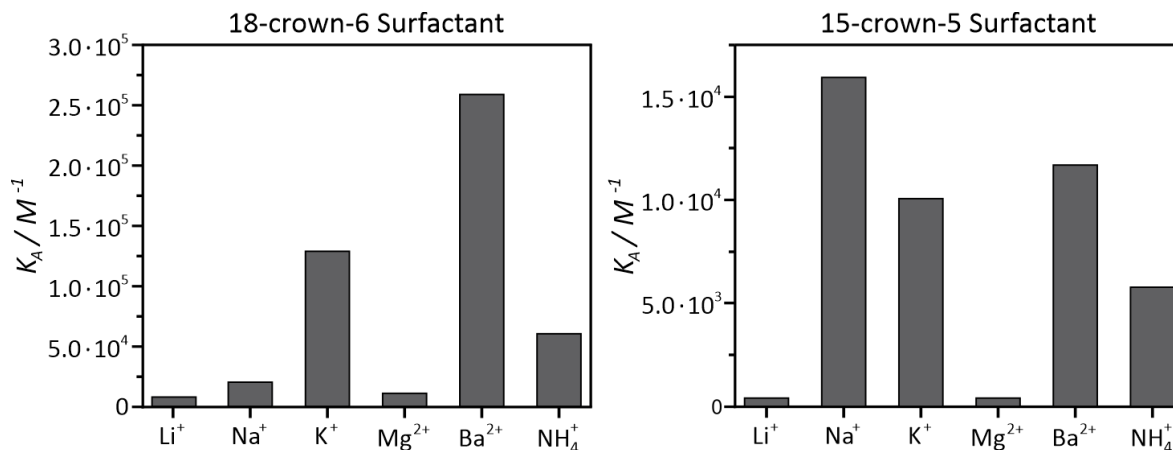

Figure 55. Calculated association constants for the interfacial complexation of different metal and ammonium ions for the 18-crown-6 (left) and the 15-crown-5 surfactant (right).

4.3.4   Phase-transfer Catalysis

After validating the responsiveness of crown ether-functionalized double emulsion droplets towards various metal ions, the supramolecularly regulated uptake and release mechanisms should be extended for potential applications. The use of crown ethers in phase transfer catalysis has been intensively investigated over decades.[227-229] Since emulsion droplets are widely employed as droplet-based microreactors, it was hypothesized that the crown ether surfactant-mediated uptake of catalytic reagents can be used to control a chemical reaction rate inside complex droplets.[230, 231] In this context, a K_2CO_3-catalyzed alkylation of phenol with 1-bromohexane was carried out within the hydrocarbon phase of the droplets (Figure 56).
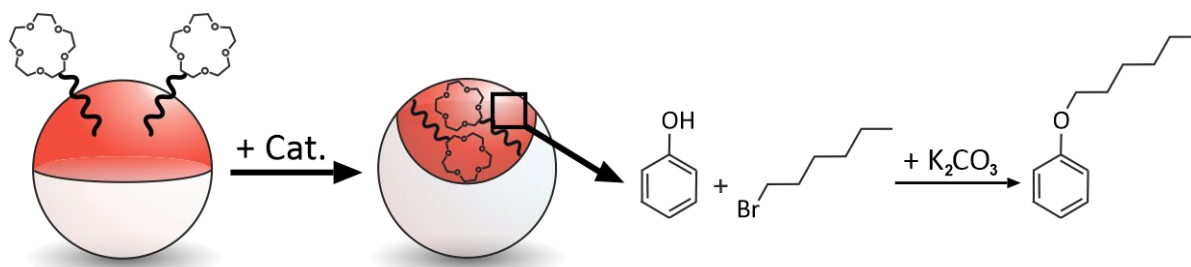

Figure 56. Schematic representation of crown ether-functionalized Janus droplets as phase-transfer catalysis microreactors for an alkylation of phenol with the addition of the catalyst K_2CO_3.

Droplets functionalized with the 15-crown-5 surfactant (6 mM) were prepared in an aqueous surfactant solution containing 0.02 wt.% Triton and 0.05 wt.% Zonyl. Additionally, 0.21 M phenol and 0.21 M 1-bromohexane were selectively compartmentalized inside the HC phase of the double emulsions made of a HC/FC oil mixture in a 1:0.9:0.1 ratio of toluene/HFE-7500/FC-43. After emulsification the emulsion was cooled down to room temperature before 0.02 M of the the K_2CO_3 catalyst was added to the continuous phase. The catalyst uptake was accompanied by a morphological reconfiguration towards a more encapsulated morphology, as displayed in figure 57.
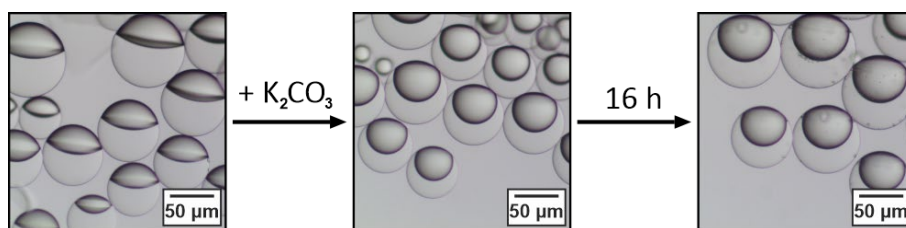
Figure 57. Optical side-view micrographs of the Janus droplet microreactors, functionalized with the 15-crown-5 surfactant before and after the addition of the catalyst K_2CO_3 as well as after a reaction time of 16 h.

As a result, when crown ether-functionalities were exposed to the catalyst-containing continuous phase, a transfer to the organic phase occurred, resulting in an acceleration of the reaction rate. After the reaction has proceeded for 16 hours, the emulsion was de-emulsified using saturated brine, extracted with hexane and analyzed by GC-MS. The received chromatogram revealed a yield of the final product ((hexyloxy)benzene) of 46 % when crown ether-functionalities were in contact with the continuous phase (Figure 58).[224]

Figure 58. GC-MS chromatogram of the phenol alkylation in the presence of 15-crown-5 surfactant. First peak of the graph at ca. 5.70 min corresponds to the starting material (phenol), while the final compound was detected after ca. 9.54 min. Integration of the peaks revealed a conversion of 46 %.

In comparison, a reaction performed inside the Janus droplet microreactors conducted under the same reaction conditions without the presence of crown ether surfactants resulted in significantly decreased conversion rates after 16 hours of 18 % yield (Figure 59).

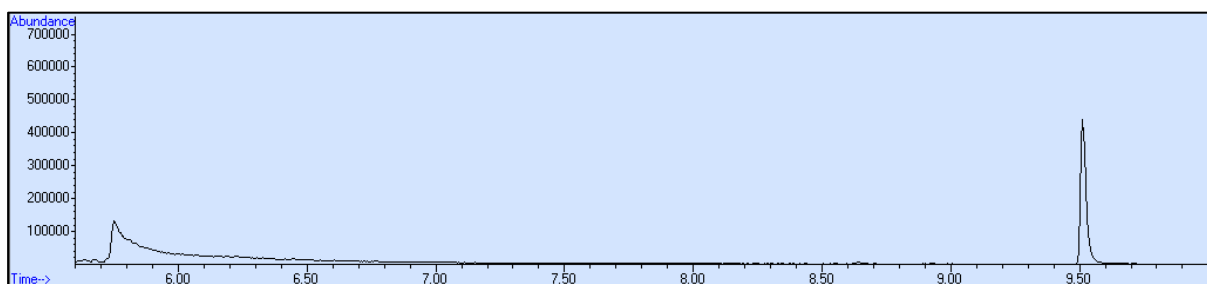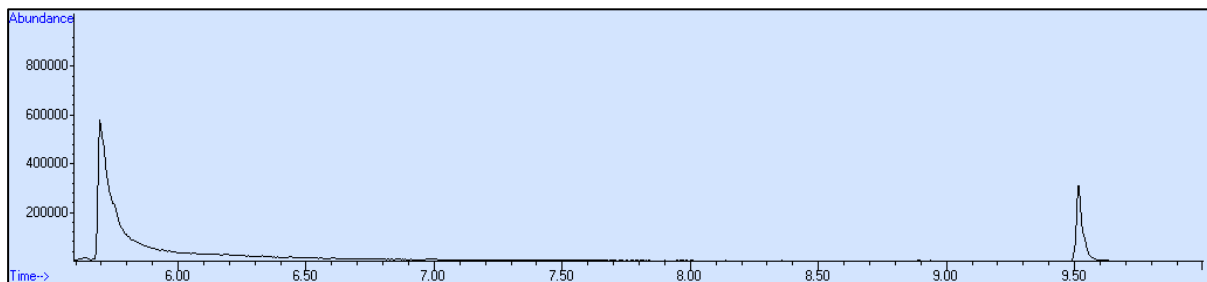Figure 59. GC-MS chromatogram of the phenol alkylation in the absence of 15-crown-5 surfactant. First peak of the graph at ca. 5.70 min corresponds to the starting material (phenol), while the final product was detected after ca. 9.52 min. Integration of the peaks revealed a conversion of 18 %.

Moreover, the crown ether-mediated phase-transfer of the catalyst could be independently regulated by variations in the Zonyl concentration within the continuous phase. When the alkylation was performed under the exact same conditions but inside encapsulated double emulsion droplets at much higher Zonyl concentrations of 1.0 wt.% without Triton, no conversion to the final product was detected, outlining the importance of the reactant-containing HC phase being exposed to the catalyst-containing aqueous phase (Figure 60).[224]
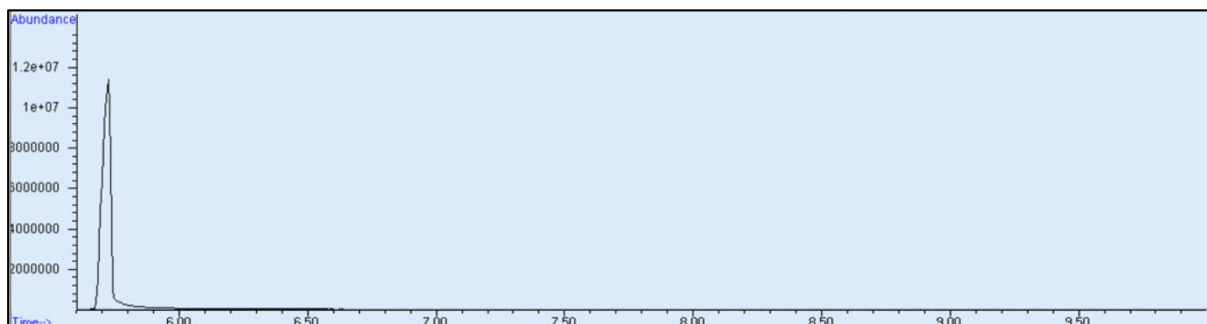
Figure 60. GC-MS chromatogram of the phenol alkylation with fully encapsulated HC/FC/W emulsions bearing phenol, 1-bromohexane and 15-crown-5 surfactant in the encapsulated hydrocarbon phase. The graph shows only the peak corresponding to phenol and no conversion to the final product.

In the following, the signals from the mass spectra were compared with the signals of the corresponding chemical compounds from the database (Figures 61 and 62).

4 Results and Discussion
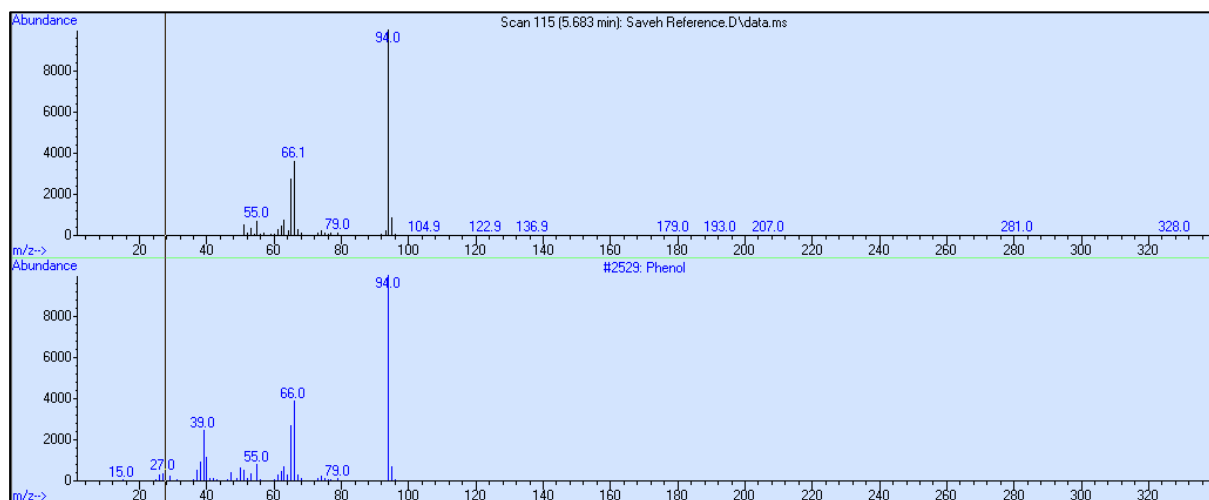
Figure 61. GC-MS mass-spectrum obtained at 5.68 min (top). Direct comparison of the signals with the database spectrum of phenol (bottom).
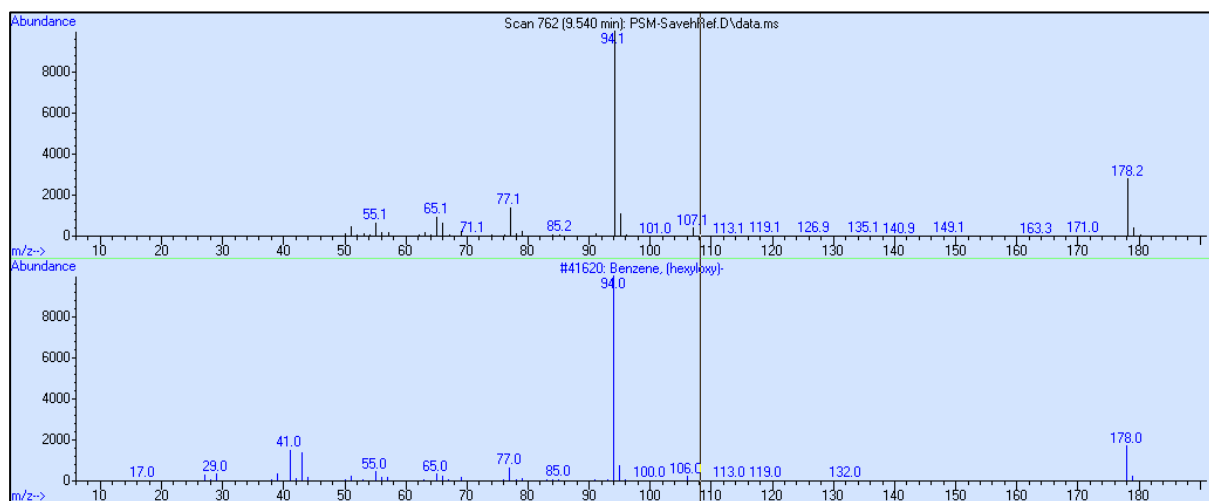
Figure 62. GC-MS mass-spectrum obtained at 9.54 min (top). Direct comparison of the signals with the database spectrum of (hexyloxy)benzene (bottom).
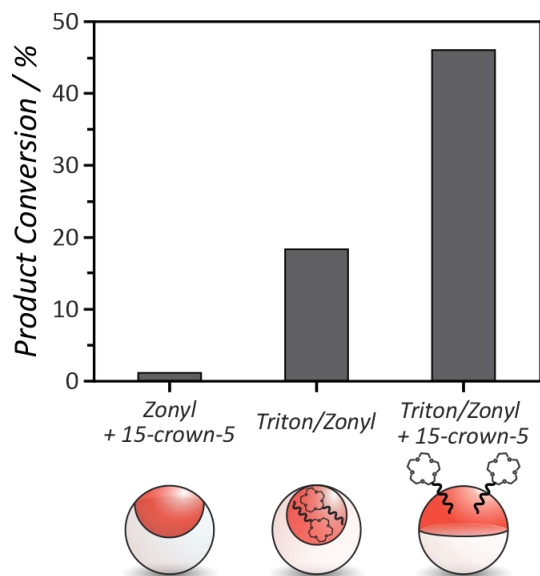
Figure 63. Product conversions of the phase-transfer studies under three different experimental conditions determined after a reaction time of 16 h.

The optical micrographs of the phase-transfer studies conducted under three different starting conditions can be seen in figure 64.
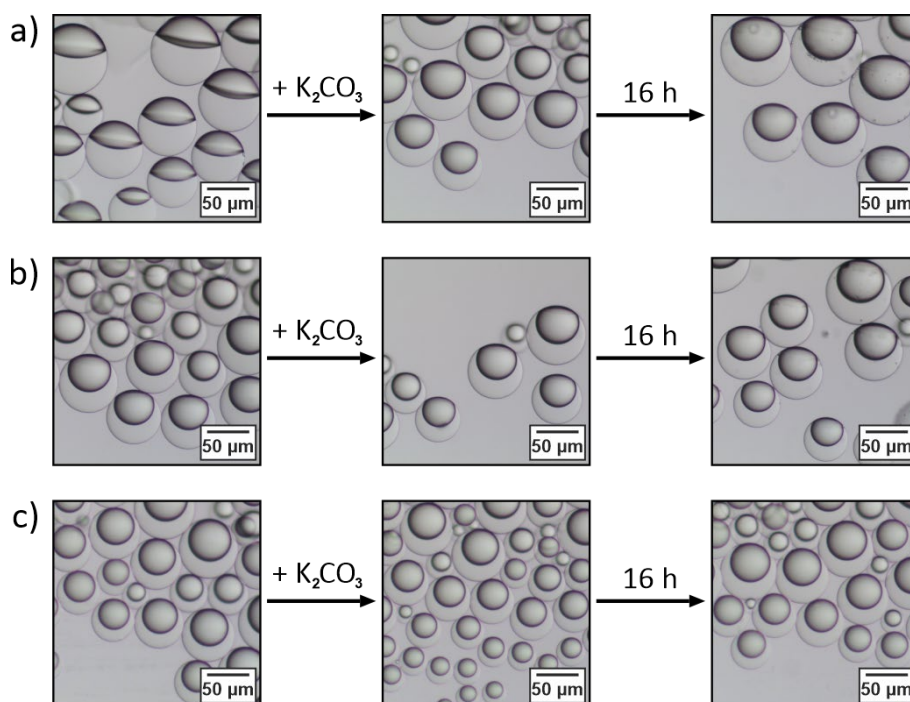
Figure 64. Optical side-view micrographs of the phase-transfer catalysis studies captured before and after the addition of the catalyst K_2CO_3 as well as after a reaction time of 16 h under three different starting conditions. a) Droplet-based microreactors generated in an aqueous surfactant solution containing 0.02 wt.% Triton and 0.05 wt.% Zonyl with the addition of the 15-crown-5 surfactant and b) in absence of the latter. c) Droplet-based microreactors functionalized with the 15-crown-5 surfactant and generated in pure 1.0 wt% Zonyl.

4.3.5   Supramolecular Bioconjugation

Since both crown ether surfactants showed moderate to good affinity towards ammonium ions in the ion sensing experiments (Figures 54 and 55), the complexation of ammonium-containing organic compounds should be investigated next. In contrast to the complexation of metal ions, the addition of the hydrophilic ammonium compound 2-[2-(3-aminopropoxy)ethoxy]ethan-1-ol (PEG-NH$_2$), was followed by a further 'opening up' of the Janus droplet morphology towards contact angles of $\theta > 90°$, which corresponds to a decrease of the HC/W interfacial tension γ_{HC}. In this scenario, complexation of the hydrophilic ammonium compound led to an increase of the hydrophilic-lipophilic balance of the surfactant, resulting in a more effective surfactant. Horizontal imaging allowed *in situ* visualization of the two morphological transitions of the droplets evoked by the different molecular recognition processes during the addition of hydrophilic ammonium compounds and metal salts (Figure 65).
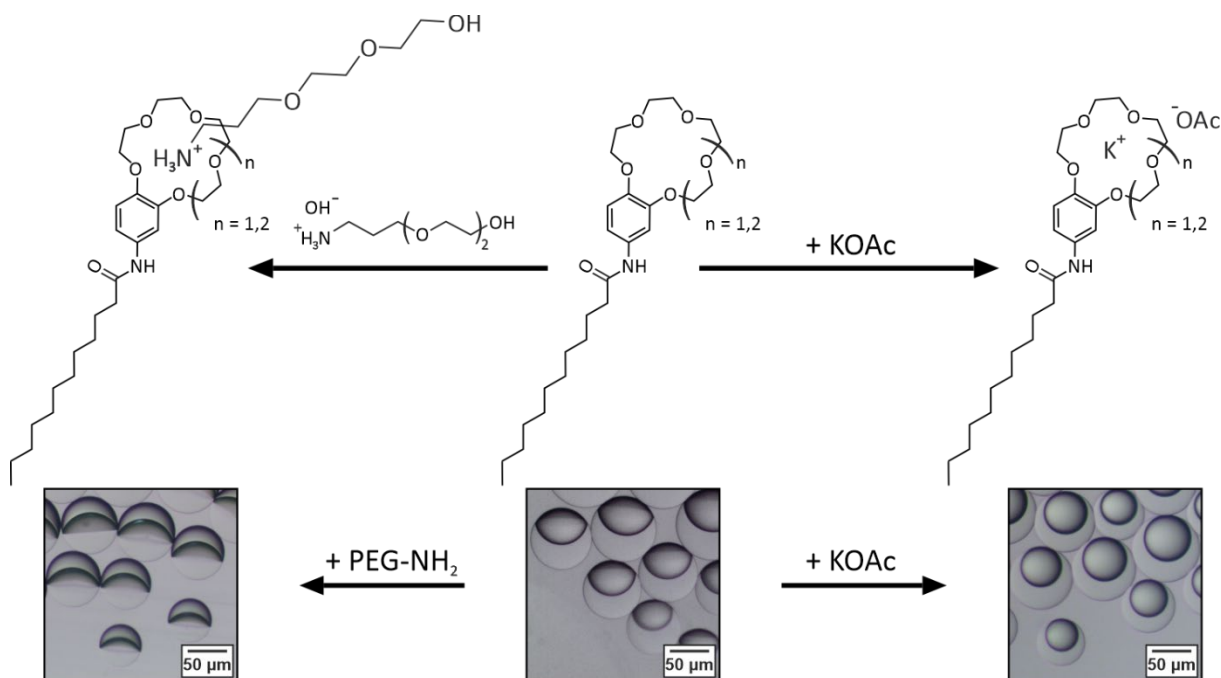
Figure 65. Chemical structure of the 4'[N-dodecanoylamino]benzo-15-crown-5 and 4'-[N-dodecanoylamino]-benzo-18-crown-6 surfactants and their ability to complexate metal ions and hydrophilic ammonium compounds such as 2-[2-(3-aminopropoxy)ethoxy]ethan-1-ol (PEG-NH$_2$) (top). Side-view micrographs of the morphological transitions evoked by the different molecular recognition events (bottom): complexation of a hydrophilic ammonium compound (left) and encapsulation of potassium acetate (right).

An addition of fluoresceinamine hydrochloride, a water-soluble ammonium compound, resulted in confocal micrographs that displayed a bright fluorescent ring located selectively at the HC-W interface

of the droplets, due to the interfacial post-functionalization of the crown ether-functionalized emulsions (Figure 66).
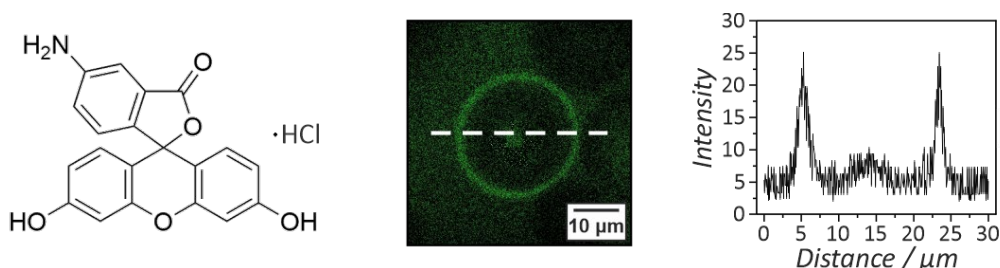
Figure 66. Chemical structure of fluoresceinamine hydrochloride (left). Confocal micrograph of a droplet after the complexation of fluoresceinamine hydrochloride (middle) with the associated horizontal fluorescence intensity profile (right). The image shows a bright fluorescent ring selectively located at the HC/W interface.

To ensure that changes of the pH-value caused by the addition of the basic PEG-NH$_2$ or the mere presence of amines does not influence the morphology of the Janus droplets, two different control experiments were performed. For both experiments Janus droplets in 0.05 wt.% Zonyl and 0.015 wt.% Triton were prepared without any crown ether surfactant. After the preparation, in one sample the pH-value was raised with the addition of sodium hydroxide to pH 13 (Figure 67 left). In the other sample, 5.9 mmol (3 eq. related to the non-present 18-crown-6 surfactant) of PEG-NH$_2$ was added to the system (Figure 67 right). In both experiments the initial droplets' morphology remained unchanged, proving that neither the basic pH-value nor the presence of amines in the continuous phase do influence the droplets' morphology.
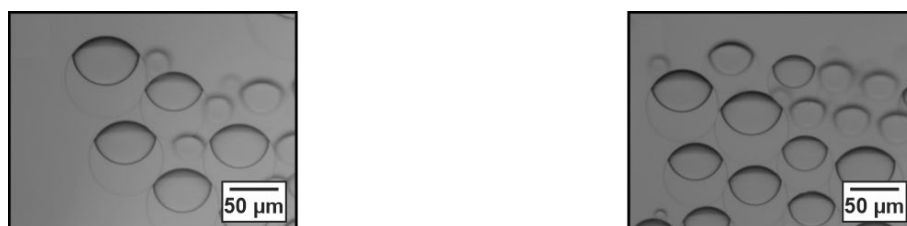
Figure 67. Side-view images of the ammonium complexation control experiments. Raising of the pH-value to 13 by adding sodium hydroxide (left) and presence of 2-[2-(3-aminopropoxy)ethoxy]ethan-1-ol (PEG-NH$_2$) (right) did not change the initial droplet morphology.

Having validated the two opposite morphological transitions, the interfacial attachment mechanism of hydrophilic organic compounds should be extended to other biologically important substance classes. The motivation was to use the morphology-dependent spontaneous and reversible supramolecular interfacial coupling for a post-conjugation with biomacromolecules to develop a potential material

platform for the generation of biosensors. In each of the following experiments, complex emulsions were used that were prior functionalized with 1.96 mM of 18-crown-6 surfactant.

4.3.5.1 Amino acids

Amino acids are a wide class of organic compounds that contain a NH_3^+ functionality and form monomer units of peptides, including proteins, of which 22 amino acids are found in the genetic code.[232] Under the same experimental conditions as for the complexation of the various metal ions, the attachment of different hydrophilic amino acids that are present as zwitterionic compounds at pH = 7 were tracked. The 18-crown-6 ether-functionalized emulsions visually responded to the presence of L-lysine, L-hystidine, and L-arginine. Upon complexation, the contact angles and thus the HC/W interface increased as a function of the hydrophilicity of the respective amino acids (Figure 68). In analogy to the complexation of metal ions, association constants for the binding of amino acids and the ammonium compound 2-[2-(3-aminopropoxy)ethoxy]ethan-1-ol (PEG-NH$_2$) were determined to K_A = 1088 M^{-1} for L-lysine, K_A = 1346 M^{-1} for L-hystidine, K_A = 3463 M^{-1} for L-arginine and K_A = 2468 M^{-1} for PEG-NH$_2$.
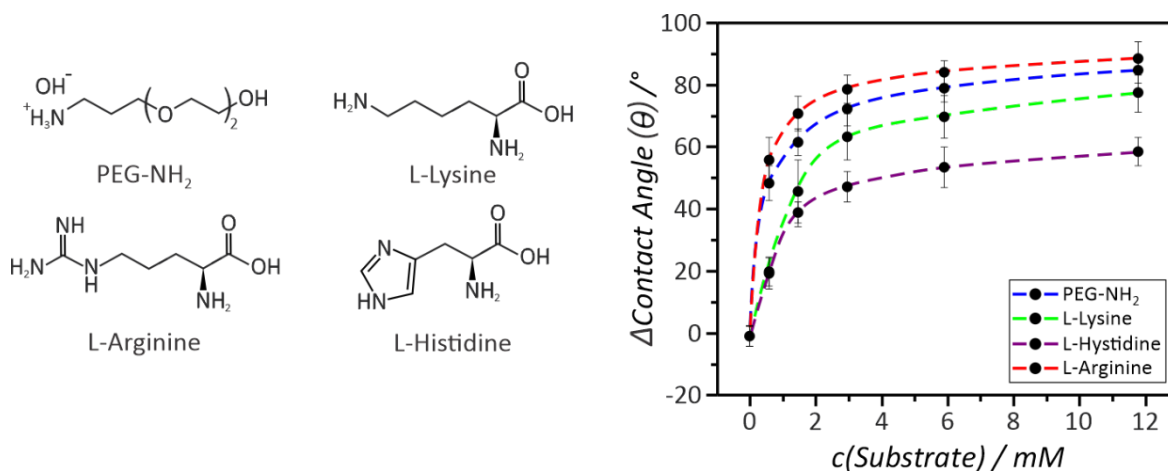
Figure 68. Droplet morphological transition upon complexation of different hydrophilic amino acids and ammonium compounds. Contact angle error bars refer to N ≥ 10 measurements.

4.3.5.2 Carbohydrates

To access the substance class of carbohydrates for a potential biosensor platform, post-functionalization of crown ether surface functionalities with boronic acid-based carbohydrate receptors was attempted by the NH_3^+-mediated complexation through the addition of 3-aminophenylboronic acid hydrochloride (0.2 mM). Next to amino acids or proteins, carbohydrates

play an important role in many physiological and pathological processes and synthetic boronic acid-based receptors are well known for this compound class.[233] Boronic acids form reversible 1,2- and 1,3-complexes with diols and therefore a pronounced reconfiguration of the droplet shape upon addition of the carbohydrates D(+)-glucose and D(-)-fructose was observed. Complexation of the polysaccharide Mannan caused the strongest change in droplet morphology as a result of its hydrophilicity and multivalency and resulted in almost fully encapsulated HC/FC/W double emulsions ($\theta = 173°$) (Figure 69).
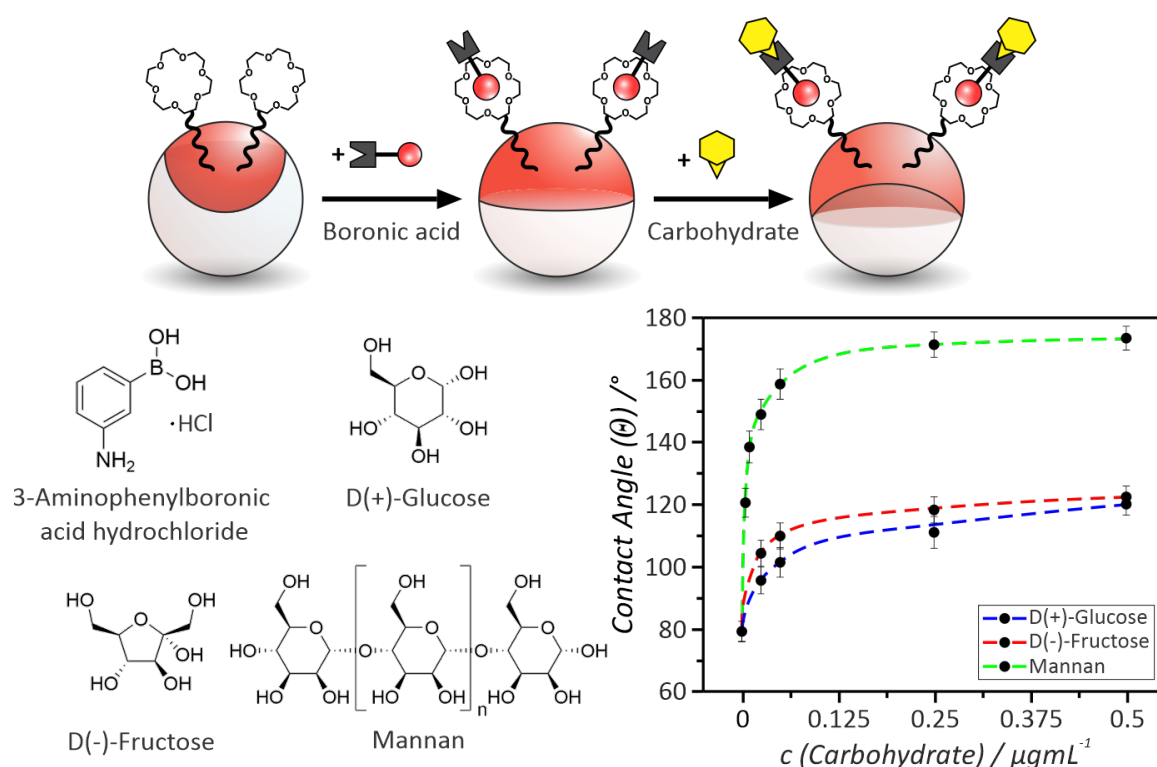
Figure 69. Schematic representation of the supramolecular bioconjugation scheme (top). Chemical structures of the boronic acid and the carbohydrates used for the carbohydrate complexation schemes (bottom left). Janus droplet morphological reconfiguration in response to varying concentrations of added carbohydrates (bottom right). Contact angle error bars refer to N ≥ 10 measurements.

4.3.5.3 Antibodies

Recently, dynamic double emulsions modified with proteins and carbohydrates have attracted great interest as powerful transducers for liquid-based biosensor platforms, including rapid detection of antibodies, bacterial pathogens, and viruses.[113, 115] For this purpose, researchers conjugated proteins and carbohydrates to the oil-water interface using covalent or dynamic covalent bioconjugation schemes. This required tailored and complex engineering of specific surfactants and droplet platforms for a particular target.

In this context, the NH_3^+-mediated complexation was exploited to conjugate the crown ether-functionalized droplets with fluorescein isothiocyanate-labeled (FITC) human Immunoglobulin G (IgG) antibodies via simple addition to the aqueous continuous phase ($2.67 \cdot 10^{-4}$ mM) (Figure 70 left; for further details see chapter 6.4). Addition of the antibodies led to an expansion of the HC/W interface of the droplets from $\theta = 74°$ to $102°$, due to the increased hydrophilicity of the resulting assembly.
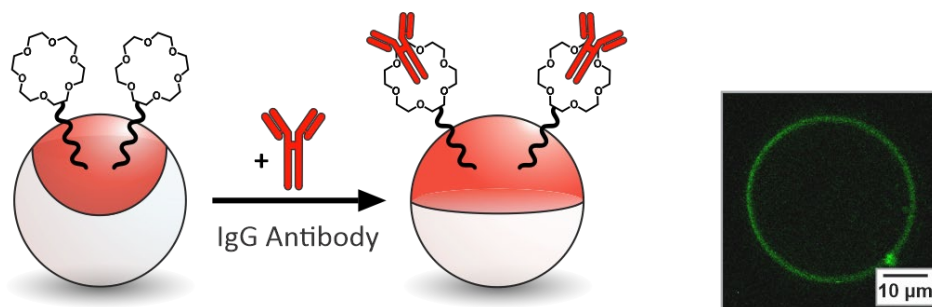
Figure 70. Schematic representation of the supramolecular bioconjugation of IgG antibodies (left). The confocal micrograph displays a bright fluorescent ring, proving the successful conjugation of the FITC-labeled antibodies selectively to the crown ether-functionalized hemisphere of the Janus emulsion (right).

The successful attachment of the antibodies was confirmed using confocal laser scanning microscopy. The obtained confocal micrographs displayed a bright fluorescent ring showing the conjugation of the antibodies selectively to the hydrocarbon hemisphere of the crown ether-functionalized Janus droplets (Figure 70 right). In the control experiment, which was carried out under the same experimental conditions but in absence of the 18-crown-6 surfactant, no fluorescence emission at the HC/W interface was detected, confirming the key role of crown ether-functionalities in the bioconjugation mechanism (Figure 71 left). In addition to the inverted confocal cross section image showing the successful conjugation of the antibodies selectively to the HC/W hemisphere of the crown ether-functionalized Janus droplets, an image of a trapped complex emulsion droplet was captured. The antibody-functionalized droplet was confined between two glass slides and was therefore tilted sideways. The yielded confocal micrograph shows exclusive emission from the HC/W interface and no emission from the FC/W interface, proving the anisotropic IgG antibody functionalization at the HC/W interface in the presence of crown ether surfactants (Figure 71 middle and right).
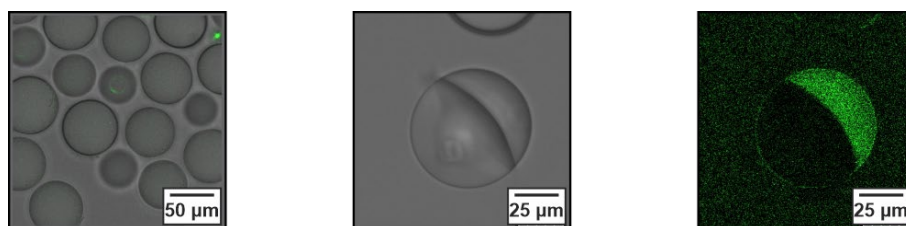
Figure 71. Inverted confocal optical micrograph of a complex emulsion droplet in an IgG antibody-containing surfactant solution (left). The image shows no emission at the HC/W interface, proving that the IgG antibodies are exclusively attached at the HC/W interface, if crown ether surfactant is present. Optical (middle) and fluorescent confocal micrographs (right) of a confined complex droplet, which is tilted sideways, in an IgG antibody-containing surfactant solution. The image shows exclusive emission at the HC/W interface and no emission at the FC/W interface, proving the selective IgG antibody functionalization at the HC/W interface in the presence of the 18-crown-6 surfactant.

The results of the crown ether-mediated supramolecular bioconjugation demonstrate a reversible and straightforward approach for the conjugation of functional cellular recognition units, such as antibodies, to a universal multiresponsive droplet platform. The findings may help to expand the capabilities of Janus emulsions in their application as biosensor arrays, providing advanced sensitivities, as they more closely resemble the dynamic interfacial recognition processes at the interface of natural cells.

4.3.6   Interaction with Functionalized Surfaces

Next, based on the unique ability of droplets to selectively present and hide reactive liquid interfaces, an interaction with surface-encoded functionalities was investigated. The objective was to exploit the independent chemical equilibrium-controlled interfacial recognition of functional groups and the associated translation into dynamic droplet responses to trigger manipulation or destruction of double emulsions in interaction with solid interfaces. In a first experiment, crown ether-functionalized complex droplets were immersed in a pure Zonyl-containing (0.1 wt%) continuous phase and placed on a glass surface pre-functionalized with the hydrophilic amino silane 3-(aminopropyl)trimethoxy-silane. To functionalize the glass substrates (cover slips and microscope slides), they were placed overnight in toluene containing 3-(aminopropyl)trimethoxysilane (0.2 M) and washed twice with toluene and acetone before use. Submerged in the continuous phase, the droplets adopted a stable encapsulated double emulsion morphology and were able to move freely on the glass substrate. However, upon addition of small quantities (0.05 wt.%) of the HC-surfactant Triton, the droplets assumed a Janus emulsion morphology. The concomitant exposure of the HC/W interface led to binding of the crown ether receptors to the NH_3^+-functionalities on the substrate surface, which caused

a tilting of the double-emulsion droplets out of their gravitational alignment and ultimately a spontaneous rupture of the droplet network. Figure 72 shows micrographs of the wetting of the glass surface with the dye-containing droplet phase upon destruction of the droplets.
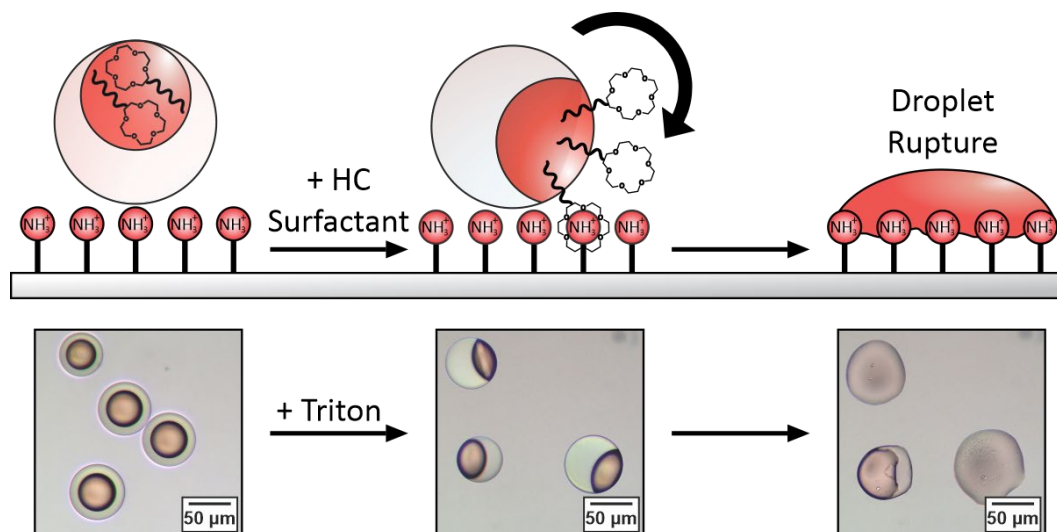
Figure 72. Schematic representations and optical micrographs of the behavior of double emulsion droplets sitting on a glass surface functionalized with 3-(aminopropyl)trimethoxysilane. After addition of the HC surfactant Triton, the droplets decorated with crown ether surfactants bound to the NH_3^+ groups at the glass surface, which caused them to tilt, followed by a spontaneous destruction of the droplet network.

The observed phenomenon could be attributed to the formation of a locally lipophilic surface upon complexation of the NH_3^+ functionalities that caused a wetting and consequently breaking of the emulsion droplets. Besides a triggered rupture of the emulsion, a controlled change in the orientation of the droplets can be of interest to induce alterations in their unique dynamic refractive, reflective, and light-emitting optical properties. As described above, the double emulsion droplets were able to undergo stimulated changes in their orientation due to surface interaction before the surface was wetted by the droplet phase. Tilting of complex emulsion droplets out of their gravitational alignment was previously observed only in direct droplet-droplet interactions.[116] To facilitate the reversible chemical-equilibrium-controlled tilting without emulsion breakage, the amount of active ammonium sites on the substrate surface was reduced. Therefore, the glass substrates were functionalized in toluene containing a mixture of the hydrophilic 3-(2,3-epoxypropoxy)-propyl]-trimethoxysilan (0.16 M) and the active amino silane 3-aminopropyl)trimethoxysilane (0.04 M). Crown ether-functionalized Janus droplets that were placed on the modified substrates remained stable, however, tilted side-ways by the complexation of surface NH_3^+ groups with the crown ether surfactants that were located at the upper HC-interface. The re-orientation of the tilted crown ether-functionalized

droplets could either be achieved by the competitive binding of PEG-NH$_2$ (1.5 mM) or by adding small amounts (0.5 mM) of metal ions, e.g. potassium acetate (Figure 73).
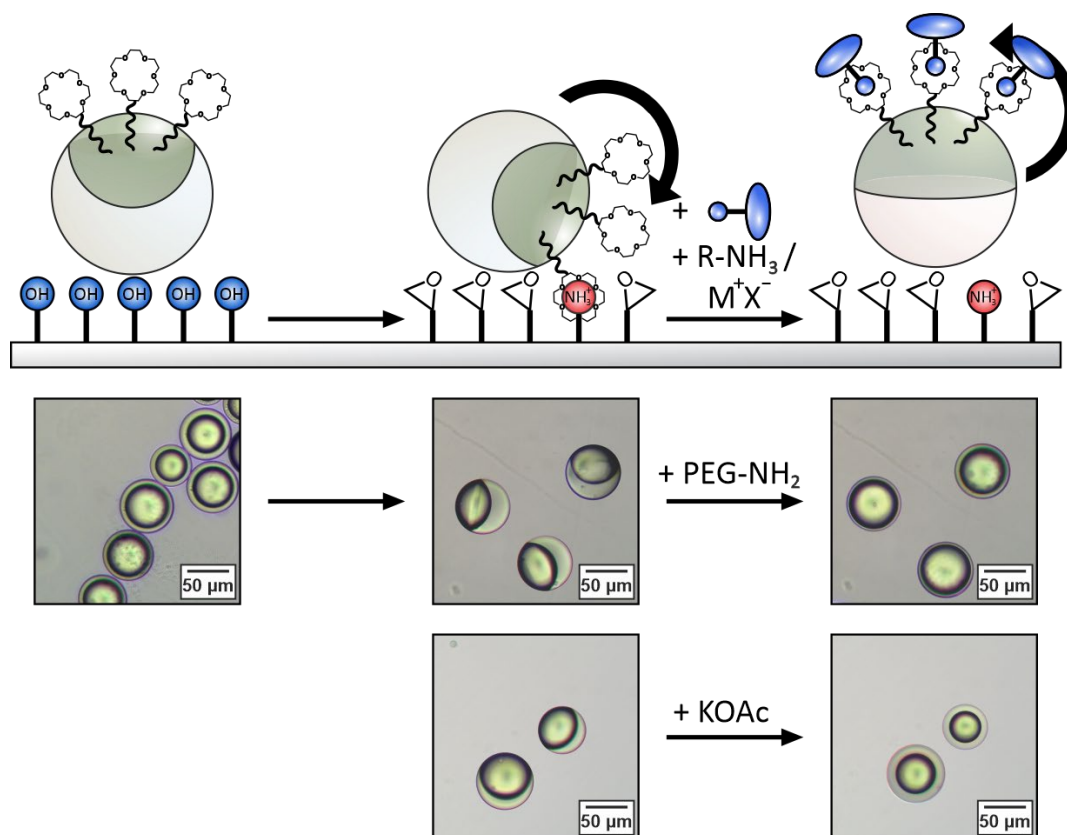
Figure 73. Schematic representations and optical micrographs of the crown ether-functionalized Janus droplets on a mixed functionalized glass surface (3-(2,3-epoxypropoxy)-propyl]-trimethoxysilan/3-(aminopropyl)tri-methoxysilane 80:20), where interfacial supramolecular complexation led to a tilting of the droplets. A re-orientation of the latter could be achieved by the addition of a competitive hydrophilic ammonium compound (2-[2-(3-aminopropoxy)ethoxy]ethan-1-ol) or small amounts of metal ions (e.g. 0.5 mM of KOAc).

It was assumed that the strong anchoring of the crown ether modalities in the emulsion droplets in these experiments was a result of the preferred partitioning of these compounds in the HC phase of the emulsion droplets, which prevented their extraction into the aqueous continuous phase. To address this assumption, ^{1}H-NMR-based phase partitioning studies were performed in the following chapter.

4.3.7   Phase Partitioning Investigation of the 15-crown-5 Surfactant

To determine the partitioning of the 15-crown-5 surfactant between the droplet HC phase, which was toluene and the continuous aqueous phase under different conditions, an external quantitative NMR approach was used.[234] For this purpose, a measuring tube containing a capillary with 1,3,5-

trimethoxybenzene dissolved in toluene-d$_8$ was used as a reference substance and internal standard (for further details see chapter 6.4). In a separate vial 3 mgmL^{-1} of the 15-crown-5 surfactant was dissolved in 2 mL of a phase-separated 1:1 mixture of toluene-d$_8$ and D$_2$O. The mixture was agitated and left 1 h for equilibration. Subsequently, an aliquot of each phase was extracted and a ^{1}H-NMR-spectrum was recorded. The spectra displayed in figure 74 show preferred partionioning of the 15-crown-5 surfactant inside the toluene phase and only marginal partitioning inside the aqueous phase as determined via comparison of the integrals of the NMR peaks of the terminal CH$_3$-group of the crown ether surfactant.
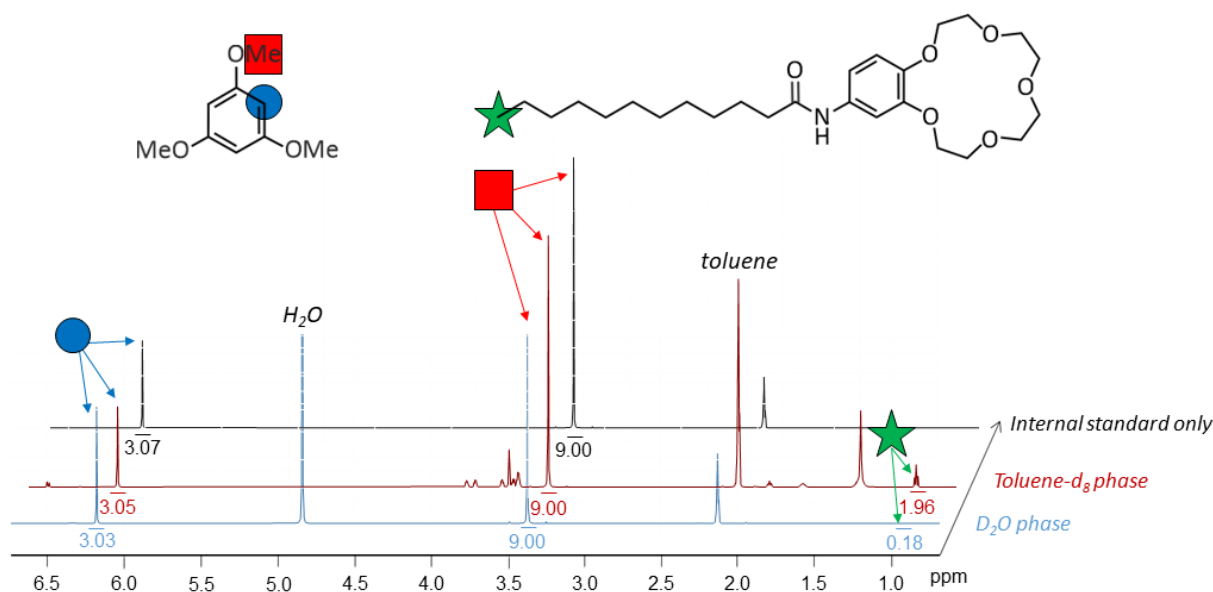
Figure 74. ^{1}H-NMR spectra of the 15-crown-5 surfactant upon extraction from a two phase mixture (1:1 v/v) of toluene-d$_8$ and D$_2$O.

Similar partition behavior was observed in two separate experiments, in which in addition to the 15-crown-5 surfactant KOAc (10 mM) or PEG-amine (2-[2-(3-aminopropoxy)ethoxy]ethan-1-ol; 12 mM) were added prior to the equilibration step (Figures 75 and 76).
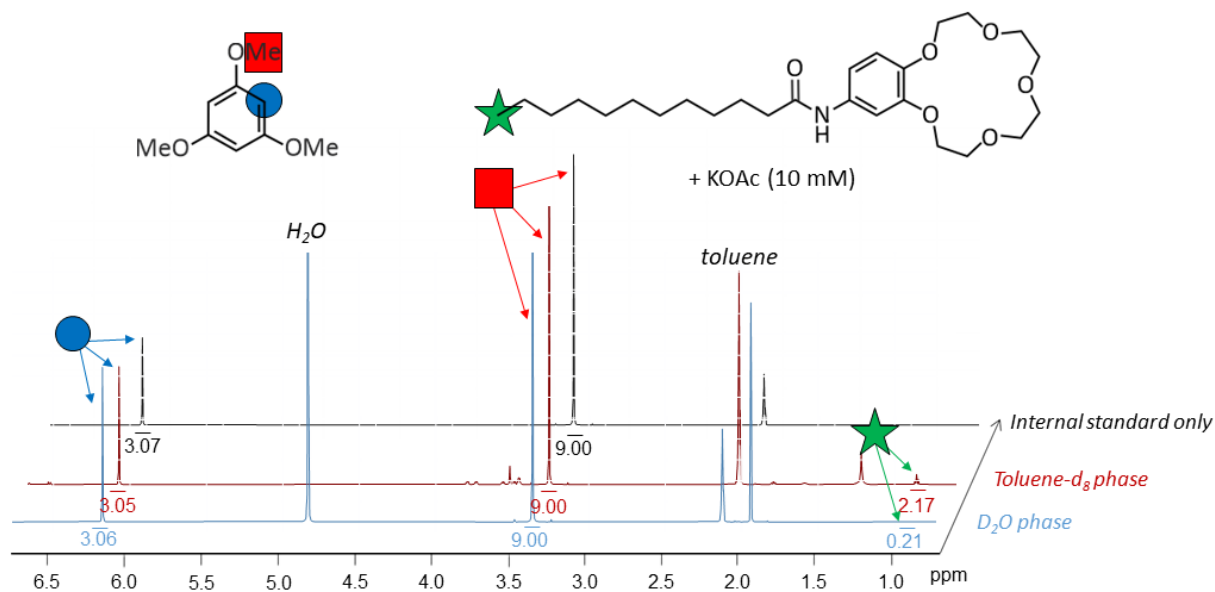
Figure 75. ^{1}H-NMR spectra of the 15-crown-5 surfactant upon extraction from a two phase mixture (1:1 v/v) of toluene-d$_8$ and D$_2$O containing 10 mM KOAc.
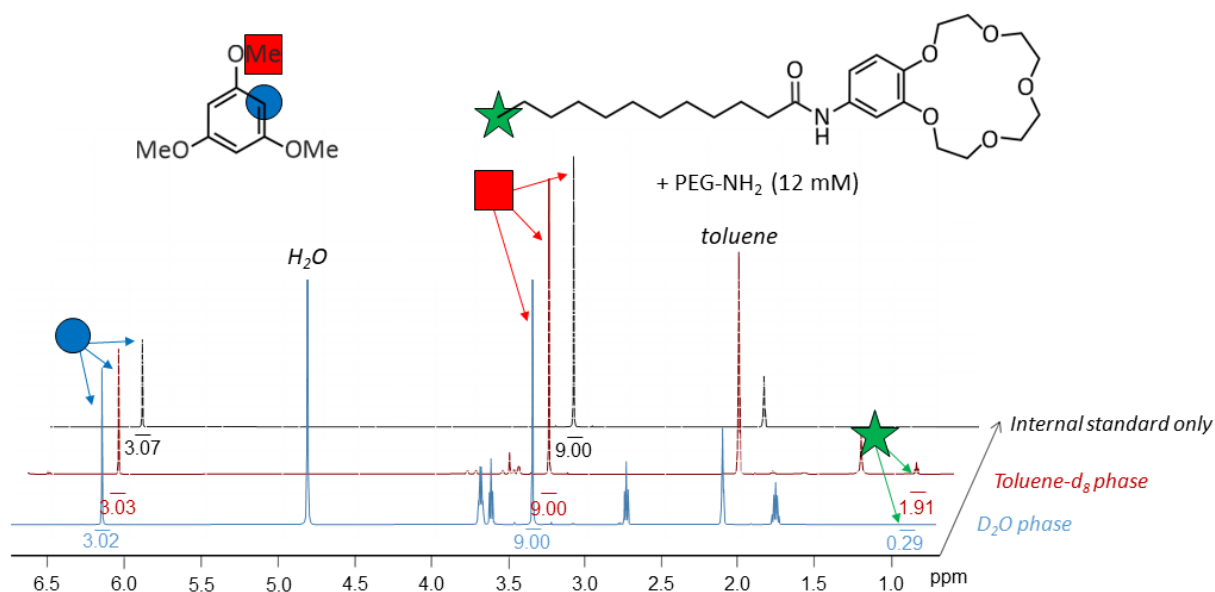
Figure 76. ^{1}H-NMR spectra of the 15-crown-5 surfactant upon extraction from a two phase mixture (1:1 v/v) of toluene-d$_8$ and D$_2$O containing 12 mM 2-[2-(3-aminopropoxy)ethoxy]ethan-1-ol (PEG-NH$_2$).

4.3.8   Competitive Binding Studies

The two opposite molecular recognition-induced morphological reconfigurations of complex droplets that were identified during the exploration of the multiresponsive liquid-colloidal material platform were solely driven by the respective chemical equilibrium constants. To demonstrate that the respective concentrations determined the degree of competitive binding of both, metal ions and

hydrophilic ammonium compounds a set of experiments was prepared. Complex emulsions were generated in a surfactant solution containing pure Zonyl (0.05 wt.%) and functionalized with 1.96 mM of the 18-crown-6 surfactant. When 1 mM of potassium acetate was added to the continuous phase of the emulsion, a transition of the droplets towards a fully encapsulated HC/FC/W morphology was observed. The transition can be referred to the complexation of the potassium ions followed by a phase transfer of the metal salts into the organic phase, which was in accordance to the results described in chapter 4.3.3. When 3 mM of the amino acid L-arginine was added to the droplets, they retained their fully encapsulated HC/FC/W morphology (Figure 77a).
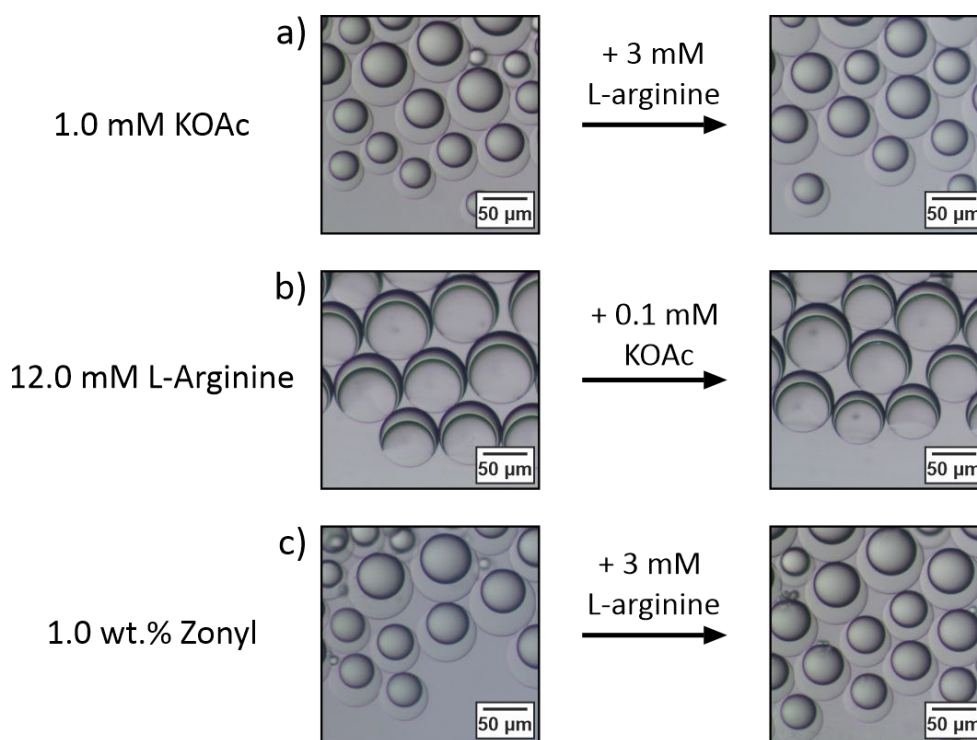
Figure 77. Optical side-view micrographs of competitive complexation studies. a) When the amino acid L-arginine was added to the crown ether-functionalized droplets disposed within a more concentrated aqueous salt solution (1 mM of potassium acetate), droplets retained their encapsulated morphology. b) Upon addition of 0.1 mM potassium acetate to an emulsion functionalized with L-arginine at high concentrations (12 mM) droplets retained their 'opened-up' Janus morphology due to insufficient competition of potassium acetate against the excess of L-arginine. c) Increase of the Zonyl concentration from 0.05 wt.% to 1.0 wt.% resulted in a transition towards an encapsulated double emulsion obstructing following post-functionalization events.

The fact that a higher concentration of L-arginine (3 mM) compared to potassium acetate (1 mM) in the continuous phase did not affect the droplets morphology, confirms that the molecular recognition-induced droplet morphological reconfigurations are driven by the respective chemical equilibrium

constants. The much higher affinity of the 18-crown-6 surfactant towards potassium acetate compared to L-arginine (log(K_A) = 5.39 vs. log(K_A) = 3.54) leads to a favored complexation of the former.

Vice versa, upon addition of 0.1 mM potassium acetate to an emulsion functionalized with L-arginine at high concentrations (12 mM), droplets retained their 'opened-up' Janus morphology (Figure 77b). In this case, these small amounts of potassium acetate were not sufficient to compete with the excess of L-arginine. In the last experiment, crown ether-functionalized droplets were prepared in a pure Zonyl containing surfactant solution with a significant higher concentration of 1.0 wt.%. The increased Zonyl concentration resulted in a fully encapsulated HC/FC/W starting morphology, preventing the crown ether molecules from assembling at the HC/W interface. Again, addition of the amino acid L-arginine (3 mM) did not lead to a change of the initial droplet morphology, underlining the importance of the crown ether functionalities being exposed to the HC/W-interface to take part in supramolecular post-functionalization events.

Beyond the crown ether-mediated variations in the droplet morphology, all double emulsion droplets retained their ability to respond to variations in the ratio and concentration of other, non-stimuli-responsive HC- and FC-surfactants, demonstrating the autonomous regulative and adaptive behavior of the droplet-based soft material platform. As an example, an increase of the Zonyl concentration within the continuous phase from 0.05 wt.% to 1.0 wt.% resulted in a decrease of the FC-W-interfacial tension and therefore a transition towards an encapsulated double emulsion morphology with the HC-phase encapsulated by the FC-phase, thus obstructing interfacial supramolecular recognition or post-functionalization events.

Combining the intrinsic reconfigurability of dynamic double emulsions with multiple reversible and competitive interfacial host-guest complexation events yields a synthetically minimal material system that can be actuated and adapt its internal droplet morphology to different independent equilibrium controlled pathways. Figure 78 shows schematically the various chemical equilibrium-controlled pathways, including the presence of metal ions, ammonium compounds, or amino acids, as well as variations in surfactant composition or effectiveness.
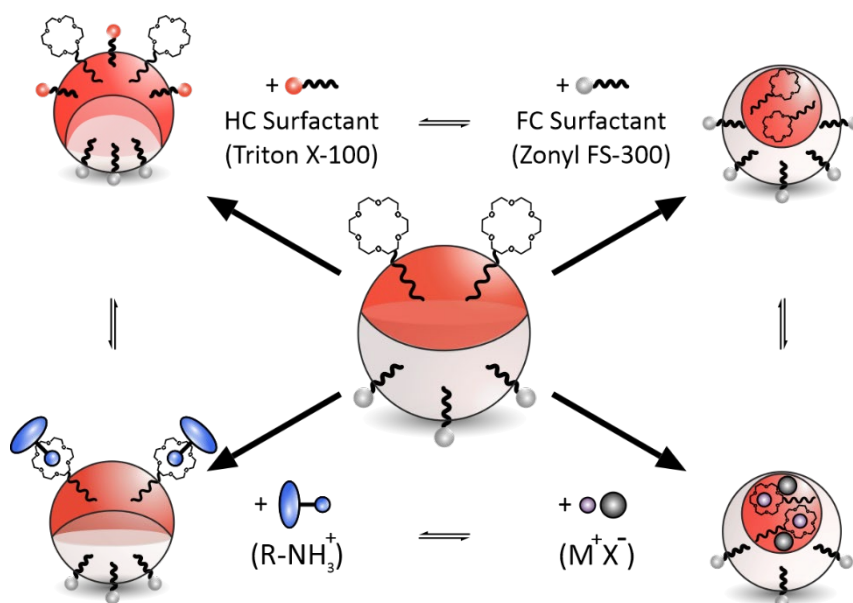
Figure 78. Schematic side-view illustration of independent competitive chemical equilibrium-controlled molecular recognition events causing morphological reconfigurations of crown ether-functionalized complex double emulsions.

4.3.9   Conclusion

In summary, the design of a synthetically minimal material platform based on biphasic, anisotropic double emulsion droplets that can autonomously and reversibly adapt to their chemical environment through various supramolecular recognition processes was elaborated. The recognition mechanism was achieved by the selective assembly of synthetic crown ether surfactants on the hydrocarbon hemisphere of the emulsion droplets. Supramolecular complexation events at the liquid-liquid interface of the emulsions enabled interfacial complexation and thus triggered responses of the droplets to a variety of chemical triggers including metal ions, ammonium compounds, amino acids, antibodies, carbohydrates as well as amino-functionalized solid interfaces.

Horizontal imaging allowed *in situ* visualization of different supramolecular host-guest recognition events at the interface, resulting in two opposite morphological transitions. With the addition of inorganic metal salts, such as potassium acetate, the droplets transitioned from their initial Janus configuration to an encapsulated double emulsion morphology ($\rightarrow\theta = 0°$). Confocal microscope studies revealed that the mechanism can be attributed to the formation of hydrophobic complexes by the coordination of crown ether units to suitable metal ions, leading to a phase-transfer of the complexes into the organic phase. The reduced effectiveness of the crown ether surfactants thus led to an increase in the HC/W interfacial tension γ_{HC}. In contrast, the addition of hydrophilic ammonium

compounds resulted in a further 'opening up' of the Janus droplet morphology towards contact angles of θ > 90°, which corresponds to a decrease of the HC/W interfacial tension. In this scenario, complexation of hydrophilic ammonium compounds led to an increase of the hydrophilic-lipophilic balance of the surfactant, resulting in a more effective surfactant.

The individual competing supramolecular recognition events as well as variations in the composition and effectiveness of external surfactants independently determined the dynamic droplet responses, solely controlled by the respective individual chemical equilibrium constants. Anisotropic supramolecular crown ether-functionalized bi-phase emulsion droplets thus constitute a novel type of adaptive, chemo-intelligent soft material platform that can autonomously regulate its response to multiple independent chemical binding events. It was showcased how the multiresponsive nature of the droplets can be pre-programmed and orchestrated via triggered changes in the chemical environment. This may prove useful for the design of new and improved emulsion technologies including droplet-based microreactors, Janus emulsion biosensors, and triggered payload release applications as well as the emulation of biomimetic model systems to pave the way towards artificial dynamic and self-regulatory adaptive systems.

4.4   Concepts for Multiresponsive Janus Emulsions as Droplet-based Optical Logic Gates

4.4.1   Introduction

In today's computers, information is managed by circuit-based solid-state semiconductors that transmit electrical input and output signals according to a binary coding scheme.[153] The circuits consist of a number of interconnected basic elements, the logic gates, which are organized in large arrays to perform complex functions.[235] In order to filter out noises the signal transmission in computers relies on a reliable "all or nothing" principle that utilizes a threshold voltage value of the incoming electrical signal and an affiliated logical convention.[157] In this convention a "0" is used to represent a signal that is below the defined threshold voltage and a "1" to indicate a signal that is above that value.[157] This binary information processing of logic gates is following the rules of George Boole`s binary algebra.[155] Although this principle enables data transmission in modern communication networks in bundles of fiber optic cables at a speed of several terabits per second, the underlying binary state system is at the same time a bottleneck regarding parallel signal processing.[236] For this reason, scientists are pushing ahead with research into quantum computers, which, by the superposition of the two basic states "0" and "1", can generate a plethora of intermediate states that enable parallel computing operations.[237]

Inspiration for the next generation of information-processing devices is also provided by biological systems in which information is processed simultaneously and continuously.[19] For example, gustatory perception is based sensory-physiologically only on the five to six basic qualities sweet, salty, sour, bitter, umami and fat, which are responsible for the human sensory impression "taste" through an interplay with the senses of smell, touch and temperature.[238, 239] In other words, the multitude of tastes that exist are the result of the interaction of few receptors that process stimuli and transmit the corresponding output signals in the form of electrical impulses to the brain.[240] In the brain, the spatial and temporal summation of the impulses from gustatory neurons are then combined to generate a specific taste perception.[241]

In this context, based on the previous results of this thesis, concepts for droplet-based optical logic gates using multiresponsive Janus emulsions as a soft colloidal material platform should be elaborated.[180, 224] For this purpose, the unique reconfigurability and multiresponsiveness of complex emulsion droplets should be exploited in combination with stimuli-responsive surfactants to process information from their environment and to convert the triggered changes of the surfactants into physical actuations.[94] The morphology-dependent alterations of the optical properties of biphasic complex emulsions mentioned in the introduction (see chapter 3.2.3) will serve as readout mechanisms and thus as output signals for the droplet-based logic gates.

4.4.2   Droplet-based Logic Gates

In the following chapters, concepts for droplet-based logic gates and circuits are presented, which become increasingly complex in their presented order. Each utilize different underlying readout methods as output signals for optical information processing to demonstrate the versatility of biphasic complex emulsions as a material platform for the realization of logic gates and combinational logic circuits.

4.4.2.1 Single Input "YES" and "NOT" Gates

Based on the results of chapter 4.2.5, which dealt with the UV-induced reconfiguration of complex emulsions functionalized with the light-responsive surfactant AzoTAB, a simple single-input logic "YES" gate should be realized with the use of complex emulsions. To convert the optical input "UV radiation" via the emulsion droplets into an optically detectable and readable output signal, the morphology-dependent Lensing effect of biphasic complex droplets discussed in chapter 3.2.3.1 was used as a readout method.[138, 139] Therefore, complex emulsions were generated of toluene/HFE-7500/FC-43 in

a 1:0.9:0.1 ratio. The oil mixture was emulsified in an adjusted surfactant solution (0.05 wt.% AzoTAB and 0.15 wt.% Zonyl) so that the Janus droplets exhibited a contact angle of approximately 90°.

In the initial starting morphology, the droplets, placed as a monolayer on a sample holder, showed high transmission of incident white light, which was positioned vertically (0° angle) above the sample holder (Figure 79). The transmitted light was measured with a spectrometer probe placed directly below the sample holder. The fiber optic probe was connected to an optical spectrometer. To initiate the triggered change in the droplets' morphology, a UV-light source (λ = 365 nm) was arranged at a 45° angle above the sample holder. Upon UV-light irradiation, the droplets assumed a more encapsulated droplet morphology (θ < 90°), through the triggered isomerization of AzoTAB. Figure 79 shows the described measurement setup and micrographs of the triggered reconfiguration of the complex droplets.
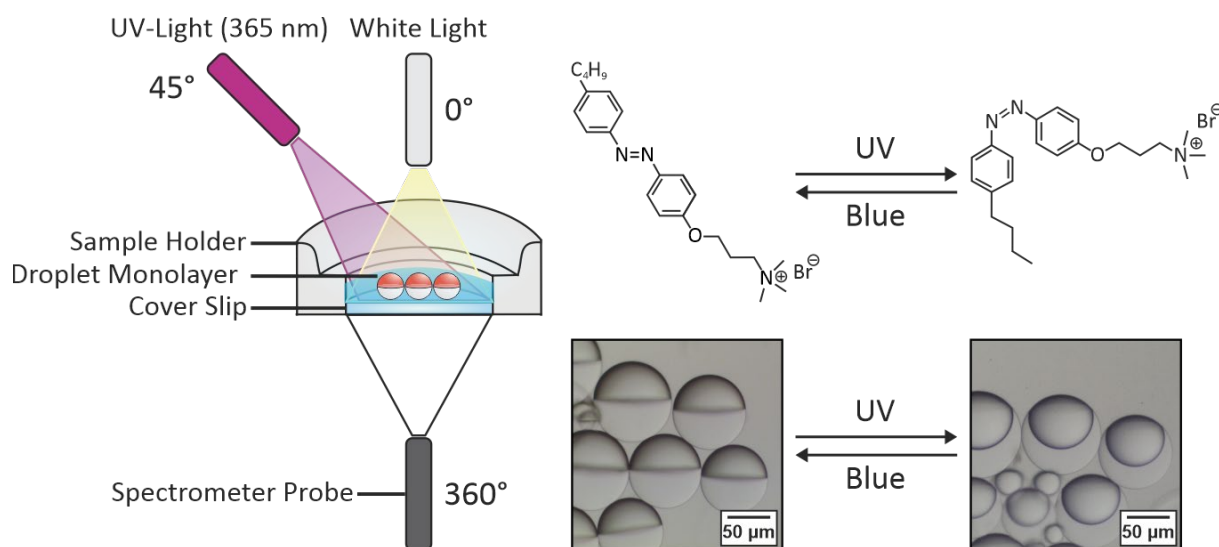
Figure 79. Measurement setup for the detection of transmitted white light through a monolayer of complex emulsion droplets (left). Chemical structure of the light-responsive hydrocarbon surfactant AzoTAB (top right). Optical micrographs of Janus droplets functionalized with the light-responsive surfactant AzoTAB that undergo morphological transitions in response to the wavelength of incident light (bottom right).

Due to the morphology change of the droplets and the associated rearrangement of the internal droplet interface, the incident light was increasingly scattered, which led to a reduction of the measured light intensity by about 40 % (Figure 80 right). The UV-induced morphology change and the associated change in the optical properties of the droplets were reversible by irradiation with an external blue light (λ = 470 nm). This demonstrates that the measured light intensity can be used as a reliable output signal for an optical droplet-based logic gate that can be readily evaluated with the naked eye. If the output light intensity measured with the droplets in the perfect Janus morphology is

defined as output signal "0", the reduced light intensity caused by the applied UV-trigger can be defined as output signal "1". This means no UV radiation ("0") provides full transmission ("0") as an output signal, while induced UV radiation ("1") provides reduced transmission ("1"). In the same way the binary definitions of "0" and "1" could also be reversed. The so generated logic gate corresponds in its design and functionality to a basic "YES"-gate. Figure 80 shows the truth table (left) and the measured light intensities of the droplet-based logic gate.

Figure 80. Symbol and truth table of a droplet-based logic "YES"-gate using the intensity of white light transmitted through a monolayer of complex droplets as an optical output signal (left). Normalized light intensity against the wavelength of incident light before and after UV-triggered reconfiguration of the complex emulsion droplets. The measured light intensity spectra were normalized to the highest intensity peak at a wavelength of λ = 570 nm.

Furthermore, the UV-triggered light scattering that led to a reduction in the transmitted light could be visualized by a printed image (Roman Minerva) that was placed under the sample holder. Due to the reconfiguration of the droplets to a more encapsulated morphology and the accompanying enhancement in light scattering, the details of the Minerva were only barely visible (Figure 81). The process was reversible and the blurred image became clear again after the monolayer of droplets was illuminated with blue light.
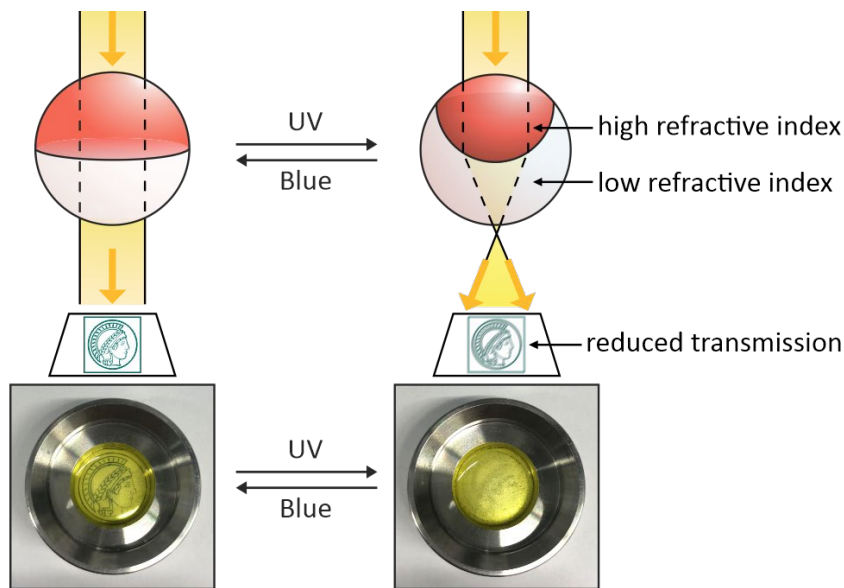
Figure 81. Droplet-based logic "YES"-Gate using the light-responsive surfactant AzoTAB and a droplet shape-depending transmission change as an optical readout. The image of the Roman Minerva, which was placed underneath the sample holder became blurry after applying a UV-light trigger (λ = 365 nm) and clear again after illumination with blue light (λ = 470 nm).

To further demonstrate the recovery and reversibility of the presented droplet-based logic "Yes"-gate, the measurement setup was extended to include a blue LED fiber (λ = 470 nm) placed at a 45° angle above the sample holder. The droplet monolayer was then irradiated alternately with UV- and blue light for 20 seconds each. After every irradiation step, the light transmission of the monolayer was measured throughout five cycles.
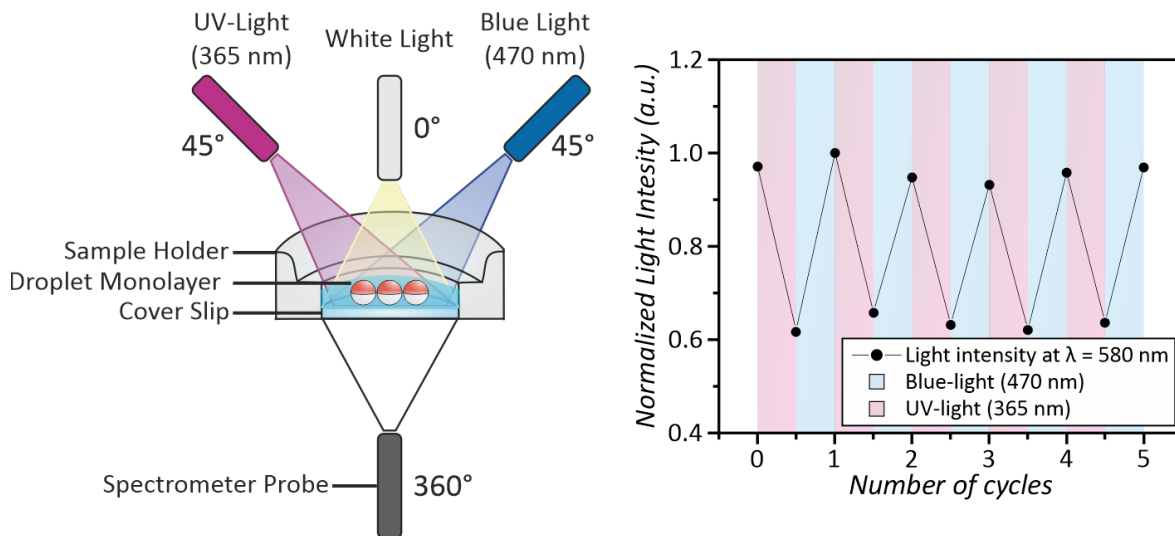
Figure 82. Extended measurement setup for the detection of transmitted white light through a monolayer of complex emulsion droplets (left). Measured light intensity of transmitted light through a monolayer of complex

emulsion droplets over five cycles of alternating UV and blue light irradiation (right). Light intensity values were determined at a wavelength of λ = 570 nm and normalized to the highest recorded intensity peak.

The recovery of the initial intensity after each cycle of alternating irradiation with UV and blue light over five cycles, illustrates the robustness of the droplet-based logic gate. The described logic "YES"-gate with the previously set binary definitions can be converted into the inverse single input "NOT"-gate without much effort by adjusting the surfactant concentrations and the associated starting morphology of the emulsion droplets (Figure 83 left). By keeping the AzoTAB concentration constant (0.15 wt.%) and decreasing the Zonyl concentration (0.1 wt.%), the droplets adopted a FC/HC/W double emulsion morphology (θ > 90°) without UV excitation. Consequently, the measured light intensity was initially reduced due to light scattering at the encapsulated droplets resulting in an output signal of "1". The droplet morphology could be converted to a Janus morphology after UV light irradiation, by tuning the surfactant concentrations, resulting in an increased transmitted light intensity and an output signal of "1" (Figure 83 right).
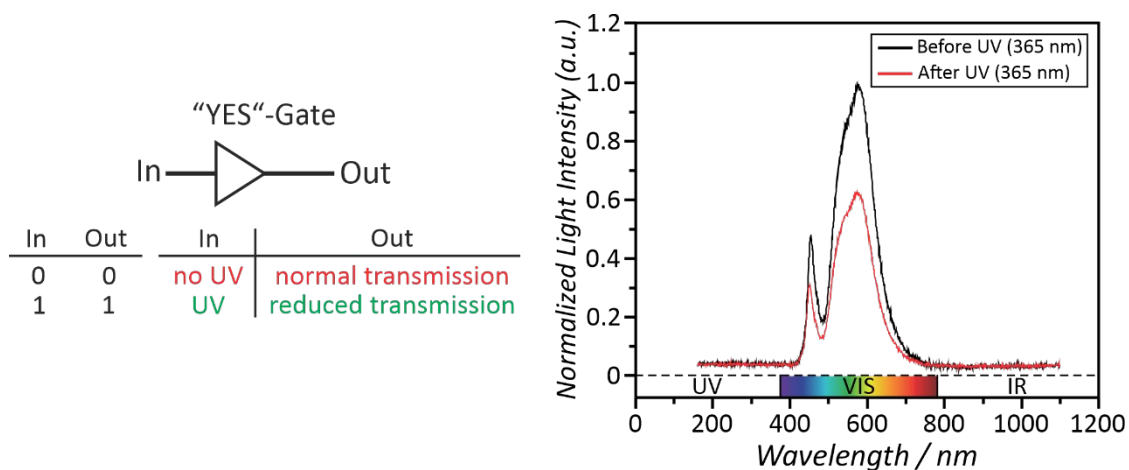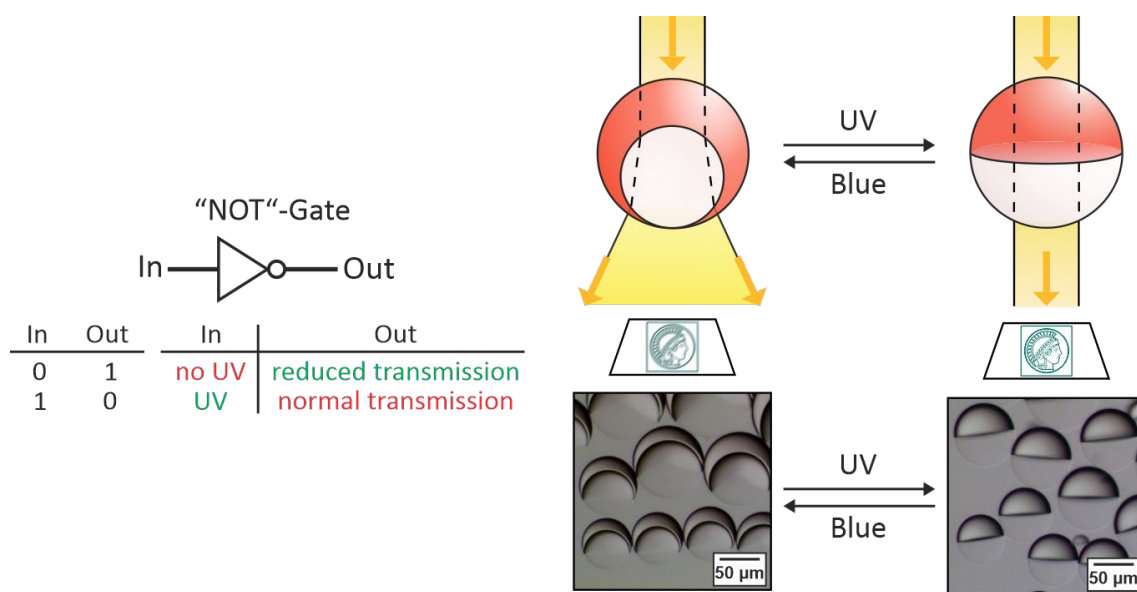

Figure 83. Symbol and truth table of a droplet-based "NOT"-gate using the intensity of white light transmitted through a monolayer of complex droplets as an optical output signal (left). Light-induced change in the lensing properties of complex droplets (right).

4.4.2.2 Double-Input "AND"-Gate

To realize a logic gate with two different input signals, complex emulsion droplets were functionalized with a dual pH- and light-responsive spiropyran-based surfactant 5-(5'-butyl-1',3',3'-trimethylspiro[chromene-2,2'-indolin]-6-yl)pent-4-yn-1-(trimethyl-ammonium)   bromide   (SP

surfactant), which was synthesized and provided by Dr. Martin Reifarth.[242] The unique characteristic of the SP surfactant is that the spiropyran moiety has been incorporated into the hydrophobic tail of the surfactant. This allows the SP surfactant to isomerize to a zwitterionic merocyanine (MC) species in a reversible ring-opening reaction depending on the pH and under the irradiation of light.[243, 244] While the SP form exhibits nonpolar properties, the MC form exists as either a zwitterionic (MC) or as a cationic (MCH+) species depending on the external pH-level (Figure 84). Due to the positive charge within the hydrophilic tail, there is a loss of the amphiphilic character of the cationic MCH+ species and thus a significant impairment of the interfacial activity. In a previous study, the differentiated surface-active behavior of the SP surfactant was already investigated and used to manipulate the stability of oil-in-water emulsions.[242]
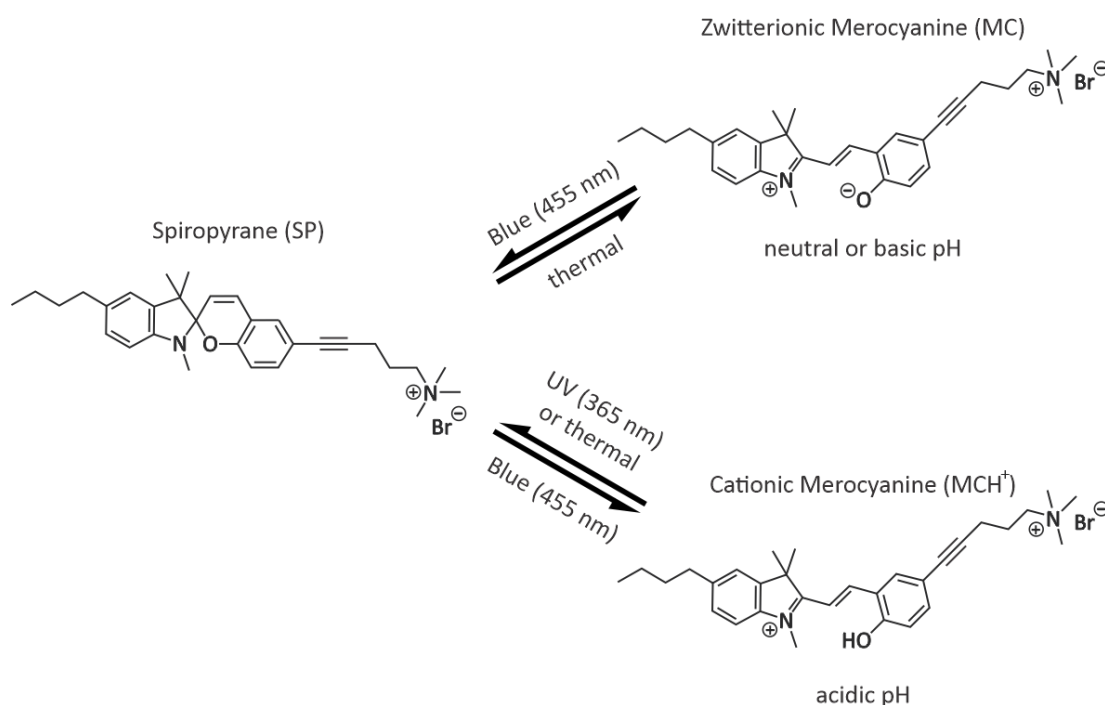
Figure 84. Light switching behavior and chemical structures of the different species of the dual-responsive spiropyrane surfactant (SP) at different pH levels.

Due to the dual-responsivity and reduced surfactant effectiveness under UV irradiation and acidic conditions, the SP surfactant can be considered as a molecular logic "AND"-Gate. To translate the triggerable change in surfactant effectiveness of the SP surfactant into a readable output signal, the morphology-dependent directional light emission of complex emulsions described in section 3.2.3.2 was used. For this purpose, the fluorescent dye N,N-Bis(2,6-diisopropylphenyl)perylene-3,4,9,10-bis(dicarboximide) (iPr-PDI) was incorporated into the HC phase of complex emulsion droplets comprising toluene/HFE-7500/FC-43 in a 1:0.9:0.1 ratio (Figure 85 left). The absorption and emission

spectra of the dye each exhibit three characteristic bands occurring at an absorption wavelength of λ = 460 nm, 490 nm, 530 nm and an emission wavelength of at λ = 540 nm, 580 nm and 630 nm, respectively (Figure 85 right).
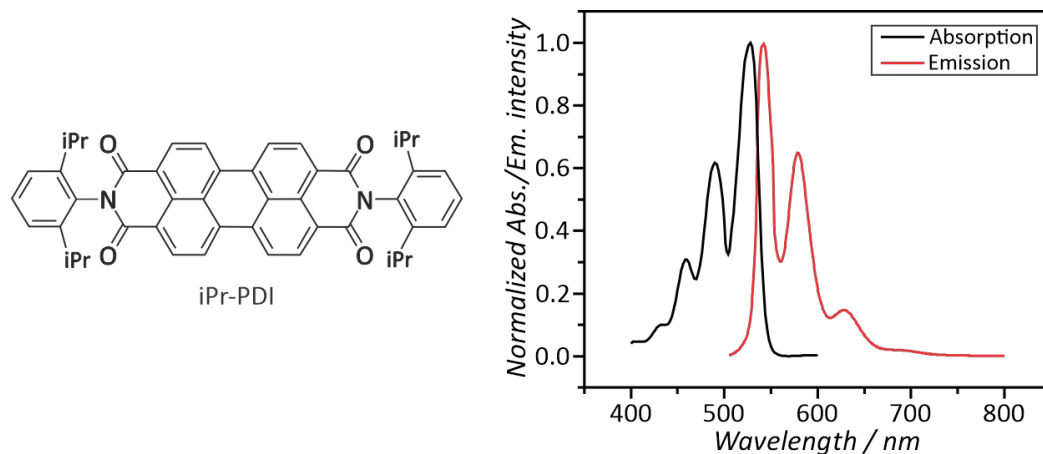
Figure 85. Chemical structure (left) and absorption and emission spectra of the fluorescent dye iPr-PDI (right). The dye exhibits absorption bands at λ = 460 nm, 490 nm, 530 nm and emission bands at λ = 540 nm, 580 nm and 630 nm.

To excite the fluorescent dye, the measurement setup described in context with the previous logic gate (Figure 82) was modified. Instead of the blue light source, a green optical fiber LED with an emitted light wavelength of λ = 530 nm was placed at an angle of 45° above the sample holder to coincide with the highest absorption band of the dye. In addition, the white light source of the previous measurement setup was replaced by a spectrometer probe to collect the light emitted by the complex droplets in vertical direction, which is the highest at a contact angle of θ ≈ 27° due to total internal reflection at the internal droplet interface (Figure 86 left).[139] The droplet-based logic "AND"-gate should be designed in a way that the complex droplets start in a Janus morphology and the enhanced emission in vertical direction is measured only when the droplets reconfigure towards a contact angle of θ ≈ 27° due to the reduced surfactant effectiveness by the two applied triggers (Figure 86 right).
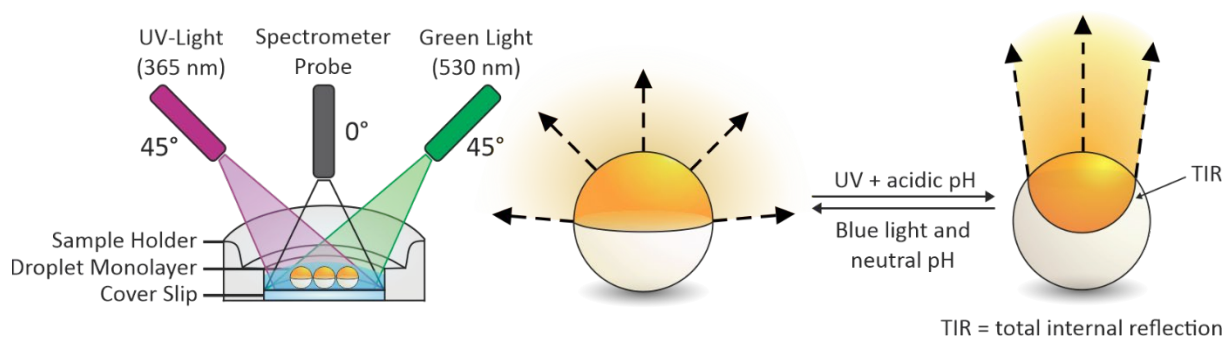
Figure 86. Measurement setup for the detection of emitted light from the fluorecent dye iPr-PDI incorporated in complex emulsion droplets (left). Morphology-dependent directional light emission of complex emulsions triggered by variations in incident light and pH.

To meet these criteria, the droplet phases were emulsified in a surfactant solution containing 0.35 wt.% Triton, 0.6 wt.% Zonyl and 0.043 wt.% of the SP surfactant. The nonionic Triton surfactant was necessary to ensure a final contact angle of θ ≈ 27° after deactivating the SP surfactant. Under neutral conditions the prepared emulsions showed a violet color and the droplets adopted a Janus morphology, which did not show any morphological transition in response to UV-irradiation (Figure 87 middle). By changing the pH from pH = 7 to pH = 3 with hydrochloric acid and applying the UV light trigger, the color of the emulsion changed rapidly from violet to light yellow (Figure 87 right), and the complex droplets changed their morphology from Janus to a nearly encapsulated HC/FC/W double emulsion morphology (Figure 87 left).
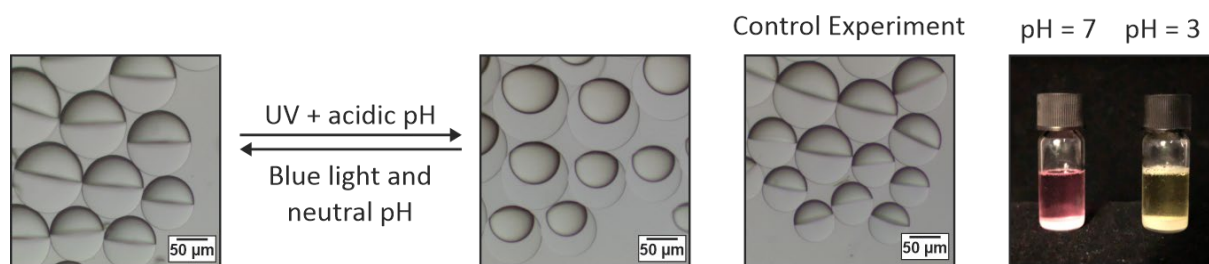
Figure 87. Triggered morphology change by applying a UV-light trigger under acidic conditions on complex emulsion droplets functionalized with a dual-responsive SP surfactant (left). Control experiment that was conducted under neutral pH conditions (middle). The complex emulsion droplets did not show any morphological change in response to UV-irradiation. Color change of complex emulsions containing the dual-responsive SP surfactant after irradiation with UV-light and at different pH levels (right). In the left vial, the color remained violet at pH = 7, while in the right vial the color changed from violet to light yellow under acidic conditions.

Subsequently, the light collected by the spectrometer probe placed above a monolayer of complex emulsion droplets functionalized with the SP surfactant was analyzed. The experiments were conducted in the dark to prevent light collection from external sources. The light spectra were recorded before and after changing the pH from neutral to acidic and after applying the UV light trigger for about 10 seconds in both cases. The received spectra revealed an exclusive emission of the fluorescent dye at a wavelength of $\lambda = 580$ nm and 630 nm under acidic conditions and prior UV-irradiation (Figure 88). However, most of the collected light origins from the scattered excitation light ($\lambda = 530$ nm).
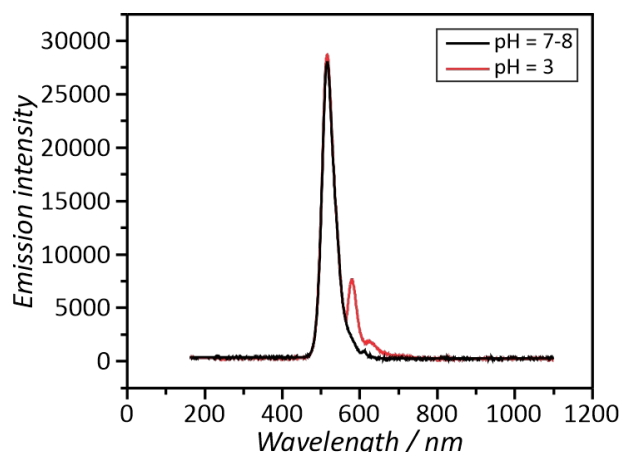
Figure 88. Wavelength-dependent emission intensity of light detected by a spectrometer probe positioned vertically above a monolayer of emitting complex droplets functionalized with the dual-responsive SP surfactant. Both spectra were recorded after the monolayer was irradiated with UV light for 10 seconds. Exclusive dye emission at a wavelength of λ = 580 nm and 630 nm was observed only under acidic conditions.

The so received droplet-based logic "AND"-Gate with its associated truth table is shown in Figure 89.
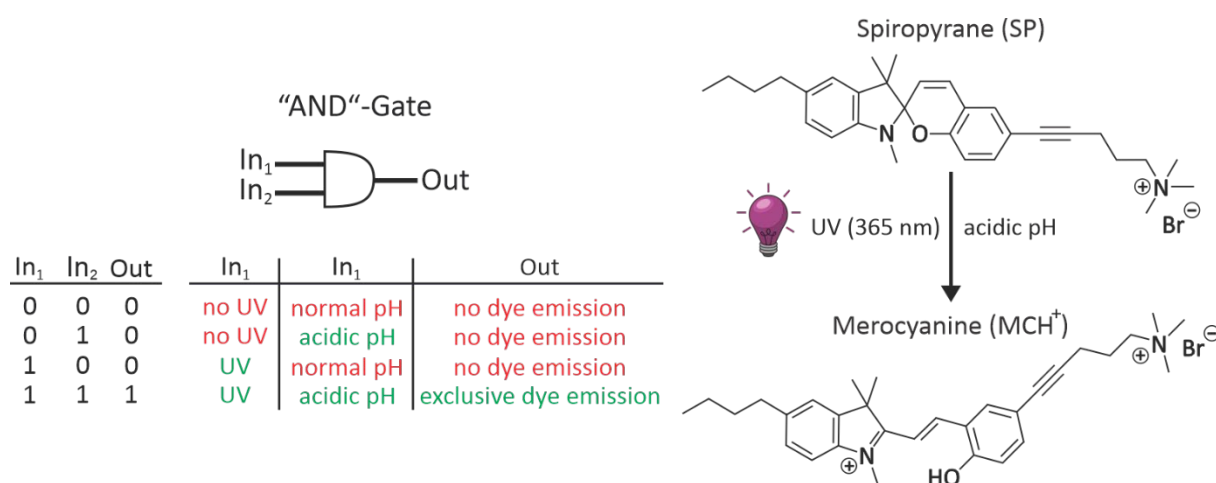
Figure 89. Truth table and symbol of the droplet-based logic "AND"-Gate (left) realized with the dual-responsive SP surfactant that can isomerize to a cationic (MCH$^+$) species upon UV-irradiation and under acidic conditions (right). Light emission due to the incorporated iPr-PDI dye can only be detected in vertical direction when both external triggers are applied.

4.4.3   Droplet-based Combinational Logic Circuits

In a last concept, a combinatorial logic circuit based on complex emulsion droplets should be realized. The so-called "Half-Adder" is a logic circuit which is able to add two one-digit binary numbers together.[19] The special characteristic about this logic circuit is that it consists of two inputs and two outputs (Figure 90).
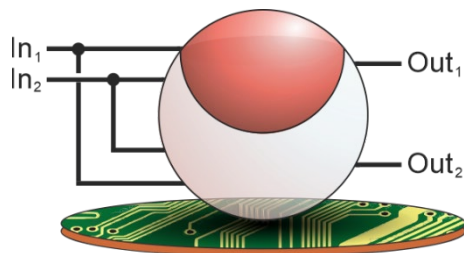
Figure 90. Illustration of a combinational logic circuit based on complex emulsion droplets offering two inputs and two outputs.

The distinguishability of two different output signals allows in principle a higher information throughput. In order to translate two potential output signals into detectable optical signals, the occurrence of morphology-dependent structural colors in biphasic complex emulsions discussed in chapter 3.2.3.3 was used as a readout method. The structural colors can be observed by illuminating the droplets with collimated white light and subsequent total internal reflection at the internal droplet interface, resulting in interference of the light rays, which take different paths along the internal interface of the droplets.[145] The interference results in the cancellation or amplification of certain wavelengths. The advantage of this readout method is that, depending on the size of the droplets, which correlates with the size of the internal interface, two to three different structural colors can be observed.

The study of structural colors observed from polydisperse complex emulsions consisting of heptane and perfluorohexane in a 1:1 ratio showed that the colors occur in a contact angle range of $\theta \approx 28\text{-}55°$. The observed color depends on the droplet morphology and size. Furthermore, the study revealed that droplets with a size > 85-90 µm show three different colors depending on their morphology, while droplets with a size < 85-90 µm show only two different colors. Figure 91 shows typical optical micrographs obtained when illuminating polydisperse complex emulsion droplets in a contact angle range of $\theta \approx 28\text{-}55°$ with collimated white light. The micrographs were captured in reflection with an upright microscope.

Figure 91. Reflectance optical micrographs of complex emulsion droplets showing how the color emanates from near the contact line and varies with droplet diameter.

To realize a droplet-based "Half-Adder", the application of either of the two input triggers should each result in the same output signal, while the application of both input triggers should result in a second, distinguishable output signal. Therefore, two stimuli-responsive surfactants were assembled at the HC/W interface of complex emulsion droplets. The UV-responsive AzoTAB surfactant combined with the pH-responsive 16-(dimethylamino)-*N*,*N*,*N*-trimethylhexadecan-1-aminium iodide (N$^+$-(16)-N) surfactant (For synthesis details see chapter 10.3.4). The pH-responsive surfactant behaves in neutral and alkaline media as a normal cationic surfactant, stabilizing conventional emulsions. In acidic media the surfactant becomes a hydrophilic Bola-type surfactant (N$^+$-(16)-NH$^+$), resulting in a reduced surfactant effectiveness (Figure 92).[245]
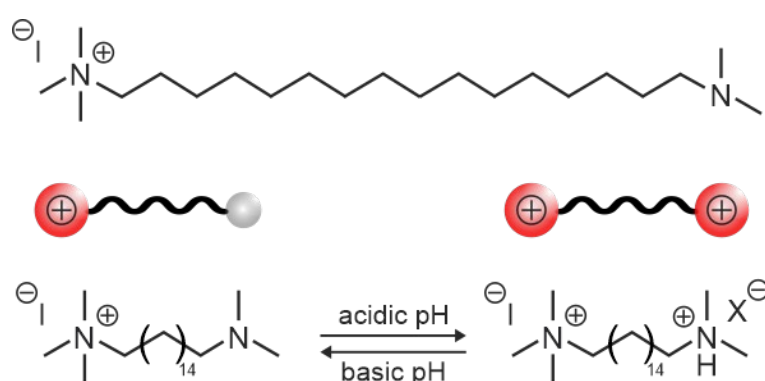
Figure 92. Chemical structure and switching behavior of the pH-responsive surfactant 16-(dimethylamino)-*N*,*N*,*N*-trimethylhexadecan-1-aminium iodide (N$^+$-(16)-N).

To obtain a uniform output signal with unambiguous coloration, monodisperse droplets were produced using microfluidics. The droplets had an average diameter of approximately 75 µm. A surfactant concentration of 0.05 wt.% Triton, 0.15 wt.% Zonyl, 0.01 wt.% AzoTAB and 0.002 wt.% N$^+$-(16)-N yielded complex emulsion droplets with contact angles θ ≈ 90 that did not exhibit structural color. The surfactant concentrations were adjusted in a way that applying of either one of the triggers, UV or acidic pH, resulted in a morphological reconfiguration of the droplets that allowed the appearance of a bright violet ring when the droplets were illuminated with collimated white light and observed under the microscope (Figure 93).
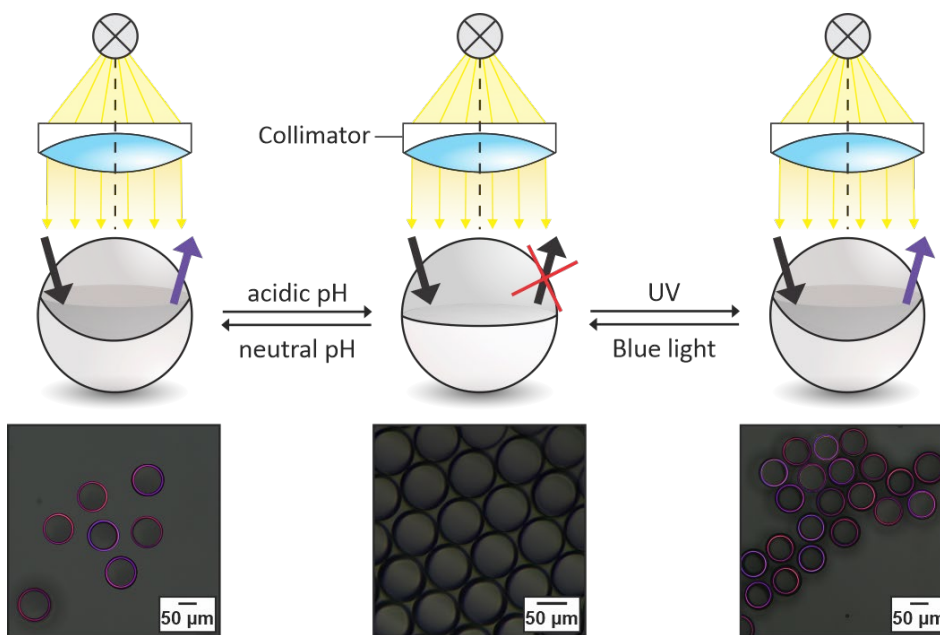
Figure 93. Morphological reconfiguration of complex emulsion droplets functionalized with the UV-responsive surfactant AzoTAB and the pH-responsive surfactant N^+-(16)-N. By applying either one of the triggers, UV or acidic pH, the droplets transition towards a morphology that allows the appearance of a violet structural color.

However, by applying both triggers at the same time, the contact angle of the complex droplets decreased even further, resulting in a color change from violet to bright yellow. Figure 94 shows the associated symbol and truth table of the droplet-based combinational logic circuit and optical micrographs of the complex droplets after applying both triggers. The so generated "Half-Adder" can process two different input trigger and is able to distinguish between one and two applied triggers.

In_1	In_2	Out_1	Out_2	In_1	In_1	Output
0	0	0	0	no UV	normal pH	no color
0	1	1	0	no UV	acidic pH	purple
1	0	1	0	UV	normal pH	purple
1	1	0	1	UV	acidic pH	yellow
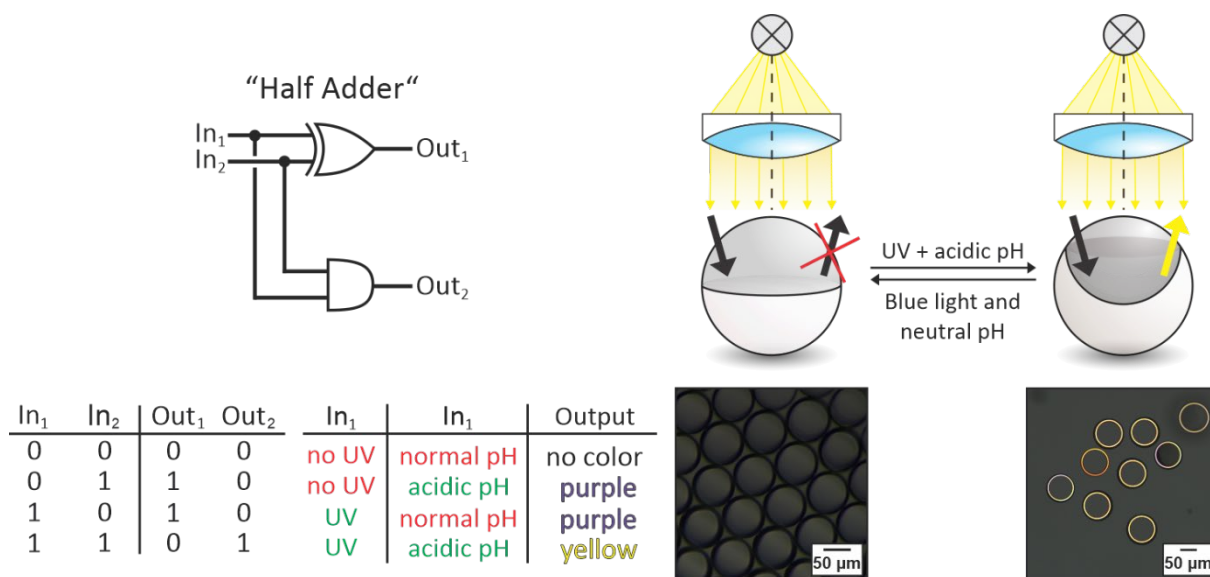
Figure 94. Truth table and symbol of the droplet-based "Half-Adder" (left) realized with a combination of the light-responsive AzoTAB surfactant and the pH-responsive N^+-(16)-N surfactant. By applying both trigger, UV and

acidic pH, the droplets transition towards a morphology that allows the appearance of a bright yellow structural color.

4.4.4   Conclusion

For the first time, concepts for three different logic gates or combinatorial logic circuits based on complex emulsions as material platform were presented. The logic gates exploit the unique properties of complex emulsions, specifically their reconfigurability and multiresponsiveness, in combination with stimuli-responsive surfactants. By using different readout methods, it was demonstrated how the physical trigger "UV radiation" and the chemical trigger "pH value change" could be converted into different optically readable output signals. Furthermore, it was shown that complex emulsion droplets have the potential for the realization of different types of logic gates, which are reversible and can be converted into other logic gates by simple adjustment of the surfactant concentrations. The presented concepts can be considered as templates or as proof-of-concepts offering great flexibility for customization and tailoring to different application areas. Due to their freely functionalizable hydrocarbon phase and the variety of available stimuli-responsive surfactants, complex emulsions offer the outstanding possibility of processing almost any external chemical or physical trigger, including temperature, pH, redox, light, enzymes, salts, presence of specific chemicals or biologicals, as well as external electric or magnetic fields, and transducing them into optically readable signals.[94, 95]

The last presented concept of the "Half-Adder" was featured by the special property of generating more than one output signal, which allows an increased information throughput. This underlines the versatility and efficiency of logic gates based on complex emulsions in information processing of environmental stimuli. The presented concepts offer great potential for the automation of sensor platforms as the generated output signals of the presented logic gates can be processed digitally with simple and inexpensive devices such as microscopes or optical spectrometers.

5   Conclusion and Outlook

Within the scope of this thesis, complex emulsions have been widely explored as a material platform for the design of multiresponsive, active and adaptive liquid colloidal systems. Different variations in droplet composition and the influence of additives and co-solvents on the external shape of complex droplets were studied in detail. The underlying principles and mechanics that influence the equilibrium of interfacial tensions have been uncovered, which allowed the targeted design of non-spherical anisotropic complex emulsions by combining two preparation approaches for the generation of complex emulsions, namely the thermal phase separation approach and the solvent evaporation method. Functionalization with a stimuli-responsive photosurfactant (AzoTAB) resulted in shape-changing soft colloids that exhibited a jellyfish inspired movement behavior, holding great promise for the design of biological inspired active material architectures and shape-changing soft robotics. A potential application of this shape-changing locomotion of complex droplets lies is in the active transport of payloads, for example of lipophilic substances, through the continuous aqueous medium.

In situ observations of spherical Janus emulsion droplets with a simple customized side-view imaging setup with accompanying pendant drop measurements disclosed the sensitivity regime of the unique chemical-morphological coupling inside biphasic O/W Janus emulsions. Recording of a calibration curve enabled the introduction of a new "responsive drop" method for a convenient and cost-efficient quantification and comparison of the CMC's and effectiveness' of various cationic, anionic, and nonionic surfactants. Further, the method allowed insightful characterization of stimuli-responsive surfactants and monitoring of the impact of inorganic salts on the CMC and surfactant effectiveness of ionic and nonionic surfactants. In this context, the "responsive drop" method could be applied to further commercial and stimuli-responsive surfactants to allow a complementary characterization of these compounds. The stimuli-responsive surfactants used in this work could serve as a basis for these studies. For example, the dual-responsive spiropyrane-based surfactant (SP surfactant) or the pH-responsive N^+-(16)-N surfactant.

The selective placement of synthetic crown ether surfactants on the hydrocarbon hemisphere of complex emulsion droplets yielded a synthetic minimal material platform capable of autonomous and reversible adaptation to its chemical environment through different supramolecular recognition events. Horizontal imaging allowed in situ visualization of different supramolecular host-guest recognition events at the interface and revealed two opposite morphological transition mechanics. Addition of metal or ammonium salts resulted in the formation of hydrophobic complexes by the coordination of crown ether units to suitable cations, leading to a phase-transfer of the complexes into the organic phase paired with a decrease in the measured contact angle θ of the complex droplets. In

contrast, the addition of hydrophilic ammonium compounds such as amino acids or polypeptides like antibodies resulted in an increase of the measured contact angle θ due to an improved hydrophilic-lipophilic balance of the resulting complexes. In summary, the multiresponsive material platform enabled interfacial complexation and thus triggered responses of the droplets to a variety of chemical triggers including metal ions, ammonium compounds, amino acids, antibodies, carbohydrates as well as amino-functionalized solid interfaces. Based on the presented results, further crown ether surfactants could be synthesized and investigated for their supramolecular complexation properties. Specially designed binding pockets could increase the selectivity towards specific ion species and thus enable highly sensitive droplet-based metal ion sensors. In this context, photo-responsive crown ether surfactants would be of interest, as they would allow switchable uptake and release of metal ions by the complex droplets.[246, 247] In addition, the crown ether-functionalized complex emulsions could serve as the basis for biomimetic model systems to investigate the supramolecular mechanics of natural ionophores in biological systems.

At the end of the thesis, the first documented logic gates and combinatorial logic circuits based on complex emulsions were presented. The previously extensively studied reconfigurability and multiresponsiveness of complex emulsions was used to realize complex droplet-based logic gates of varying complexity. The selection of different stimuli-responsive surfactants in combination with varying readout methods demonstrated the versatility and flexibility of the material platform, which can in principle be adapted to almost any external chemical or physical trigger, including temperature, pH, redox, light, enzymes, salts, presence of specific chemicals or biologicals, as well as external electric or magnetic fields. In this framework, the previously addressed crown ether surfactants offer further possibilities for the detection of various cations and biologically relevant molecules. Further, with the introduction of the droplet-based "Half-Adder" and the morphology-dependent occurrence of structural colors as readout method, it was proven that droplet-based logic gates are capable of generating more than one output signal, which allows increased information throughput. The presented logic gates can be considered as templates, offering great flexibility for customization and tailoring to different application areas. The received output signals of the various readout methods can be processed digitally, which paves the way for fully automated, adaptive and parallel processing sensing platforms, which could be arranged in large arrays in analogy to silicon-based logic gates, allowing live monitoring of aqueous environments.

6   Experimental Section

6.1   List of used Chemicals

If not other mentioned, all chemicals listed herein were used as received without further purification. Acetone (Honeywell), 3-aminophenylboronic acid hydrochloride (98%, Sigma Aldrich), 4'-aminobenzo-15-crown-5 (Sigma Aldrich), 4'-aminobenzo-18-crown-6 (Sigma Aldrich), 2-[2-(3-aminopropoxy)-ethoxy]ethan-1-ol (95%, Enamine), 3-(aminopropyl)trimethoxysilane (97%, Sigma Aldrich), ammonium acetate (Sigma Aldrich), ammonium chloride (Sigma Aldrich), anti-human IgG (Fc specific)–FITC antibody produced in goat (Sigma Aldrich), AOT (98%, Sigma Aldrich), barium acetate (Sigma Aldrich), 4-butylanilin (Sigma Aldrich), Brij 58 (Sigma Aldrich), 1-bromohexane (99%, Alfa Aesar), calcium acetate monohydrate (Alfa Aesar), chloroform (Honeywell), CTAB (99%, Sigma Alrich), D-(-)-fructose (>99%, Sigma Aldrich), D-(+)-glucose (>99.5%, Sigma Aldrich), 1,3-dibromopropane (abcr GmbH), dichloromethane (Honeywell), dimethylamine (40% in water), diehtylbenzene (95%, Sigma Aldrich), diethylether (Honeywell), 4-(dimethylamino)pyridine (Sigma Aldrich), *N,N*-dimethylformamide (Honeywell), dodecanoyl chloride (Sigma Aldrich), [3-(2,3-epoxypropoxy)-propyl]-trimethoxysilan (>98%, Sigma Aldrich), ethylacetate (Honeywell), FC-43 (85%, abcr GmbH), fluoresceinamine hydrochloride isomer (Sigma Aldrich), 1,16-hexadecanedioic acid (Sigma Aldrich), HFE 7500 (99%, abcr GmbH), L-arginine (>99,5%, Sigma Aldrich), L-histidine (>99%, Sigma Aldrich), lithium acetate dihydrate (Sigma Aldrich), lithium aluminium hydride (Sigma Aldrich), L-lysine (>98,5%, Sigma Aldrich), magnesium acetate tetrahydrate Alfa Aesar), magnesium sulfate (Sigma Aldrich), mannan from saccharomyces cerevisiae (Sigma Aldrich), methanol (Supelco), 1-(methoxy)nonafluorobutane (98%, abcr GmbH), methyl iodide (abcr GmbH), n-decane (Sigma Aldrich), n-heptane (Fluka Chemika), n-hexane (Sigma Aldrich), *N-N`*-Bis(2,6-diisopropylphenyl)-3,4,9,10-perylenetetracarboxylic diimide (Tokyo chemical industry co.), perfluorodecalin (98% cis and trans, abcr GmbH), phenol detached crystals (99+%, Alfa Aesar), potassium acetate (Alfa Aesar), potassium carbonate anhydrous (99.5%, potassium carbonate (Sigma Aldrich), Fisher scientific U.K.), potassium hydroxide (Sigma Aldrich), potassium iodide (Sigma Aldrich), riboflavin (Sigma Aldrich), sodium acetate (Sigma Aldrich), sodium carbonate (Sigma Aldrich), sodium chloride (Sigma Aldrich), sodium dodecyl sulfate (99%, Sigma Aldrich), sodium hydrogencarbonate (Sigma Aldrich), sodium nitrite (Merck), Sudan Red 7B (Sigma Aldrich), tert-butyl-2-bromoacetate (abcr GmbH), tetrahydrofuran (Honeywell), thionyl chloride (Sigma Aldrich), toluene (VWR chemicals), triethylamine (Sigma Aldrich), trifluoroacetic acid (Sigma Aldrich), trimethylamine (35% in ethanol) (Sigma Aldrich), Trition X-100 (eurobio), Tween 20 (Sigma Aldrich), zinc acetate (Sigma Aldrich), Zonyl FS-300 (40% solid in water, abcr GmbH).

6.2   Characterization Methods

Nuclear Magnetic Resonance (NMR)

[1]H- and ^{13}C-nuclear magnetic resonance (NMR) spectra were recorded using a Bruker Advance and Agilent 400 MHz NMR spectrometer.

High-Resolution Mass Spectrometry (HRMS)

High-resolution mass spectrometry (HRMS) was measured with a Xevo G2-XS Qtof high-resolution mass spectrometer (Waters) coupled with an Acquity UPLC H-Class system (Waters).

Confocal Laser Scanning Microscopy (CLSM)

Confocal laser scanning microscopy (CLSM) was performed on a Leica SP8 confocal microscope. Samples were excited with an argon laser at 476 and 488 nm, and emission detected at 500-550 nm. Images were acquired at 1024 × 1024 pixels at 400 Hz scanning speed.

Density Functional Theory (DFT) Calculations

Gas-phase ground-state equilibrium geometries and frequencies were obtained by performing density functional theory (DFT) optimization, using the B3LYP[248] energy functional and the 6-31G(d,p) split-valence Pople's basis set for all the atomic species. Besides, the electron density with an isovalue contour was mapped for the metal-free and sodium chelated 15-crown ether surfactant. DFT calculations were performed using the GAUSSIAN03 package.

Imaging and Microscopy

For the *in situ* observation of the complex emulsions and the determination of the contact angles a custom designed side-view setup was used, which was equipped with a variable zoom, composed of two tube 200 mm tube lenses and Olympus planar optical microscopy lenses. The apparatus was connected to an area scan CCD camera from HIKVision. For imaging monolayers we used generic cavity slides. Horizontal images have been captured on an inverted microscope (Bresser) mounted with an area scan CCD camera from HIKVision. Structural colors were measured in reflection using an VH-Z100 upright microscope from Keyence.

Droplet Geometry Measurements

To overcome the problem of stacking and squishing of emulsion droplets, which should be avoided for correct contact angle determination, a special preparation technique was utilized. By applying only a small amount of droplets on the center (highest depth) of a horizontal lying cavity slides ensures that the droplets can fill up the cavity slide from bottom to top, when the cavity slide is brought afterwards into a vertical position. This technique avoids the squishing of the droplets. At the left and right end of the cavity slide center a monolayer of droplets forms, which are neither stacked nor squished. This monolayer can be used to take high quality side-view images.

Contact angles at the three-phase contact line of Janus particles were determined from side view images taken with a custom side-view setup mentioned above. All studied droplets appeared overall to be spherical as a result of the ultralow interfacial tension between both oil phases. As described in chapter 3.2.1, the contact angle θ_{FC} was used as the key parameter to quantitatively describe the Janus droplets' morphology. The contact angle θ_{FC} was determined by taking the middle points of two circles that outline the inner and outer interfaces of a side-viewed droplet and applying the law of cosines according to equation (6) (with R_i: radius of inner droplet; R_d: radius of Janus droplet; and d: distance between the centers of the two circles). The outer contact angle θ_0 of non-spherical snowman-shaped droplets was determined by drawing circles around the hemispheres of the two oil phases (Figure 13). Starting from the three-phase junction point, tangents can be applied to the respective circles that outline the oil phases. The angle between the two tangents corresponds to the contact angle θ_0.

Pendant-Drop Tensiometry

Interfacial tension measurements were performed on a drop shape analyzer tensiometer (DSA10-MK2, Krüss) in the pendant drop configuration. A CCD camera recorded the image of the drop. To obtain values of the surface tension, the drop profiles were fitted to the Laplace equation. The interfacial tension decreased exponentially with time after the formation of the pendant drop because surfactant molecules continued to adsorb at the droplets' interface. To keep the results comparable and to take the exponential decline of the interfacial tension into consideration, the process was monitored over time. Therefore, the interfacial tension values were taken when the rate of decrease was slower than 0.2 mNm^{-1} per 30 seconds.

6.3   Software

All illustrations of molecules were specially created with the program Chemdraw Professional, Version 20.0 from PerkinElmer. Self-generated schematic illustrations were made with the program CorelDRAW 2020 from Corel Corporation. The NMR spectra were analyzed with the software MestReNova from Mestrelab Research. The computational determination of the contact angle was performed with either the imaging software Fiji or with a custom-written Matlab script (v2019b) using the image processing toolbox. Utilizing high-contrast side-view optical micrographs containing multiple droplets of similar size in a plane, the droplets are first separated from the main image using edge detection. The program uses an adaptive threshold algorithm to distinguish areas with higher transparency from the opaque regions of the higher refractive index and dyed hydrocarbon phases and calculates θ_{FC} from the respective circles. The separated droplets are processed separately to detect the internal interface, its curvature, and its centerpoint. In cases where $R_{droplet} \cong R_{curvature}$, the two circles are simply detected. In cases where $R_{curvature} \gg R_{droplet}$, the interfacial curvature is defined by the right and left-most points of the detected internal interface and the upper- and lower-most points. The detected centerpoints and curvatures are then used to calculate the intersection points. The contact angle between the two droplets is calculated using the law of cosines.

6.4   Experimental Procedure

General Instruction for Droplet Generation

The complex emulsions in this work were prepared by a one-step temperature-induced phase-separation method (see chapter 3.2.2). The droplet oil phases consisted of various hydrocarbon and fluorocarbon oils that were mixed in a 1:1 ratio unless otherwise specified. The continuous aqueous phase consisted of ultrapure MilliQ water with different concentrations of the following surfactants: AOT, AzoTAB, Brij 58, CTAB, N$^+$-(16)-N, SDS, Triton X-100, Tween 20, and Zonyl FS-300. For each emulsion 100 µl of the hydrocarbon-fluorocarbon mixture was heated above the respective upper critical solution temperature (UCST) and added to 1 mL of a preheated aqueous surfactant solution. The resulting mixture was emulsified subsequently by using a vortex mixer (10 s, 2500 rpm, Vortex Genie 2, scientific industries). The prepared complex emulsions were cooled down to room temperature before used. For higher contrast micrographs of the droplets, the dye Sudan Red 7B was added to the hydrocarbon phase of the emulsion samples if it did not interfere in the experiments.

Monodisperse biphasic droplets were generated with a thermal phase separation approach in a microfluidic device. The fluid flow rates of the continuous and dispersed phase were controlled with a Fluigent Flow-EZ pressure control platform. Both phases were guided through a X-shaped junction in a hydrophilic glass chip produced by Dolomite and were brought together under elevated temperature in a custom-built heat chamber. Inside the heat chamber the air was heated by a heating unit to raise the temperature above the UCST of the particular oil mixture. Droplets were generated and collected in a surfactant mixture for the desired experimental sample. The droplets were then cooled to induce phase separation, resulting in Janus droplets with a uniform internal droplet morphology. Generated microfluidic droplets were stored in sealed containers to prevent evaporation and used within 3 days.

CMC and γ_{HC}* Determination with the Dynamic Drop Method

To determine the surfactants CMC and γ_{HC}* values the droplets' contact angle was measured at different hydrocarbon surfactant concentrations and the concentration of fluorocarbon surfactant (Zonyl FS-300) was kept constant. The constant fluorocarbon surfactant concentration acted as an internal standard and served to maintain overall droplet stability. Initially, the droplet contact angle increased rapidly with an increasing amount of hydrocarbon surfactant until the CMC was reached. After the CMC the slope of the contact angle change was significantly lower. To extract the surfactants' CMC and γ_{HC}* values from the droplet morphology diagram the linear fit functions describing the two different areas where the slope of the droplets contact angle change differ from each other were used. The CMC value was extracted from the crossing point of the two linear fit functions. The corresponding y-value describing the droplet contact angle at the surfactant's CMC was then translated into an interfacial tension value using the function of the linear fit from Figure 35 of the dissertation. The contact angle is directly proportional to the parameter γ_{FC} - γ_{HC}. With the function describing the calibration curve of Figure 35 at hand ($\theta = 26.41° \cdot (\gamma_{FC} - \gamma_{HC}) + 95.02°$) , and knowing the value of γ_{FC} at the particular fluorocarbon surfactant concentration, the respective γ_{HC}* value could be calculated (Table 3).

Characterization of the Photo-responsive Surfactant AzoTAB

For measurements with the amphiphilic light-responsive azo-surfactant AzoTAB the complex emulsions have been irradiated until the droplets' topology reached a constant state. As UV-light source we used a UV lamp from Herolab GmbH (Type NU-4, 220 Volt, 2x4 Watt) with a wavelength of λ = 366 nm. As blue light source we used a custom designed LED with a wavelength of λ = 461 nm and a power of 74.6 mW/cm². The Lamp Spectra of the UV- and blue light source were measured with an

optical spectrometer from Avantes (StarLine, AvaSpec-ULS2048CL-EVO-RS) which was connected to an optical fiber from ThorLabs (diameter: 400 µm).

^{1}H-NMR Investigation of Crown Ether Phase Partitioning

To determine the partitioning of the 15-crown-5 surfactant between the toluene and water phase under different conditions an external quantitative NMR approach was used.[234] For this purpose, a measuring tube containing a capillary with 1,3,5-trimethoxybenzene dissolved in toluene-d_8 was used as a reference substance. Through this approach contamination of the analyte solution with the reference substance can be avoided. The concentration of the internal standard was 5 mgmL^{-1}. In a separate vial 3 mgmL^{-1} of the 15-crown-5 surfactant was dissolved in 2 mL of a phase-separated 1:1 mixture of toluene-d_8 (1 mL) and D_2O (1 mL). The mixture was agitated and left 1 h for equilibration. Subsequently, 500 µL of each phase was extracted and a ^{1}H-NMR-spectrum was recorded. The spectra were recorded using a Bruker Avance Neo 600 MHz NMR spectrometer with a broad band fluorine observation (BBFO) probe head. To minimize measurement-related errors the amount of scans was raised to 128, spinning was turned off to prevent artefacts known as "spinning sidebands" and the relaxation delay was set manually (d1) to 5 s to ensure that all signals have fully relaxed between pulses. Before integrating the signals of interest phase- and baseline correction have been applied to the spectra. NMR signals of 1,3,5-Trimethoxybenzene (reference compound) in toluene-d_8 are δ (ppm): 6.14 (s, 3H), 3.33 (s, 9H).

IgG Antibody Attachment to Crown Ether-functionalized Complex Emulsions

For the attachment experiment of the FITC-labeled anti-human IgG antibody produced in goat, 500 µl of the surfactant solution containing 0.05 wt.% Zonyl, 0.015 wt.% Triton and 40 µg/mL anti-human IgG antibodies was added to the fluorescence sample holder. Next, complex emulsion droplets functionalized with 1 mg/mL (1.96 mM) of the 18-crown-6 surfactant, which were prepared in a surfactant solution with 0.05 wt.% Zonyl and 0.015 wt.% Triton, were added to the sample holder using a glass pipette. The images were taken after the droplets were gently swirled in the antibody containing surfactant solution for 60 seconds.

7 List of Abbreviations and Symbols

AOT	Sodium bis(2-ethylhexyl) sulfosuccinate
BBFO	Broad band fluorine observation
Brij 58	Polyethylenglycolhexadecylether
CLSM	Confocal laser scanning microscopy
CTAB	Cetyltrimethylammonium bromide
CMC	Critical micelle concentration
DCM	Dichloromethane
DEB	Diethylbenzene
DFT	Density functional theory
DNA	Deoxyribonucleic acid
DMSO	Dimethyl sulfoxide
FC	Fluorocarbon
FC/HC/W	Fluorocarbon-in-hydrocarbon-in-water emulsion
FC-43	Perfluorotributylamine
FITC	Fluorescein isothiocyanate
γ	Interfacial tension
HC	Hydrocarbon
HC/FC/W	Hydrocarbon-in-fluorocarbon-in-water emulsion
HFE-7500	2-(Trifluoromethyl)-3-ethoxydodecafluorohexane
HLB	Hydrophilic-Lipophilic Balance
HRMS	High-resolution mass spectrometry

7   List of Abbreviations and Symbols

IFT	Interfacial tension
IgG	Immunoglobulin G
iPr-PDI	*N,N*-Bis(2,6-Diisopropylphenyl)perylene-3,4,9,10-bis(dicarboximide)
K-TARF	Potassium 2-(7,8-dimethyl-2,4-dioxo-10-((2S,3S,4R)-2,3,4,5-tetraace-toxypentyl)-4,10-dihydropyrimido[4,5-b]quinolin-3(2H)yl)acetate
LCST	Lower critical solution temperature
LED	Light emitting diode
MC	Zwitterionic merocyanine
MCH$^+$	Cationic merocyanine
MPFB	Methoxyperfluorobutane
N$^+$-(16)-N	16-(Dimethylamino)-*N,N,N*-trimethylhexadecan-1-aminium iodide
NMR	Nuclear magnetic resonance
O/W	Oil-in-water emulsion
O/W/O	Oil-in-water-in-oil emulsion
PEG-NH$_2$	2-[2-(3-Aminopropoxy)ethoxy]ethan-1-ol
PET	Photoinduced electron transfer
PFH	Perfluorohexane
QED	Quantum electrodynamics
SDS	Sodium dodecyl sulfate
SP surfactant	5-(5'-Butyl-1',3',3'-trimethylspiro[chromene-2,2'-indolin]-6-yl)pent-4-yn-1-(trimethyl-ammonium)

7   List of Abbreviations and Symbols

Γ	Surface excess
σ	Surface tension
THF	Tetrahydrofuran
Triton	Triton X-100
Tween 20	Polyoxyethylen(20)-sorbitan-monolaurat
Tween 80	Polyoxyethylen(20)-sorbitan-monooleat
UCST / T_c	Upper critical solution temperature
UV	Ultraviolet
Vis	Visible
W/O	Water-in-oil emulsion
W/O/W	Water-in-oil-in-water emulsion
Zonyl	Zonyl FS-300

8   References

[1]   S. S. Schweber, *QED and the men who made it: Dyson, Feynman, Schwinger, and Tomonaga, Vol. 104*, Princeton University Press, **2020**.

[2]   L. Palm, *Isis* **1998**, *89*; 'The Fabric of Life: Microscopy in the Seventeenth Century. Marian Fournier'.

[3]   A. R. Parker, V. L. Welch, D. Driver, N. Martini, *Nature* **2003**, *426*, 786-787; 'Opal analogue discovered in a weevil'.

[4]   H. Ghiradella, *Applied optics* **1991**, *30*, 3492-3500; 'Light and color on the wing: structural colors in butterflies and moths'.

[5]   S. Kinoshita, S. Yoshioka, *ChemPhysChem* **2005**, *6*, 1442-1459; 'Structural colors in nature: the role of regularity and irregularity in the structure'.

[6]   S. Kinoshita, S. Yoshioka, J. Miyazaki, *Reports on Progress in Physics* **2008**, *71*, 076401; 'Physics of structural colors'.

[7]   J. P. Vigneron, P. Simonis, *Physica B: Condensed Matter* **2012**, *407*, 4032-4036; 'Natural photonic crystals'.

[8]   R. Dahm, *Developmental biology* **2005**, *278*, 274-288; 'Friedrich Miescher and the discovery of DNA'.

[9]   D. Whitford, *Proteins: structure and function*, John Wiley & Sons, **2013**.

[10]   J. Audouze, S. Vauclair, *An introduction to nuclear astrophysics: the formation and the evolution of matter in the universe, Vol. 18*, Springer Science & Business Media, **2012**.

[11]   P. Clayton, P. Davies, *The re-emergence of emergence: The emergentist hypothesis from science to religion*, OUP Oxford, **2006**.

[12]   R. B. Bourret, A. M. Stock, *Journal of Biological Chemistry* **2002**, *277*, 9625-9628; 'Molecular information processing: lessons from bacterial chemotaxis'.

[13]   S. L. Mintz, A. Perlmutter, *Information processing in biological systems, Vol. 21*, Springer Science & Business Media, **2012**.

[14]   S. Niiranen, A. Ribeiro, *Information Processing and Biological Systems, Vol. 11*, Springer Science & Business Media, **2011**.

[15]   P. Godfrey-Smith, K. Sterelny, **2007**; 'Biological information'.

[16]   L. S. Tsimring, *Reports on Progress in Physics* **2014**, *77*, 026601; 'Noise in biology'.

[17]   S. Ji, *BioSystems* **1999**, *52*, 123-133; 'The cell as the smallest DNA-based molecular computer'.

[18]   Y. Benenson, *Nature Reviews Genetics* **2012**, *13*, 455-468; 'Biomolecular computing systems: principles, progress and potential'.

8   References

[19]   V. Balzani, A. Credi, M. Venturi, *Molecular devices and machines: concepts and perspectives for the nanoworld*, John Wiley & Sons, **2008**.

[20]   N. G. Rambidi, *Computer* **1992**, *25*, 51-54; 'An approach to computational complexity: nondiscrete biomolecular computing'.

[21]   L. Mao, Y. Liu, S. Yang, Y. Li, X. Zhang, Y. Wei, *Dyes and Pigments* **2019**, *162*, 611-623; 'Recent advances and progress of fluorescent bio-/chemosensors based on aggregation-induced emission molecules'.

[22]   A. Salehi-Reyhani, O. Ces, Y. Elani, *Experimental Biology and Medicine* **2017**, *242*, 1309-1317; 'Artificial cell mimics as simplified models for the study of cell biology'.

[23]   N. Linn, J. Vining, P. A. Feeley, *Journal of Applied Social Psychology* **1994**, *24*, 1550-1572; 'Toward a Sustainable Society: Waste Minimization Through Environmentally Conscious Consuming 1'.

[24]   D. Myers, *Surfaces, interfaces, and colloids, Vol. 415*, Wiley New York, **1999**.

[25]   T. Cosgrove, *Colloid science: principles, methods and applications*, John Wiley & Sons, **2010**.

[26]   H.-J. Butt, K. Graf, M. Kappl, *Physics and chemistry of interfaces*, John Wiley & Sons, **2013**.

[27]   F. Leal-Calderon, V. Schmitt, J. Bibette, *Emulsion science: basic principles*, Springer Science & Business Media, **2007**.

[28]   H.-D. Dörfler, *Grenzflächen und kolloid-disperse Systeme: Physik und Chemie*, Springer, **2002**.

[29]   B. A. Khan, N. Akhtar, H. M. S. Khan, K. Waseem, T. Mahmood, A. Rasul, M. Iqbal, H. Khan, *African journal of pharmacy and pharmacology* **2011**, *5*, 2715-2725; 'Basics of pharmaceutical emulsions: A review'.

[30]   F. Goodarzi, S. Zendehboudi, *The Canadian Journal of Chemical Engineering* **2019**, *97*, 281-309; 'A comprehensive review on emulsions and emulsion stability in chemical and energy industries'.

[31]   T. F. Tadros, *Colloids in Cosmetics and Personal Care: Colloids and Interface Science* **2008**, *4*, 1-34; 'Colloid aspects of cosmetic formulations with particular reference to polymeric surfactants'.

[32]   P. Mulqueen, *Advances in colloid and interface science* **2003**, *106*, 83-107; 'Recent advances in agrochemical formulation'.

[33]   A. K. Barkat, A. Naveed, M. S. K. Haji, W. Khalid, M. Tariq, R. Akhtar, I. Muhammad, K. Haroon, *African Journal of Pharmacy and Pharmacology* **2011**, *5*, 2715-2725; 'Basics of pharmaceutical emulsions: A review'.

[34]   M. J. Rosen, J. T. Kunjappu, *Surfactants and interfacial phenomena*, John Wiley & Sons, **2012**.

[35]   H. Wennerstro, O. So, U. Olsson, B. Lindman, *Colloids and Surfaces A: Physicochemical and Engineering Aspects* **1997**, *123*, 13-26; 'Macroemulsions versus microemulsions'.

8   References

[36]   D. J. McClements, *Soft matter* **2012**, *8*, 1719-1729; 'Nanoemulsions versus microemulsions: terminology, differences, and similarities'.

[37]   K. J. Lissant, *Colloids and surfaces* **1988**, *29*, 1-5; 'Emulsification and demulsification—an historical overview'.

[38]   S. Hartland, *Surface and interfacial tension: measurement, theory, and applications*, CRC Press, **2004**.

[39]   T. F. Tadros, *Emulsion science and technology* **2009**, *1*, 1-55; 'Emulsion science and technology: a general introduction'.

[40]   E. Ruckenstein, *Langmuir* **1996**, *12*, 6351-6353; 'Microemulsions, macroemulsions, and the Bancroft rule'.

[41]   R. P. Borwankar, L. A. Lobo, D. T. Wasan, *Colloids and surfaces* **1992**, *69*, 135-146; 'Emulsion stability—kinetics of flocculation and coalescence'.

[42]   M. M. Robins, *Current opinion in colloid & interface science* **2000**, *5*, 265-272; 'Emulsions—creaming phenomena'.

[43]   R. Chanamai, D. J. McClements, *Journal of agricultural and food chemistry* **2000**, *48*, 5561-5565; 'Impact of weighting agents and sucrose on gravitational separation of beverage emulsions'.

[44]   P. Taylor, *Advances in colloid and interface science* **1998**, *75*, 107-163; 'Ostwald ripening in emulsions'.

[45]   T. F. Tadros, *Applied surfactants: principles and applications*, John Wiley & Sons, **2006**.

[46]   N. M. van Os, J. R. Haak, L. A. M. Rupert, *Physico-chemical properties of selected anionic, cationic and nonionic surfactants*, Elsevier, **2012**.

[47]   D. Rubingh, *Cationic surfactants: physical chemistry, Vol. 37*, CRC Press, **1990**.

[48]   W. D. Bancroft, *The Journal of Physical Chemistry* **2002**, *17*, 501-519; 'The theory of emulsification, V'.

[49]   W. D. Bancroft, *The Journal of Physical Chemistry* **2002**, *19*, 275-309; 'The theory of emulsification, VI'.

[50]   K. Golemanov, S. Tcholakova, P. Kralchevsky, K. Ananthapadmanabhan, A. Lips, *Langmuir* **2006**, *22*, 4968-4977; 'Latex-particle-stabilized emulsions of anti-Bancroft type'.

[51]   L. Besnard, M. Protat, F. Malloggi, J. Daillant, F. Cousin, N. Pantoustier, P. Guenoun, P. Perrin, *Soft Matter* **2014**, *10*, 7073-7087; 'Breaking of the Bancroft rule for multiple emulsions stabilized by a single stimulable polymer'.

[52]   W. C. Griffin, *J. Soc. Cosmet. Chem.* **1949**, *1*, 311-326; 'Classification of surface-active agents by" HLB"'.

8   References

[53]   R. C. Pasquali, N. Sacco, C. Bregni, *Lat Am J Pharm* **2009**, *28*, 313-317; 'The studies on hydrophilic-lipophilic balance (HLB): Sixty years after William C. Griffin's pioneer work (1949-2009)'.

[54]   R. Miller, E. Aksenenko, V. Fainerman, *Advances in colloid and interface science* **2017**, *247*, 115-129; 'Dynamic interfacial tension of surfactant solutions'.

[55]   R. M. Pashley, M. E. Karaman, *Applied colloid and surface chemistry*, Wiley Online Library, **2004**.

[56]   D. Otzen, *Biochimica et Biophysica Acta (BBA)-Proteins and Proteomics* **2011**, *1814*, 562-591; 'Protein–surfactant interactions: a tale of many states'.

[57]   D. W. Wong, W. M. Camirand, A. E. Pavlath, N. Parris, M. Friedman, *Critical Reviews in Food Science & Nutrition* **1996**, *36*, 807-844; 'Structures and functionalities of milk proteins'.

[58]   S. Friberg, K. Larsson, J. Sjoblom, *Food emulsions*, CRC Press, **2003**.

[59]   T. Tadros, *Advances in Colloid and Interface Science* **2009**, *147*, 281-299; 'Polymeric surfactants in disperse systems'.

[60]   Y. Chevalier, M.-A. Bolzinger, *Colloids and Surfaces A: Physicochemical and Engineering Aspects* **2013**, *439*, 23-34; 'Emulsions stabilized with solid nanoparticles: Pickering emulsions'.

[61]   L. L. Schramm, *Emulsions, foams, and suspensions: fundamentals and applications*, John Wiley & Sons, **2006**.

[62]   D. G. Ortiz, C. Pochat-Bohatier, J. Cambedouzou, M. Bechelany, P. Miele, *Engineering* **2020**, *6*, 468-482; 'Current trends in Pickering emulsions: Particle morphology and applications'.

[63]   C. Albert, M. Beladjine, N. Tsapis, E. Fattal, F. Agnely, N. Huang, *Journal of Controlled Release* **2019**, *309*, 302-332; 'Pickering emulsions: Preparation processes, key parameters governing their properties and potential for pharmaceutical applications'.

[64]   J. Zhou, X. Qiao, B. P. Binks, K. Sun, M. Bai, Y. Li, Y. Liu, *Langmuir* **2011**, *27*, 3308-3316; 'Magnetic Pickering emulsions stabilized by Fe3O4 nanoparticles'.

[65]   C. Casagrande, P. Fabre, E. Raphael, M. Veyssié, *EPL (Europhysics Letters)* **1989**, *9*, 251; '"Janus beads": realization and behaviour at water/oil interfaces'.

[66]   A. Walther, A. H. Muller, *Chemical reviews* **2013**, *113*, 5194-5261; 'Janus particles: synthesis, self-assembly, physical properties, and applications'.

[67]   J. Wu, G. H. Ma, *Small* **2016**, *12*, 4633-4648; 'Recent studies of Pickering emulsions: particles make the difference'.

[68]   M. Rayner, P. Dejmek, *Engineering aspects of food emulsification and homogenization*, CRC Press, **2015**.

[69]   T. F. Tadros, *Emulsion formation and stability* **2013**, *1*, 1-75; 'Emulsion formation, stability, and rheology'.

8 References

[70]   K. Köhler, I. H. P. Schuchmann, *Emulgiertechnik: Grundlagen, Verfahren und Anwendungen*, Behr's Verlag DE, **2012**.

[71]   Y.-F. Maa, C. Hsu, *Journal of Controlled Release* **1996**, *38*, 219-228; 'Liquid-liquid emulsification by rotor/stator homogenization'.

[72]   T. Leong, T. Wooster, S. Kentish, M. Ashokkumar, *Ultrasonics sonochemistry* **2009**, *16*, 721-727; 'Minimising oil droplet size using ultrasonic emulsification'.

[73]   M. Ashokkumar, *Ultrasonics sonochemistry* **2011**, *18*, 864-872; 'The characterization of acoustic cavitation bubbles–an overview'.

[74]   S. M. M. Modarres-Gheisari, R. Gavagsaz-Ghoachani, M. Malaki, P. Safarpour, M. Zandi, *Ultrasonics Sonochemistry* **2019**, *52*, 88-105; 'Ultrasonic nano-emulsification–A review'.

[75]   S. G. Gaikwad, A. B. Pandit, *Ultrasonics sonochemistry* **2008**, *15*, 554-563; 'Ultrasound emulsification: effect of ultrasonic and physicochemical properties on dispersed phase volume and droplet size'.

[76]   G. Vladisavljević, I. Kobayashi, M. Nakajima, *Microfluidics and nanofluidics* **2012**, *13*, 151-178; 'Production of uniform droplets using membrane, microchannel and microfluidic emulsification devices'.

[77]   C. Charcosset, I. Limayem, H. Fessi, *Journal of Chemical Technology & Biotechnology: International Research in Process, Environmental & Clean Technology* **2004**, *79*, 209-218; 'The membrane emulsification process—a review'.

[78]   T. Nakashima, M. Shimizu, M. Kukizaki, *Advanced drug delivery reviews* **2000**, *45*, 47-56; 'Particle control of emulsion by membrane emulsification and its applications'.

[79]   A. A. Maan, A. Nazir, M. K. I. Khan, R. Boom, K. Schroën, *Journal of Food Engineering* **2015**, *147*, 1-7; 'Microfluidic emulsification in food processing'.

[80]   K. Ren, J. Zhou, H. Wu, *Accounts of chemical research* **2013**, *46*, 2396-2406; 'Materials for microfluidic chip fabrication'.

[81]   P. Zhu, L. Wang, *Lab on a Chip* **2017**, *17*, 34-75; 'Passive and active droplet generation with microfluidics: a review'.

[82]   K. S. Elvira, R. C. Wootton, A. J. deMello, *Nature chemistry* **2013**, *5*, 905-915; 'The past, present and potential for microfluidic reactor technology in chemical synthesis'.

[83]   G. T. Vladisavljević, R. Al Nuumani, S. A. Nabavi, *Micromachines* **2017**, *8*, 75; 'Microfluidic production of multiple emulsions'.

[84]   A. Yaqoob Khan, S. Talegaonkar, Z. Iqbal, F. Jalees Ahmed, R. Krishan Khar, *Current drug delivery* **2006**, *3*, 429-443; 'Multiple emulsions: an overview'.

[85]   N. Singh, *Asian Journal of Pharmaceutics (AJP)* **2021**, *15*; 'Technology, Recent Advancement, and Application of Multiple Emulsions: An Overview'.

8   References

[86]   L. Y. Chu, A. S. Utada, R. K. Shah, J. W. Kim, D. A. Weitz, *Angewandte Chemie* **2007**, *119*, 9128-9132; 'Controllable monodisperse multiple emulsions'.

[87]   W. Seifriz, *J. phys. Chem.* **1925**, *29*, 738-749; 'Studies in emulsions'.

[88]   S. Ding, C. A. Serra, T. F. Vandamme, W. Yu, N. Anton, *Journal of controlled release* **2019**, *295*, 31-49; 'Double emulsions prepared by two–step emulsification: History, state-of-the-art and perspective'.

[89]   N. Pannacci, H. Bruus, D. Bartolo, I. Etchart, T. Lockhart, Y. Hennequin, H. Willaime, P. Tabeling, *Physical review letters* **2008**, *101*, 164502; 'Equilibrium and nonequilibrium states in microfluidic double emulsions'.

[90]   I. Kovach, S. Friberg, J. Koetz, *Journal of Dispersion Science and Technology* **2017**, *38*, 594-597; 'A "perfect Janus emulsion": thermodynamic factors'.

[91]   J. Guzowski, P. M. Korczyk, S. Jakiela, P. Garstecki, *Soft Matter* **2012**, *8*, 7269-7278; 'The structure and stability of multiple micro-droplets'.

[92]   H. Hasinovic, S. Friberg, I. Kovach, J. Koetz, *Journal of dispersion science and technology* **2013**, *34*, 1683-1689; 'Janus emulsion drops: equilibrium calculations'.

[93]   S. E. Friberg, I. Kovach, J. Koetz, *ChemPhysChem* **2013**, *14*, 3772-3776; 'Equilibrium topology and partial inversion of Janus drops: a numerical analysis'.

[94]   R. V. Balaj, L. D. Zarzar, *Chemical Physics Reviews* **2020**, *1*, 011301; 'Reconfigurable complex emulsions: Design, properties, and applications'.

[95]   L. D. Zarzar, V. Sresht, E. M. Sletten, J. A. Kalow, D. Blankschtein, T. M. Swager, *Nature* **2015**, *518*, 520-524; 'Dynamically reconfigurable complex emulsions via tunable interfacial tensions'.

[96]   J. H. Simons, *Fluorine Chemistry V2, Vol. 2*, Elsevier, **2012**.

[97]   E. P. Wesseler, R. Iltis, L. C. Clark Jr, *Journal of Fluorine Chemistry* **1977**, *9*, 137-146; 'The solubility of oxygen in highly fluorinated liquids'.

[98]   H. Hasinovic, S. E. Friberg, G. Rong, *Journal of colloid and interface science* **2011**, *354*, 424-426; 'A one-step process to a Janus emulsion'.

[99]   H. Hasinovic, S. E. Friberg, *Langmuir* **2011**, *27*, 6584-6588; 'One-step inversion process to a Janus emulsion with two mutually insoluble oils'.

[100]   L. Ge, S. Lu, R. Guo, *Journal of colloid and interface science* **2014**, *423*, 108-112; 'Janus emulsions formed with a polymerizable monomer, silicone oil, and Tween 80 aqueous solution'.

[101]   M. Sindoro, S. Granick, *Angewandte Chemie International Edition* **2018**, *57*, 16773-16776; 'Ionic Janus liquid droplets assembled and propelled by electric field'.

[102]   A. Concellón, C. A. Zentner, T. M. Swager, *Journal of the American Chemical Society* **2019**, *141*, 18246-18255; 'Dynamic complex liquid crystal emulsions'.

8 References

[103] A. Concellón, D. Fong, T. M. Swager, *Journal of the American Chemical Society* **2021**, *143*, 9177-9182; 'Complex liquid crystal emulsions for biosensing'.

[104] S. Nagelberg, L. D. Zarzar, N. Nicolas, K. Subramanian, J. A. Kalow, V. Sresht, D. Blankschtein, G. Barbastathis, M. Kreysing, T. M. Swager, *Nature communications* **2017**, *8*, 1-9; 'Reconfigurable and responsive droplet-based compound micro-lenses'.

[105] L. Zeininger, E. Weyandt, S. Savagatrup, K. S. Harvey, Q. Zhang, Y. Zhao, T. M. Swager, *Lab on a Chip* **2019**, *19*, 1327-1331; 'Waveguide-based chemo-and biosensors: complex emulsions for the detection of caffeine and proteins'.

[106] S. Savagatrup, D. Ma, H. Zhong, K. S. Harvey, L. C. Kimerling, A. M. Agarwal, T. M. Swager, *ACS sensors* **2020**, *5*, 1996-2002; 'Dynamic complex emulsions as amplifiers for on-chip photonic cavity-enhanced resonators'.

[107] R. V. Balaj, S. W. Cho, P. Singh, L. D. Zarzar, *Polymer Chemistry* **2020**, *11*, 281-286; 'Polyelectrolyte hydrogel capsules as stabilizers for reconfigurable complex emulsions'.

[108] B. D. Frank, M. Antonietti, L. Zeininger, *Macromolecules* **2020**, *54*, 981-987; 'Structurally anisotropic Janus particles with tunable amphiphilicity via polymerization of dynamic complex emulsions'.

[109] B. D. Frank, M. Perovic, S. Djalali, M. Antonietti, M. Oschatz, L. Zeininger, *ACS Applied Materials & Interfaces* **2021**, *13*, 32510-32519; 'Synthesis of Polymer Janus Particles with Tunable Wettability Profiles as Potent Solid Surfactants to Promote Gas Delivery in Aqueous Reaction Media'.

[110] C. A. Zentner, A. Concellón, T. M. Swager, *ACS central science* **2020**, *6*, 1460-1466; 'Controlled movement of complex double emulsions via interfacially confined magnetic nanoparticles'.

[111] B. D. Frank, S. Djalali, A. W. Baryzewska, P. Giusto, P. H. Seeberger, L. Zeininger, *Nature communications* **2022**, *13*, 1-12; 'Reversible morphology-resolved chemotactic actuation and motion of Janus emulsion droplets'.

[112] C. H. Meredith, A. C. Castonguay, Y.-J. Chiu, A. M. Brooks, P. G. Moerman, P. Torab, P. K. Wong, A. Sen, D. Velegol, L. D. Zarzar, *Matter* **2022**, *5*, 616-633; 'Chemical design of self-propelled Janus droplets'.

[113] L. Zeininger, S. Nagelberg, K. S. Harvey, S. Savagatrup, M. B. Herbert, K. Yoshinaga, J. A. Capobianco, M. Kolle, T. M. Swager, *ACS central science* **2019**, *5*, 789-795; 'Rapid detection of Salmonella enterica via directional emission from carbohydrate-functionalized dynamic double emulsions'.

[114] C.-J. Lin, L. Zeininger, S. Savagatrup, T. M. Swager, *Journal of the American Chemical Society* **2019**, *141*, 3802-3806; 'Morphology-dependent luminescence in complex liquid colloids'.

[115] Q. Zhang, L. Zeininger, K.-J. Sung, E. A. Miller, K. Yoshinaga, H. D. Sikes, T. M. Swager, *ACS sensors* **2019**, *4*, 180-184; 'Emulsion agglutination assay for the detection of protein–protein interactions: an optical sensor for zika virus'.

8   References

[116] V. Trinh, C. S. Malloy, T. J. Durkin, A. Gadh, S. Savagatrup, *ACS sensors* **2022**, *7*, 1514-1523; 'Detection of PFAS and Fluorinated Surfactants Using Differential Behaviors at Interfaces of Complex Droplets'.

[117] M. Pavlovic, M. Antonietti, B. V. Schmidt, L. Zeininger, *Journal of colloid and interface science* **2020**, *575*, 88-95; 'Responsive Janus and Cerberus emulsions via temperature-induced phase separation in aqueous polymer mixtures'.

[118] S. Matsumoto, Y. Kita, D. Yonezawa, *Journal of Colloid and Interface Science* **1976**, *57*, 353-361; 'An attempt at preparing water-in-oil-in-water multiple-phase emulsions'.

[119] G. M. Whitesides, *nature* **2006**, *442*, 368-373; 'The origins and the future of microfluidics'.

[120] K. Raj M, S. Chakraborty, *Journal of Applied Polymer Science* **2020**, *137*, 48958; 'PDMS microfluidics: A mini review'.

[121] J. Zhou, A. V. Ellis, N. H. Voelcker, *Electrophoresis* **2010**, *31*, 2-16; 'Recent developments in PDMS surface modification for microfluidic devices'.

[122] S. Okushima, T. Nisisako, T. Torii, T. Higuchi, *Langmuir* **2004**, *20*, 9905-9908; 'Controlled production of monodisperse double emulsions by two-step droplet breakup in microfluidic devices'.

[123] A. S. Utada, E. Lorenceau, D. R. Link, P. D. Kaplan, H. A. Stone, D. Weitz, *Science* **2005**, *308*, 537-541; 'Monodisperse double emulsions generated from a microcapillary device'.

[124] R. K. Shah, H. C. Shum, A. C. Rowat, D. Lee, J. J. Agresti, A. S. Utada, L.-Y. Chu, J.-W. Kim, A. Fernandez-Nieves, C. J. Martinez, *Materials Today* **2008**, *11*, 18-27; 'Designer emulsions using microfluidics'.

[125] A. Abate, D. Weitz, *Small* **2009**, *5*, 2030-2032; 'High-order multiple emulsions formed in poly (dimethylsiloxane) microfluidics'.

[126] R. Alex, R. Bodmeier, *Journal of microencapsulation* **1990**, *7*, 347-355; 'Encapsulation of water-soluble drugs by a modified solvent evaporation method. I. Effect of process and formulation variables on drug entrapment'.

[127] L. R. Beck, D. R. Cowsar, D. H. Lewis, R. J. Cosgrove Jr, C. T. Riddle, S. L. Lowry, T. Epperly, *Fertility and sterility* **1979**, *31*, 545-551; 'A new long-acting injectable microcapsule system for the administration of progesterone'.

[128] P. Couvreur, M. J. Blanco-Prieto, F. Puisieux, B. Roques, E. Fattal, *Advanced drug delivery reviews* **1997**, *28*, 85-96; 'Multiple emulsion technology for the design of microspheres containing peptides and oligopeptides'.

[129] C. X. Zhao, A. P. Middelberg, *Angewandte Chemie International Edition* **2009**, *48*, 7208-7211; 'Microfluidic Mass-Transfer Control for the Simple Formation of Complex Multiple Emulsions'.

[130] C. H. Choi, D. A. Weitz, C. S. Lee, *Advanced materials* **2013**, *25*, 2536-2541; 'One step formation of controllable complex emulsions: from functional particles to simultaneous encapsulation of hydrophilic and hydrophobic agents into desired position'.

8 References

[131]   M. F. Haase, J. Brujic, *Angewandte Chemie* **2014**, *126*, 11987-11991; 'Tailoring of high-order multiple emulsions by the liquid–liquid phase separation of ternary mixtures'.

[132]   Q. Zhang, M. Xu, X. Liu, W. Zhao, C. Zong, Y. Yu, Q. Wang, H. Gai, *Chemical Communications* **2016**, *52*, 5015-5018; 'Fabrication of Janus droplets by evaporation driven liquid–liquid phase separation'.

[133]   D. G. Aarts, M. Schmidt, H. N. Lekkerkerker, *Science* **2004**, *304*, 847-850; 'Direct visual observation of thermal capillary waves'.

[134]   P. Brocos, Á. Piñeiro, R. Bravo, A. Amigo, *Physical Chemistry Chemical Physics* **2003**, *5*, 550-557; 'Refractive indices, molar volumes and molar refractions of binary liquid mixtures: concepts and correlations'.

[135]   J. A. Riddick, W. B. Bunger, T. K. Sakano, **1986**; 'Organic solvents: physical properties and methods of purification'.

[136]   A. Grosse, G. Cady, *Industrial & Engineering Chemistry* **1947**, *39*, 367-374; 'Properties of fluorocarbons'.

[137]   K. K. Sharma, *Optics: principles and applications*, Elsevier, **2006**.

[138]   L. D. Zarzar, J. A. Kalow, X. He, J. J. Walish, T. M. Swager, *Proceedings of the National Academy of Sciences* **2017**, *114*, 3821-3825; 'Optical visualization and quantification of enzyme activity using dynamic droplet lenses'.

[139]   S. Nagelberg, *Dynamic and Stimuli-Responsive Multi-Phase Emulsion Droplets for Optical Components*, Springer Nature, **2020**.

[140]   D. Fong, T. M. Swager, *Journal of the American Chemical Society* **2021**, *143*, 4397-4404; 'Trace Detection of Hydrogen Peroxide via Dynamic Double Emulsions'.

[141]   P. A. M. Dirac, *Proceedings of the Royal Society of London. Series A, Containing Papers of a Mathematical and Physical Character* **1927**, *114*, 243-265; 'The quantum theory of the emission and absorption of radiation'.

[142]   M. Katz, *Introduction to geometrical optics*, World scientific, **2002**.

[143]   P. G. Hewitt, *The Science Teacher* **2019**, *87*, 14-16; 'The Physics of Rainbows'.

[144]   A. E. Goodling, S. Nagelberg, B. Kaehr, C. H. Meredith, S. I. Cheon, A. P. Saunders, M. Kolle, L. D. Zarzar, *Nature* **2019**, *566*, 523-527; 'Colouration by total internal reflection and interference at microscale concave interfaces'.

[145]   A. E. Goodling, S. Nagelberg, M. Kolle, L. D. Zarzar, *ACS Materials Letters* **2020**, *2*, 754-763; 'Tunable and responsive structural color from polymeric microstructured surfaces enabled by interference of totally internally reflected light'.

[146]   P. Brown, C. P. Butts, J. Eastoe, *Soft Matter* **2013**, *9*, 2365-2374; 'Stimuli-responsive surfactants'.

8 References

[147] S. Shinkai, K. Matsuo, A. Harada, O. Manabe, *Journal of the Chemical Society, Perkin Transactions 2* **1982**, 1261-1265; 'Photocontrol of micellar catalyses'.

[148] K. Jia, X. Zhang, L. Zhang, L. Yu, Y. Wu, L. Li, Y. Mai, B. Liao, *Langmuir* **2018**, *34*, 11544-11552; 'Photoinduced reconfiguration of complex emulsions using a photoresponsive surfactant'.

[149] Y. Liu, P. G. Jessop, M. Cunningham, C. A. Eckert, C. L. Liotta, *Science* **2006**, *313*, 958-960; 'Switchable surfactants'.

[150] X. Li, Y. Yang, J. Eastoe, J. Dong, *ChemPhysChem* **2010**, *11*, 3074-3077; 'Rich Self-Assembly Behavior from a Simple Amphiphile'.

[151] A. Tehrani-Bagha, K. Holmberg, *Current opinion in colloid & interface science* **2007**, *12*, 81-91; 'Cleavable surfactants'.

[152] Y. Lu, D. Sun, J. Ralston, Q. Liu, Z. Xu, *Journal of colloid and interface science* **2019**, *557*, 185-195; 'CO2-responsive surfactants with tunable switching pH'.

[153] P. Siffert, E. Krimmel, *Silicon: evolution and future of a technology*, Springer Science & Business Media, **2013**.

[154] G. E. Moore, McGraw-Hill New York, **1965**.

[155] J. E. Whitesitt, *Boolean algebra and its applications*, Courier Corporation, **2012**.

[156] R. L. Goodstein, *Boolean algebra*, Courier Corporation, **2007**.

[157] M. Ben-Ari, *Mathematical logic for computer science*, Springer Science & Business Media, **2012**.

[158] P. A. de Silva, N. H. Gunaratne, C. P. McCoy, *Nature* **1993**, *364*, 42-44; 'A molecular photoionic AND gate based on fluorescent signalling'.

[159] J. Huang, J.-H. Su, H. Tian, *Journal of Materials Chemistry* **2012**, *22*, 10977-10989; 'The development of anthracene derivatives for organic light-emitting diodes'.

[160] S. Erbas-Cakmak, S. Kolemen, A. C. Sedgwick, T. Gunnlaugsson, T. D. James, J. Yoon, E. U. Akkaya, *Chemical Society Reviews* **2018**, *47*, 2228-2248; 'Molecular logic gates: the past, present and future'.

[161] D. S. Goodsell, *Bionanotechnology: lessons from nature*, John Wiley & Sons, **2004**.

[162] R. A. L. Jones, *Soft machines: nanotechnology and life*, Oxford University Press, **2004**.

[163] R. M. Erb, J. S. Sander, R. Grisch, A. R. Studart, *Nature communications* **2013**, *4*, 1-8; 'Self-shaping composites with programmable bioinspired microstructures'.

[164] A. R. Studart, *Angewandte Chemie International Edition* **2015**, *54*, 3400-3416; 'Biologically inspired dynamic material systems'.

[165] D. Wei, L. Ge, S. Lu, J. Li, R. Guo, *Langmuir* **2017**, *33*, 5819-5828; 'Janus particles templated by Janus emulsions and application as a pickering emulsifier'.

8   References

[166]   S. I. Cheon, L. Batista Capaverde Silva, R. Ditzler, L. D. Zarzar, *Langmuir* **2020**, *36*, 7083-7090; 'Particle stabilization of oil–fluorocarbon interfaces and effects on multiphase oil-in-water complex emulsion morphology and reconfigurability'.

[167]   B. McClain, M. Yoon, J. Litster, S. Mochrie, *The European Physical Journal B-Condensed Matter and Complex Systems* **1999**, *10*, 45-52; 'Interfacial roughness in a near-critical binary fluid mixture: X-ray reflectivity and near-specular diffuse scattering'.

[168]   D. LeGrand, G. Gaines Jr, *Journal of Colloid and Interface science* **1975**, *50*, 272-279; 'Immiscibility and interfacial tension between polymer liquids: dependence on molecular weight'.

[169]   G. M. Whitesides, *Angewandte Chemie International Edition* **2018**, *57*, 4258-4273; 'Soft robotics'.

[170]   M. C. Puerto, *Chemical Engineering Journal* **2001**, *1*, 63; 'Surfactants: Fundamentals and Applications in the Petroleum Industry-Cambridge University Press, 2000, pp. 621,@ $85.00 (US $140.00)(hardback), ISBN 0-521-64067-9'.

[171]   P. Raffa, D. A. Wever, F. Picchioni, A. A. Broekhuis, *Chem Rev* **2015**, *115*, 8504-8563; 'Polymeric Surfactants: Synthesis, Properties, and Links to Applications'.

[172]   E. Kissa, *Fluorinated surfactants and repellents, Vol. 97*, CRC Press, **2001**.

[173]   L. Zeininger, L. M. Stiegler, L. Portilla, M. Halik, A. Hirsch, *ChemistryOpen* **2018**, *7*, 282-287; 'Manufacturing Nanoparticles with Orthogonally Adjustable Dispersibility in Hydrocarbons, Fluorocarbons, and Water'.

[174]   X. Y. Hua, M. J. Rosen, *Journal of Colloid and Interface Science* **1988**, *124*, 652-659; 'Dynamic surface tension of aqueous surfactant solutions: I. Basic paremeters'.

[175]   A. Fluksman, O. Benny, *Analytical Methods* **2019**, *11*, 3810-3818; 'A robust method for critical micelle concentration determination using coumarin-6 as a fluorescent probe'.

[176]   S. Wu, F. Liang, D. Hu, H. Li, W. Yang, Q. Zhu, *Analytical chemistry* **2019**, *92*, 4259-4265; 'Determining the critical micelle concentration of surfactants by a simple and fast titration method'.

[177]   S. Deodhar, P. Rohilla, M. Manivannan, S. P. Thampi, M. G. Basavaraj, *Langmuir* **2020**, *36*, 8100-8110; 'Robust Method to Determine Critical Micelle Concentration via Spreading Oil Drops on Surfactant Solutions'.

[178]   G. Ren, L. Wang, Q. Chen, Z. Xu, J. Xu, D. Sun, *Langmuir* **2017**, *33*, 3040-3046; 'pH switchable emulsions based on dynamic covalent surfactants'.

[179]   M. Pavlovic, A. Plucinski, L. Zeininger, B. V. Schmidt, *Chemical Communications* **2020**, *56*, 6814-6817; 'Temperature sensitive water-in-water emulsions'.

[180]   S. Djalali, B. D. Frank, L. Zeininger, *Soft Matter* **2020**, *16*, 10419-10424; 'Responsive drop method: Quantitative in situ determination of surfactant effectiveness using reconfigurable Janus emulsions'.

8 References

[181]   P. Mukerjee, K. J. Mysels, National Standard reference data system, **1971**.

[182]   S. Maaref, S. Ayatollahi, *Journal of Dispersion Science and Technology* **2018**, *39*, 721-733; 'The effect of brine salinity on water-in-oil emulsion stability through droplet size distribution analysis: A case study'.

[183]   M. Pavlovic, H. K. Ramiya Ramesh Babu, S. Djalali, M. Vraneš, V. Radonić, L. Zeininger, *Analytical Chemistry* **2021**, *93*, 9390-9396; 'Facile Monitoring of Water Hardness Levels Using Responsive Complex Emulsions'.

[184]   A. Wołowicz, K. Staszak, *Journal of Molecular Liquids* **2020**, *299*, 112170; 'Study of surface properties of aqueous solutions of sodium dodecyl sulfate in the presence of hydrochloric acid and heavy metal ions'.

[185]   K. D. Danov, P. A. Kralchevsky, K. P. Ananthapadmanabhan, *Advances in colloid and interface science* **2014**, *206*, 17-45; 'Micelle–monomer equilibria in solutions of ionic surfactants and in ionic–nonionic mixtures: A generalized phase separation model'.

[186]   B. Naskar, A. Dey, S. P. Moulik, *Journal of Surfactants and Detergents* **2013**, *16*, 785-794; 'Counter-ion effect on micellization of ionic surfactants: A comprehensive understanding with two representatives, sodium dodecyl sulfate (SDS) and dodecyltrimethylammonium bromide (DTAB)'.

[187]   E. Dutkiewicz, A. Jakubowska, *Colloid and Polymer Science* **2002**, *280*, 1009-1014; 'Effect of electrolytes on the physicochemical behaviour of sodium dodecyl sulphate micelles'.

[188]   S. Woolfrey, G. Banzon, M. Groves, *Journal of colloid and interface science* **1986**, *112*, 583-587; 'The effect of sodium chloride on the dynamic surface tension of sodium dodecyl sulfate solutions'.

[189]   E. Weißenborn, B. Braunschweig, *Molecules* **2019**, *24*, 2911; 'Specific ion effects of dodecyl sulfate surfactants with alkali ions at the air–water interface'.

[190]   V. Fainerman, E. Lucassen-Reynders, *Advances in colloid and interface science* **2002**, *96*, 295-323; 'Adsorption of single and mixed ionic surfactants at fluid interfaces'.

[191]   V. Kolev, K. Danov, P. Kralchevsky, G. Broze, A. Mehreteab, *Langmuir* **2002**, *18*, 9106-9109; 'Comparison of the van der Waals and Frumkin adsorption isotherms for sodium dodecyl sulfate at various salt concentrations'.

[192]   Z. Zhu, Y. Wen, J. Yi, Y. Cao, F. Liu, D. J. McClements, *Journal of colloid and interface science* **2019**, *536*, 80-87; 'Comparison of natural and synthetic surfactants at forming and stabilizing nanoemulsions: Tea saponin, Quillaja saponin, and Tween 80'.

[193]   M. J. Qazi, R. W. Liefferink, S. J. Schlegel, E. H. Backus, D. Bonn, N. Shahidzadeh, *Langmuir* **2017**, *33*, 4260-4268; 'Influence of surfactants on sodium chloride crystallization in confinement'.

[194]   T. R. Carale, Q. T. Pham, D. Blankschtein, *Langmuir* **1994**, *10*, 109-121; 'Salt effects on intramicellar interactions and micellization of nonionic surfactants in aqueous solutions'.

8 References

[195] N. Nishikido, R. Matuura, *Bulletin of the Chemical Society of Japan* **1977**, *50*, 1690-1694; 'The effect of added inorganic salts on the micelle formation of nonionic surfactants in aqueous solutions'.

[196] W. Jin, L. Chen, M. Hu, D. Sun, A. Li, Y. Li, Z. Hu, S. Zhou, Y. Tu, T. Xia, *Applied Energy* **2016**, *175*, 82-90; 'Tween-80 is effective for enhancing steam-exploded biomass enzymatic saccharification and ethanol production by specifically lessening cellulase absorption with lignin in common reed'.

[197] Y. Suzuki, K. H. Nagai, A. Zinchenko, T. Hamada, *Langmuir* **2017**, *33*, 2671-2676; 'Photoinduced Fusion of Lipid Bilayer Membranes'.

[198] E. Chevallier, A. Mamane, H. A. Stone, C. Tribet, F. Lequeux, C. Monteux, *Soft Matter* **2011**, *7*, 7866-7874; 'Pumping-out photo-surfactants from an air–water interface using light'.

[199] Y. Tu, F. Peng, A. Adawy, Y. Men, L. K. Abdelmohsen, D. A. Wilson, *Chemical reviews* **2016**, *116*, 2023-2078; 'Mimicking the cell: bio-inspired functions of supramolecular assemblies'.

[200] S. Mann, *Accounts of chemical research* **2012**, *45*, 2131-2141; 'Systems of creation: the emergence of life from nonliving matter'.

[201] T. Y.-C. Tsai, Y. S. Choi, W. Ma, J. R. Pomerening, C. Tang, J. E. Ferrell Jr, *Science* **2008**, *321*, 126-129; 'Robust, tunable biological oscillations from interlinked positive and negative feedback loops'.

[202] A. Deutsch, G. Theraulaz, T. Vicsek*, Vol. 2*, The Royal Society, **2012**, pp. 689-692.

[203] G. Ashkenasy, T. M. Hermans, S. Otto, A. F. Taylor, *Chemical Society Reviews* **2017**, *46*, 2543-2554; 'Systems chemistry'.

[204] S. Mann, *Angewandte Chemie International Edition* **2008**, *47*, 5306-5320; 'Life as a nanoscale phenomenon'.

[205] E. Gouaux, R. MacKinnon, *science* **2005**, *310*, 1461-1465; 'Principles of selective ion transport in channels and pumps'.

[206] L. A. Barlow, *Development* **2015**, *142*, 3620-3629; 'Progress and renewal in gustation: new insights into taste bud development'.

[207] A. L. Chang-Graham, J. L. Perry, M. A. Engevik, K. A. Engevik, F. J. Scribano, J. T. Gebert, H. A. Danhof, J. C. Nelson, J. S. Kellen, A. C. Strtak, *Science* **2020**, *370*, eabc3621; 'Rotavirus induces intercellular calcium waves through ADP signaling'.

[208] W. Wickner, R. Schekman, *science* **2005**, *310*, 1452-1456; 'Protein translocation across biological membranes'.

[209] K. Xiao, L. Chen, R. Chen, T. Heil, S. D. C. Lemus, F. Fan, L. Wen, L. Jiang, M. Antonietti, *Nature communications* **2019**, *10*, 1-7; 'Artificial light-driven ion pump for photoelectric energy conversion'.

[210] C. J. Pedersen, *Journal of the American Chemical Society* **1967**, *89*, 7017-7036; 'Cyclic polyethers and their complexes with metal salts'.

8   References

[211]   Z. Sun, M. Barboiu, Y. M. Legrand, E. Petit, A. Rotaru, *Angewandte Chemie* **2015**, *127*, 14681-14685; 'Highly Selective Artificial Cholesteryl Crown Ether K+-Channels'.

[212]   L. Wang, L. Cheng, G. Li, K. Liu, Z. Zhang, P. Li, S. Dong, W. Yu, F. Huang, X. Yan, *Journal of the American Chemical Society* **2020**, *142*, 2051-2058; 'A self-cross-linking supramolecular polymer network enabled by crown-ether-based molecular recognition'.

[213]   X. Ji, J. Li, J. Chen, X. Chi, K. Zhu, X. Yan, M. Zhang, F. Huang, *Macromolecules* **2012**, *45*, 6457-6463; 'Supramolecular micelles constructed by crown ether-based molecular recognition'.

[214]   G. W. Gokel, W. M. Leevy, M. E. Weber, *Chemical reviews* **2004**, *104*, 2723-2750; 'Crown ethers: sensors for ions and molecular scaffolds for materials and biological models'.

[215]   R. Merindol, A. Walther, *Chemical Society Reviews* **2017**, *46*, 5588-5619; 'Materials learning from life: concepts for active, adaptive and autonomous molecular systems'.

[216]   H. Löw, E. Mena-Osteritz, K. M. Mullen, C. M. Jäger, M. von Delius, *ChemPlusChem* **2020**, *85*, 1008-1012; 'Self-assembly, adaptive response, and in, out-stereoisomerism of large orthoformate cryptands'.

[217]   H. W. van Roekel, B. J. Rosier, L. H. Meijer, P. A. Hilbers, A. J. Markvoort, W. T. Huck, T. F. de Greef, *Chemical Society Reviews* **2015**, *44*, 7465-7483; 'Programmable chemical reaction networks: emulating regulatory functions in living cells using a bottom-up approach'.

[218]   F. Soto, E. Karshalev, F. Zhang, B. Esteban Fernandez de Avila, A. Nourhani, J. Wang, *Chemical Reviews* **2021**, *122*, 5365-5403; 'Smart materials for microrobots'.

[219]   M. Cinquini, F. Montanari, P. Tundo, *Journal of the Chemical Society, Chemical Communications* **1975**, 393-394; 'Alkyl substituted aza-macrobicyclic polyethers: highly efficient catalysts in two-phase reactions'.

[220]   F. F. Chou, J. S. Shih, *Journal of the Chinese Chemical Society* **2002**, *49*, 599-605; 'Micellar formation study of crown ether surfactants'.

[221]   V. Rüdiger, H. J. Schneider, V. P. Solov'ev, V. P. Kazachenko, O. A. Raevsky, *European Journal of Organic Chemistry* **1999**, *1999*, 1847-1856; 'Crown ether–ammonium complexes: binding mechanisms and solvent effects'.

[222]   M. Kralj, L. Tušek-Božić, L. Frkanec, *ChemMedChem: Chemistry Enabling Drug Discovery* **2008**, *3*, 1478-1492; 'Biomedical potentials of crown ethers: prospective antitumor agents'.

[223]   H. Tsukube, *Coordination chemistry reviews* **1996**, *148*, 1-17; 'Armed crown ether complexes in supramolecular assembly'.

[224]   S. Djalali, P. Simón Marqués, B. D. Frank, L. Zeininger, *Advanced Functional Materials* **2022**, *32*, 2107688; 'Crown Ether-Functionalized Complex Emulsions as an Artificial Adaptive Material Platform'.

[225]   F. Arnaud-Neu, R. Delgado, S. Chaves, *Pure and Applied Chemistry* **2003**, *75*, 71-102; 'Critical evaluation of stability constants and thermodynamic functions of metal complexes of crown ethers (IUPAC Technical Report)'.

8 References

[226] P. Thordarson, *Chemical Society Reviews* **2011**, *40*, 1305-1323; 'Determining association constants from titration experiments in supramolecular chemistry'.

[227] T. Ooi, K. Maruoka, *Angewandte Chemie International Edition* **2007**, *46*, 4222-4266; 'Recent advances in asymmetric phase-transfer catalysis'.

[228] A. W. Herriott, D. Picker, *Journal of the American chemical Society* **1975**, *97*, 2345-2349; 'Phase transfer catalysis. Evaluation of catalysis'.

[229] K. Maruoka, *Asymmetric phase transfer catalysis*, John Wiley & Sons, **2008**.

[230] X. Yan, R. M. Bain, R. G. Cooks, *Angewandte Chemie International Edition* **2016**, *55*, 12960-12972; 'Organic reactions in microdroplets: Reaction acceleration revealed by mass spectrometry'.

[231] A. Fallah-Araghi, K. Meguellati, J.-C. Baret, A. El Harrak, T. Mangeat, M. Karplus, S. Ladame, C. M. Marques, A. D. Griffiths, *Physical Review Letters* **2014**, *112*, 028301; 'Enhanced chemical synthesis at soft interfaces: A universal reaction-adsorption mechanism in microcompartments'.

[232] A. Meister, *Biochemistry of the amino acids*, Elsevier, **2012**.

[233] T. D. James, K. S. Sandanayake, S. Shinkai, *Angewandte Chemie International Edition in English* **1996**, *35*, 1910-1922; 'Saccharide sensing with molecular receptors based on boronic acid'.

[234] Y. Huang, B.-N. Su, Q. Ye, V. A. Palaniswamy, M. S. Bolgar, T. V. Raglione, *Journal of Pharmaceutical and Biomedical Analysis* **2014**, *88*, 1-6; 'Improving the efficiency of quantitative 1H NMR: An innovative external standard–internal reference approach'.

[235] J.-P. Deschamps, E. Valderrama, L. Terés, *Digital systems: From logic gates to processors*, Springer, **2017**.

[236] G. P. Agrawal, *Fiber-optic communication systems*, John Wiley & Sons, **2012**.

[237] E. G. Rieffel, W. H. Polak, *Quantum computing: A gentle introduction*, MIT Press, **2011**.

[238] D. Kikut-Ligaj, J. Trzcielińska-Lorych, *Cellular and Molecular Biology Letters* **2015**, *20*, 699-716; 'How taste works: cells, receptors and gustatory perception'.

[239] D. Gal, S. C. Wheeler, B. Shiv, *Available at SSRN 1030197* **2007**; 'Cross-modal influences on gustatory perception'.

[240] D. M. Small, *Taste and Smell* **2006**, *63*, 191-220; 'Central gustatory processing in humans'.

[241] M. Kobayashi, M. Takeda, N. Hattori, M. Fukunaga, T. Sasabe, N. Inoue, Y. Nagai, T. Sawada, N. Sadato, Y. Watanabe, *Neuroimage* **2004**, *23*, 1271-1282; 'Functional imaging of gustatory perception and imagery:"top-down" processing of gustatory signals'.

[242] M. Reifarth, M. Bekir, A. M. Bapolisi, E. Titov, F. Nußhardt, J. Nowaczyk, D. Grigoriev, A. Sharma, P. Saalfrank, S. Santer, *Angewandte Chemie International Edition* **2022**, *61*, e202114687; 'A Dual pH-and Light-Responsive Spiropyran-Based Surfactant: Investigations on Its Switching Behavior and Remote Control over Emulsion Stability'.

8 References

[243] H. Sakai, H. Ebana, K. Sakai, K. Tsuchiya, T. Ohkubo, M. Abe, *Journal of colloid and interface science* **2007**, *316*, 1027-1030; 'Photo-isomerization of spiropyran-modified cationic surfactants'.

[244] K. Sakai, Y. Imaizumi, T. Oguchi, H. Sakai, M. Abe, *Langmuir* **2010**, *26*, 9283-9288; 'Adsorption characteristics of spiropyran-modified cationic surfactants at the silica/aqueous solution interface'.

[245] X. Pei, S. Zhang, W. Zhang, P. Liu, B. Song, J. Jiang, Z. Cui, B. P. Binks, *Angewandte Chemie* **2021**, *133*, 5295-5299; 'Behavior of Smart Surfactants in Stabilizing pH-Responsive Emulsions'.

[246] S. Shinkai, O. Manabe, in *Host Guest Complex Chemistry III*, Springer, **1984**, pp. 67-104.

[247] D.-H. Qu, Q.-C. Wang, Q.-W. Zhang, X. Ma, H. Tian, *Chemical reviews* **2015**, *115*, 7543-7588; 'Photoresponsive host–guest functional systems'.

[248] A. D. Becke, *The Journal of chemical physics* **1993**, *98*, 1372-1377; 'A new mixing of Hartree–Fock and local density-functional theories'.

[249] S. Shinkai, K. Torigoe, O. Manabe, T. Kajiyama, *Journal of the American Chemical Society* **1987**, *109*, 4458-4464; 'Temperature regulation of crown-mediated ion transport through polymer/liquid crystal composite membranes. Remarkable transport ability of fluorocarbon-containing crown ethers'.

[250] T. Liu, C. Bao, H. Wang, L. Fei, R. Yang, Y. Long, L. Zhu, *New Journal of Chemistry* **2014**, *38*, 3507-3513; 'Self-assembly of crown ether-based amphiphiles for constructing synthetic ion channels: the relationship between structure and transport activity'.

[251] A. V. Silva, A. López-Sánchez, H. C. Junqueira, L. Rivas, M. S. Baptista, G. Orellana, *Tetrahedron* **2015**, *71*, 457-462; 'Riboflavin derivatives for enhanced photodynamic activity against Leishmania parasites'.

9   Acknowledgement

9   Acknowledgement

Großer Dank gilt außerdem meinen Doktorandenkollegen Bradley DEAN Frank und Agata Baryzewska die mit mir viel Blut und Schweiß verloren haben. Es war eine schöne Zeit mit euch! Auch hier hoffe ich, dass wir in Kontakt bleiben und uns nicht aus den Augen verlieren.

Zu guter Letzt möchte ich mich bei meiner Familie bedanken, die mich zu jeder Zeit voll und ganz unterstützt hat. Der Verlust meines Vaters im zweiten PhD-Jahr hat mir schwer zu schaffen gemacht und ohne sie hätte ich die Doktorarbeit niemals beendet. Diese Arbeit wäre ohne die Liebe von meinem Vater und sein so bedeutsames Lebenswerk niemals zustande gekommen. Du hast mir die Selbstbestimmtheit als dein größtes Geschenk mit auf den Weg gegeben.

Ganz besonders danke ich meinem Bruder (bald Dr.) Surusch Djalali der mir in dieser dunklen Zeit beiseite stand und dank ihm mein Herz nun wieder regelmäßig schlägt. Auch meinen Freunden und Menschen die mir Nahe stehen (Minh-Anh Nguyen, Martin Diekmann, Robin van Esch und Ching-Yi Choi) danke ich für die Unterstützung und dafür, dass sie nie aufgehört haben an mich zu glauben, selbst als ich den Glauben an mich bereits verloren hatte.

10 Appendix

10.1 List of Publications and Achievements

[1] S. Djalali, M. Antonietti, L. Zeininger, 'Concepts for multiresponsive Janus emulsions as droplet-based optical logic gates'. In prepartion (2022).

[2] S. Djalali, M. Antonietti, L. Zeininger 'Jellyfish-inspired motion of Janus emulsions via targeted chemical design of stimuli-responsive snowman-droplets'. In preparation (2022).

[3] M. Pavlovic, H. K. Ramiya Ramesh Babu, S. Djalali, Z. Pavlovic, M. Vraneš, L. Zeininger, *Langmuir* **2022**, 'Dynamic in-situ monitoring of the salt counter-ion effect on surfactant effectiveness using reconfigurable Janus emulsions'. Submitted (2022).

[4] B. D. Frank, S. Djalali, A. W. Baryzewska, P. Giusto, P. H. Seeberger, L. Zeininger, *Nature communications* **2022**, *13*, 1-12; 'Reversible morphology-resolved chemotactic actuation and motion of Janus emulsion droplets'.

[5] S. Djalali, P. Simón Marqués, B. D. Frank, L. Zeininger, *Advanced Functional Materials* **2021**, *32*, 2107688; 'Crown Ether-Functionalized Complex Emulsions as an Artificial Adaptive Material Platform'.

[6] M. Pavlovic, H. K. Ramiya Ramesh Babu, S. Djalali, M. Vraneš, V. Radonić, L. Zeininger, *Analytical Chemistry* **2021**, *93*, 9390-9396; 'Facile Monitoring of Water Hardness Levels Using Responsive Complex Emulsions'.

[7] B. D. Frank, M. Perovic, S. Djalali, M. Antonietti, M. Oschatz, L. Zeininger, *ACS Applied Materials & Interfaces* **2021**, *13*, 32510-32519; 'Synthesis of Polymer Janus Particles with Tunable Wettability Profiles as Potent Solid Surfactants to Promote Gas Delivery in Aqueous Reaction Media'.

[8] S. Djalali, B. D. Frank, L. Zeininger, *Soft Matter* **2020**, *16*, 10419-10424; 'Responsive drop method: Quantitative in situ determination of surfactant effectiveness using reconfigurable Janus emulsions'.

[9] Design of the back cover: Soft Matter Volume 16, Number 46, 14 December 2020, Pages 10389–10576, ISSN 1744-6848.
https://pubs.rsc.org/en/content/articlepdf/2020/sm/d0sm01724h.

10.2   Supporting Information

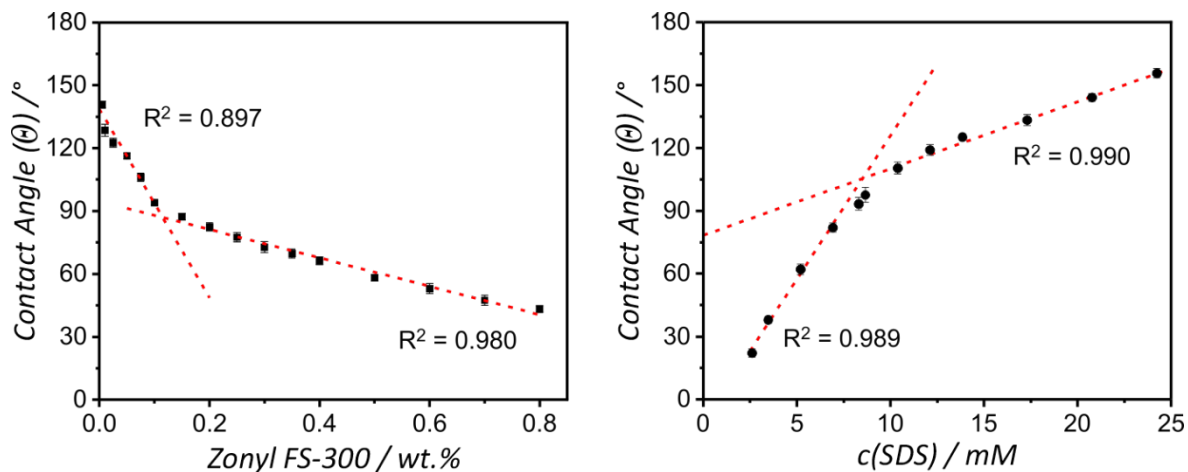### 10.2.1   Additional Graphs for Chapter 5.2

Figure S1. Droplet morphology diagrams measured against different concentrations of Zonyl (left) and SDS (right). The Zonyl and SDS concentrations were kept at a constant concentration of 1.0 wt.%. The CMCs of Zonyl and SDS were determined using the responsive drop method at ≈ 0.115 wt.% and 8.44 ± 0.17 mM, respectively. Contact angle error bars refer to N ≥ 10 measurements.
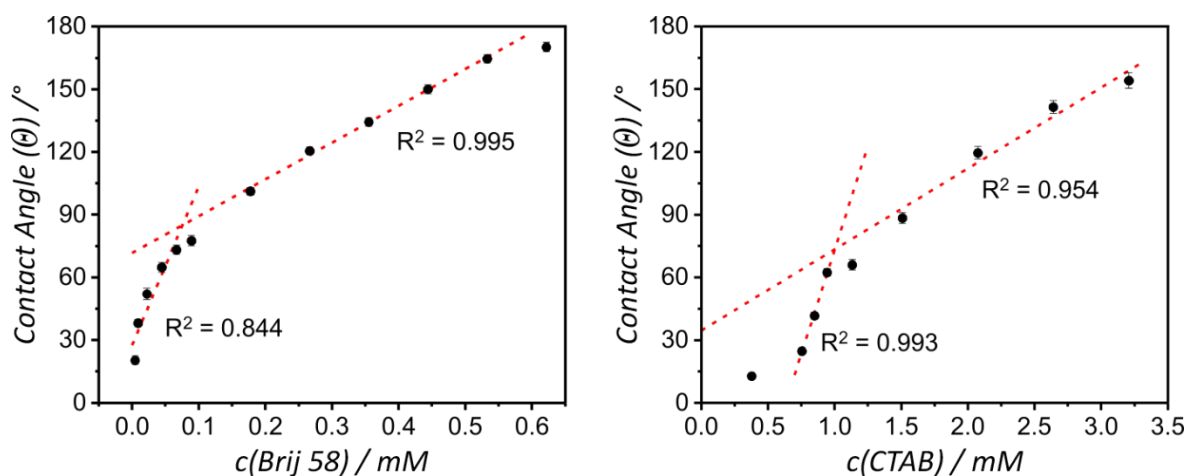

Figure S2. Droplet morphology diagrams measured against different concentrations of Brij 58 (left) and CTAB (right). The Brij and CTAB concentrations were kept at a constant concentration of 0.025 wt.% and 0.25 wt.%. The CMCs of Brij and CTAB were determined using the responsive drop method at 0.076 ± 0.012 mM and 1.00 ± 0.05 mM, respectively. Contact angle error bars refer to N ≥ 10 measurements.
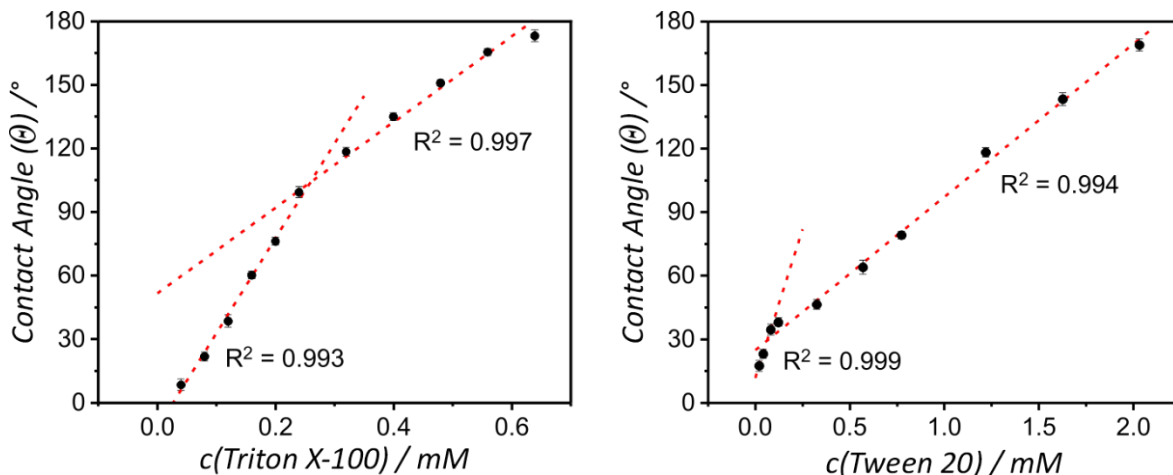
Figure S3. Droplet morphology diagrams measured against different concentrations of Triton X-100 (left) and Tween 20 (right). The Triton and Tween 20 concentrations were kept at a constant concentration of 0.025 wt.% and 0.25 wt.%. The CMCs of Triton and Tween 20 were determined using the responsive drop method at 0.258 ± 0.003 mM and 0.063 ± 0.001 mM, respectively. Contact angle error bars refer to N ≥ 10 measurements.
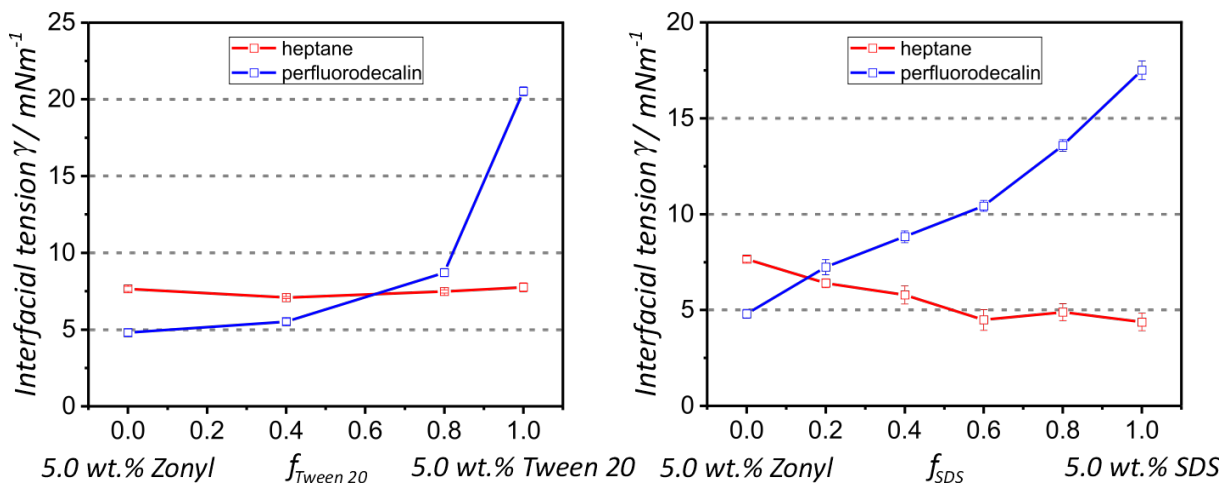

Figure S4. Interfacial tension of the perfluorodecalin-water- and the n-heptane-water interface as a function of the fraction of 5 wt.% Tween 20 ($f_{Tween\ 20}$) and the fraction of 5.0 wt.% SDS (f_{SDS}), where the other fraction is 5.0 wt.% Zonyl FS-300. Interfacial tension error bars refer to N ≥ 5 measurements.
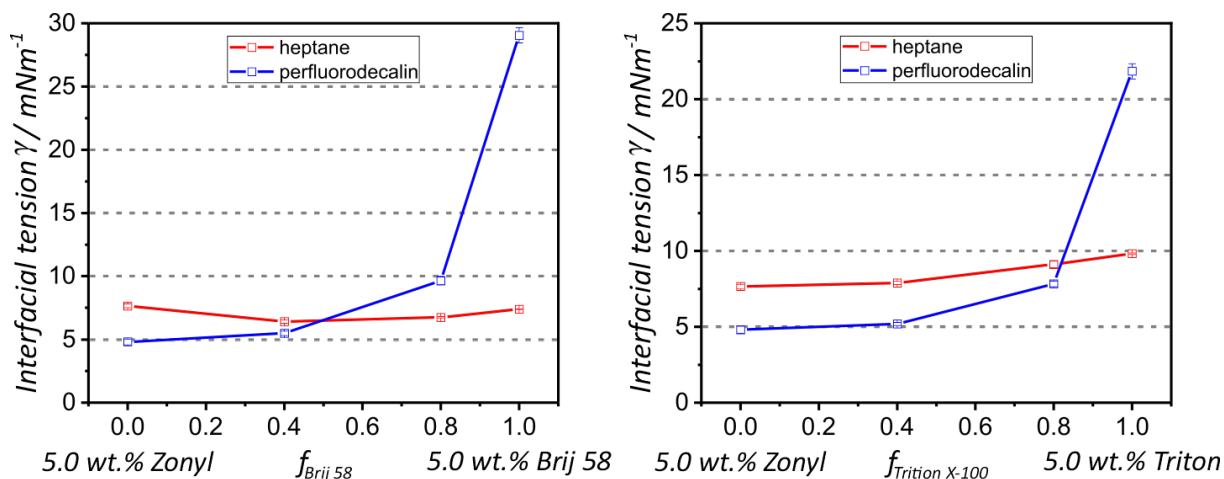
Figure S5. Interfacial tension of the perfluorodecalin-water- and the n-heptane-water interface as a function of the fraction of 5 wt.% Brij 58 ($f_{Brij\ 58}$) and the fraction of 5.0 wt.% Trition-X100 ($f_{Trition\ X-100}$), where the other fraction is 5.0 wt.% Zonyl FS-300. Interfacial tension error bars refer to N ≥ 5 measurements.

10.3   Surfactant and Fluorescent Dye Synthesis

10.3.1   Light-responsive Surfactant AzoTAB

1) 4-butyl-4'-hydroxyazobenzene

15 g (100.5 mmol, 1 eq.) of 4-butylanilin was dissolved in 60 mL of HCl (5 M) at 0 °C. Then 6.934 g (100.5 mmol, 1 eq.) of sodium nitrite in 15 mL of water was added. The reaction mixture was left to react for 1 h at 0 °C. Then 9.458 g (100.5 mmol, 1 eq.) of Phenol and 29.279 g (251.3 mmol, 2.5 eq.) of sodium carbonate in 50 mL water was added. The product was precipitated as a brown solid. The reaction solution was filtered and the product was recrystallized in n-hexane. Then the product was dissolved in acetone and filtered again to separate the NaCl.

Yield: 18.997 g (74 %).

^{1}H-NMR (400 MHz, CDCl$_3$): 7.85 (d, 2H), 7.78 (d, 2H), 7.30 (d, 2H), 6.93 (d, 2H), 2.68 (t, 2H), 1.64 (m, 2H), 1.38 (m, 2H), 0.94 (t, 3H).

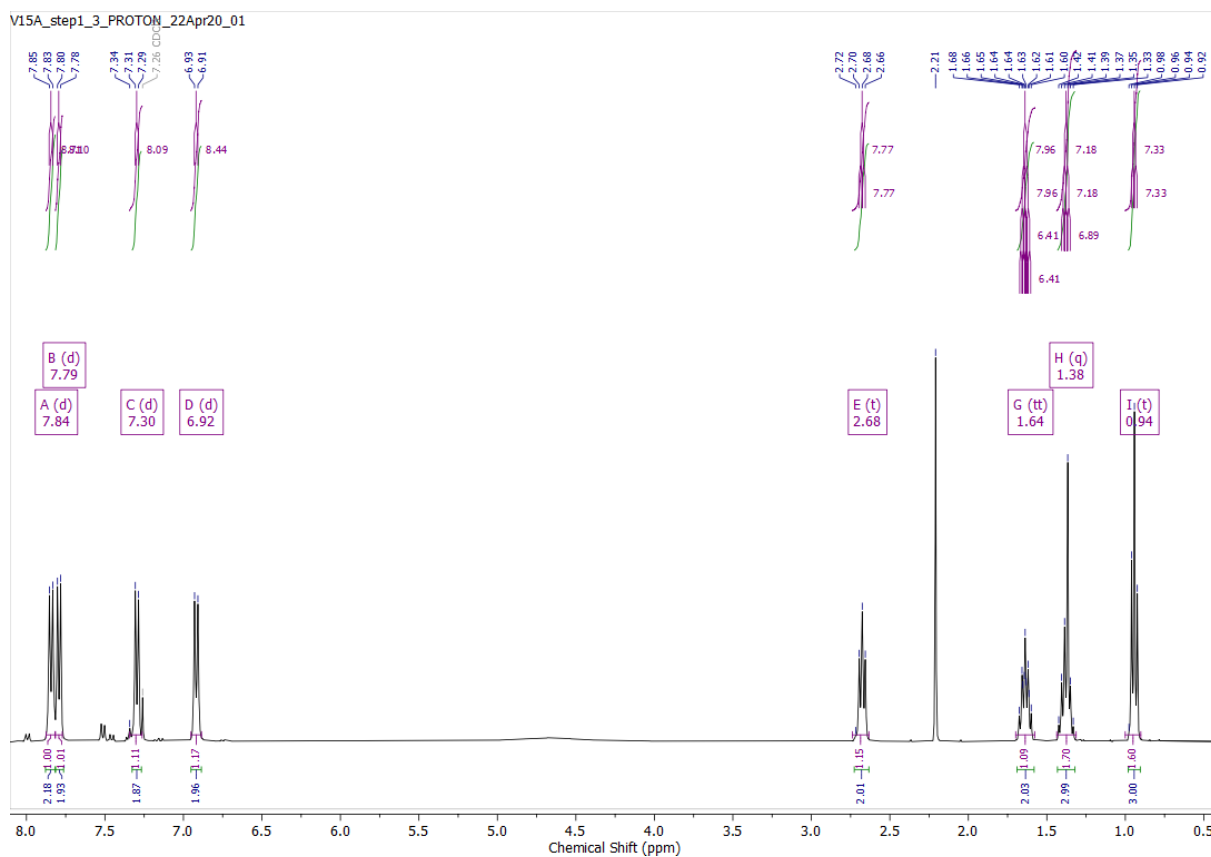Figure S6. ¹H-NMR-spectrum of 4-butyl-4'-hydroxyazobenzene.

2) 4-butyl-4'-(3-bromopropxy)azobenzene

18.997 g of 4-butyl-4'-hydroxyazobenzene (74.7 mmol, 1 eq.) in 100 mL THF was added dropwise into a mixture of 5.029 g potassium hydroxide (89.64 mmol, 1.2 eq.) and 8.38 mL of 1,3-dibromopropane (82.17 mmol, 1.1 eq.). The reaction was refluxed overnight. The crude was filtered to remove the KBr and then evaporated down to an oily solution that was resuspended in n-hexane for precipitation at low temperature. The precipitate was recrystallized and the hot solution was filtered to remove the solid dimer.

Yield: 8.210 g (29 %).

¹H-NMR (400 MHz, CDCl₃): 7.95 (d, 2H), 7.84 (d, 2H), 7.31 (d, 2H), 7.03 (d, 2H), 4.20 (t, 2H), 3.63 (t, 2H), 2.68 (t, 2H), 2.36 (m, 2H), 1.64 (m, 2H), 1.38 (m, 2H), 0.94 (t, 3H).

V15A_step2_3_PROTON_24Apr20_01
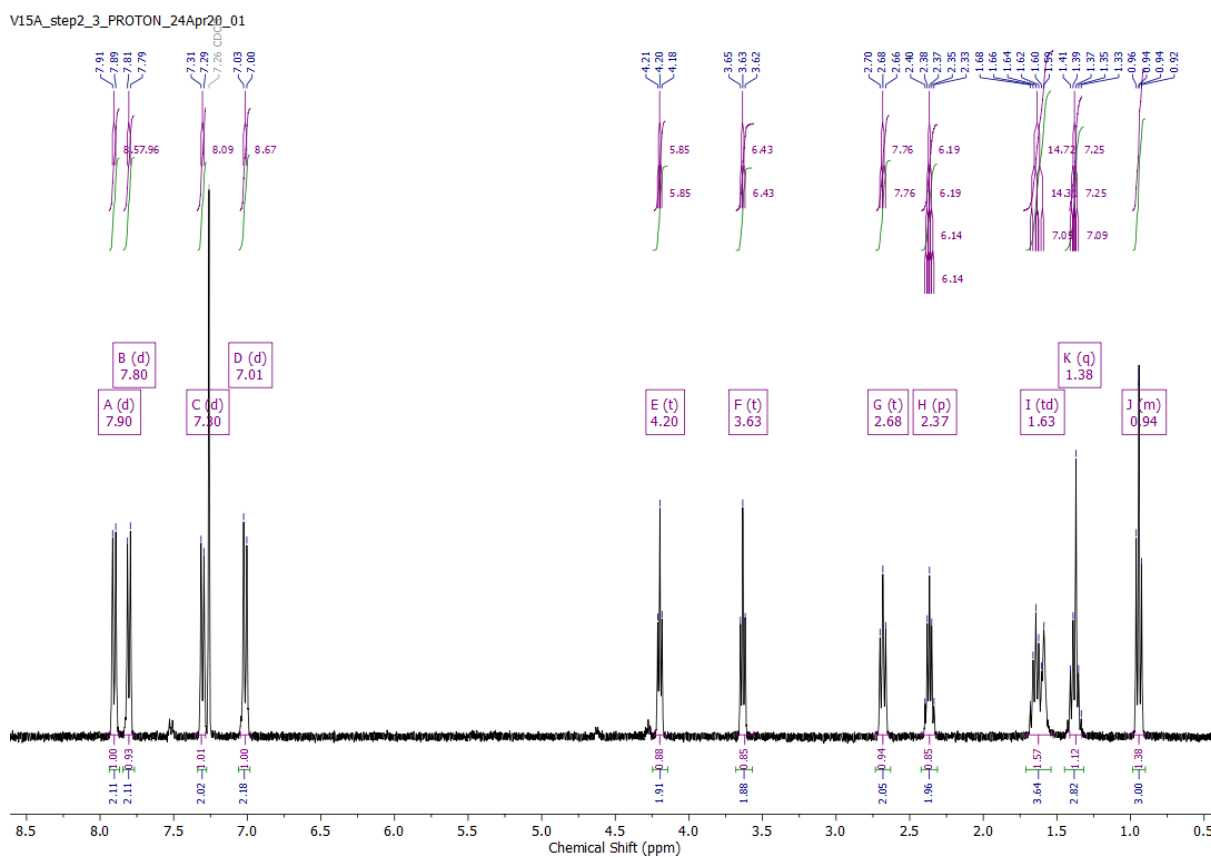
Figure S7. ^{1}H-NMR-spectrum of 4-butyl-4'-(3-bromopropxy)azobenzene.

3) 4-butyl-4'-(3-trimethylammoniumpropoxy)phenylazobenzene (AzoTAB)

8 g of 4-butyl-4'-(3-bromopropxy)azobenzene (21.3 mmol, 1 eq.) was dissolved in 120 mL of ethylacetate and 180 mL of ethanol at 70 °C. 20.36 mL of trimethylamine (35 % in ethanol, 85.3 mmol, 4 eq.) was added dropwise. The reaction was refluxed for 48 h. Upon cooling to RT a precipitate of AzoTAB forms. The precipitate was filtered and recrystallized in a 90:10 v/v mixture of ethylacetate and ethanol.

Yield: 6.631 g (88 %), overall yield: 19 %.

^{1}H-NMR (400 MHz, CDCl$_3$): 7.89 (d, 2H), 7.80 (d, 2H), 7.29 (d, 2H), 7.00 (d, 2H), 4.20 (t, 2H), 3.90 (t, 2H), 3.49 (s, 9H), 2.67 (t, 2H), 2.34 (m, 2H), 1.63 (m, 2H), 1.37 (m, 2H), 0.93 (t, 3H).

Figure S8. ^{1}H-NMR-spectrum of 4-butyl-4'-(3-trimethylammoniumpropoxy)phenylazobenzene (AzoTAB).

10.3.2   4'-[*N*-Dodecanoylamino]benzo-15-crown-5

The synthesis of 4'-[*N*-Dodecanoylamino]benzo-15-crown-5 was adapted from a preparation reported in the literature.[249] It was modified with the addition of column chromatography purification on silica gel.

Dodecanoyl chloride (0.49 mL, 2.05 mmol) solubilized of THF (10 mL) was dropwise added to an anhydrous solution of THF (20 mL) containing 4'-aminobenzo-15-crown-5 (0.5 g, 1.86 mmol) and triethylamine (0.52 mL, 3.72 mmol) under nitrogen atmosphere. The reaction was stirred at room temperature for 2 h, the resulting precipitate was filtered and the solid was concentrated to dryness in vacuo. The residue was dissolved in chloroform (30 mL), washed with water (10 mL), dried over MgSO$_4$, filtered and concentrated. The crude product was purified by column chromatography on silica gel (eluent: 10:1 dichloromethane/methanol) giving the desired compound as colorless crystals.

Yield: 0.538 g (62 %)

^{1}H-NMR (400 MHz, CD$_2$Cl$_2$): δ (ppm) 7.30 (d, J = 2.4 Hz, 1H), 7.24 (s, 1H), 6.91 (dd, J = 8.7, 2.4 Hz, 1H), 6.80 (d, J = 8.6 Hz, 1H), 4.07 (m, 4H), 3.82 (m, 4H), 3.85 (m, 8H), 2.30 (t, J = 7.6 Hz, 2H), 1.67 (m, 2H), 1.20-1.39 (m, 16H), 0.87 (t, 3H).

^{13}C-NMR (100 MHz, CD$_2$Cl$_2$): δ (ppm) 171.4, 149.2, 145.5, 132.9, 114.4, 112.3, 106.8, 70.9, 70.8, 70.4, 70.3, 69.6, 69.4, 68.7, 37.9, 32.3, 30.0, 30.0, 29.9, 29.8, 29.7, 29.6, 25.9, 23.1, 14.3.

HRMS (ESI+/Q-TOF): m/z: [M+Na]$^+$ Calcd. for C$_{26}$H$_{43}$NO$_6$Na: 488.2982; found: 488.2852.
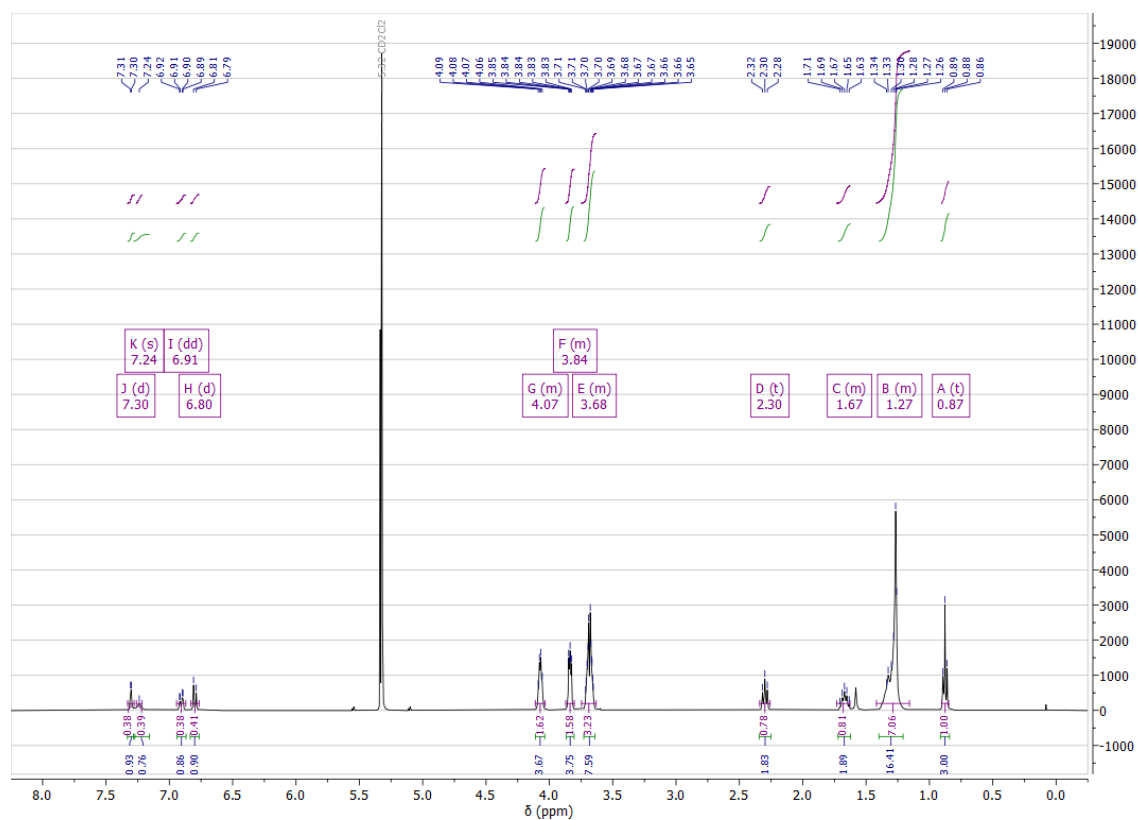
Figure S9. ^{1}H-NMR-spectrum of 4'-[N-dodecanoylamino]benzo-15-crown-5.
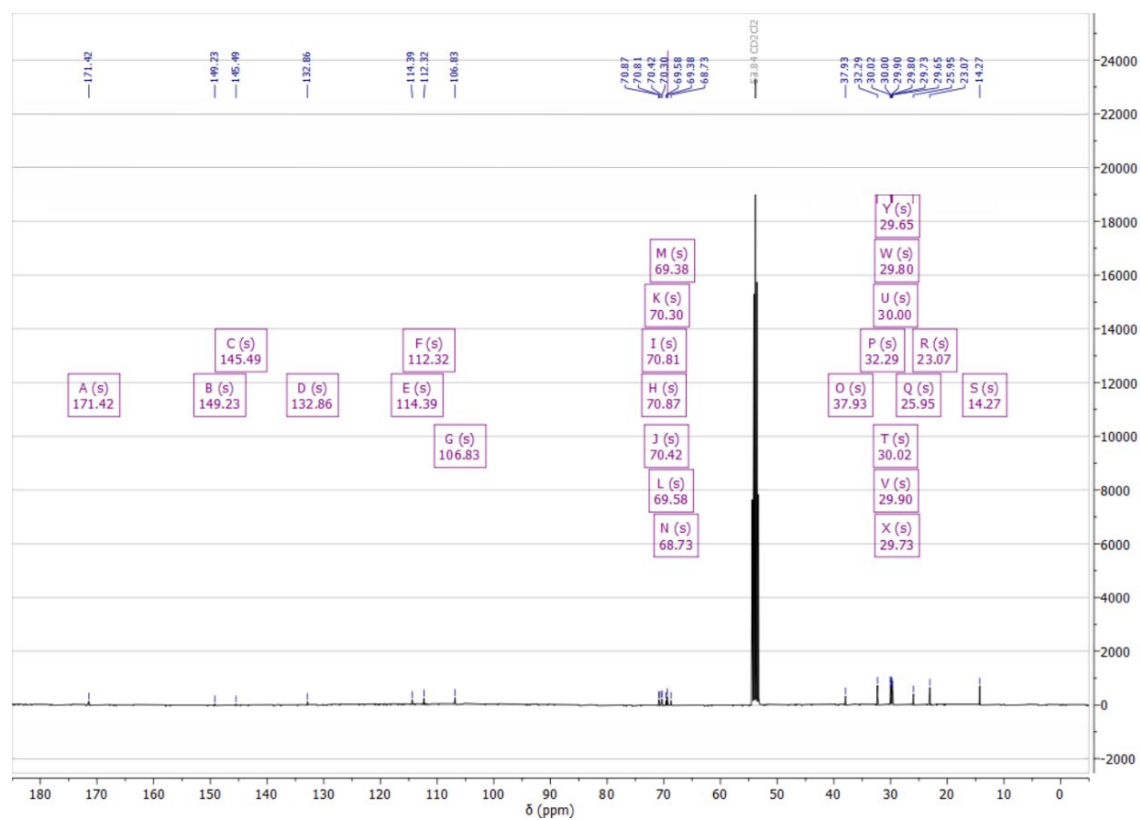
Figure S10. ^{13}C-NMR-spectrum of 4'-[*N*-dodecanoylamino]benzo-15-crown-5.
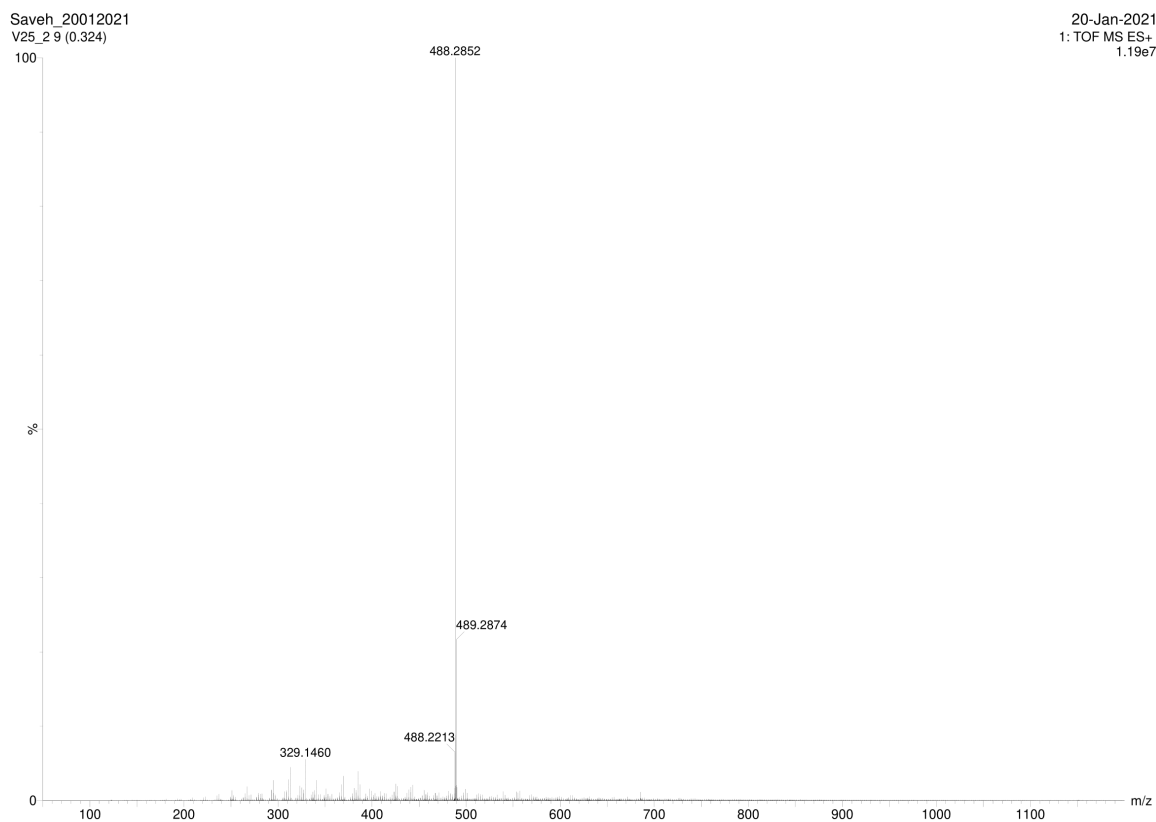
Figure S11. HRMS of 4'-[*N*-dodecanoylamino]benzo-15-crown-5.

10.3.3   4'-[*N*-Dodecanoylamino]benzo-18-crown-6

The synthesis of 4'-[*N*-Dodecanoylamino]benzo-18-crown-6 was adapted from a preparation reported in the literature.[250] It was modified with the addition of column chromatography purification on silica gel.

Dodecanoyl chloride (0.4 mL, 1.68 mmol) solubilized in DCM (10 mL) was added dropwise to an anhydrous DCM solution (20 mL) containing 4'-aminobenzo-18-crown-6 (0.5 g, 1.53 mmol) and triethylamine (0.42 mL, 3.06 mmol). The reaction was stirred at room temperature for 2 h, the resulting precipitate was filtered and the solid was concentrated to dryness in vacuo. The residue was dissolved in chloroform (30 mL), washed with water (10 mL), dried over $MgSO_4$, filtered and concentrated. The crude was purified by column chromatography on silica gel (eluent: 9:1 dichloromethane/methanol) giving the desired compound as colorless crystals.

Yield: 0.24 g (31 %)

^{1}H-NMR (400 MHz, CD_2Cl_2): δ (ppm) 7.72 (s, 1H), 7.31 (d, *J* = 2.4 Hz, 1H), 6.97 (dd, *J* = 8.7, 2.4 Hz, 1H), 6.75 (d, *J* = 8.6 Hz, 1H), 3.82 (m, 4H), 4.08 (m, 4H), 3.65 (m, 12H), 2.31 (t, *J* = 7.6 Hz, 2H), 1.66 (m, 2H), 1.20-1.39 (m, 16H), 0.87 (t, *J* = 6.7 Hz, 3H).

^{13}C-NMR (100 MHz, CD_2Cl_2): δ (ppm) 171.7, 148.5, 144.9, 132.8, 113.1, 112.2, 106.2, 70.4, 69.5, 69.4, 68.5, 68.1, 37.8, 32.3, 30.0, 29.9, 29.8, 29.7, 29.7, 26.0, 23.1, 14.3.

HRMS (ESI+/Q-TOF): m/z: [M+Na]$^+$ Calcd. for $C_{28}H_{47}NO_7Na$: 532.3244; found: 532.3115.

Figure S12. ^{1}H-NMR-spectrum of 4'-[*N*-dodecanoylamino]benzo-18-crown-6.

Figure S13. ^{13}C-NMR-spectrum of 4'-[*N*-dodecanoylamino]benzo-18-crown-6.
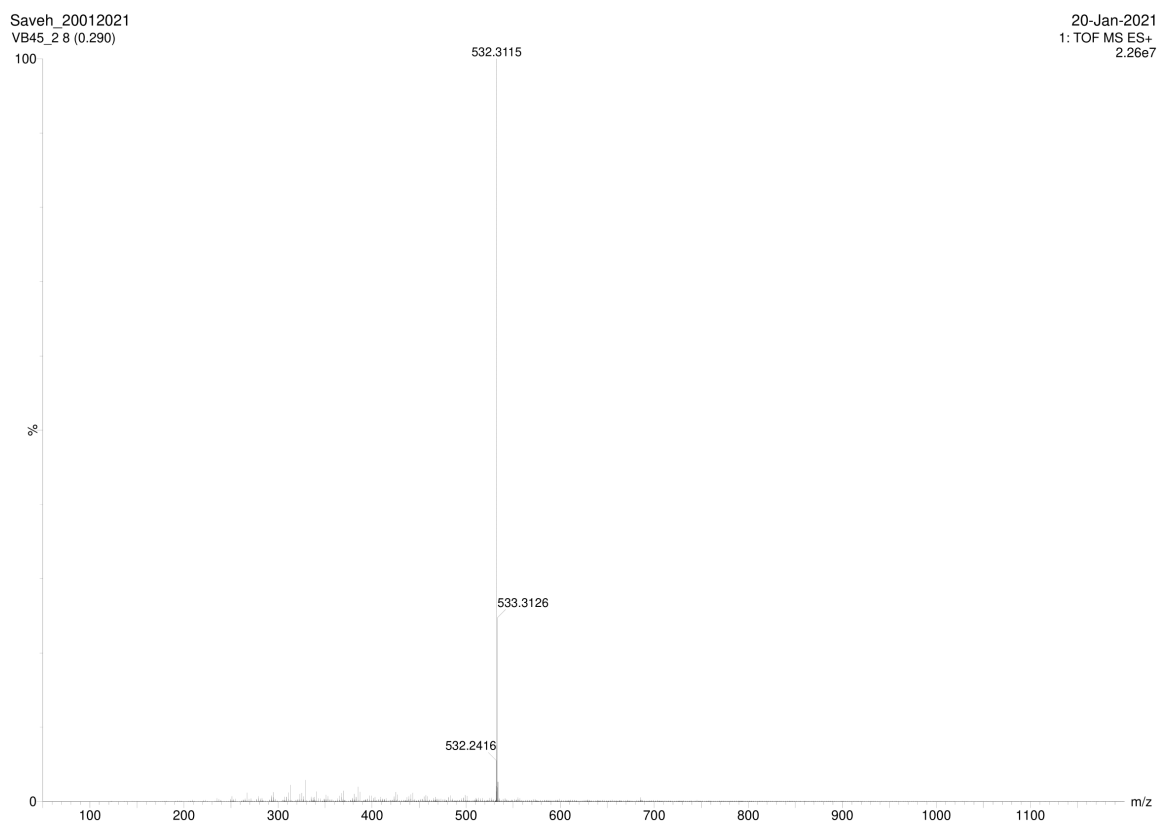
Figure S14. HRMS of 4'-[*N*-dodecanoylamino]benzo-18-crown-6.

10.3.4   pH-Responsive Surfactant N$^+$-(16)-N

The following synthesis route was adapted from literature.[245]

1) Hexadecanedioyl dichloride

1,16-hexadecanioc acid (2.5 g, 8.7 mmol) was added to a three-necked flask equipped with a condenser. Then three drops of *N,N*-dimethylformamide were added as a catalyst. Then thionyl chloride (2.6 g, 22 mmol) was slowly dropped in over 30 min. The mixture was stirred at 60 °C for 1 h. After that, excess thionyl chloride was removed by vacuum distillation under reduced pressure. Hexadecanedioyl dichloride was obtained as a slightly yellow liquid.

Yield: 2.51 g (98 %)

^{1}H-NMR (400 MHz, CDCl$_3$): δ (ppm) 2.88 (t, 4H), 1.70 (m, 4H), 1.31 (m, 16H).
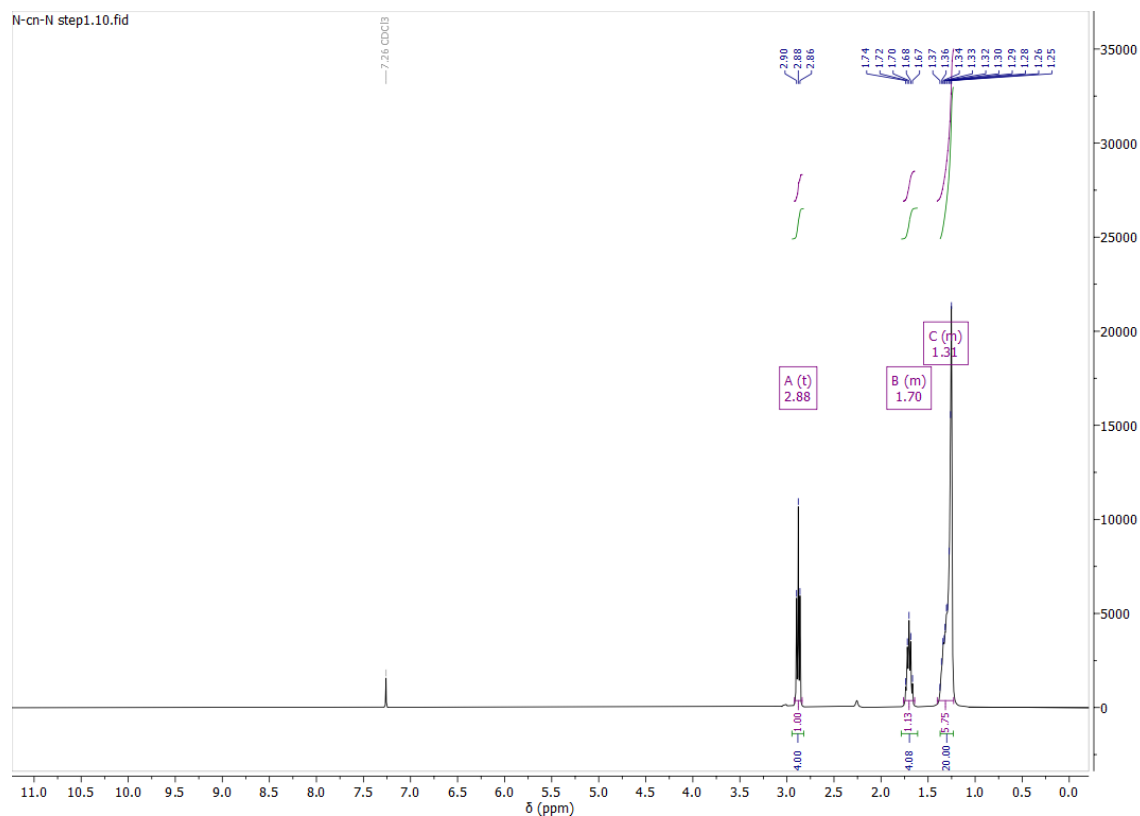
Figure S15. ^{1}H-NMR-spectrum of hexadecanedioyl dichloride.

2) N^1,N^1,N^{16},N^{16}-Tetramethylhexadecanediamide

An aqueous solution of diemethylamine (40 % in water, 15.4 g, 137 mmol) was placed in an ice bath and then a DCM solution of hexadecanedioyl dichloride (2.5g, 8.47 mmol) awas added dropwise. After reacting for 2 h the solution was extracted with DCM three times and the extract was dried with anhydrous MgSO$_4$. After filtration and removing the solvent, the residue was recrystallized in acetone. After vacuum drying, N^1,N^1,N^{16},N^{16}-tetramethylhexadecanediamide was obtained as a white solid.

Yield: 2.184 g (82.5 %)

^{1}H-NMR (400 MHz, CDCl$_3$): δ (ppm) 2.97 (d, 12H), 2.30 (t, 4H), 1.62 (m, 4H), 1.28 (m, 20H).
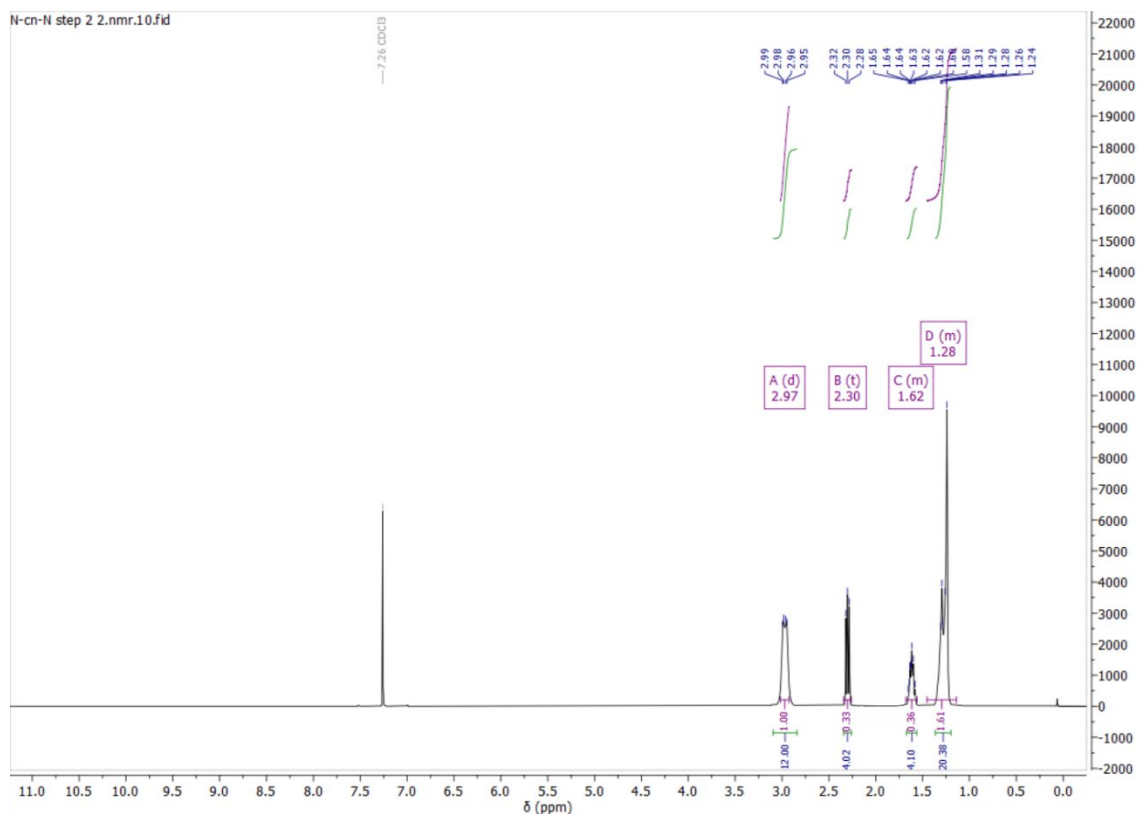
Figure S16. ¹H-NMR-spectrum of N^1,N^1,N^{16},N^{16}-tetramethylhexadecanediamide.

3) N^1,N^1,N^{16},N^{16}-Tetramethylhexadecane-1,16-diamine

30 mL dry THF as a solvent was added to a three-necked flask. Then LiAlH₄ (0.588 g, 17 mmol) and N^1,N^1,N^{16},N^{16}-tetramethylhexadecanediamide (2.1 g, 6.72 mmol) were added in batch. The mixture was was brought to reaction at 72 °C for about 2 h. After cooling to room temperature, the reaction mixture was quenched by adding 0.5 mL water and 0.5 mL aqueous NaOH solution (15 wt.%) and stirred for 30 min. Excess anhydrous MgSO₄ was added to remove water and the mixture was filtered afterwards. The resulting filtrate was evaporated under reduced pressure to remove the solvent. N^1,N^1,N^{16},N^{16}-Tetramethylhexadecane-1,16-diamine was obtained as a yellow liquid.

Yield: 1.621 g (77 %)

¹H-NMR (400 MHz, CDCl₃): δ (ppm) 2.35-2.22 (m, 16H), 1.49 (m, 4H), 1.26 (m, 24H).
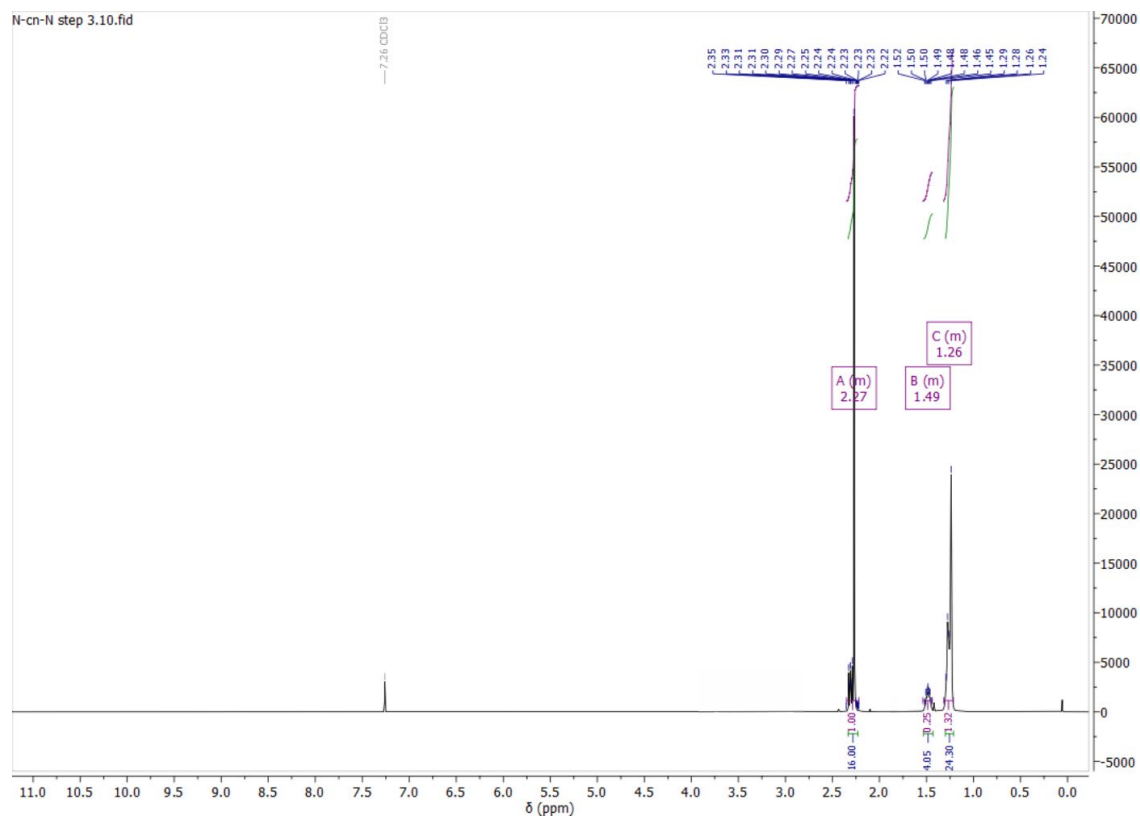
Figure S17. ¹H-NMR-spectrum of N^1,N^1,N^{16},N^{16}-tetramethylhexadecane-1,16-diamine.

4) 16-(Dimethylamino)-*N,N,N*-trimethylhexadecan-1-aminium iodide (N⁺-(16)-N)

N^1,N^1,N^{16},N^{16}-Tetramethylhexadecane-1,16-diamine (1.621 g, 5.18 mmol) was added into the reaction vessel, which contained 25 mL cooled ethanol as a solvent. Cooled methyl iodide (0.22 mL, 3.52 mmol) was added quickly. The mixture was brought to reaction at 60 °C for 10 h. The ethanol was removed under reduced pressure after the reaction was complete. The residue was recrystallized with acetone. 16-(Dimethylamino)-*N,N,N*-trimethylhexadecan-1-aminium iodide (N⁺-(16)-N) was received as a white powder.

Yield: 2.2148 g (94 %)

¹H-NMR (400 MHz, DMSO-d₆): δ (ppm) 3.24 (t, 2H), 3.02 (s, 9H), 2.14 (t, 2H), 2.07 (s, 6H), 1.65 (m, 2H), 1.43-1.25 (m, 26H).
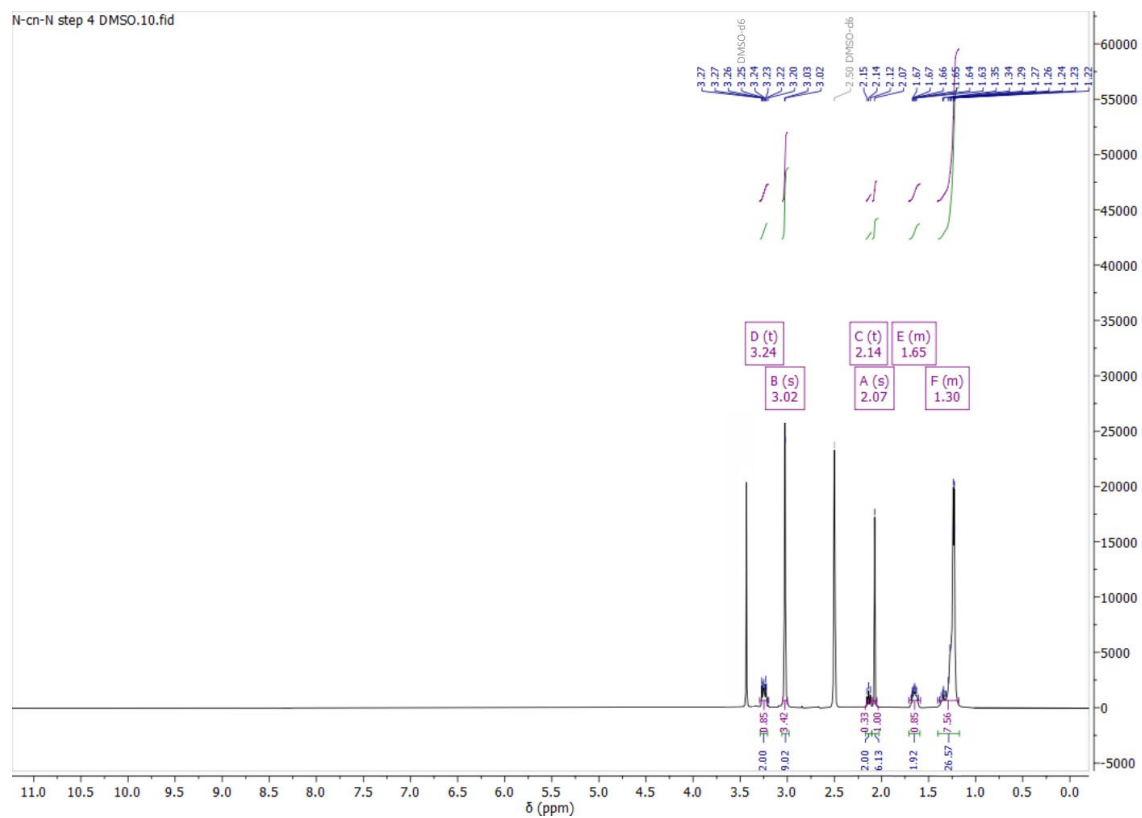
Figure S18. ¹H-NMR-spectrum of 16-(dimethylamino)-*N,N,N*-trimethylhexadecan-1-aminium iodide (N⁺-(16)-N).

10.3.5   Potassium Tetraacetate-Riboflavin (K-TARF)

The following synthesis route towards potassium 2-(7,8-dimethyl-2,4-dioxo-10-((2S,3S,4R)-2,3,4,5-tetraacetoxypentyl)-4,10-dihydropyrimido[4,5-b]quinolin-3(2H)-yl)acetate (K-TARF) was performed by my co-worker Dr. Pablo Simón Marqués who contributed to the crown ether project:
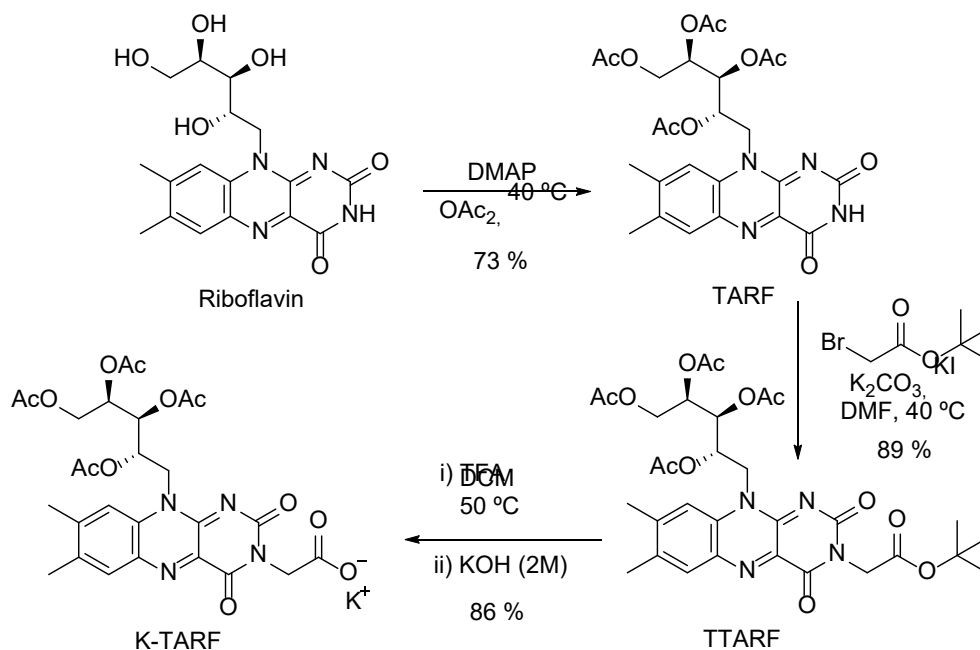

Figure S19. Synthesis route to K-TARF.

1) (2R,3S,4S)-5-(7,8-Dimethyl-2,4-dioxo-3,4-dihydrobenzo[g]pteridin-10(2H)-yl)pentane-1,2,3,4-tetrayl tetraacetate (TARF)

Under an inert atmosphere of nitrogen, a round bottom flask was charged with riboflavin (2.0 g, 5.3 mmol) and DMAP (2.6 g, 21.3 mmol). The solid was suspended in acetic anhydride and the reaction stirred overnight at 40 °C. Thereafter, the crude was diluted in chloroform (60 mL), washed with NH_4Cl saturated aqueous solution (40 mL) and extracted again with chloroform (2 x 60 mL).The combined organic layers were dried over Mg_2SO_4 and concentrated under reduced pressure. 2.1 g of the final product were obtained, after successive recrystallizations with EtOH/Et_2O as an orange-yellow solid.

Yield: 2.1 g (73 %)

^{1}H-NMR (400 MHz, $CDCl_3$): δ (ppm) 8.50 (s, 1H), 8.03 (s, 1H), 7.57 (s, 1H), 5.66 (d, J = 9.4 Hz, 1H), 5.50 – 5.36 (m, 2H), 4.90 (s, 2H), 4.43 (dd, J = 12.4, 2.8 Hz, 1H), 4.24 (dd, J = 12.3, 5.7 Hz, 1H), 2.57 (s, 3H),

2.48 – 2.40 (m, 3H), 2.28 (s, 3H), 2.21 (s, 3H), 2.08 (s, 3H), 1.76 (s, 3H). Signals in accordance with the literature.[251]
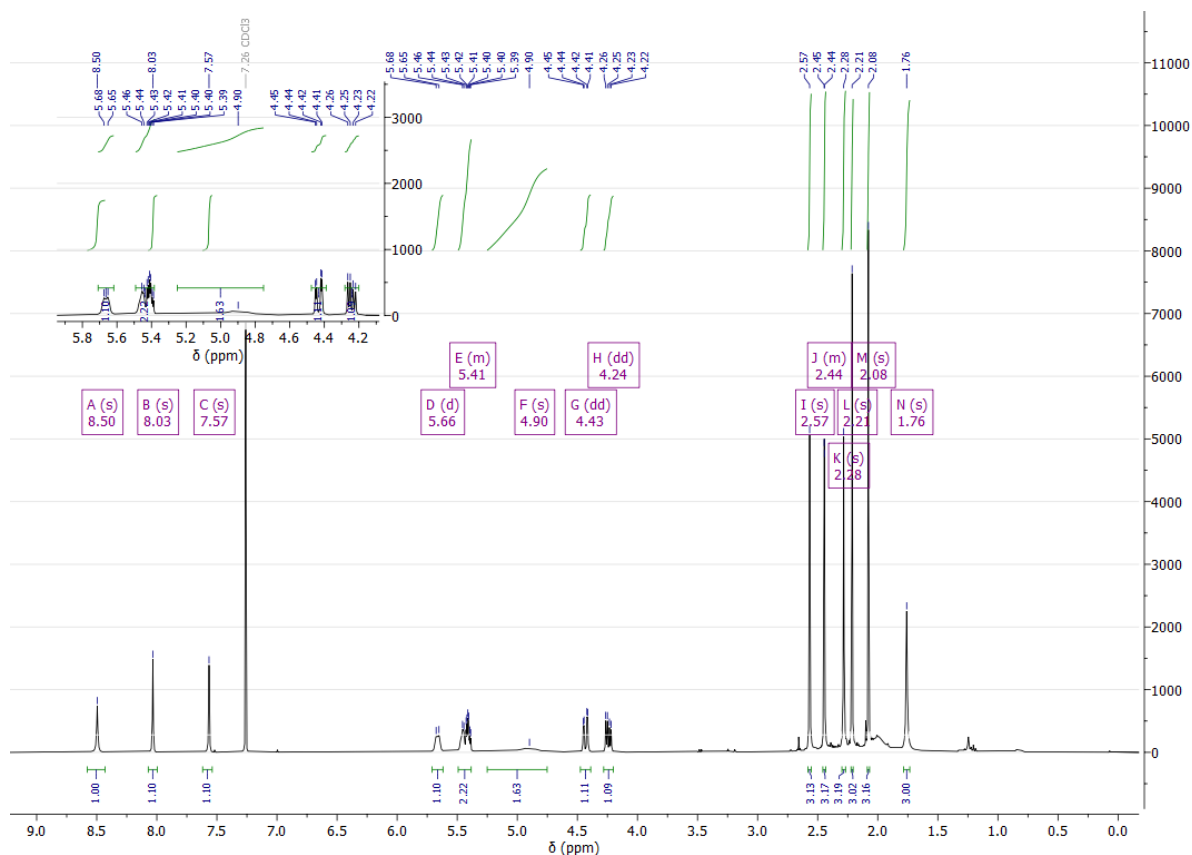

Figure S20. ^{1}H-NMR-spectrum of TARF.

2) (2R,3S,4S)-5-(3-(2-(Tert-butoxy)-2-oxoethyl)-7,8-dimethyl-2,4-dioxo-3,4-dihydrobenzo[g]pteridin-10(2H)-yl)pentane-1,2,3,4-tetrayl tetraacetate (TTARF)

A spatula-tip of KI was added to a suspension of TARF (500 mg, 0.9 mmol) and K$_2$CO$_3$ (152 mg, 1.1 mmol) in DMF (10 mL). After stirring the mixture for 30 min under inert atmosphere, t-Bu-2-bromoacetate (0.94 mL, 6.43) was dropwise added and then the reaction stirred for 20 h at 40 °C. Once cooled-down, the crude was diluted in DCM and washed with NaHCO$_3$ saturated aqueous solution, brine and water and the organic phase was dried under vacuum. Eventually, the final compound was obtained as a orange powder after purification by column chromatography (eluent: ethyl acetat/dichloromethane 1:1).

Yield: 0.537 g (89 %)

^{1}H-NMR (400 MHz, CDCl$_3$)**:** δ (ppm) 8.01 (s, 1H), 7.55 (s, 1H), 5.68 – 5.60 (m, 1H), 5.47 – 5.35 (m, 2H), 4.84 (s, 2H), 4.71 (s, 2H), 4.41 (dd, J = 12.4, 2.7 Hz, 1H), 4.24 (dd, J = 12.3, 5.5 Hz, 1H), 2.55 (s, 3H), 2.42

(3, 3H), 2.29 (s, 3H), 2.20 (s, 3H), 2.06 (s, 3H), 1.75 (s, 3H), 1.45 (s, 9H). Signals in accordance with the literature.[251]
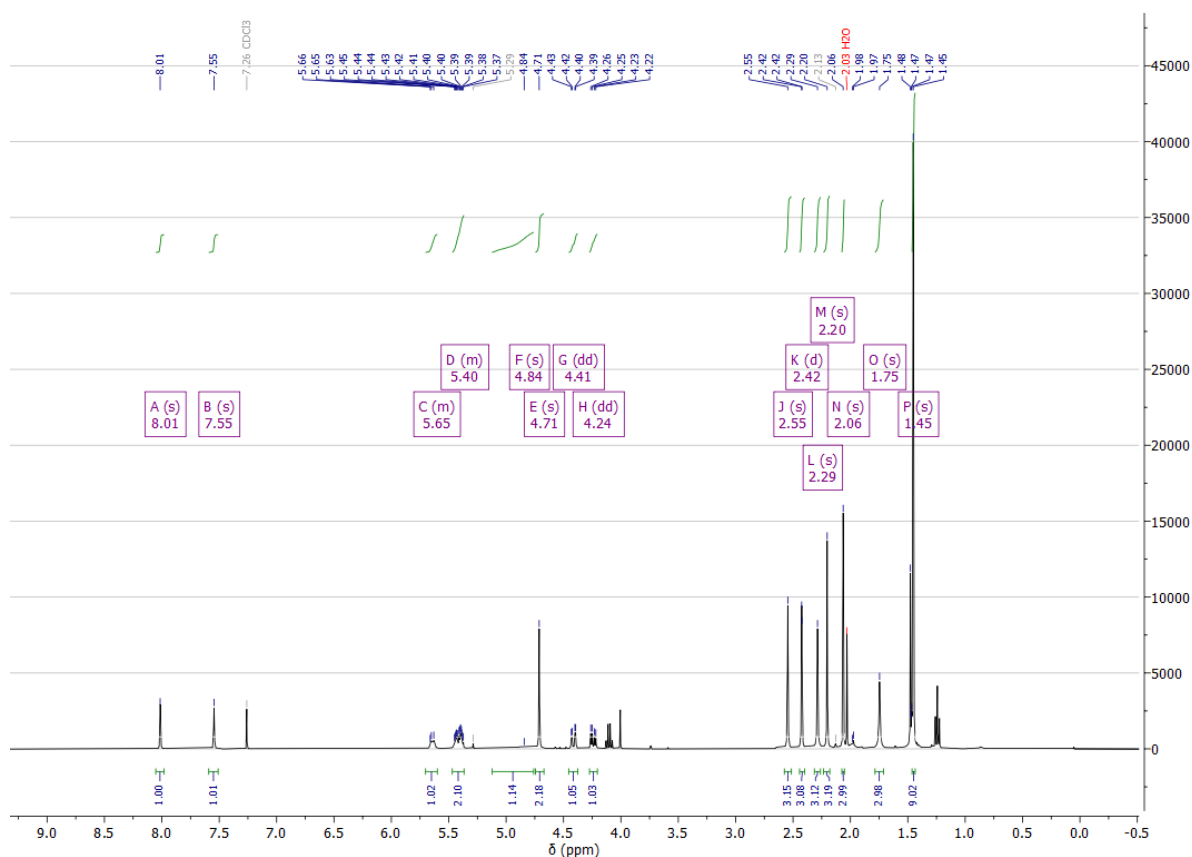

Figure S21. ^{1}H-NMR spectrum of TTARF.

3) Potassium 2-(7,8-dimethyl-2,4-dioxo-10-((2S,3S,4R)-2,3,4,5-tetraacetoxypentyl)-4,10-dihydropyrimido[4,5-b]quinolin-3(2H)-yl)acetate (K-TARF)

TTARF (750 mg, 1.14 mmol) was solved in dry DCM (10 mL) under nitrogen atmosphere. At 0 °C 2 mL of TFA were dropwise added to the solution and the reaction stirred for 5 h in reflux. After cooling to room-temperature the crude was poured into ice water and TFA quenched with NaHCO3 until pH 6. The organic phase was separated and the aqueous one extracted with DCM (15 mL x 2). The combined organic layers were dried over Mg_2SO_4 and the solvent evaporated under rotatory vacuum to obtained the desired acid as an orange solid.

To obtain the potassium salt, 100 mg of the acid (0.16 mmol) were solubilized in 2 mL of DMF and KOH aqueous solution (2 M, 83 µL, 0.16 mmol) was added to the solution. After 1 h of stirring the solvent was removed in vacuum and the final product was obtained as an orange solid.

Yield: 166 mg (86 %, in two steps)

^{1}H-NMR (400 MHz, D$_2$O): δ (ppm) 7.81 (s, 1H), 7.73 (s, 1H), 5.64 – 5.57 (m, 1H), 5.53 – 5.48 (m, 1H), 5.45 – 5.40 (m, 1H), 5.05 (s, 2H), 4.53 – 4.43 (m, 3H), 4.33 (dd, J = 12.6, 5.5 Hz, 1H), 2.53 (s, 3H), 2.39 (3, 3H), 2.19 (s, 3H), 2.18 (s, 3H), 2.00 (s, 3H), 1.66 (s, 3H).

^{13}C-NMR (100 MHz, D$_2$O): δ (ppm) 174.4, 173.6, 172.7, 172.6, 160.6, 156.4, 150.3, 148.8, 138.9, 134.6, 134.0, 131.2, 130.8, 116.0, 70.5, 69.7, 62.0, 45.0, 44.5, 36.8, 31.3, 20.8, 20.4, 20.1, 20.0, 19.6, 18.5.

MS (ES+): m/z: 663.4 [M+Na]$^+$, 685.4 [M+Na2-H]$^+$. HRMS (ES+/Q-TOF): m/z: [M-K+H]$^+$ Calcd. for C$_{27}$H$_{30}$N$_4$O$_{12}$: 603.1932; found: 603.1930.
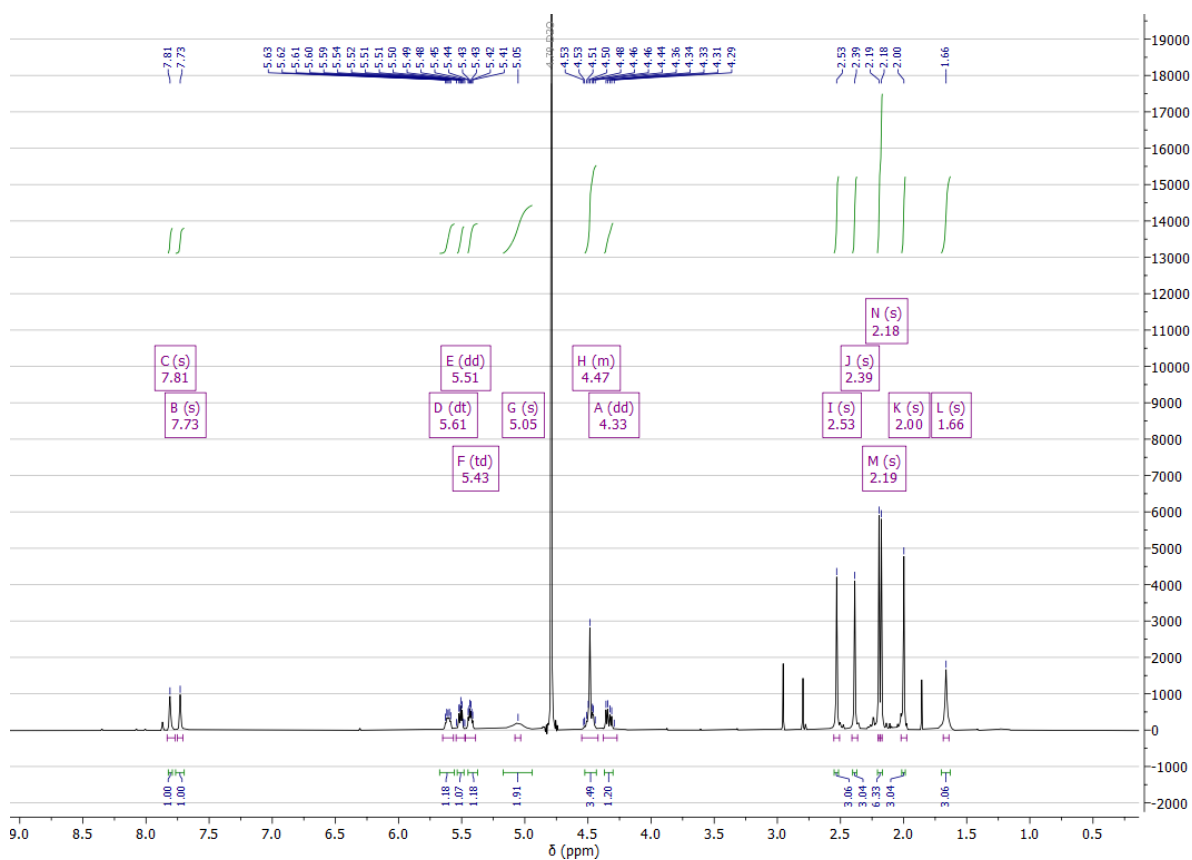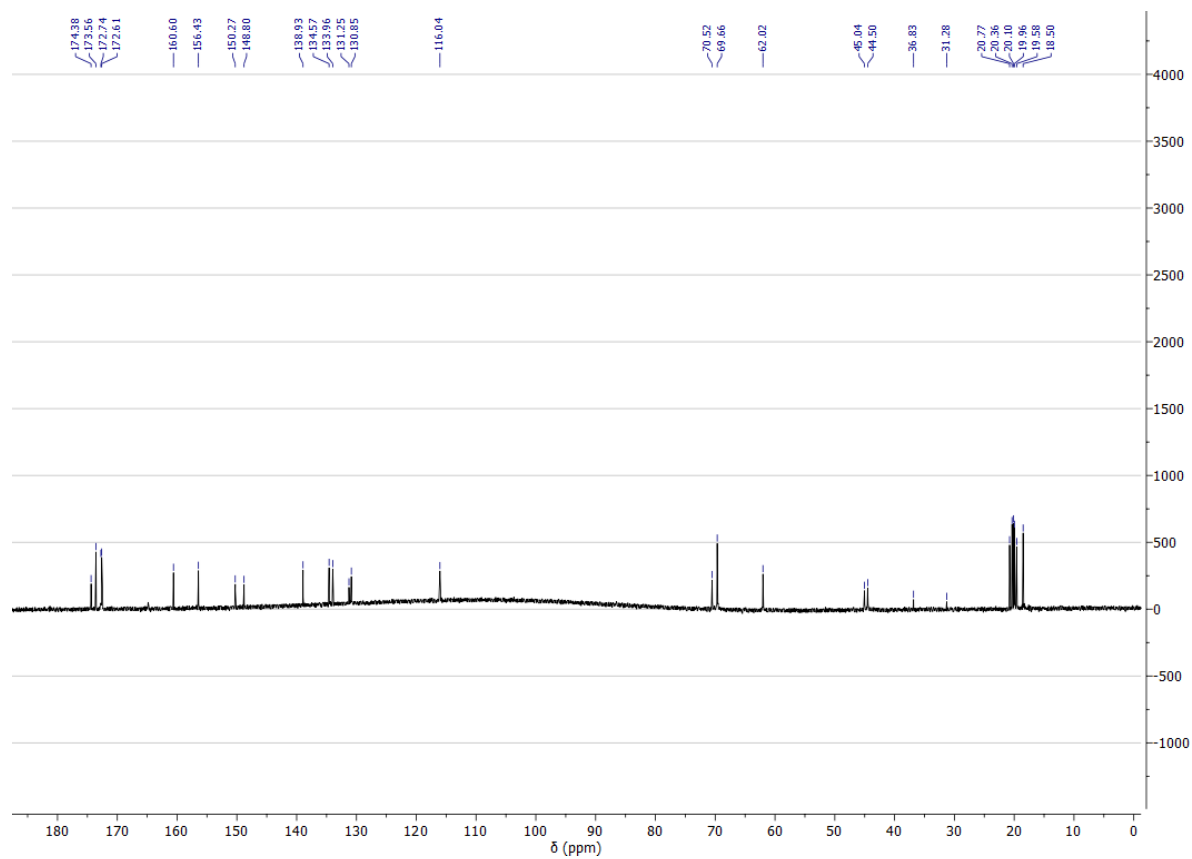

Figure S22. ^{1}H-NMR-spectrum of K-TARF.

Figure S23. ^{13}C-NMR-spectrum of K-TARF.